Studying the Inner Regions of Young Binary Systems with Near-Infrared Interferometry

Sebastian Antonio Zarrilli

Submitted by Sebastian Antonio Zarrilli to the University of Exeter as a thesis for the degree of Doctor of Philosophy in Physics, 3rd of January 2023.

I certify that all material in this thesis which is not my own work has been identified and that no material has previously been submitted and approved for the award of a degree by this or any other University.

Signed: .....

Sebastian Antonio Zarrilli

Date: .....

Abstract

The circumstellar regions of young stellar objects (YSOs) are some of the most interesting environments in astronomy. The leftover material from star formation takes the form of enormous discs of dust and gas extending out to a thousand astronomical units. The outer regions of these protoplanetary discs, being cold and relatively large in scale, have been extensively studied by radio telescopes. Usually shrouded in opaque dust, the regions closer to the stars are best studied in the infrared. Here, the central YSO interacts with the disc, accreting and ejecting material, and planets, asteroids and comets are formed. Understanding how stars interact with their discs can therefore tell us how both evolve, and can help us understand the origin of our own solar system. It also can teach us more about systems very different to our own – such as binary systems. The majority of stars are part of multiple systems, and in recent years we have also found increasing numbers of binary YSOs. The dynamical interaction between the stars and the inner disc can lead to complex features such as spirals, warps and disc truncation, affecting their rates of accretion and ejection, as well as affecting planetary formation. As the population of binary YSOs grows, we are finding a much larger diversity in the inner regions of their discs than previously thought. Observing these processes has historically been difficult because of the extremely small angular scales on which they occur – on the order of milli-arcseconds – which limits their study with traditional telescopes.

In spite of this, the study of young stars and their discs has rapidly become one of the most dynamic areas of astronomy in recent decades. Advances in computing power have allowed for more complex simulations of circumstellar environments. Simultaneously, developments in technology and engineering have substantially increased the set of observable protoplanetary discs, allowing us to rapidly develop and advance ideas of star formation and evolution. The focus of my PhD was on one such technique: near-infrared interferometry. By interfering the light from multiple individual telescopes, it is possible to obtain resolutions far in excess of any single-dish telescope, allowing us to probe inner disc regions with a precision never before possible. This is especially important in the context of close binary YSOs, where dynamic interactions between the stars and the disc can cause large changes to the circumstellar environment which cannot be reliably determined from simulations. In these cases, the feedback from observations of individual systems can be used to calibrate and inform further refinements to the theory.

The thesis is laid out as follows. Chapter 1 introduces the general star formation

paradigm, including star formation and YSO classification, as well as a discussion on circumstellar discs around single stars. In Chapter 2, I extend this to binary objects, which were the focus of my research. Chapter 3 describes the basic theory behind optical and near-infrared interferometry, its history and the challenges which it poses to anyone wishing to interpret its observables. In this chapter I describe the basic operation of the interferometers which I used over the course of my PhD, the VLTI and the CHARA Array. After this theoretical overview, I present the work which was the focus of my PhD: a deep study into two individual young binary systems.

Chapter 4 is dedicated to analysis of observations we took of MWC 166 A, a massive YSO with a combined mass of 17 $M_\odot$ located at a distance of 1 kpc. This is a mysterious system with very strong K-band line emission, often associated with disc accretion, but little evidence of a substantial disc itself. In this chapter, I define for the first time a full three-dimensional orbit of the system, which has a period of 368 d, and establish stellar parameters and the evolutionary state of both components, finding that the primary component is likely a main-sequence object while the secondary is just in the process of final contraction. I also constrain the geometry and spectral characteristics of the Br γ and He I emission lines, and find the most likely origin to be a Be decretion disc in Keplerian rotation. Chapter 5 uses similar techniques to analyse a rather different young binary, HD 104237 A. This T Tauri with a combined mass of 4.3 $M_\odot$ lies about ten times closer to us and has a much tighter orbit of 20 d. It also has a much denser inner disc region than MWC 166 A, with both components actively accreting from the circumbinary disc, and this is reflected in the strong but variable Br γ emission arising from the two components. In this chapter, I derive an orbit for the system, constrain its age and determine fundamental stellar parameters for both components. I also model the circumstellar emission both in the dust continuum, which takes the form of a truncated circumbinary disc, and analyse the rapidly-changing Br γ emission in the inner region on an epoch-by-epoch basis. This emission shows signs of variable accretion onto both stars, as well as components originating from the circumbinary environment.

Both these studies use spectro-astrometric and spectro-interferometric techniques to showcase the usefulness of the high angular resolution afforded by near-infrared interferometry to gain unique insights into binary-disc interaction, dynamical truncation and binary accretion. This process will only accelerate in future, as new designs of interferometers with even greater precision will unlock an ever-larger tranche of systems, expanding our knowledge of these endlessly-fascinating objects further and further.

Contents

List of Figures

List of Tables

Declaration

This thesis contains work published or pending publication as papers. Chapter 4 is an adaptation of my paper, "Characterising the orbit and circumstellar environment of the high-mass binary MWC 166 A", published as Article 146 in Astronomy & Astrophysics Volume 665. Sections of this paper have also been used in Chapters 1, 2 and 6. The work on HD 104237 A in Chapter 5 is currently in preparation to be published as an article in the near future.

Acknowledgements

The last four and a half years have been at times a joy, an elation, an ecstasy; at times they have been a frustrating, maddening Sisyphean struggle. They certainly have been the most memorable years of my life. The astrophysics department at the University of Exeter is truly like no other place I have ever experienced. The privilege of working in an environment which is – all at once – a support group, a think tank, a sports club and a fraternity is something I will treasure for the rest of my days. It helped me enjoy highest of highs and to endure the lowest of lows – even in the depths of the coronavirus pandemic, which seemed endless, my friends were there to help me through. I couldn't have done it without them.

I would like to thank the many people who helped me on my academic journey, but space constraints restrict me to just a couple. First of all, I would like to thank my supervisor, Stefan Kraus, for introducing me to this world and for giving me the opportunity to explore my love of astronomy using some of the most advanced telescopes in the world. I would like to thank all the other members of the 'Exeter Disc Interferometry Group' members past and present, but I want to resrve a special mention for Claire Davies. Claire helped me to fit in not only at Exeter, but also in the world of research more generally. Her drive and work ethic are inspirational, and the pastoral support which she excels at was indispensable for helping me to achieve my potential. I would like to thank Antoine Mérand for all of his help with geometric modelling using PMOIRED. A lot of the work in this thesis would be of a much worse standard, were it not for his clever and concise explanations of the functioning of both the general scientific principles and the software itself – not to mention the time he took to help me with very specific issues regarding my research.

Finally, I would like to thank my family, which was an invaluable source of support for me before and throughout my PhD. It was my grandfather, Colin, who first sparked a lifelong love in me for all things space-related. Every time my grandparents would visit me and my family in Italy, he would bring cassettes of astronomy documentaries and little booklets of fun space facts which he would write himself. It is no exaggeration to say that he started me on the path which has culminated in this thesis. And, of course, I wouldn't be where I am today without the help, support and unconditional love of my parents. Their belief in me gave me courage to continue even when it sometimes felt impossible.

Seb Zarrilli

Exeter, U.K.

Christmas 2022

Chapter 1

Star formation, young stellar objects and protoplanetary discs

1.1 Star formation

The birth of a star is not a discrete event, but rather a continuous process of evolution, from molecular cloud to fully self-sustaining main sequence object. Star forming regions are enormous complexes of mainly hydrogen gas stretching for dozens of parsecs. Small perturbations within these clouds can, over long timescales, cause regions to begin to collapse under their own gravity, leading to the formation of stars (e.g. McKee and Ostriker 2007). The perturbations that can bring about fragmentation and collapse are generally caused by external events, such as cloud-cloud collision or shockwaves due to supernovae (e.g. Dobbs et al. 2014). Molecular cloud fragmentation is a complex process which has been extensively studied with smoothed particle hydrodynamics (SPH) simulations (e.g. Bonnell et al. 2003). In the following sections I will outline the physical basis for how clouds form stars.

1.1.1 Cloud collapse

A spherical cloud with radius R and at a uniform temperature T is said to be in hydrostatic equilibrium when gravitational contraction is balanced by gas pressure. It is described by

the following equation:

$$\frac{\mathrm{d}P}{\mathrm{d}r} = -\rho(r)\frac{Gm(r)}{r^2}, \tag{1.1}$$

where m is the mass inside r, ρ is the density at r, P is the gas pressure, G is the gravitational constant, and $r \in [0, R]$. If we multiply equation 1.1 by the volume $V = \frac{4}{3}\pi r^3$, substitute $\mathrm{d}r = \mathrm{d}m/(4\pi r^2\rho)$, and integrate over the entire cloud:

$$\int_0^M P\frac{\mathrm{d}m}{\rho} = \frac{1}{3}\int_0^M \frac{Gm}{r}\mathrm{d}m, \tag{1.2}$$

where the total cloud mass is defined as $M \equiv m(R)$, and the boundary conditions $V(0) = 0$ and $P(R) = 0$ have been applied. Within the context of a molecular cloud, assuming an ideal gas, we can additionally substitute for the pressure exerted by a single particle $P = \frac{\rho k_\mathrm{B} T}{(1-\gamma)m_\mathrm{H}\mu}$, where m_H is the atomic mass of hydrogen, μ is the mean molecular weight, γ is the adiabatic index, and k_B is the Boltzmann constant. Since the energy per particle of an ideal gas is given by $E_\mathrm{k} = \frac{3}{2}\frac{k_\mathrm{B}T}{(1-\gamma)m_\mathrm{H}\mu}$, we can write the left-hand side of Equation 1.2 in terms of energy:

$$\int_0^M E_\mathrm{k}\,\mathrm{d}m = -\frac{1}{2}\int_0^M \frac{Gm}{r}\,\mathrm{d}m. \tag{1.3}$$

Since the right-hand side is simply the gravitational potential energy, Equation 1.3 is actually a representation of the virial theorem, $K = \frac{1}{2}|U|$, where K is the total kinetic energy and U is the total potential energy. K and U naturally follow from Equation 1.3:

$$K = M\frac{k_\mathrm{B}T}{(1-\gamma)m_\mathrm{H}\mu}, \tag{1.4}$$

$$U = -\frac{3}{5}\frac{GM^2}{R}, \tag{1.5}$$

with the factor of $\frac{3}{5}$ originating from the geometry of a spherical cloud. Small differences in density within the cloud can, over long timescales, cause it to begin to collapse, as long as the mass of the cloud exceeds a critical mass where the cloud is in virial equilibrium, known as the Jeans mass M_J (Jeans 1902). By looking at Equation 1.3, we can find that this criterion is fulfilled at a length scale of $r = R_\mathrm{J}$, the Jeans radius, such that

$M_{\rm J} = \frac{4}{3}\pi\rho R_{\rm J}^3$:

$$\frac{k_{\rm B}T}{(1-\gamma)m_{\rm H}\mu} = \frac{3}{10}\frac{GM_{\rm J}}{R_{\rm J}},$$

$$\Rightarrow R_{\rm J} = \left[\frac{5}{2\pi G}\frac{k_{\rm B}T}{\rho(1-\gamma)m_{\rm H}\mu}\right]^{1/2}, \tag{1.6}$$

$$\Rightarrow M_{\rm J} = \left(\frac{16}{9\pi\rho}\right)^{1/2}\left[\frac{5}{2G}\frac{k_{\rm B}T}{(1-\gamma)m_{\rm H}\mu}\right]^{3/2}. \tag{1.7}$$

Equation 1.7 shows that the Jeans mass is dependent on the cloud density and temperature. As our initial cloud with mass $M > M_{\rm J}$ contracts, the average temperature of the cloud will increase, as will its density. Since $M_{\rm J} \propto T^{3/2}\rho^{-1/2}$, the Jeans mass will change as the cloud contracts (I will define this new critical mass as $M'_{\rm J}$). If $M'_{\rm J} > M_{\rm J}$, then one of two outcomes are possible. If the increase is small enough for the mass of the cloud to still fulfil the criterion $M > M'_{\rm J}$, then the cloud will continue to collapse and the critical mass will continue to increase. At the point where the increase is large enough such that $M < M'_{\rm J}$, then the cloud will stop collapsing and reach a state of equilibrium. This mechanism explains the origin of interstellar clouds with low and intermediate masses.

1.1.2 Fragmentation

On the other hand, if $M'_{\rm J} < M_{\rm J}$, the initial collapse will accelerate. In these conditions, individual regions within the cloud may also fulfil the criterion $M_{\rm region} > M'_{\rm J}$, and begin to collapse themselves. This process is known as fragmentation, and can continue in a hierarchical manner, with regions of increasingly lower mass fragmenting (Hoyle 1953), eventually leading to the formation of dense molecular cores, self-gravitating regions with $\rho \sim 10^4 - 10^6\,{\rm cm}^{-1}$ and masses on the order of individual stars (Bergin and Tafalla 2007).

1.1.3 From molecular cores to stars

Once dense molecular cores form, they continue accreting gas from their surroundings. Eventually, the increase in temperature and density reaches the point of rendering the core optically thick. This is generally regarded as the very first stage in the life of a protostar (Stahler and Palla 2004). As the core grows, the gravitational energy of infalling material increases the temperature and density further, up until the point where deuterium

and subsequently hydrogen fusion is possible – as long as there is enough material available. At this point, the radiation pressure within the protostar balances its gravitational contraction, i.e. hydrostatic equilibrium is achieved (Equation 1.1). This process takes $\sim 500\,\mathrm{kyr}$ for stars of roughly Solar mass (e.g. Dunham et al. 2014). The young stellar object (YSO) stops accreting directly from the cloud, which flattens into a disc due to the conservation of angular momentum. The subsequent evolution of the YSO depends on its mass, as can be seen on Figure 1.1. For stars with $M \lesssim 0.5 M_\odot$, which are entirely convective, contraction onto the main sequence occurs exclusively along the Hayashi track (Hayashi 1961), with the YSO decreasing in luminosity at a constant temperature until it reaches the zero-age main sequence (ZAMS). Stars with masses $0.5 M \lesssim M_\odot \lesssim 3$ have a high enough temperature to be partially radiative, and so the Hayashi contraction is eventually replaced by contraction along the Henyey track, which is characterised by collapse close to hydrostatic equilibrium (Henyey et al. 1955). On Fig. 1.1, this is shown by the more horizontal parts of the track where the luminosity remains almost constant. Fig. 1.1 also shows that YSOs with a mass $\gtrsim 2 M_\odot$ evolve fully on the Henyey track.

The YSO will accrete from its disc until it is dispersed, a process that can take up to 10^7 yr (e.g. Hartmann 2009). At this point, the star contracts until it reaches the main sequence, where it will remain until its supply of core hydrogen is exhausted.

1.2 YSO classification

The process of cloud collapse and fragmentation detailed above results in cores with a large range of masses. The minimum Jeans mass of a cloud fragment is $\sim 7 \times 10^{-3}\, M_\odot$ (Low and Lynden-Bell 1976), well below the threshold for deuterium fusion, meaning that brown dwarfs condense directly from molecular cores as well as stars. The objects that emerge from molecular cores therefore can have wildly different properties.

The evolution of a protostar onto the main sequence is very sensitive to its mass and, therefore, two objects of the same mass can also present very differently depending on their age. Figure 1.1 shows a Hertzsprung-Russell (HR) diagram for a range of protostar masses. It can be seen that low-mass objects, up to $\sim 0.5 M_\odot$, contract at a roughly constant temperature. Conversely, higher-mass objects have a more complicated relation

between $T_{\rm eff}$ and L as they evolve towards the ZAMS. For young stars above a mass $\sim 6M_{\odot}$, the protostellar stage is short enough to be almost negligible, and these objects emerge from their cores as main-sequence objects. This dependence of YSO properties and evolution on mass have led YSOs to have been categorised based on their mass.

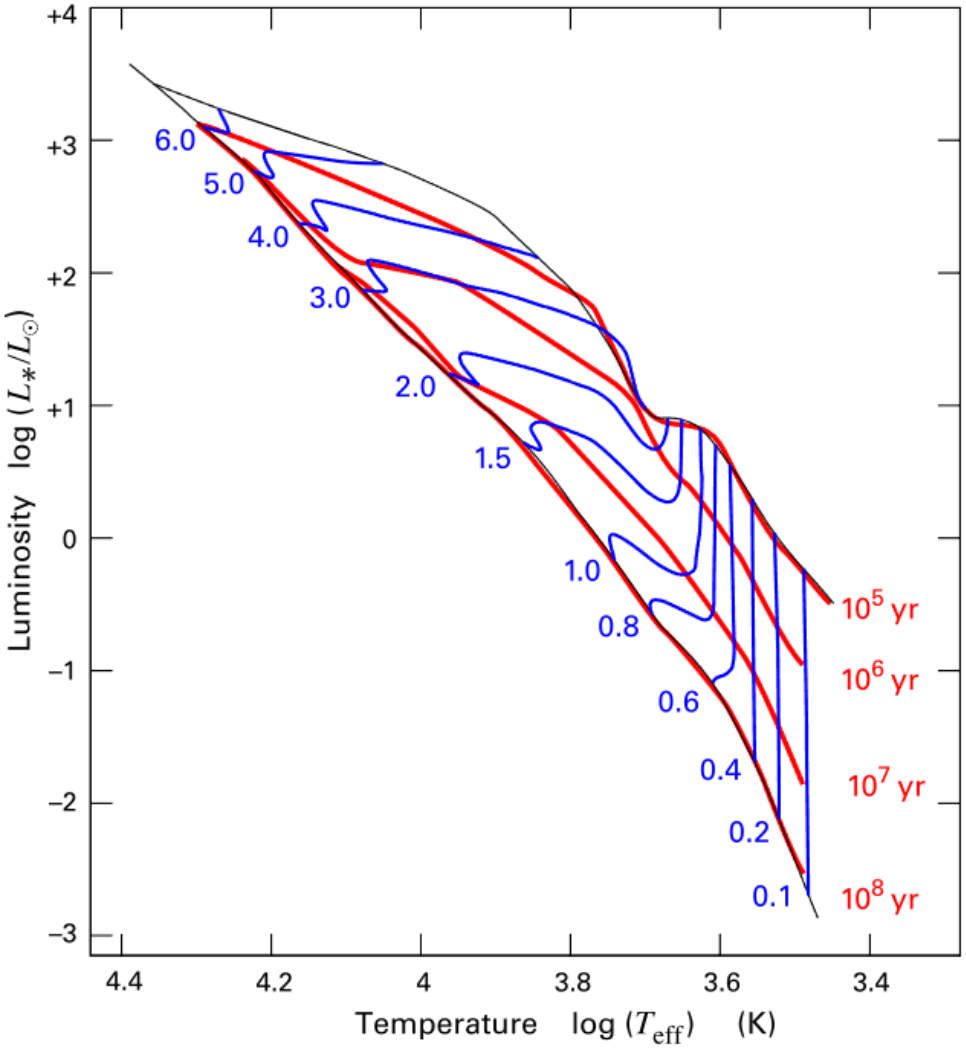

Figure 1.1: HR diagram showing evolution of T Tauri and Herbig Ae/Be stars from the end of direct cloud accretion (upper black line) to the zero-age main sequence (ZAMS, lower black line). The blue lines are evolution tracks by mass (in $M_{\odot}$), while the red lines are isochrones for the ages listed. Figure taken from Stahler and Palla (2004).

1.2.1 T Tauri stars

The lowest-mass YSOs are known as T Tauri stars (TTSs), named after the prototype of the class. T Tauri stars are highly-variable protostellar objects with a mass of $\lesssim 2\,M_{\odot}$, contracting on the Hayashi track for at least part of their PMS stage (see Section 1.1.3).

The class was defined by Joy (1945) by analysing 11 objects, defining the following criteria for membership:

- Irregular variations of ~ 3 mag.;
- Spectral type F5-G5;
- Emission lines similar to those of the Sun's chromosphere;
- Low luminosity;
- Association with dark or bright nebulosity.

As more T Tauri stars were discovered, the definition was expanded to cover all spectral types later than F0. T Tauri stars are further subdivided into two categories, classical and weak-lined (CTTSs and WTTSs respectively, e.g. Martín 1998), depending on the strength of their spectral lines. This distinction is representative of different stages of disc evolution, with CTTSs hosting optically-thick discs, and WTTSs having already dispersed their disc (Johnstone et al. 2013). CTTSs typically have very strong magnetic fields of $\sim 1\,\mathrm{kG}$, a thousand times stronger than that of the Sun (Johns-Krull 2007), which play an important role in accretion (e.g. Bouvier et al. 2007, see Section 1.4.3).

1.2.2 Herbig Ae/Be stars

Herbig Ae/Be (HAeBe) stars were first distinguished from T Tauri stars by Herbig (1960), and can be thought of as more massive counterparts to T Tauri stars. With a spectral type earlier than F0, HAeBes have masses in the range $\sim 2\text{-}8\,M_\odot$. The short amount of time that an evolving intermediate-mass star spends as a HAeBe object, $\lesssim 1$ Myr (Boissier et al. 2011), as well as their relative scarcity, means that they are much rarer than T Tauri stars. Strong outflows are often associated with Herbig stars, and the interaction of these jets with the cold dust and gas in star-forming regions can produce plumes known as Herbig-Haro objects.

1.2.3 Massive YSOs

YSOs that have $M \geq 8M_\odot$ are known as Massive YSOs (MYSOs). They are much less common than T Tauri or Herbig Ae/Be stars, both due to their relative paucity and the limited amount of time that MYSOs spend in the pre-main-sequence stage. Due to their

rapid evolution, MYSOs are typically found as embedded objects, with no optical emission escaping their natal clouds, and as such have been difficult to observe historically. This has led to much speculation over the physics of these systems. In recent years, however, our knowledge of MYSOs has advanced considerably, with many studies exploring the properties of these elusive objects. A main finding of the last decade of study of MYSOs is the confirmation that they can host circumstellar discs, which have been observed both in the infrared (e.g. Kraus et al. 2010) and radio domain (e.g. Johnston et al. 2015).

The very large observed multiplicity rate of massive stars, with certain clusters showing more than half of their massive stars being multiple (e.g. Sana 2017), has suggested that their mechanism of formation differs from lower-mass objects. Two main scenarios are thought to be possibilities for the dominant formation mechanism in massive stars. The core accretion model, or monolithic collapse model, generalises the typical star formation process of lower-mass stars (see Sections 1.2.1, 1.2.2) to the highest-mass YSOs. A collapsing region of a molecular cloud fragments into a cluster of self-gravitating cores, which then subsequently collapse through discs into individual stars (e.g. McKee and Ostriker 2007; Tan et al. 2014). While this is the simplest explanation for MYSO formation, it neglects fundamental differences between very massive stars and smaller objects. The stellar wind associated with MYSOs is much stronger, due to their large radii and thus comparatively low surface gravity. It has been theorised that these very strong outflows could prevent circumstellar discs from forming, preventing cores from accreting enough mass to evolve to the observed size of MYSOs (e.g. McKee and Tan 2003; Zinnecker and Yorke 2007). On the other hand, in the competitive accretion model, the stellar cores formed from the original cloud interact with each other much more than in the monolithic collapse model, 'competing' to accrete gas. If we consider a small cluster of protostars, the gas density will be higher towards the centre of the cluster, leading to much more accretion among the central stars. This results in a variety of stellar masses in the same cluster, which has been suggested to be a better explanation for the observed initial mass function (Bonnell et al. 2001).

Massive stars also are so luminous that they exert a radiation pressure on the surrounding environment which is often higher than the strength of gravity. In spherically

symmetric models, this limits the final MYSO mass to values smaller than have been observed (Yorke and Kruegel 1977; Krumholz et al. 2009). This problem can be solved by considering non-spherical geometry for the circumstellar envelope. If the core is initially slightly rotating, it will generate an accretion disc that, if of a sufficient optical depth, is enough to break the isotropy of the radiation field enough to allow accretion to continue to the highest masses of observed stars, $> 100\,M_{\odot}$ (Kuiper et al. 2014).

1.3 SED shapes and evolution

YSOs are commonly categorised by the shape of their spectral energy distribution (SED), which typically have excess near-infrared (NIR) emission compared to the approximate black-body curve that main-sequence objects exhibit. This is caused by leftover material from stellar formation, taking the form of a circumstellar disc, absorbing some of the light from the star and re-emitting it at longer wavelengths. As YSOs evolve, they interact with this disc, accreting material from it and dispersing it through stellar winds and photoevaporation. These processes will reduce the amount of circumstellar material in a circumstellar disc, as will any planetesimals forming within the disc, therefore reducing the strength of the NIR excess, until the classic photosphere SED is eventually recovered. It is through this mechanism that we can classify the evolutionary stage of a YSO, and Figure 1.2 shows sketches of the effect of stellar evolution on the SED up to the main sequence. It is important to note that the 'bump' in the SED caused by a NIR excess is not negligible in T Tauri and Herbig Ae/Be objects – it can contain almost all the emission coming from the inner few AU of the disc, and as much as 50% of the infrared flux from the entire system (Dullemond and Monnier 2010).

T Tauri and Herbig Ae/Be stars are commonly placed into four classes, depending on the strength of their infrared excess. This can be quantitatively defined by introducing the *spectral index*, α, which is defined as $\alpha = \frac{\mathrm{d}\log(\lambda F_{\lambda})}{\mathrm{d}\log(\lambda)}$, with F_{λ} representing the flux density such that $F_{\lambda} \propto \lambda^{\alpha}$. In reference to this calculation for α, the wavelength interval used is $\lambda \sim 2-20\,\mu\mathrm{m}$ (Lada 1987). The class of a YSO is defined by the value of its spectral index. Table 1.1 shows this in summary. Massive YSOs are not generally observable for long enough to be distinguishable by class in this way, and therefore the following classes

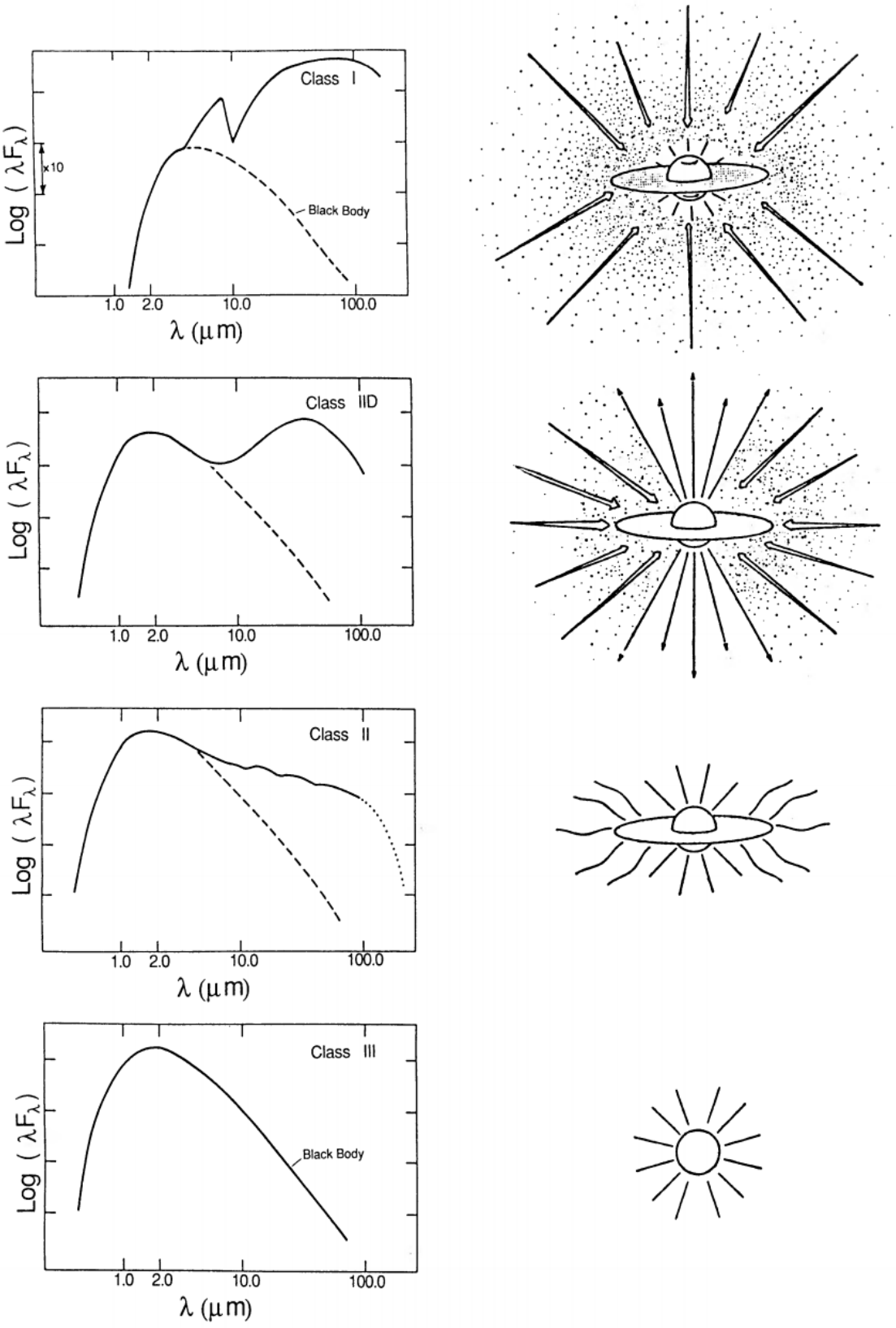

Figure 1.2: Left: Sketches showing the evolution of SEDs for young stellar objects. As expected, the NIR excess decreases as a star ages and its disc dissipates. The dashed line indicates a black-body spectrum. Right: Cartoons showing YSO evolution through the same ages. From Wilking (1989).

Class	Spectral index	Peak emission region
0	Undetectable	Submillimetre
I	$\alpha > 0.3$	Far-infrared
II	$-0.3 < \alpha < 0.3$	Near-infrared
III	$-1.6 < \alpha < -0.3$	Visible
Main-sequence	$\alpha \sim -4$	Ultraviolet

Table 1.1: A table showing the defining characteristics of the different classes of YSOs. Class 0 YSOs do not substantially radiate in the $\sim 2 - 20\,\mu$m wavelength region used to calculate α.

are usually only referred to when dealing with TTSs and HAeBe objects.

1.3.1 Class 0 objects

The earliest stage of stellar evolution occurs within a molecular cloud. As minuscule variations in density propagate with time, the gravitational influence of these initial clumps of gas causes the cloud to begin to collapse around them, as described in Section 1.1.1. As for all YSOs, in Class 0 objects the greatest source of luminosity by far is the release of gravitational potential energy by the infall of material onto the central object (Stahler 2011). What sets Class 0 objects apart, however, is that the majority of the final stellar mass has not yet been gathered from the surrounding cloud (André et al. 1993). This is in contrast to the more evolved objects of later classes, which have a mass approaching their final main-sequence mass. This initial period in the life of the YSO is very short, lasting on the order of $10^4 - 10^5$ yr (Froebrich et al. 2006; Dunham et al. 2015), although this is heavily mass-dependent. For Class 0 objects, the majority of the emission is still sub-millimetre in character (André et al. 1993), and therefore these objects are best suited to radio or far-infrared observations. Relatively recent advancements in sensitive space-based infrared observatories such as *Spitzer*, *Herschel*, and most recently *JWST*, have increased the known population of Class 0 YSOs, and consequently increased our understanding of them. Recent surveys have suggested that Class 0 YSOs accrete very rapidly due to their young age, with their accretion rate being as high as $\dot{M} \sim 10^{-6}\,M_\odot\,\mathrm{yr}^{-1}$ (Laos et al. 2021).

1.3.2 Class I objects

Class I sources represent the next stage in the evolution of YSOs. They are still deeply embedded in the surrounding cloud, and hence do not significantly emit in the visible

spectrum. They do, however, emit quite strongly in the infrared - making it possible to study them at these wavelengths. As shown in Figure 1.2, the SED of these objects has a very large NIR excess, compared to a black body of a similar temperature. This is due to the environment around the YSO – a thick, opaque disc will absorb light emitted by the central object, and re-emit it at longer wavelengths (Lada and Shu 1990). The discs surrounding Class I YSOs are very massive and gravitationally unstable, leading to the accretion rate of Class I objects to be modelled as very high, comparable to the Class 0 YSOs (e.g. Hartmann et al. 1998; Alexander and Armitage 2009). Observations of Class I sources support this large theorised accretion rate, with observed values of $\dot{M} \sim 10^{-9} - 10^{-6}\, M_{\odot}\, \mathrm{yr}^{-1}$ (Fiorellino et al. 2021). The Class 0 and I stages represent the bulk of the accretion onto the YSO, but generally only last ~ 0.5 Myr (Williams and Cieza 2011).

1.3.3 Class II objects

Class II objects are still embedded in the progenitor cloud, with peak emission in the infrared – however, since the cloud is optically thin compared to that of Class I objects, they emit at visible wavelengths as well (Lada 1987). Class II objects can include both accreting protostars with well-developed outflows (Wilking 1989), and objects at a slightly later evolutionary stage, which have weaker outflows but also a correspondingly depleted disc. The NIR excess of TTSs and HAeBes usually categorises them as Class II YSOs (Daemgen et al. 2012). However, this is dependent on their age, especially for more massive objects. For example, MWC 166 A (See Chapter 4) is a Herbig Be star which has a very small NIR excess, having cleared most of its immediate circumstellar area. The accretion rates for Class II objects have been found to be at least an order of magnitude smaller than comparable Class I objects, with Fiorellino et al. (2021) deriving $\dot{M} \sim 10^{-11} - 10^{-9}\, M_{\odot}$. By this stage of evolution their surrounding discs are generally only a few percent of the mass of the central object (Williams and Cieza 2011). The discs described in Section 1.4 are typically found around Class II YSOs.

1.3.4 Class III objects

The Class III objects are the final stage in evolution towards the main sequence. They are typically at or near their final mass, with accretion rates much lower than other classes of YSO, and often close to zero (Manara et al. 2013; Fiorellino et al. 2021). Their SEDs have a much smaller NIR excess than less-evolved objects, if any is present at all, as shown in Figure 1.2. Class III YSOs are usually therefore identified primarily by X-ray activity (Feigelson and Montmerle 1999). More massive YSOs are more likely to be observed as Class III objects due to the strength of photoevaporation and outflows dissipating disc material more rapidly.

1.4 Circumstellar discs around single stars

As described in Section 1.1, a typical feature of YSOs is the presence of substantial amounts of circumstellar material left over from stellar formation. The vast size of progenitor molecular clouds means that even small overall rotations translate to very large rotational velocities as they contract into hydrostatic cores (Shu et al. 1987), due to the conservation of angular momentum. Indeed, hydrostatic cores generally have much more angular momentum than that of their resultant stars (Larson 2003), which are found to form at relatively low velocities before *spinning up* – implying that there must be a mechanism to account for this discrepancy.

The formation of circumstellar discs is the main way that protostars shed excess angular momentum inherited from their progenitor cloud, along with jets and outflows (e.g. Marchand et al. 2020). If we consider a particle within a cloud, the force it experiences due to gravity can be balanced by centripetal force if it is in the equatorial plane. The result of this is that the cloud will flatten into a disc and increase in rotational velocity, forming a circumstellar or protoplanetary disc, so named due to its role in the formation of planets. It has been found that around half of T Tauri stars host a circumstellar disc (e.g. Daemgen et al. 2012). In single systems, dispersal of the disc occurs from a combination of accretion onto the star, depletion from stellar wind, photoevaporation and condensation into protoplanets. A typical disc has a lifetime of up to 3 Myr (Li and Xiao 2016), although in some cases they can survive for up to 10 Myr (Hartmann 2009).

1.4.1 Structure and evolution

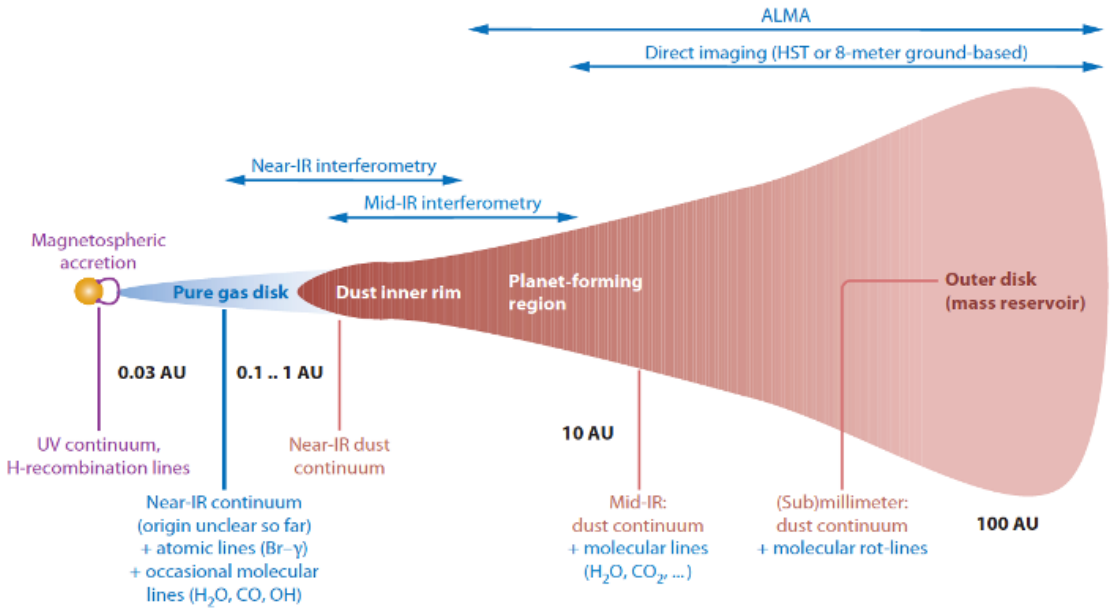

Figure 1.3: Sketch of the structure of a circularly symmetric circumstellar disc. The flared structure of the outer disc can be seen. Taken from Dullemond and Monnier (2010).

Protoplanetary discs are structures which occupy a vast range of length scales, stretching from just a few stellar radii from the central object to hundreds of astronomical units, as shown on Figure 1.3. Their temperature, density and other properties are therefore strongly radially-dependent, and thus difficult to observe and model holistically. As Figure 1.3 shows, different regions of the disc emit in different wavelength regimes, so in order to build up an accurate picture of the entirety of a circumstellar disc, multiple techniques and instruments must be used. Protoplanetary discs are primarily composed of hydrogen and helium, like the interstellar medium, but also contain large quantities of silicates, organic compounds and ices (Henning and Semenov 2013; Walsh et al. 2015). Due to the radial temperature gradient of protoplanetary discs, different species 'freeze out' at different radii, termed *snow lines* (Piso et al. 2015). This can lead to complex interactions between different molecules.

In the closest regions to the star, the high temperatures ($T \gg 1000\,\mathrm{K}$) cause dust to evaporate, leaving a pure gas disc (see Figure 1.6). At the inner edge of the gas disc, material is accreted onto the stellar surface (described in more detail in Section 1.4.3). The pure gas disc is optically thin, and extends up to the dust sublimation radius, where

the temperature is low enough to permit dust grains to survive, at which point dist and gas are both present in the disc. The dust inner rim, generally found at radii from ~ 0.1 au to a few au from the central star depending on stellar luminosity and the dust makeup, is a highly complex environment at the interface between the hot, gaseous disc, and the cooler dusty material which can extend for up to hundreds of au from the central star, and is described more fully in Section 1.4.2.1.

Behind the inner rim lies the dusty disc, which has a characteristic flared structure, meaning that its scale height (H) increases with radius (as shown on Figure 1.3). Flaring in dusty discs was first introduced to account for substantial far-infrared excesses in the SEDs of T Tauri stars (Kenyon and Hartmann 1987), and has since been readily observed in scattered light images (e.g. Stolker et al. 2016). The density profile for an azimuthally-symmetric disc in hydrostatic equilibrium is dependent on both the radius from the star R and the vertical height Z (Williams and Cieza 2011):

$$\rho(R, Z) = \frac{\Sigma(R)}{\sqrt{2\pi}H} \exp\left(-\frac{Z^2}{2H^2}\right), \tag{1.8}$$

where $\Sigma(R)$ is the surface density profile, an observable for resolved discs (Miotello et al. 2018). Chiang and Goldreich (1997) developed a near-power-law relation between H and R ($H \propto R^{4/3}$), and also first introduced a model of the dusty disc which characterises it as two distinct layers – a hot, optically-thin surface layer irradiated by the star and comprised of heated dust grains, and a cold midplane layer where dust 'settles'.

These two-layer models were subsequently improved by including the effects of different dust grain sizes and compositions, as well as the inclusion of full radiative transfer (Chiang et al. 2001). The incoming stellar radiation is absorbed by the heated layer, with roughly half of it then re-emitted inward, with the effect of regulating the disc's inner temperature. The remaining radiation is emitted outwards as dilute blackbody radiation, contributing to the infrared excess of the object. At large enough radii from the star, the thermal energy imparted by this heating eventually outweighs the disc gravitational binding energy, leading to escape of material in a pressure-driven wind (Alexander et al. 2014). This process is termed *photoevaporation*, and is generally driven by high-energy ultraviolet

and X-ray emission from the star. By the end of the disc's lifetime, the mass accretion rate drops to the point where the disc photoevaporates rapidly and at smaller radii.

The paucity of intermediate objects between disc-bearing CTTSs and disc-less WTTSs implies that the transition between these two evolutionary states appears to take place very rapidly, on the order of 10^5 yr (Simon and Prato 1995), and photoevaporation is thought to be the primary method for this rapid disc dispersal (Picogna et al. 2019). Photoevaporation has also been shown to affect the semi-major axes of exoplanets formed in the disc (Ercolano and Rosotti 2015).

1.4.2 Disc evolution

The processes of accretion and ejection necessarily result in the disc losing mass over time. As a disc evolves, the rate of accretion of the central object decreases by multiple orders of magnitude (see Section 1.3). Discs which have been substantially depleted with respect to the median CTT discs are termed 'transition discs' (Strom et al. 1989). They were first discovered from their SED, which has a smaller NIR excess than comparable CTT discs, but still retains a substantial FIR excess (e.g. Calvet et al. 2002). In addition, their SEDs can show dips rather than the smooth decreases in intensity with wavelength that are standard in younger discs. This implies that the dust distribution in these discs contains gaps and cavities (Espaillat et al. 2014), which have since been confirmed by sub-millimetre interferometry (primarily with ALMA, e.g. Francis and van der Marel 2020) and scattered light imaging (e.g. Benisty et al. 2022).

The average age of protoplanetary discs is ∼2-3 Myr before being depleted (Williams and Cieza 2011), with Li and Xiao (2016) fitting an exponential decay curve with a characteristic lifetime of 3.7 Myr. By the point that young stars reach an age of $\sim 10^7$ yr, the majority have no discernible primordial disc, with most remaining circumstellar discs being comprised of debris from planetesimal interaction at this stage (e.g. Haisch et al. 2001). Depletion can occur due to accretion, but by the time a YSO evolves beyond Class I, most of its final mass has already been accreted (see Section 1.3). Therefore, by the latter stages of YSO evolution, stellar winds, planetary formation and photoevaporation will be the main drivers of disc depletion. The effect of protoplanets on the evolution of the

disc is one which has received much attention in recent years, in part due to spectacular images of asymmetries, gaps and spiral arms. Figure 1.4 shows a sample of these discs, highlighting their variety.

1.4.2.1 The dust inner rim

The boundary between the purely gaseous disc and the dusty disc is termed the dust inner rim. In reality, different species of dust will have different sublimation temperatures, but for simplicity I will assume a simple model of a single species of dust. The most common form of dust in protoplanetary discs is comprised of silicates, which have a sublimation temperature $T_{\rm sub} \sim 1500\,{\rm K}$ (Kama et al. 2009). The size and geometry of the dust inner rim is of particular importance. Since the rim is located at the boundary between optically thin and optically thick material, the cross-sectional area of the rim, the 'covering fraction', will determine how much light from the central star is absorbed and re-emitted at longer wavelengths. This is the manner in which the geometry of the rim affects the star's NIR excess. Comparing observations of the SEDs of young systems with models of the rim can therefore allow us to constrain its shape.

The simplest models of the dust inner rim, (e.g. Natta et al. 2001), consisted of a vertical wall with surface height $H_{s,{\rm rim}}$, located at the dust sublimation radius and emitting as a black body at the sublimation temperature ($T_{\rm rim} = T_{\rm sub}$). The radius of such a rim can be found by the relation $R_{\rm rim} = R_*(T_*/T_{\rm rim})$, and the luminosity of the re-emitted radiation is simply $L_{\rm rim} = L_*(H_{\rm rim}/R_{\rm rim})$ (Dullemond and Monnier 2010). This also assumes that no radiation is re-absorbed by the disc, that temperature is independent of vertical height, and additionally that the wall is very thin – meaning that face-on objects do not display an NIR excess. This latter point especially was quickly found to be incompatible with SED observations, as all observations of Herbig Ae/Be stars show some NIR emission regardless of their disc inclination (Hillenbrand et al. 1992; Millan-Gabet et al. 2001; Dominik et al. 2003).

More advanced modelling involves propagating the incident radiation through the disc using radiative transfer codes (such as TORUS (Harries 2000), PLUTO (Flock et al. 2013), RADMC3D (Dullemond et al. 2012)), which has changed our understanding of

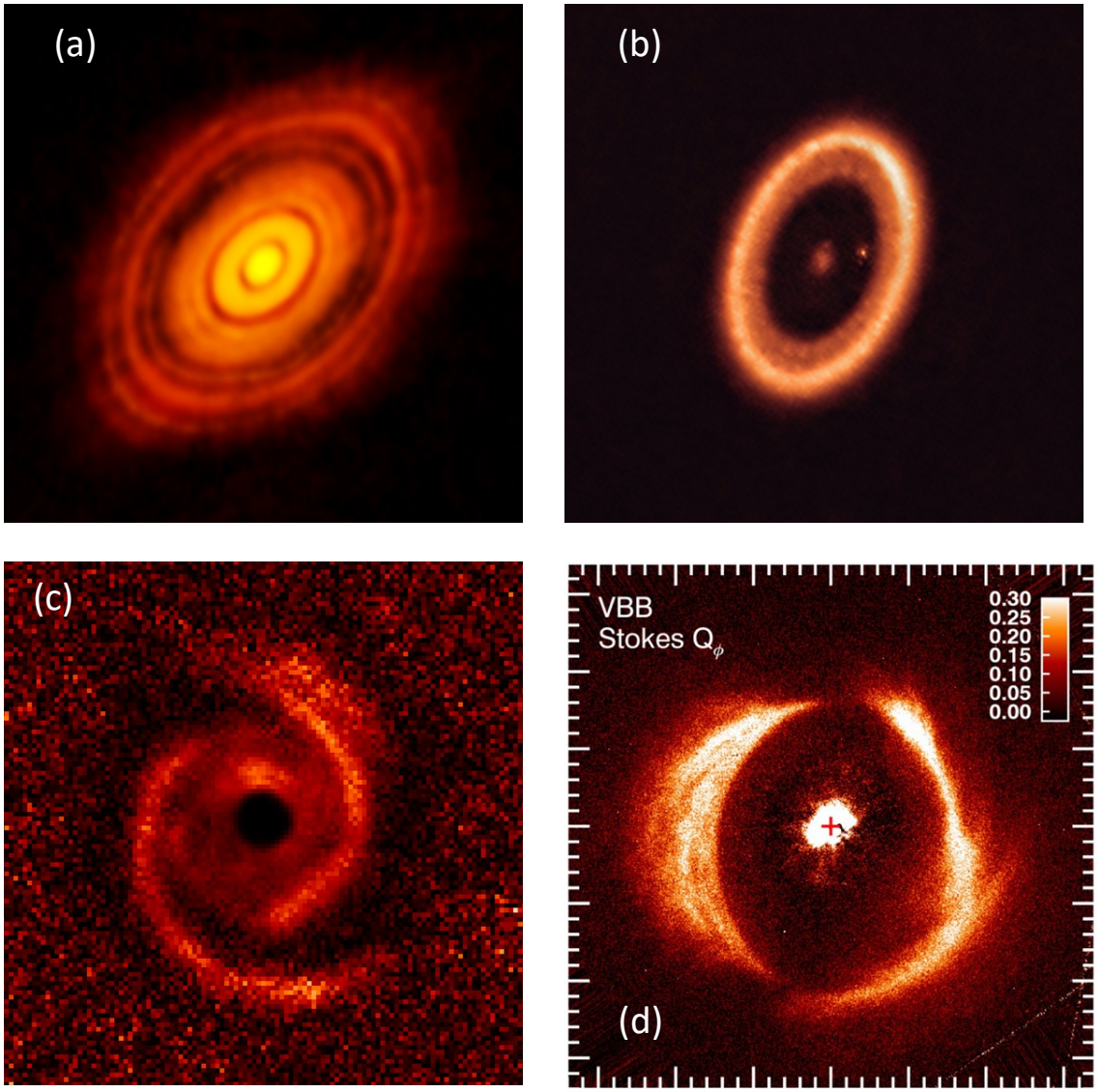

Figure 1.4: Examples of the diversity of protoplanetary disc systems. **(a)**: The protoplanetary disc around HL Tau imaged with ALMA, with cavities carved by three planets visible (ALMA Partnership et al. 2015). **(b)**: A direct image of the planet PDS 70 c and its newly-discovered circumplanetary disc, taken with ALMA (Benisty et al. 2021). The disc clearing effect caused by planetary accretion is very prominent. **(c)**: ALMA image of the disc around MWC 758, showing the spiral arms which dominate its geometry (Benisty et al. 2015). **(d)**: SPHERE polarised scattered light image of the circumbinary disc around HD 142527 (Hunziker et al. 2021). Disc asymmetries and shadowing are visible in the disc structure.

the geometry of the inner rim. Radiative transfer modelling allows us to treat the rim as a collection of individual grains, which are affected by other grains at different radii from the star. Isella and Natta (2005) produced the first model with a curved rim (see Figure 1.6), which is now the standard interpretation. The curved rim model of Isella and Natta (2005) is defined by a large vertical density gradient, leading $T_{\rm sub}$ to vary by hundreds of degrees over a small change in vertical height. This has the effect of causing dust to evaporate at lower temperatures the further one moves from the disc midplane – leading to the curved shape seen in Fig. 1.6. The temperature for a grain of dust ($T_{\rm dust}$) at a radius from the star r then becomes dependent on optical depth (τ_d):

$$T_{\rm dust}(\tau_d) = T_* \sqrt{\frac{R_*}{2r}} \left[\mu(2 + 3\mu\epsilon) + \left(\frac{1}{\epsilon} - 3\epsilon\mu^2 \right) \exp\left(\frac{-\tau_d}{\mu\epsilon} \right) \right]^{1/4}. \tag{1.9}$$

In the above equation, $\mu = \sin\theta$ (where θ is the incident angle between the incoming radiation and the disc surface) and ϵ is the 'radiative efficiency parameter', defined as the ratio of the mean opacity of grains at the local temperature $T_{\rm dust}$ to the mean opacity at the stellar temperature T_* (Isella and Natta 2005). If we set $\mu = \tau_d = 0$, Equation 1.9 simplifies to $T_{\rm dust} = T_* \epsilon^{-1/4} \sqrt{\frac{R_*}{2r}}$, which is an expression for the temperature of a dust grain in isolation (Dullemond and Monnier 2010). The additional factors in Equation 1.9 therefore model the effect of 'backwarming' caused by other grains more deeply embedded in the disc. The exponential term, being dependent on the optical depth, models extinction rising as light penetrates further into the disc. As can be seen from Figure 1.5, the value of ϵ has a large impact on the temperature. If $\epsilon = 1/\sqrt{3}$, then the temperature will be constant throughout the dust rim. For values smaller than this, the temperature will decrease with optical depth, while larger values cause the temperature to increase with optical depth. The shape of the near-infrared excess in the SED of a YSO is therefore dependent both on the structure of the inner rim and the flared outer disc (see Section 1.4).

1.4.3 Mass accretion in T Tauri and Herbig Ae/Be stars

For T Tauri stars, the main process of accretion is tied to their very strong magnetic fields. Hartmann et al. (1994) posited that the strong emission lines in T Tauri stars are caused

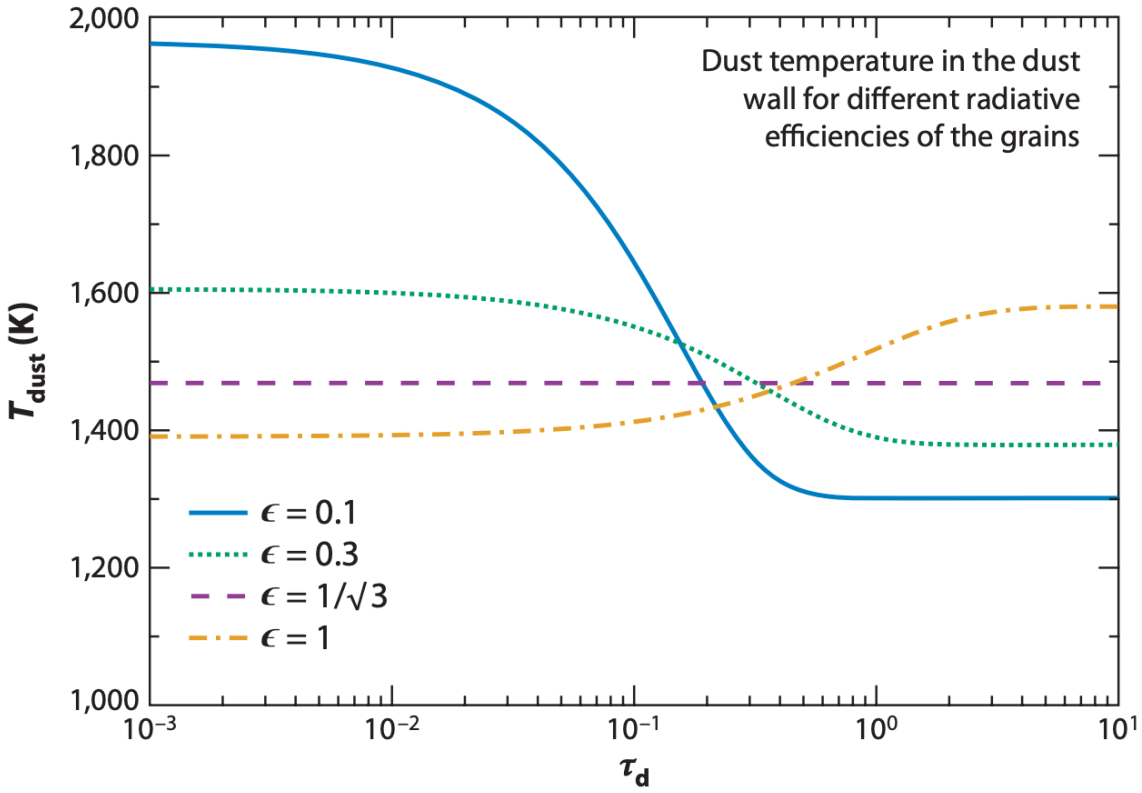

Figure 1.5: Dust temperature plotted against optical depth for four representative values of ϵ, for a dust rim around AB Aur with inner radius 0.5 au. The model used was the curved rim with temperature described by Equation 1.9. The critical value of $\epsilon = 1/\sqrt{3}$ leads to a flat temperature throughout the rim, and separates two families of solutions. Taken from Dullemond and Monnier (2010).

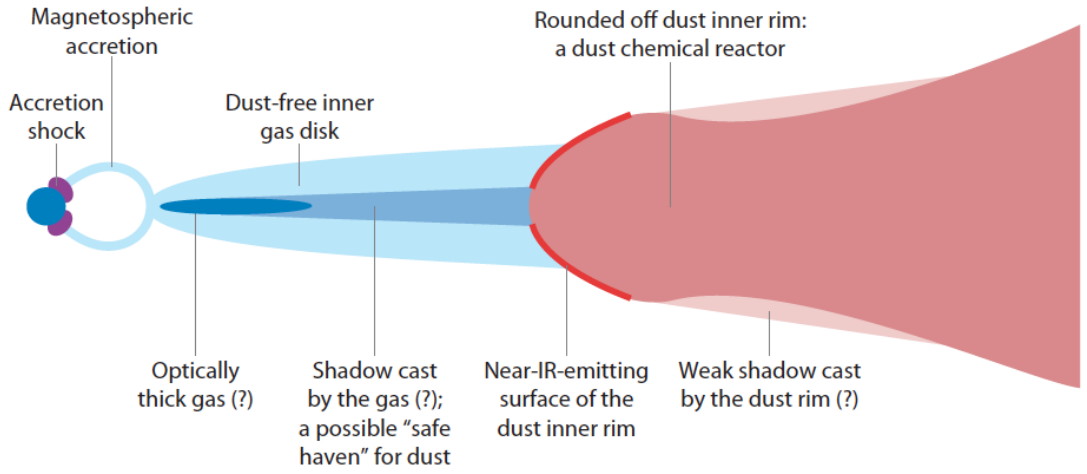

Figure 1.6: Sketch of a typical circumstellar disc around a T Tauri star, showing the magnetospheric accretion region, the gas disc feeding the accretion, and the inner dusty disc with a curved and puffed-up rim (Dullemond and Monnier 2010).

by their very strong magnetic fields ($\sim$ 1 kG, Johns-Krull 2007) channelling infalling material onto the stellar surface along field lines. This magnetospheric accretion process also has the effect of explaining the lower-than-expected rotation rates of T Tauri stars. The magnetic field also causes the ejection of material in jets parallel to the magnetic field axis, and drives stellar winds at high velocities (Camenzind 1990). Outflows of disc material are extremely common in T Tauri stars (e.g. Johns-Krull 2007; Hartmann et al. 2016). Because the accretion in these objects is driven by their strong magnetic fields, accretion rates are strongly correlated with rates of mass ejection (Matsushita et al. 2017).

Herbig Ae/Be stars generally have magnetic fields that are an order of magnitude weaker than those of T Tauri stars (Hubrig et al. 2019; Järvinen et al. 2019), despite showing many of the same strong spectral lines. The efficiency of magnetospheric accretion in HAeBes is therefore much weaker, implying there is another way that they accrete enough material to explain their spectra. Koenigl (1991) showed that, if the magnetic field is weak, the inner edge of the accretion disc is not disrupted by magnetic stress and can extend to the stellar surface. However, as we have seen in Section 1.4, there is a large difference in the rotation rate of the star and the much faster, supersonic Keplerian rotation of the inner disc. The region where material must slow down to accrete onto the central object is called the boundary layer (BL), and thus accretion directly from the disc, without involvement of magnetic fields, is termed boundary layer accretion (Belyaev and Rafikov 2012). Material passing through the BL causes shear instabilities that generate azimuthal acoustic waves (Coleman et al. 2022). These waves propagate both towards and away from the star, transporting angular momentum. Magnetohydrodynamic simulations have confirmed that this mechanism is robust and the likely source of the majority of accretion in HAeBe stars (Belyaev et al. 2013).

1.4.3.1 Calculating accretion rates

As material accretes onto the stellar surface, there is an associated luminosity generated by the dissipation of the kinetic energy of the material, which is funnelled through accretion columns at almost free-fall velocity ($v \sim 300\mathrm{km\,s^{-1}}$). This is termed the *accretion luminosity* (L_{acc}), and measuring the intensity of this luminosity can give us an estimate

for the accretion rate $\dot{M}$ of the star:

$$L_{\rm acc} = \frac{1}{2}\dot{M}v^2 \simeq \frac{G\dot{M}M_*}{R_*}\left(1 - \frac{R_*}{R_{\rm trunc}}\right), \tag{1.10}$$

where the assumptions are made that the kinetic energy of the infalling material is entirely converted to luminosity, and that the disc truncation radius $R_{\rm trunc} \gtrsim 5\,R_*$ (e.g. Hartmann et al. 2016). The speed of the infalling material causes X-ray emission which is then absorbed and re-radiated to produce a continuum UV excess, as well as strong emission lines both in the UV and IR. Due to the large amounts of energy released in accretion shocks, hydrogen recombination lines such as the Balmer, Paschen and Brackett series are particularly common in accreting YSOs (Edwards et al. 1994; Muzerolle et al. 1998).

The accretion luminosity is directly related to the luminosity of these spectral lines associated with accretion, with Muzerolle et al. (1998) establishing a strong correlation between $L_{\rm acc}$ and the luminosity of the Br γ line ($L_{\rm Br\gamma}$) in TTSs. This correlation was further extended to HAe objects by Calvet et al. (2004). However, this relationship is different and poorly-calibrated for most HBe stars, implying the Br γ emission from these more massive objects is significantly contributed to by stellar winds – which can be very strong in HBes (Donehew and Brittain 2011). The accretion luminosity is also strongly dependent on stellar mass , as can be seen on Figure 1.7. This suggests that the accretion regime changes from magnetospheric to boundary-layer above $\sim 4\,M_\odot$ (Wichittanakom et al. 2020), such that late-type HAe objects accrete similarly to TTSs.

Everything described in this chapter covers the evolution of stars as single objects or, at the very least, as multiple systems separated widely enough such that interactions are minimal. In the next chapter, I will explore how the star formation and evolution paradigm can change in the context of binary stars.

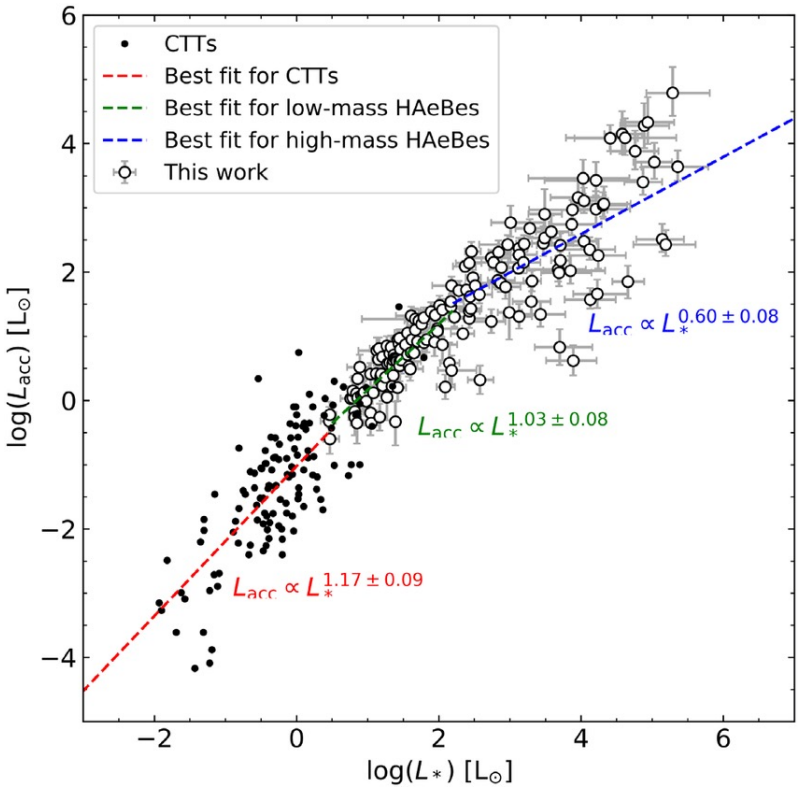

Figure 1.7: $L_{\rm acc}$ vs L, for a sample of CTTSs and HAeBe objects. The relation is clearly poorly-defined for higher-mass Herbig Be objects. Taken from Wichittanakom et al. (2020).

Chapter 2

Binary YSOs and protoplanetary discs

2.1 Binary star formation

The star formation paradigm has traditionally been developed by considering stars as mainly single. However, as instrumentation has improved over the years, it has become apparent that this is too simplistic a view and that the majority of stars are indeed part of multiple systems (e.g. Zinnecker and Yorke 2007; Duchêne and Kraus 2013). Multiplicity is also correlated with mass, with more massive stars being more likely to host companions. At the higher end of this scale, very massive O-type stars are almost always multiple (Sana et al. 2012).

This stellar multiplicity also extends to YSOs. Joy and van Biesbroeck (1944) discovered five double stars among his newly-defined T Tauri objects, with further detections continuing ever since. More recently, surveys focusing on YSO-rich associations have allowed constraint of their multiplicity fraction. It has been found that, for many star forming regions (SFRs), the rate of multiplicity in YSOs is roughly twice as high as that for main sequence objects (e.g. Leinert et al. 1993; Duchêne 1999). A survey of protostars in Perseus revealed that even Class 0 YSOs have a multiplicity rate of at least $\sim 28\%$ down to a separation of 25 au (Tobin et al. 2016), and this rate will be even higher when

taking into account binaries with a closer separation – implying that binary systems form very early in the lifetime of stars.

Therefore, the process of star formation must be able to explain the high incidence of binary systems. Possibly the simplest scenario for binary formation is from fragmentation of a molecular core into multiple gravitationally-bound accreting protostellar objects. In the event of more than two YSOs emerging from a core, it is possible for gravitational interactions to expel certain members, while arranging others into complex hierarchical systems. For example, the system HD 104237 A, which I study in detail in chapter 5, is composed of at least five objects in a hierarchical system (Feigelson et al. 2003). Stable examples of these hierarchical systems are typically either single stars orbiting close binaries ($\lesssim 10$ au) at comparatively large enough distances that their interactions are minimal, or 'nested' close binaries in a similar structure (e.g. Hamers and Portegies Zwart 2016).

However, hydrodynamical simulations have shown that binaries with periods of $P \leq 10$ d cannot directly form from fragmentation due to the large size of condensing hydrostatic cores ($\sim$ 5 au, Bate 1998), meaning that other mechanisms must exist to account for them. In the densely populated environment of a condensing molecular cloud (roughly 2000 stars per parsec for the Orion nebula cluster, Hillenbrand and Hartmann 1998), stars which are expelled from a forming system can often find themselves interacting with other nearby stars. Such interactions can lead to gravitational capture of the incoming object to form a binary system, with the respective protoplanetary discs coalescing (Turner et al. 1995). This can result in highly-eccentric orbits and large mass disparities between the two stars, which can be seen clearly in the increasing abundance of gravitational wave sources originating from highly-unequal binaries (e.g. Zevin et al. 2020).

2.2 The significance of binary YSO systems

Determining accurate stellar masses is a quintessential problem in astrophysics, due to the large dependence of other fundamental stellar parameters on the mass. High-mass stars especially suffer from poorly-calibrated evolutionary tracks, with models tending to overpredict the mass (e.g. Massey et al. 2012). Young stars also suffer from this issue, with predicted and measured masses differing by $\sim 10\%$ (Stassun et al. 2014).

Evolutionary tracks are very sensitive to the mass of the YSO, and as such need to be calibrated from observed systems with well-constrained masses. The most direct way of measuring stellar masses with a minimum of bias is by taking advantage of the orbital mechanics of close binary systems. Deriving these dynamical masses requires astrometric and spectroscopic orbit information on binary systems that are sufficiently close for obtaining a full orbit solution (see Section 2.4). Close binary systems are therefore often studied in detail to calibrate our understanding of fundamental stellar parameters derived from mass.

2.3 Discs in binary systems

Binarity in young stars is believed to play an important role in shaping the structure of their discs. In wide binary systems, each individual star can host its own circumstellar disc. On the other hand, in luminous and close Herbig Ae and Be binaries, a single circumbinary disc is likely the only possible structure for circumstellar material (Pichardo et al. 2005). This is due to dynamical interactions between the stars and the disc, which can affect both the accretion properties of the system and the disc's shape and lifetime. If the binary separation is small enough, on the order of $a \lesssim 10\,\mathrm{au}$, the dynamical interactions between the two stars and the disc material will preclude individual discs from surviving (Harris et al. 2012). The resulting circumbinary disc is heavily shaped by the orbit of the central objects, for instance by truncating the disc or by inducing misalignments, especially if the stars' orbit is very close (~ 1 au) and eccentric (Pichardo et al. 2005). Orbital resonances are very likely to cause disc truncation in close binary systems. For a circular binary, this is likely to be on the order of 1.7 times the semi-major axis of the binary, with this increasing with eccentricity up to a value around four times the semi-major axis for the most eccentric orbits (Artymowicz and Lubow 1994).

Furthermore, the binary-disc interaction can also in turn affect the binary orbit. Orbital resonances can drive angular momentum transfer from the binary to the disc (Lynden-Bell and Kalnajs 1972), which subsequently makes the orbit tighter and more eccentric while causing spiral density waves to propagate through the disc material (Artymowicz et al. 1991; Lubow and Ogilvie 1998). If the stars are sufficiently massive, this

process can cause mass transfer between the stars, further complicating the evolution of the system, eventually potentially resulting in cataclysmic events such as Type Ia supernovae and black hole mergers (e.g. Heath and Nixon 2020).

These dynamical interactions between the stars and the disc will also affect the accretion properties of the system and might affect the disc lifetime, although it is unclear whether under what conditions they will either delay or accelerate disc dispersal (Cieza et al. 2009). This can have consequences far beyond the lifetime of the disc itself, as planet formation will be substantially disrupted in a binary system compared to that of a single star. Indeed, the evolution of planetary systems is still poorly understood. The vast majority of known exoplanets have been found around single stars (e.g. Mullally et al. 2015), so *post hoc* evidence for planet formation in binary systems is scarce. As a result, most of our knowledge comes from smoothed particle hydrodynamics (SPH) simulations (e.g. Bate et al. 2003). However, due to the sensitivity of orbital parameters on the resulting disc structure (Dunhill et al. 2015), it is also difficult to properly calibrate SPH simulations unless the orbit of the components is known. Considering the fact that a large fraction of stars – especially high-mass stars – are formed in multiple systems (Reipurth and Zinnecker 1993), constraining the behaviour of protoplanetary discs in binaries is key to our understanding of planetary evolution over both short and long timescales.

Dynamical truncation will affect the potential of the disc to form planetary systems by removing or rearranging the material available for planet formation. The known population of circumbinary planets has been substantially increased by Kepler observations (e.g. Doyle et al. 2011), and numerical simulations suggest that features rare in planets around single stars, such as large eccentricities and planet-star misalignment, are more common in circumbinary systems (Chen et al. 2019). Further studies on well-characterised young multiple star systems are also essential for studying other dynamical mechanisms that might shape the architecture of exoplanetary systems, for instance by moving disc material onto oblique orbits (Kraus et al. 2020).

2.3.1 High-angular resolution observations on young binaries and their discs

With the development of adaptive optics, space-based telescopes, and interferometers over the last few decades, we have been able to resolve an increasingly large number of binary and multiple YSOs as visual binaries. These systems have been shown to host exceptionally diverse discs.

The dynamical interactions between stars and discs in YSO binaries result in the disc changing significantly over its lifespan. Observations of binary systems hosting circumbinary discs have revealed to us the very large diversity of shapes and morphologies that circumbinary discs can take. Theoretical studies have shown that circumbinary discs around eccentric binaries can take one of two stable configurations: co-planar with the binary orbit, or perpendicular to the orbital plane (Martin and Lubow 2017; Zanazzi and Lai 2018). Discs in binary systems have been often been found to have complex features, including:

- Dust-cleared gaps and cavities;
- Gas kinematics signatures (e.g. spirals, kinks);
- Dust asymmetries (e.g. horseshoes);
- Misalignments which can cause warps and shadowing.

Radio interferometry and scattered light imaging have provided a large sample of outer disc geometries in recent years. Below, I highlight some examples of the diversity of disc structures in binary YSOs.

The recent DSHARP survey at the Atacama Large Miillimeter Array (ALMA) found examples of spiral structures in some Class II systems such as Elias 2-27 (Pérez et al. 2016) and IM Lup (Huang et al. 2018), showing that complex disc structures are not limited to the very early stages of star formation, but persist well into the lifetime of the disc.

HD 142527, shown on panel (d) of Figure 1.4, is an example of a nearly face-on ($i \sim 20°$) young system which has recently been found to host a low-mass stellar companion (Biller et al. 2012). The circumbinary material takes the form of a transitional disc which is co-planar with the binary (Boehler et al. 2017), and where spiral arms and shadows have been observed. This star also has the largest gas-cleared region yet observed in any binary

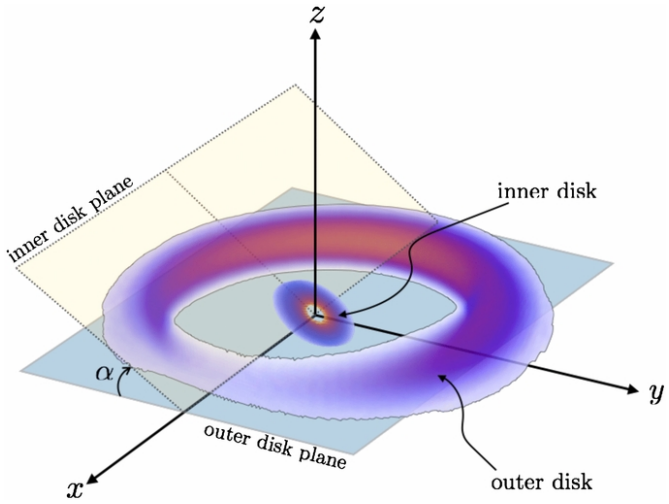

Figure 2.1: Sketch of the misalignment between the inner and outer discs in HD 142527, with the inner disc scaled up in size to enable better comparison. The orbit of the stars is the likely cause of the misalignment. Figure taken from Marino et al. (2015).

YSO, between 30 and 90 au (Lacour et al. 2016), as well as a dust-cleared gap of 140 au (Fukagawa et al. 2006). The innermost region of the circumstellar environment has been shown to host an inner disc to the interior of the observed cavity, which has a large misalignment of 70° from the outer disc (see Figure 2.1 and Marino et al. 2015).

These disc misalignments appear to be commonly caused by companions, whether stellar or planetary in nature. In the β Pictoris system, for example, an inclined planet was theorised to be responsible for the disc misalignment in the system by Mouillet et al. (1997). The planet, β Pic b, was subsequently found to orbit the primary star at an inclination aligned with the warped disc, lending credence to this interpretation (Lagrange et al. 2012). Multiple systems are commonly even more complex. HD 98800 is a system which has been discovered to be a hierarchical quadruple – consisting of two close binaries (Aa+Ab and Ba+Bb), with the latter hosting a polar disc (Kennedy et al. 2019). This disc has been observed interferometrically in the radio with ALMA (shown on Figure 2.2) and in the near-infrared with the VLTI, and the disc was found to be stable against Kozai-Lidov oscillations (Martin et al. 2022), which are perturbations caused by an orbiting third body (Kozai 1962; Lidov 1962). Furthermore, the quadruple system itself was also found to be stable over thousands of orbits (Zúñiga-Fernández et al. 2021). The stability

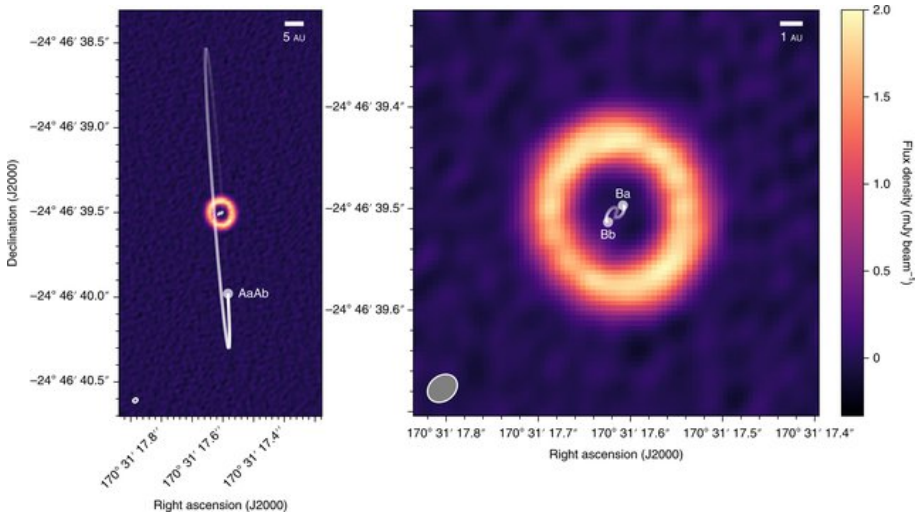

Figure 2.2: ALMA 1.2mm continuum image of the polar disc around HD98800, as well as the orbits of the components, including the extreme misalignment between the disc and the outer binary. Taken from Kennedy et al. (2019).

of such complex structures in polar orbits has consequences for the expected stability of planetary orbits in such systems, which until recently were thought to be rare (e.g. Busetti et al. 2018).

The spectacular structure of GW Orionis (Kraus et al. 2020) is an extreme example of the influence that star-disk interactions can have on a disc. GW Ori is a triple system with a disc structure comprising multiple misaligned rings, as well as substantial disc warping and tearing. Figure 2.3 shows the complex geometry of the disc and the orbit of the components of the system. The structures labelled 'R' represent the three rings of the disc, and there are also four arcs from scattered light, labelled 'A', and two shadows, labelled 'S'.

2.4 Binary orbit determination

As we have seen in Section 2.3, the orbits of binary stars, especially close binaries, can have a very large effect on their circumstellar environment. Smoothed particle hydrodynamics (SPH) simulations of young binary systems require precise knowledge of the orbit in order for reconciliation with observations (e.g. Heath and Nixon 2020). In this section I will describe how we define orbits using a set of parameters termed the orbital elements.

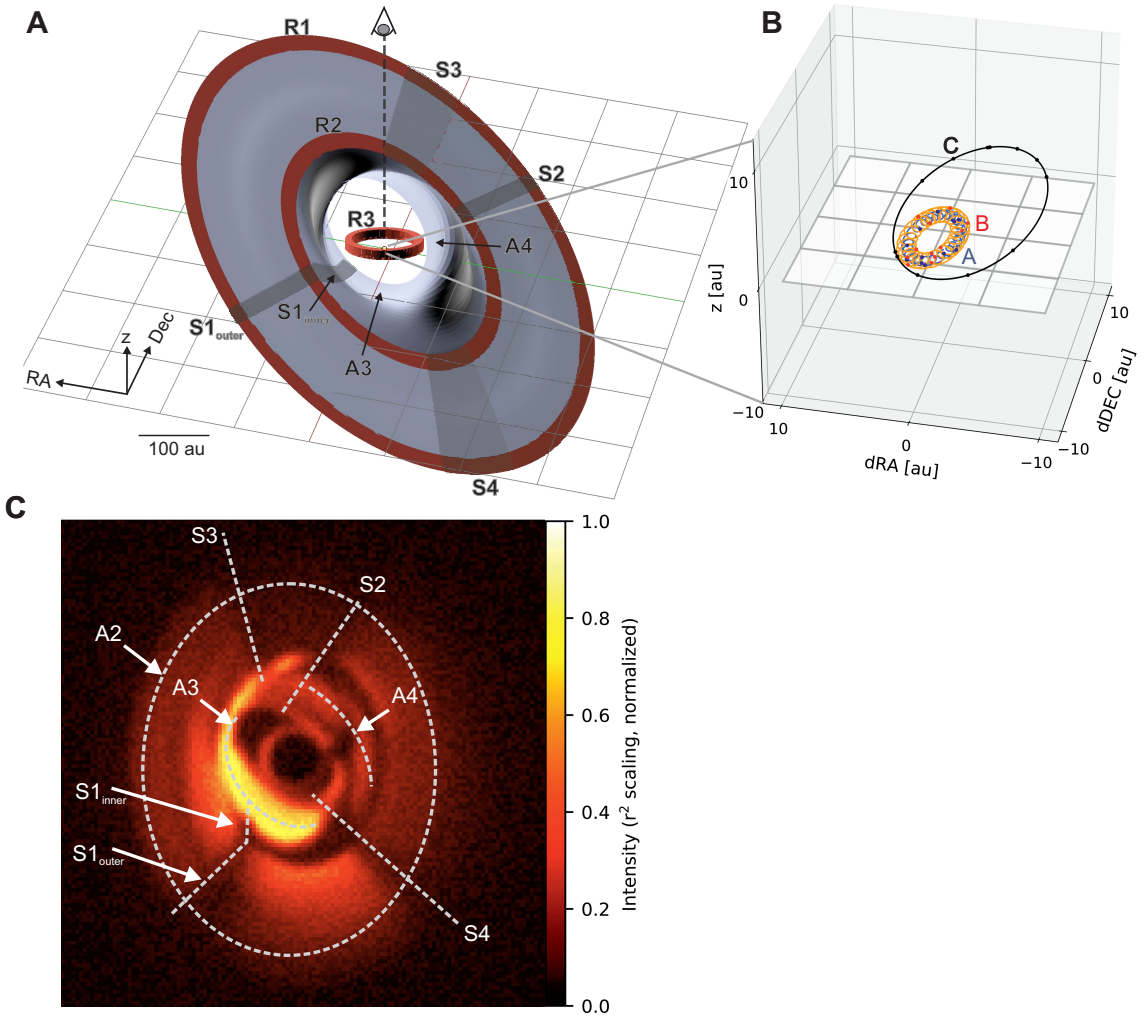

Figure 2.3: Model for the disc of GW Ori, taken from Kraus et al. (2020). **A**: diagram of the disc. **B**: orientation of the orbit of the three components of the system. **C**: synthetic scattered light image corresponding to the model in panel A, with the z axis pointing towards the observer. The main features of the disc are indicated on panels A and B.

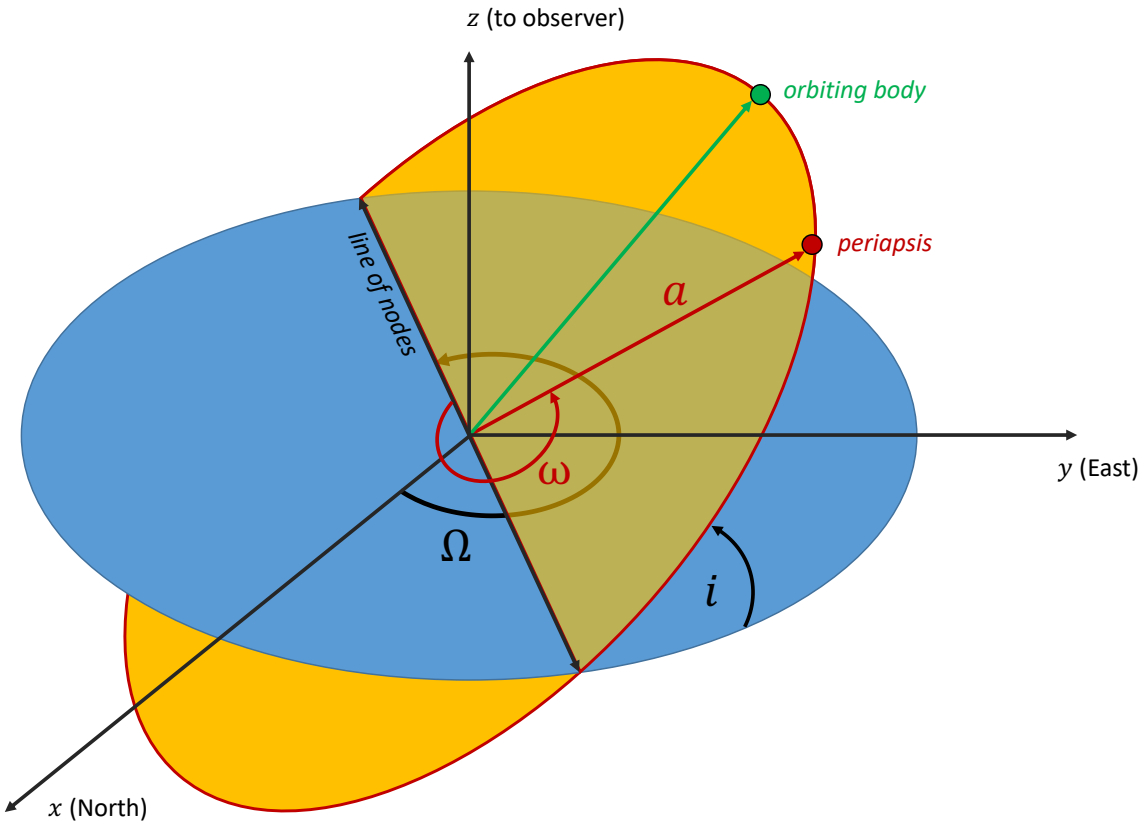

Figure 2.4: Sketch of a circular three-dimensional apparent orbit. Shown on the diagram are the argument of periapsis ω, the longitude of the ascending node Ω, the inclination i, and the semi-major axis a. The orbital plane is coloured yellow, and the reference plane is coloured blue. For an elliptical orbit, a will be half the distance between periastron and apoastron, not the distance shown on the diagram.

2.4.1 Orbital elements

The orbital elements, or 'Campbell elements', are a set of seven parameters that define an orbit as seen on the sky. The individual elements are listed in Table 2.1, and Figure 2.4 shows a sketch of the geometric relation between the elements. The two parameters which describe the size and shape of an orbit are the semi-major axis, a, and the eccentricity, e. For a circular orbit, as seen on Figure 2.4, a is equivalent to the radius, and for all other orbits is defined as half the distance between periapsis, or the point in the orbit where the two components are at their closest separation, and apoapsis, the analogous point on the other side of the orbit where the components are furthest from each other. For a stable orbit, eccentricity is between $0 \leq e < 1$, with zero corresponding to a circular orbit, and with the orbit becoming more and more elliptical as e increases. Eccentricities of $e = 1$ indicate parabolas and $e > 1$ hyperbolas, which are 'unbound' orbits that will result in the

Parameter	Description
P	Orbital period
T_0	Epoch of periapsis
e	Eccentricity
a	Semi-major axis
i	Inclination
ω	Argument of periapsis
Ω	Longitude of ascending node
K_1	RV semi-amplitude of the primary
K_2	RV semi-amplitude of the secondary (SB2 only)
V_0	Velocity of system centre of mass

Table 2.1: Campbell elements and radial velocity parameters for a binary star, allowing complete specification of a three-dimensional orbit.

companion escaping the gravitational influence of the primary. As such, values of $e \geq 1$ are not relevant to this discussion.

Once an orbit's size and shape is described, three angles are required to describe its orientation (shown in yellow on Figure 2.4) with respect to a reference plane, shown in blue on Figure 2.4. The inclination, i, is the angle between the orbital plane and the reference plane. The reference plane is typically chosen to coincide with the plane of the sky, such that orbits of 0° are seen face-on, and orbits of 90° are seen edge-on. Inclination varies between $0° \leq i \leq 180°$, with $i > 90°$ representing retrograde orbits.
The longitude of the ascending node, Ω, is an angle measured from North in the reference frame to the ascending node, one of the two points where the orbital and reference planes intersect. The ascending node is the node at which the object is moving *away* from the observer (on the far side of the orbit shown on Figure 2.4). The argument of periapsis, ω, is an angle in the orbital plane measured from the ascending node to periapsis.
There are two time parameters, the period of the orbit P, and the epoch of periapsis T_0, which is unique among the parameters in that any epoch with an orbital phase of zero behaves identically, assuming no orbital precession.

In addition to the elements described above, there are two additional RV parameters which are required to fully define a three-dimensional orbit: V_0, the velocity of the system's centre of mass, and K_1, the radial velocity semi-amplitude for the primary.

2.5 Binary orbits

The first orbit of a binary star, ξ Ursae Majoris, was calculated in 1827 by Félix Savary (Ball 1872). This was possible due to the relatively long period of the binary, at 59.8 years, and the proximity of the system to the Sun, being located only 8.8 pc away. This results in separations on the order of an arcsecond, which were detectable with the primitive telescopes available in the 19th Century – making the system a visual binary and its astrometry manageable to measure. However, such 'easy' targets are few and far between, and other techniques must be used to study the majority of binary stars which are not resolvable with traditional telescopes. About 10% of star systems are single-lined spectroscopic binaries (SB1, Birko et al. 2019). This often happens due to small separation, weak spectral lines in one of the stars, or if there is a large luminosity difference between the two stars. Double-lined spectroscopic binaries (SB2) also have a measurable RV semi-amplitude for the secondary component, denoted K_2. While this simplifies the task significantly, K_2 is not strictly necessary to define an orbit, and indeed the orbits presented in Chapters 4 and 5 are both for single-lined spectroscopic binaries.

Spectroscopic binaries are not resolvable as individual stars, and so are characterised by analysing the RV curve over an orbital period, as it changes due to the Doppler effect. In order to do this, the orbital period must be short enough for RV changes to be detectable ($P \leq 5$ yr, El-Badry et al. 2018). Due to the one-dimensional nature of RVs, not all the elements in Table 2.1 can be probed, meaning that spectroscopic orbits cannot offer a complete orbital solution, leaving a, Ω, and i undefined. The first star discovered to be a spectroscopic binary was Mizar, in 1889 (Niemela 2001). Since then, RV orbits have been the main tool used to probe small-separation binaries, save for particularly nearby objects.

If the binary is resolvable, RV measurements can be combined with astrometry to construct a three-dimensional orbit, and fully define all of the elements listed in Section 2.4.1. With the development of higher-resolution instruments, the number of binary stars resolved as visual binaries has increased substantially. Interferometers have played a large role in this, but space-based telescopes have also contributed enormously. The *Gaia* telescope has been particularly prolific in spatially-resolving binary stars, with the

third data release identifying over a million such objects (El-Badry et al. 2021), allowing a statistical approach to binary characterisation.

2.5.1 Derived quantities

2.5.1.1 Dynamical mass constraints

The growing number of binary systems with fully-defined three-dimensional orbits has allowed more precise determination of stellar parameters. The most important derived quantity, and the one which can be directly extracted from the orbit, is the mass of each component of the binary, which the other parameters are very sensitive to.

Kepler's third law states that the square of the period P of an orbit is proportional to the cube of its semi-major axis a. This takes the form:

$$P^2 = \frac{4\pi^2}{G(M_1 + M_2)} a^3. \tag{2.1}$$

In the context of the orbit around the system barycentre, this can be written in terms of either component of the system. This relation for the primary is given by:

$$P^2 = \frac{4\pi^2}{G\tilde{M}} a_1^3, \tag{2.2}$$

where a_1 is the semi-major axis of the primary component around the barycentre, and we have defined:

$$\tilde{M} \equiv \frac{M_2^3}{(M_1 + M_2)^2}. \tag{2.3}$$

Using the usual angular diameter-distance relation, a [au] $= a$ [$''$] $\times\, d$ [pc], we can show the dependence of the total system mass $M_{\rm tot} \equiv (M_1 + M_2)$ (in solar masses) on distance d (in parsecs), where G is the gravitational constant and $M_{1,2}$ the masses of the two stars:

$$M_{\rm tot} = \frac{4\pi a^3 \mathcal{Z}}{GP^2}\ d^3, \tag{2.4}$$

and where $\mathcal{Z} = 1684.14$ m$^3 {M_\odot}^{-1}$ is a constant I have introduced to account for the change in units from au to metre, and from kg to $M_\odot$. In the above equation, the total mass is also known as the 'dynamical mass', signifying it is derived from fitting the dynamical

orbit of the system. Since $M_{\rm tot} \propto d^3$, a reliable distance value is needed to obtain rigorous mass estimates.

2.5.1.2 Binary mass function

For a single-lined spectroscopic binary, where we only have RV information about the primary star, it is still possible to decompose the total mass into the individual masses, as long as the orbital elements are known. If we consider the relative orbit of the secondary around the primary, such that the primary is at one of the foci of the orbit, the radial velocity semi-amplitude of the primary is given by the following equation (Perryman 2011):

$$K_1 \equiv \frac{2\pi}{P} \frac{a_1 \sin i}{(1-e^2)^{1/2}}. \tag{2.5}$$

If Equations 2.2 and 2.3 are substituted into Equation 2.5, it is possible to eliminate the factor of a_1 and obtain the *binary mass function* $f(M)$ (e.g. Boffin 2012; Curé et al. 2015):

$$\begin{aligned} a_1 &= \frac{PK_1(1-e^2)^{1/2}}{2\pi \sin i}, \\ P^2 &= \frac{4\pi^2}{G} \frac{(M_1+M_2)^2}{M_2^3} \left[\frac{PK_1(1-e^2)^{1/2}}{2\pi \sin i}\right]^3, \\ f(M) \equiv \frac{(M_2 \sin i)^3}{(M_1+M_2)^2} &= \frac{PK_1^3(1-e^2)^{3/2}}{2\pi G}. \end{aligned} \tag{2.6}$$

As long as P, e, i, K_1, and the combined mass $(M_1 + M_2)$ are known, Equation 2.6 can be rearranged in terms of M_2:

$$\boxed{M_2 = \frac{1}{\sin i} \left[\frac{K_1^3 P \left(1-e^2\right)^{3/2}}{2\pi G} \cdot M_{\rm tot}^2\right]^{1/3}}, \tag{2.7}$$

and the mass of the primary can finally be trivially found through $M_1 = M_{\rm tot} - M_2$. The binary mass function is therefore a very powerful tool, since it allows disentanglement of individual masses – as long as the distance to the system is well-known. This is the process by which I calculated the individual masses of the components of MWC 166 A, described in Section 4.4.4, and HD 104237 A, described in Section 5.4.4.

2.5.2 Binary orbits to constrain stellar parameters

Upon determination of the individual masses, the remaining fundamental stellar parameters are able to be found from isochrone tracks, sets of calculated stellar parameters for stars of a given age. These are generally calculated for a range of masses and metallicities (e.g. Baraffe et al. 1995; Bressan et al. 2012; Haemmerlé et al. 2019), with associated further parameters such as radius, luminosity and temperature calculated for each grid location. Because of the strong dependence of all stellar properties on mass, even small changes in mass can result in large changes in other parameters. As a result, interpolating these isochrone tracks is important when constraining stellar parameters. Examples of such isochrone interpolation can be found in Sections 4.4.4 and 5.4.4.

In the context of YSOs, it is additionally important to have a reliable age constraint when determining stellar parameters. This is due to the very large differences in radius, temperature and luminosity for a given mass being dependent on the evolutionary state. Therefore, when the stellar parameters are well-known *a priori*, the above method can be used to find an estimate for the age of the system, with an example of this in Section 4.6.4.

2.6 Spectroscopic characteristics

Young binaries can have complicated spectra, with many spectral lines reflecting the complex environment. In the near-infrared, the regime which most long-baseline interferometers operate in, there are a variety of hydrogen recombination lines, as well as others including neutral helium and carbon monoxide lines (e.g. Hales et al. 2014). The shapes, intensities and variability of these lines are all indicators of activity in the circumstellar environment. Since protoplanetary discs are comprised of $\sim 99\%$ gas (e.g. Williams and Cieza 2011), being able to trace the kinematics and structure of the distribution of various gas species is important for understanding discs as a whole.

Spectro-interferometry gives us the ability to resolve emission lines both spectrally and spatially, as described in Section 3.4.6, and so has become a powerful tool in studying the origin of spectral lines in YSO spectra. The Brackett γ line, at 2.166μm, is especially significant because it can trace numerous processes in binary YSOs. Br γ originates from

the 7−4 transition of hydrogen, and as such it traces high-energy gas. As already discussed in Section 1.4.3.1, one of the main uses of Br γ is to estimate the mass accretion rate of stars. Additionally, the spatial extent and location of the Br γ line in the circumstellar environment can offer clues to the origin of the processes which cause the emission. The Br γ line is especially useful because it is less affected by optical depth than other Hydrogen lines such as H α – which commonly traces the same processes (Najita et al. 1996).

If the emission originates from very close to the stars, within the 'co-rotation radius' where material orbits at the same speed as stellar rotation, the most likely origin is magnetospheric accretion (e.g. van den Ancker 2005; Ray and Ferreira 2021). T The acceleration of material along magnetic field lines, up to very high velocities before impacting the stellar surface in accretion shocks, results in hydrogen recombination (Lynden-Bell and Pringle 1974). Therefore Br γ emission, as well as H α and other recombination lines, will originate at the base of these accretion columns (e.g. Eisner et al. 2010).

Emission slightly further from the stellar surface, yet within the dust sublimation radius, is likely to originate from a gaseous accretion disc (see discussion in Section 4.6.3.2), and in binary YSOs, this can be around either of the components, or both, depending on the relative masses and separations.

If the origin of the emission is more spatially extended, it is likely to originate in different processes. Magnetically-coupled disc winds can accelerate particles to very high speeds of hundreds of kilometres per second, leading to emission from the disc-launching region (e.g. Königl and Salmeron 2011), in a process known as a centrifugally-driven wind. For high-mass binaries with substantial stellar winds, interaction between their respective outflows can cause bow shocks, leading to emission of high-energy radiation which can ionise gas in the circumstellar environment (e.g. Bonneau et al. 2006).

Of course, the Br γ in YSOs can have origins in more than one of the processes described above. The strong magnetic fields required for centrifugally-driven winds will also channel material down onto accretion columns. Beck et al. (2010) found that spatially extended Br γ emission in eight TTSs was associated with their Herbig-Haro outflows. This was on average responsible for $\sim 10\%$ of the Br γ in these objects, the rest being attributed to magnetospheric accretion.

2.7 Variability

Young stars are very commonly variable. A study of Cygnus OB7 found $\sim$ 93% of its YSOs showing variability (Rice et al. 2012). This can be due to a variety of reasons. Physical changes in the stars themselves, such as hot and cold spots on the stellar surface, can affect their luminosity (e.g. Lakeland and Naylor 2022). Accretion can also cause variability in stars. FU Orionis objects (FUors) are a class of YSO in which periodic accretion outbursts (increasing by as much as three orders of magnitude) cause increases in luminosity that last decades or even centuries (e.g. Audard et al. 2014), while EX Lupi objects (termed 'EXors', Herbig 1989) have shorter outbursts which can repeat every few years. For close binaries, the interactions between components can cause flares and spikes in accretion. The orbital motion of the stars, especially if their orbit is eccentric, can bring the stars' magnetospheres close enough to interact and cause flaring. This is usually detected in X-ray observations, such as those of DQ Tau (Getman et al. 2011) and AK Sco (Gomez de Castro et al. 2013), which show significant X-ray spikes at periastron.

Chapter 3

Near-infrared Interferometry

3.1 The diffraction problem

Developments in astronomy have always centred on improving the resolution of our instruments. Up to a point, this is possible by increasing the size of the primary mirror. For Earth-based telescopes, the distortion imparted by the atmosphere limits the resolution of any telescope to around ~ 1 arcsec (Labeyrie et al. 2006). As we have seen in Chapter 2, this is not precise enough to image the inner regions of young binary systems. The most elegant solution to this problem is to simply remove the atmosphere completely, by using space-based telescopes. Recent advances in adaptive optics (AO) systems, whereby the mirror is deformed in real time in order to mostly cancel the effects of turbulence, have dramatically increased the resolution of ground-based telescopes as well (e.g. Woillez et al. 2019). However, even perfect atmospheric compensation does not remove all limitations, as any image captured will still be subject to the effects of diffraction.

If we consider a telescope of diameter d observing a point source, such as a star, the image will appear as a central spot surrounded by a pattern of concentric circles known as an Airy disc, blurring the image even with a 'perfect' lens. The effect of this blurring, or point-spread function (PSF), is to limit the resolution of even a perfect lens depending on its size. If we now consider two identical point sources separated by an angle $\Delta\Theta$, the resolution limit is defined as the point where the peak of the intensity of the first object overlaps with the first intensity null of the second (Buscher 2015). This is termed the

Rayleigh criterion:

$$\Delta\Theta = 1.22\frac{\lambda}{d}. \tag{3.1}$$

This can be applied to show that even space-based telescopes have a relatively-limited resolution. For example, the James Webb Space Telescope (JWST), the current state-of-the-art, has a primary mirror of diameter $d \approx 6.5\,\mathrm{m}$ and observes at a wavelength range of $\lambda = 0.6 - 28.5\,\mu\mathrm{m}$. This is equivalent to a resolution limit of $\Delta\Theta = 0.02 - 1.1\,\mathrm{mas}$. While this is a fantastic improvement on what came before, it still is not able to probe the resolutions needed for close binary orbit determinations at anything but the shortest wavelengths of operation. Furthermore, such a resolution from a ground-based telescope would require a primary mirror diameter of hundreds of metres – an extremely impractical proposition from both an engineering and financial point of view.

Interferometry allows us to overcome this limitation by taking two small telescopes separated by a *baseline* B, and interfering the light received at each of them. This offers a resolution of $\Delta\Theta = \lambda/B$ – proportional to the baseline length rather than the diameters of the telescopes themselves. Therefore, interferometry is the only technique which can currently probe micro-arcsecond length scales, and in this chapter I will provide an overview of how this is done.

3.2 Historical background

3.2.1 Wave superposition and Young's double slit experiment

The fundamentals of interferometry are based on the concept of wave superposition. The classic experiment used to demonstrate this principle is Young's double slit experiment, one which every physicist will have experienced extremely early in their career. It consists of a light source shone onto a screen, between which a shield is inserted, blocking the majority of the light from reaching the screen. The shield has two small slits to allow light to pass through, and on the screen is visible a pattern of alternating bright and dark areas, or 'fringes'. Young theorised that this visible pattern of alternating maxima or minima could be explained by light acting as a wave, with the slits causing the light coming through the two slits to interact much like water in a pond after two pebbles are thrown

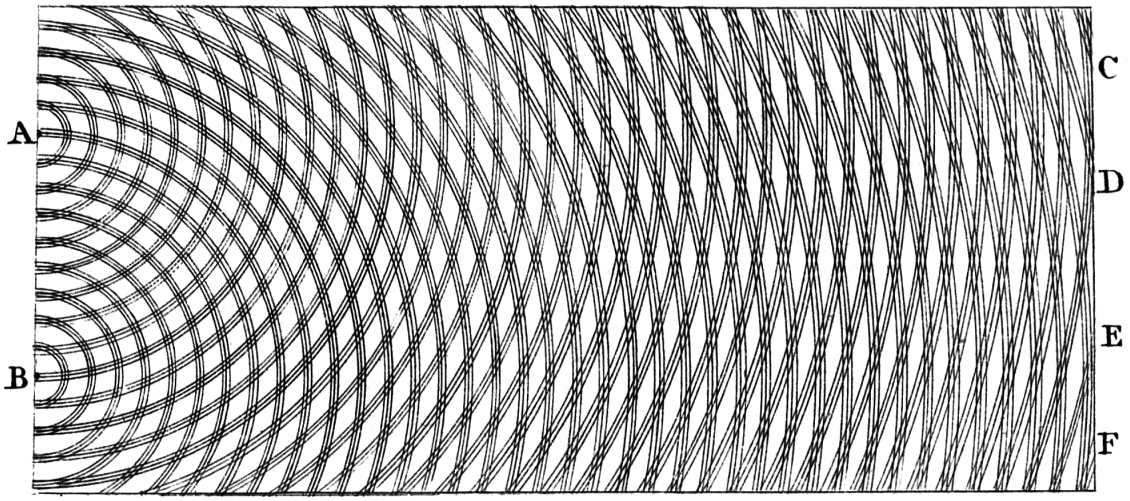

Figure 3.1: Young's sketch of the phenomenon of interference in his eponymous double slit experiment, reproduced from Young and Kelland (1845). The two slits are located at points A and B, while points C, D, E and F (supposedly) show the location of minima on the screen. The diffraction pattern here can be seen to vary with distance from left to right, as the wavefronts spread out. In the astronomical context, we approximate these wavefronts as plane waves.

in. Figure 3.1 shows Young's original sketch of his understanding of the phenomenon of interference (Young and Kelland 1845). Of course, it should be noted that Figure 3.1 shows the laboratory case, where the light source is very close to the slits. As such, the wavefronts produced at A and B are circular. When applied to astronomical sources, the distances are such that we can approximate spherical wavefronts as plane waves.

3.2.2 Early developments

While the concept of wave interference was first proposed by Young in 1802, development of interferometry was very slow for the following century. The first important scientific result came in 1887, with the conclusive proof of the absence of a medium of propagation for electromagnetic radiation, or 'luminiferous aether' (Michelson and Morley 1887). The Michelson-Morley interferometer operated by splitting a coherent light source using a half-silvered mirror, and then sending the two resultant beams along perpendicular paths. If such a luminiferous aether existed, it would cause the beams to lose coherence and produce detectable fringe displacements which would change over time, with the Earth's rotation and motion through space. The failure to detect any statistically significant fringe displacement has been called the most famous failed experiment in history (Blum and

Lototsky 2006). The Michelson-Morley interferometer design continues to make scientific discoveries to this day, as modern gravitational wave detectors such as Virgo (e.g. Accadia et al. 2012) use the same basic design – albeit on with much larger baselines and with much greater precision.

3.2.2.1 Single telescope

The application of interferometry to astronomy was first proposed by Fizeau (1868), who theorised that angular diameters of stars could be measured from analysis of their interference fringes. This was shortly thereafter independently pioneered by Michelson in the first formal description of the mathematical underpinnings of the technique (Michelson 1890), followed by the first practical demonstration: a measurement of the angular diameter of Jupiter's moons using the 12-inch refractor at the Lick Observatory (Michelson 1891). The technique used was very similar to that proposed by Fizeau (1868), and now termed *aperture masking*: superimposing a mask, which only allows light through two holes cut into it, onto the primary mirror. This creates an interferometer from an ordinary telescope. While the design of the single-mirror interferometer used by Michelson (1891) was generally superseded by multiple-telescope techniques, it was re-examined almost a century later, with applications to using multiple openings in the mask to achieve multiple baselines simultaneously (Haniff et al. 1987). Despite this blocking the vast majority of the light from reaching the telescope, it has been shown that the results are analogous to a multi-element interferometer (Haniff et al. 1987).

Speckle interferometry is the term given to the concept of taking images with a short exposure in order to minimise atmospheric turbulence, with the word 'speckle' referring to the grain-like structures seen in such images (Labeyrie 1970), which are caused by the random phase fluctuations imparted by the atmosphere (see Section 3.3.4). This is generally done with the use of aperture masking on a single telescope to increase the precision of closure phase measurements (Ireland 2016). An advantage of aperture masking interferometry is that an arbitrary number of apertures can be created with minimal cost and complexity, while for long-baseline interferometers, each additional telescope is a substantial investment. A limitation of aperture masking interferometry lies in the small size of both the apertures and the resultant baselines.

3.2.3 Long-baseline interferometry

The first example of a true astronomical interferometer was also constructed by Michelson and Pease (1921), the design of which can be seen on Figure 3.2. This interferometer was a modification of the 100-inch Hooker telescope at the Mount Wilson Observatory in California. A periscope was used to direct light through two apertures (m_1 and m_4 on Figure 3.2) to the main pupil, for a baseline length of 20 ft (6 m). Even with such a modest design, the resolving power of astronomical interferometers was immediately apparent. By analysing the visibility curve when observing Betelgeuse, Michelson and Pease (1921) found a value for its diameter of 0.047″, with an uncertainty of $\sim$ 10%. Furthermore, it was noted that limb darkening would increase this by $\sim$ 17%, leading to a corrected angular diameter of 0.055″, or "slightly less than the orbit of Mars". This was the first such measurement for a star other than the Sun. Modern estimates for this diameter range from 0.042″ to 0.069″ (Balega et al. 1982), showing that astronomical interferometry was capable of accurate high-resolution measurements even in its infancy.

However, this early success was something of a false dawn for optical astronomical interferometry. The measurement of Betelgeuse's diameter was substantially helped by its close distance and large size, and the Michelson-Pease interferometer was not sensitive enough to repeat this for many other objects. Pease (1931) used the same technique for the diameters of six other stars using a 50 ft ($\sim$ 15 m) interferometer of the same design, but apart from this the field mostly lay dormant for more than 20 years (Labeyrie et al. 2006). The first true modern long-baseline interferometer was developed by Hanbury Brown and Twiss (1956b), using correlations of intensities rather than electric fields to obtain source information, but otherwise used to calculate stellar diameters similarly to Michelson & Pease's early experiments (Hanbury Brown and Twiss 1956a).

It was only in the 1970s that optical multi-telescope interferometers, or long-baseline interferometers, were first developed, with Labeyrie (1975) observing fringes on Vega with two telescopes in the near-infrared. Long-baseline interferometry had been pioneered in the radio domain, where the longer wavelengths make maintaining coherence much easier and don't require light to be interfered in real time. Indeed, modern radio interferometers such as the Atacama Large Millimeter Array (ALMA) have dozens of telescopes, while

optical and infrared interferometers are yet to include more than six due to the inherent difficulty in ensuring cohesion at small wavelengths. Another milestone in the development of optical interferometry was the use of single-mode fibres to record data, combined in an integrated optics device – as opposed to the traditional use of mirrors to redirect light. This was pioneered by Labeyrie (1975) with the Fiber Linked Unit for Optical Recombination (FLUOR) instrument at the Kitt Peak observatory, offering baselines of 5.5 m with 0.8 m-diameter telescopes. The use of fibre-optics allows much more complicated beam combiners, since it reduces the number of reflections needed to guide incident light, leading to fainter targets being observable (Labeyrie 1975). Modern optical interferometers use multiple telescopes, often relocatable, offering baselines of up to hundreds of metres. An overview of the most prominent is given in Section 3.5.

3.3 Diffraction and interference

3.3.1 Interference

We can describe the principle of interference mathematically by looking at a simple example. Let us first consider the wavefunctions ψ_i of two plane waves, dependent on position vector $\mathbf{r} \equiv (x, y)$ and time t:

$$\psi_1(\mathbf{r}, t) = A\cos(\mathbf{k}\cdot\mathbf{r} - \omega t), \tag{3.2}$$

$$\psi_2(\mathbf{r}, t) = A\cos(\mathbf{k}\cdot\mathbf{r} - \omega t + \phi). \tag{3.3}$$

Each of these waves has identical amplitude A, wavelength λ and frequency ν. I have additionally defined the angular frequency $\omega = 2\pi\nu$, as well as the wave vector $\mathbf{k} = (2\pi/\lambda)\,\hat{\mathbf{k}}$. The wave vector is an extension of wavenumber k to a multi-dimensional space, and always points in the direction of propagation of the wave (e.g. Labeyrie et al. 2006). In the above example, the second wave is distinguished from the first solely by the addition of the phase term ϕ. The superposition of these waves, Ψ, can be mathematically described as the sum of their wavefunctions:

$$\Psi(\mathbf{r}, t) \equiv \sum_i \psi_i(\mathbf{r}, t) = 2A\,\cos\left(\frac{\phi}{2}\right)\left[\cos\left(\mathbf{k}\cdot\mathbf{r} - \omega t + \frac{\phi}{2}\right)\right], \tag{3.4}$$

with the amplitude of the resultant wave now dependent on ϕ. The sinusoidal nature of this dependence thus defines the characteristic interferometric fringe pattern of alternating maxima and minima, which we can find by substituting appropriate values for ϕ into the above equation:

$$\Psi(\mathbf{r}, t) = \begin{cases} 0, & \text{if } \phi = (2n+1)\pi; \\ 2A\cos\left(\mathbf{k}\cdot\mathbf{r} - \omega t\right), & \text{if } \phi = 2n\pi. \end{cases} \tag{3.5}$$

As can be seen above, phase differences of odd-integer multiples of π result in total destructive interference. On the other hand, phase differences of even-integer multiples of π cause the opposite effect, resulting in a wave with an amplitude equal to that of the two original waves added together. This is therefore the mechanism by which the characteristic pattern of bright and dark spots, or 'fringes' seen in the double slit experiment arises.

Interferometry is the discipline of analysing these fringe patterns. In astronomy, we use individual telescopes instead of slits, and interfere the light using optical fibres, but the principle is the same as that discovered by Young more than two centuries ago. The separation between telescopes of an astronomical interferometer is known as the baseline, and is analogous to the primary mirror size in a conventional telescope. Figure 3.2 shows a schematic of the basic concept of a two-element interferometer providing a single baseline, with the apertures located at locations m_1, m_4 and the baseline length consequently $B = |\mathbf{B}| = |m_1 - m_4|$. The optical path difference is labelled Δ, and the angle of incidence of the light is denoted θ. The contrast between these fringes is termed the *visibility*. For a simple interferometer with only two apertures, as in Figure 3.2, it can be defined very simply as the ratio of fringe amplitude to average fringe intensity:

$$V_{\text{norm}} = \frac{i_{\max} - i_{\min}}{i_{\max} + i_{\min}}, \tag{3.6}$$

with $i_{\max}$ and $i_{\min}$ denoting the maximum and minimum fringe intensity respectively. The above quantity is termed the *Michelson* or *normalised* visibility. The visibility is the most fundamental observable in interferometry, as it is relatively easy to measure and can give us substantial information about the structure of the original source, as described in

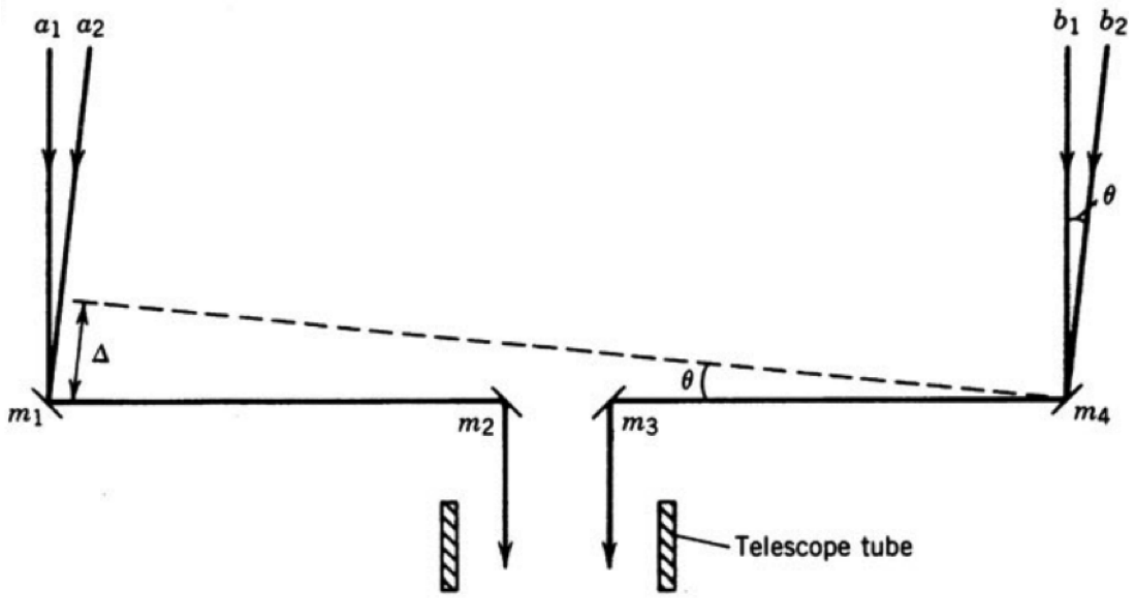

Figure 3.2: Sketch of a simple, two-element interferometer. The apertures are located at locations m_1, m_4. Adapted from Born and Wolf (1999).

Section 3.3.3.1.

3.3.2 Co-ordinates

It is helpful at this point to define our co-ordinate system. The system of telescopes used as an interferometer is located in the *ground plane*, or (x, y) plane, with the z-axis representing the direction toward the *source plane*, a region of space far from the (x, y) plane containing our object, which I have defined as the (X, Y) plane (see Figure 3.3). In order to be able to describe the transformations that result in information about the real image being encoded into interferometric observables, we need to define an 'inverse' plane. This can be done by transforming the original co-ordinates $\mathbf{r} = (x, y)$ as follows:

$$\mathbf{u} \equiv (u, v) = \frac{1}{\lambda}(x, y) = \frac{k}{2\pi}(x, y); \tag{3.7}$$

$$\therefore \ \mathbf{r} = (u, v)\lambda. \tag{3.8}$$

This effectively is a transformation which projects the baseline vector onto the plane which is normal to the direction the object lies in, normalised for wavelength (Labeyrie et al. 2006), with extension to the third dimension provided by the relation $w \equiv \sqrt{u^2 + v^2}$. This plane is the Fourier conjugate to the angular position of the object on sky, $\boldsymbol{\sigma} \equiv (l, m)$

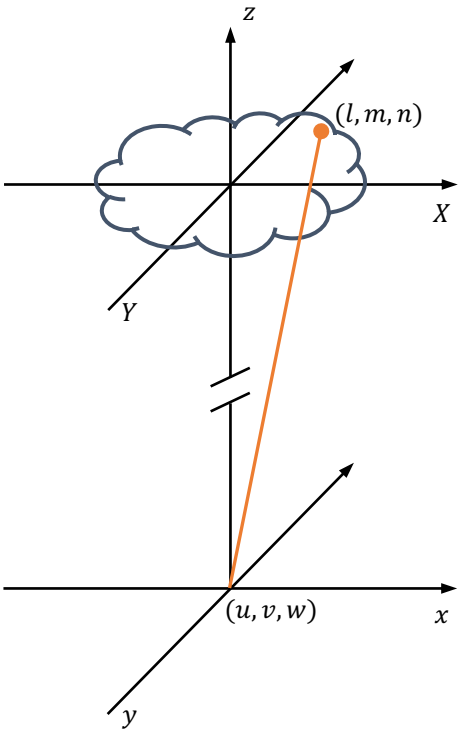

Figure 3.3: Relation between the source plane (top) and ground plane (bottom) when taking an interferometric observation. The distance scale between the planes is assumed to be much greater than that within each plane. The (l, m) and (u, v) planes are Fourier conjugates of the source and ground planes, respectively.

(see Fig. 3.3), with $n \equiv \sqrt{l^2 + m^2}$ defined analogously to w. Each instance of $\mathbf{u}$ is termed a *spatial frequency*.

3.3.3 Coherence

Fringe patterns will only be visible if the waves coming through both apertures are *coherent*, meaning that their phase at a certain point in space is constant over time (Wolf and Meystre 2008). For the simple double slit experiment, this is indeed the case, because the light coming from both apertures originates from the same source and travels a short distance. However, many of the challenges in optical and near-infrared astronomical interferometry involve ensuring the coherence of light incident at each telescope (see Section 3.5). The concept of coherence was first mathematically formalised by van Cittert (1934) and Zernike (1938), as the *coherence function* $\gamma(\mathbf{r}_1, \mathbf{r}_2)$. This characterises the relationship between waves detected at two points $\mathbf{r}_1$ and $\mathbf{r}_2$, as long as the distance between the points is much smaller than the distance to the source. The coherence function can encode both temporal and spatial correlation information, depending on the angle that the

vector $(\mathbf{r}_2 - \mathbf{r}_1)$ makes with the incident wavefronts. In the case they are perpendicular, as in Figure 3.1, the coherence function is a purely spatial relation (see Equation 3.9). Conversely, if the vectors are parallel, the points $\mathbf{r}_{1,2}$ will sample the waves at the same location, but at different times.

In practice, we usually neglect the temporal component of the coherence function, due to it having a negligible effect in most physical cases (Labeyrie et al. 2006). Let us consider two observations of a complex wave $\psi(\mathbf{r}, t)$, taken at the same time (t), but in two different places $(\mathbf{r}_{1,2})$. We can define the coherence function γ as:

$$\gamma(\mathbf{r}_1, \mathbf{r}_2) = \frac{\langle \psi(\mathbf{r}_1, t)\, \psi^*(\mathbf{r}_2, t) \rangle_t}{\sqrt{\langle |\psi(\mathbf{r}_1, t)|^2 \rangle_t \, \langle |\psi(\mathbf{r}_2, t)|^2 \rangle_t}}, \tag{3.9}$$

which is simply a time-averaged and normalised correlation of the two complex wave functions (Labeyrie et al. 2006). It follows from Equation 3.9 that $0 \leq \gamma(\mathbf{r}_1, \mathbf{r}_2) \leq 1$. For $\gamma = 1$, the beams are fully coherent, and at $\gamma = 0$ they are completely uncorrelated and therefore incoherent. In practice the coherence function is very commonly less than one, due to observed objects having an angular size rather than point sources. This partial coherence causes fringes from different parts of the object to have slightly shifted phases, reducing the coherence. The magnitude of this phase shift is given by $\phi = 2\pi(\mathbf{u} \cdot \boldsymbol{\sigma}) = 2\pi(ul + vm)$ (Buscher 2015). Therefore, the phase of the fringes is dependent on the position of the source.

3.3.3.1 The van Cittert-Zernike theorem

The van Cittert-Zernike theorem lies at the heart of coherence theory, and governs the relationship between the geometry of a source and its visibility. The van Cittert-Zernike theorem states that "the normalised value of the spatial coherence function is equal to the Fourier transform of the normalised sky brightness distribution" (Haniff 2007).

Let us define the brightness distribution of an object as $I(\hat{\mathbf{S}})$, where $\hat{\mathbf{S}}$ is the unit vector pointing to the source's location as seen by an observer. The delay, or optical path difference (OPD) between the two elements of the interferometer will be $\Delta = \mathbf{B} \cdot \hat{\mathbf{S}}/c$. Since interferometry requires coherent light in order to make fringes, this delay must be

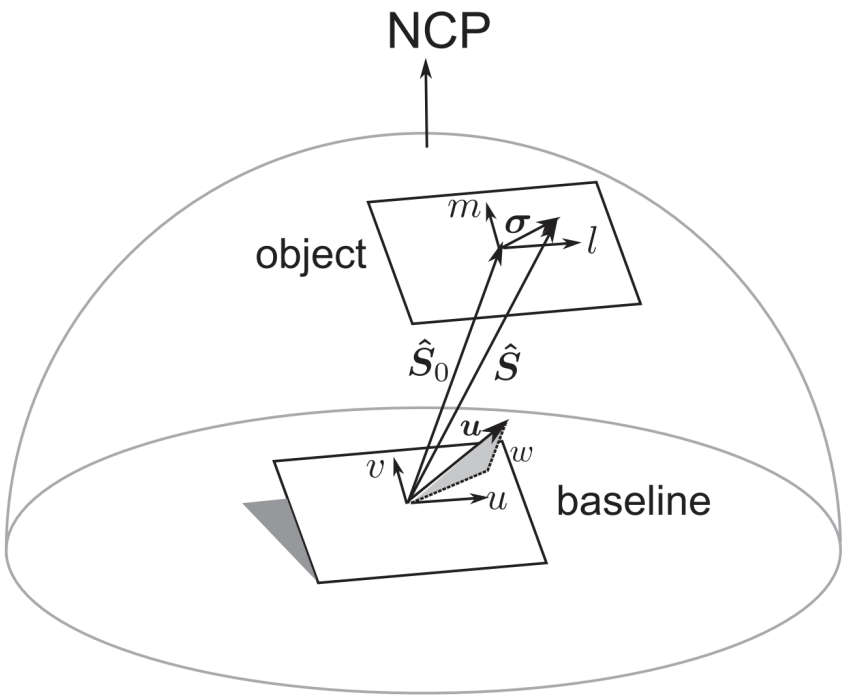

Figure 3.4: Geometry of an interferometric observation. The phase centre of the image is labelled $\hat{\mathbf{S}}_0$, while the location of the object is labelled $\hat{\mathbf{S}}$. Also shown are the spatial frequency $\mathbf{u} = \mathbf{B}/\lambda$ and its equivalent in the image plane $\boldsymbol{\sigma} = \hat{\mathbf{S}} - \hat{\mathbf{S}}_0$. Figure taken from (Buscher 2015).

subtracted, which results in the phase centre changing from the location of the object $\hat{\mathbf{S}}$ to the newly-defined $\hat{\mathbf{S}}_0$, the *phase reference* or *pointing centre* (e.g. Berger and Segransan 2007). The difference between these two vectors is another way of defining the vector $\boldsymbol{\sigma} = \hat{\mathbf{S}} - \hat{\mathbf{S}}_0$ (see Figure 3.4). By considering two incident waves having an amplitude A_i, the time-averaged intensity of the interference pattern will take the following form:

$$i(\phi) = A_1^2 + A_2^2 + A_1 A_2[\gamma \exp(\mathrm{i}\phi) + \gamma^* \exp(-\mathrm{i}\phi)] \tag{3.10}$$

$$= A_1^2 + A_2^2 + 2A_1 A_2 |\gamma| \cos(\phi + \delta), \tag{3.11}$$

where δ is the location of the central fringe and $|\gamma| = \gamma \exp(\mathrm{i}\delta)$ (Labeyrie et al. 2006). The values of $i_{\mathrm{max,min}}$ calculated from the above equation can in turn be substituted into Equation 3.6 to recover a more general expression for the visibility which also encodes phase information:

$$V\mathrm{norm} = \frac{2A_1 A_2}{A_1^2 + A_2^2} |\gamma|. \tag{3.12}$$

This *complex visibility* is directly related to the Michelson's definition of visibility (Equa-

tion 3.6) when its modulus is taken: $V_{\mathrm{M}} = |V|$. However, it also encodes phase information, unlike the simpler V_{M}. Equation 3.12 shows the intimate relationship between the visibility and the coherence function, which are indeed the same if the amplitudes of the two waves are equal. The complex visibility is commonly expressed as the following Fourier integral:

$$\boxed{V_{\mathrm{norm}}(u,v) = \frac{V(u,v)}{V(0,0)} = \frac{\iint_{-\infty}^{+\infty} I(l,m) \exp\left[-2\pi \mathrm{i}(ul+vm)\right] \mathrm{d}l \, \mathrm{d}m}{\iint_{-\infty}^{+\infty} I(l,m) \, \mathrm{d}l \, \mathrm{d}m}}, \tag{3.13}$$

which has been normalised to conform to Michelson's constraint of $V_{\mathrm{norm}} \in [0,1]$. The visibility has the property of being equal to one on short baselines where the object is unresolved. The inverse transform is shown below for completeness:

$$I(l,m) = \iint_{-\infty}^{+\infty} V(u,v) \exp\left[2\pi \mathrm{i}(lu+mv)\right] \mathrm{d}u \, \mathrm{d}v. \tag{3.14}$$

Perfect reconstruction of the source from its visibility would require a completely filled (u,v) plane, which in turn would require an infinite number of observations. Since this isn't possible in reality, interferometric measurements attempt to sample the (u,v) plane at enough places to be able to interpolate the continuous visibility function where (u,v)-coverage is lacking. The spatial structure of the source can therefore be recovered from the visibility, if enough (u,v) points are sampled. The (u,v)-coverage of observations usually benefits from the rotation of the Earth, with subsequent observations on the same physical baseline probing slightly different areas of the (u,v) plane. This is easily seen as the 'arcs' of (u,v) coverage on observations such as Fig. 4.10.

3.3.4 Visibility amplitude and phase

Since the visibility is a complex quantity, it possesses both an amplitude and a phase, both of which encode information about the source. Let us consider waves arriving at the two apertures m_1 and m_4 on Figure 3.2. The van Cittert-Zernike theorem states that, in order to reconstruct the visibility, we must measure the signal arriving at the same time. However, the signal will arrive at m_1 and m_4 at slightly different times, with the optical path difference labelled as Δ. We can account for this by using instruments known as *delay*

lines, which are movable mirrors that allow us to lengthen the path of one of the beams, ensuring coherence at the desired location. The incident angle θ can then be calculated:

$$\delta\phi = \frac{2\pi\Delta}{\lambda} = \frac{2\pi B \sin\theta}{\lambda} \approx \frac{2\pi B\theta}{\lambda}, \tag{3.15}$$

where I have used the small-angle approximation to substitute $\sin\theta \to \theta$. It is from θ that the spatial structure of the source can be found (Monnier 2007). Since the phase is inversely proportional to the wavelength, very precise time delays are required to accurately calculate $\delta\phi$ when working in the near-infrared regime. This means that random fluctuations in atmospheric turbulence can have large effects, which make measuring visibility phase difficult, especially since the angle θ is typically extremely small. The effect of atmospheric turbulence is to decouple the visibility phase from the overall structure – meaning that reconstructing a source brightness distribution becomes dependent entirely on the visibility amplitude. However, the amplitude alone is only able to describe centrosymmetric objects (e.g. Dullemond and Monnier 2010), so this problem must be solved in order to model more complex geometries. As we have seen in Section 3.2, early experiments with interferometry were mainly focused on determining stellar diameters. For this purpose, the star is approximated as a symmetric disc, meaning that analysis of the positions of the visibility nulls can indeed give useful results – as found by Michelson and Pease (1921).

3.3.5 Closure Phase

Atmospheric turbulence is not uniform, with the potential for large differences over relatively small separations both in position and time. Indeed, when considering a phase signal from the source measured on a given baseline ij ($\phi^{\star}_{ij}$), each telescope will likely have a *different* contribution from the atmosphere ($\phi^{a}_{i,j}$). Compensating for these atmospheric components can allow us to reconstruct the source phase to much greater precision. By taking a 'triangle' of three telescopes i, j, k (see Figure 3.5), it is possible to subtract the atmospheric component of each telescope to obtain a phase that is independent of

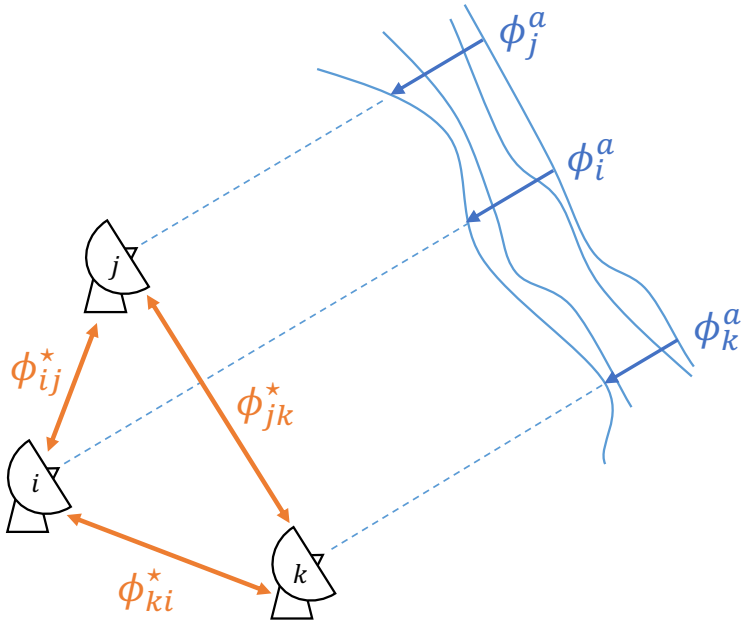

Figure 3.5: Sketch of the definitions of closure phase components in a three-element interferometer, showing how the atmospheric turbulence changes depending on location.

atmospheric changes over time:

$$\Phi_{ijk} = (\phi^\star_{ij} + \phi^a_j - \phi^a_i) + (\phi^\star_{jk} + \phi^a_k - \phi^a_j) + (\phi^\star_{ki} + \phi^a_i - \phi^a_k), \tag{3.16}$$

$$\Rightarrow \Phi_{ijk} = \phi^\star_{ij} + \phi^\star_{jk} + \phi^\star_{ki}. \tag{3.17}$$

The above quantity is termed the *closure phase*. If an interferometer is comprised of N telescopes, then there are $\binom{N}{3} = \frac{N(N-1)(N-2)}{6}$ closure triangles. However, due to duplication there will only be $\binom{N-1}{2} = \frac{(N-1)(N-2)}{2}$ independent closure phases (Monnier 2007). This means that some information is lost using closure phases compared to ordinary visibility phases. However, as one increases the number of telescopes and the number of closure phase triangles, the fraction of phase information contained in the closure phases rises rapidly to 50% with four telescopes, and 80% with ten telescopes. The closure phase is also a self-calibrating quantity – that is, it does not require measurement of a calibrator object in order to account for changes in the atmospheric quality.

Closure phases are either 0° or 180° for a centro-symmetric source, with deviations from zero being indicative of the source having an asymmetric brightness distribution (Monnier 2007). If a source is unresolved, it also will have a closure phase of zero.

In the context of binary observations, the closure phase is a very useful quantity. A binary with both components the same brightness will have a closure phase alternating between 0° and 180°, since this will also be centro-symmetric if the appropriate co-ordinate system is employed. Deviations from these values is directly correlated with the relative difference in intensity of the two components, and their periodicity to the components' separation (Bonneau et al. 2006). However, use of closure phases alone cannot recover the *absolute* position of an object, which must be constrained using other observables such as the visibility amplitude. Therefore, modelling interferometric data usually requires fitting of multiple observables simultaneously, as is the case in all the modelling in Chapters 4 and 5.

3.4 Geometric modelling

Geometric modelling of interferometric data is made possible by the Fourier transform relationship between the visibility and the source brightness distribution (as described in Section 3.3.3). The properties of this Fourier relationship allow multiple simple models to be added together to create more complex structures, a powerful tool for modelling the wide variety of geometries that astronomical objects exhibit. In the next section I will outline the most common models which are used as 'building blocks' in geometric modelling.

3.4.1 Point source

This is the simplest model, generally used to model unresolved stars with a defined flux. The intensity of a point source is described by a δ-function, and if the source is located at the phase centre $\hat{\mathbf{S}}_0$, it will be represented by a constant in the visibility curve.

3.4.2 Gaussian

This is used to represent models in which the brightness distribution smoothly reduces with radius according to a Gaussian profile. The characteristic quality of a Gaussian model is its full width at half maximum (FWHM). Since the Fourier transform of a Gaussian is itself a Gaussian, the visibility of a Gaussian model has the property of smoothly going to zero without any 'bounces' (see Figure 3.6).

Gaussians of arbitrarily large radius (comparable or larger than the field of view of the relevant instrument) are often used to represent unresolved emission originating from a very large radius, for example halo emission (see Section 4.3). This is due to the visibility curve of a Gaussian falling to zero based on its FWHM – the larger the FWHM, the faster its visibility drops to zero, meaning that a sufficiently large Gaussian will be overresolved on even the shortest baselines.

3.4.3 Ring

Ring models are very useful when studying circumbinary discs, as they can model the inner cavity while keeping material at larger radii. The model for a ring is a first-order Bessel function of the first kind. The ring models used in the analysis of HD 104237 A in Chapter 5 also had intensity variable by azimuth, allowing for the modelling of bright and dark regions within a ring, which can be caused by density variations, shadows or disc warping. The visibility curve of a ring 'bounces' upon reaching a minimum, leading to the graph being divided into regions known as *lobes*. Each lobe of the visibility curve corresponds to a 180° change in phase compared to the lobes either side.

3.4.4 Uniform disc

This model is generally used for resolved stars. The intensity distribution for a uniform disc with diameter d is a circle with uniform intensity, and its Fourier transform is described by a first-order Bessel function of the first kind.

3.4.5 Multi-component models

The additive property of Fourier transforms is what allows complex modelling, combining several simple components such as those described in the previous sections. The visibility for such a multi-component model with j components can be simply described as an addition of the visibilities of the components V_j multiplied by their respective flux F_j, normalised by the total flux. The binary model on Figure 3.6 is an example of an binary with both components having the same flux and positioned an equal distance from the phase centre $\hat{\mathbf{S}}_0$. The minimum visibility shows the flux ratio ($V^2_{\text{min}} = 0$ for an equal binary), and the separation between peaks shows the binary separation. Deviations from equal

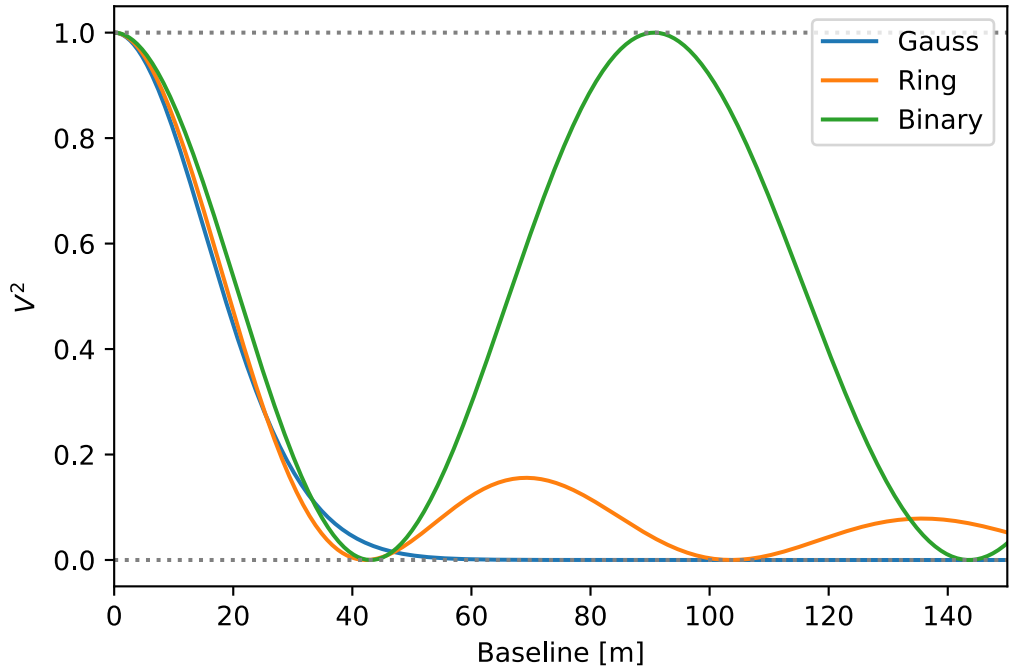

Figure 3.6: Model squared visibility curves for simple models including an equal binary with separation 5 mas, a thin ring of diameter 5 mas, and a Gaussian with FWHM 2.5 mas. The regions bounded by visibility minima are termed visibility lobes, and show where the phase changes by 180°. Note the degeneracy of the visibilities for short baselines – underlining the usefulness of long-baseline interferometry.

brightness and the presence of additional geometric components result in the visibility curve being modulated. A clear example of this can be found in the continuum modelling of MWC 166 A in Section 4.3.1.

3.4.6 Spectro- and differential interferometry

Restricting the wavelength of an observation, by observing in narrow bands, can minimise dispersion in interference fringes, increasing the precision of an observation and allowing use of visibility phase across the spectral line, known as 'differential phase'. And since the vector $\mathbf{u} = \mathbf{B}/\lambda$ is dependent on wavelength, performing interferometric measurements at multiple wavelengths also increases the (u, v)-coverage of observations substantially. Furthermore, wavelength-dependence is a key property of many physical processes in astronomical objects. For example, the models described in Section 3.4 can be given a wavelength dependence to model a temperature gradient in the circumstellar material.

As a result, observing interferometric observables across small differences in wavelength can be useful on many levels!

The resolution of spectrally-dispersed observations is expressed in two ways: the number of spectral channels in an instrument, and its wavelength spacing. For example, the PIONIER instrument (see Section 3.5.1) generally operates over six spectral channels over a wavelength range of $\sim 0.25\,\mu\text{m}$, leading to a resolution of $\mathcal{R} \sim 22$. For high data with a large spectral resolution, such as that collected by GRAVITY's high-resolution mode, it is possible to model spectral lines. Spectral lines in a YSO can have multiple origins. The Brackett γ line, at $2.166\,\mu\text{m}$, is a typical target for GRAVITY observations, due to the various physical processes that it can trace, as described in Section 2.6.

3.4.6.1 Differential interferometry

Differential interferometry is the term given to interferometry applied across spectral lines, analysing differential visibilities, phases and closure phases across the line. A very useful application of differential interferometry lies in the sensitivity of the differential phase to the astrometric photocentre shift between wavelengths. Therefore, it is possible to use differential phases to analyse the difference between the photocentre of continuum emission and the photocentre in a spectral line such as Br γ (e.g. Millour 2014). This *photocentre shift* p can be expressed in terms of the differential phase ϕ as follows, as long as the object is marginally resolved (Lachaume 2003; Le Bouquin et al. 2009):

$$p = -\frac{\phi}{2\pi}\frac{\lambda}{B}. \tag{3.18}$$

In the above equation, p is in fact the projection of the two-dimensional photocentre shift on the plane of the sky, in the direction of the baseline, and λ is the central wavelength (Lachaume 2003). The photocentre displacement is much more sensitive than the stated spatial resolution of a given instrument. This has seen much useful application in the determination of stellar spin axes, as the technique is sensitive enough to discern between red- and blue-shifted hemispheres of a star (e.g. Hadjara et al. 2022).

3.4.7 Modelling tools

A variety of tools exist to solve the inverse problem of interferometric modelling (e.g. LITpro[1], Tallon-Bosc et al. 2008; SIMTOI[2], Martinez and Baron 2020). The main tool used in the analysis throughout chapters 4 and 5 is PMOIRED[3] (Mérand 2022), a `python3` package which is capable of fitting visibilities, closure phases, differential phases and spectra simultaneously. The simple syntax and open-source nature of PMOIRED makes it very accessible to the community, and it has been used in many recent papers (such as Fabry et al. 2021a; Bordier et al. 2022; Frost et al. 2022). PMOIRED combines basic 'building blocks' such as those described in Section 3.4 to create models with varying degrees of complexity, including asymmetries, temperature gradients and arbitrary density profiles. It also includes bootstrapping and grid-searching for systematic analysis of data.

3.5 Long-baseline interferometric facilities

Long-baseline interferometry refers to interferometers where multiple telescopes are used, with baselines much larger than the dish size of a given telescope. While aperture-masking interferometers still comprise a majority of infrared interferometers (such as SPHERE-SAM, NIRC2-SAM and the new JWST-SAM), the number of modern long-baseline optical and near-infrared interferometers, which allow observations at very small angular resolutions, up to micro-arcsecond scale (e.g. Buscher 2015), is increasing rapidly. Figure 3.7 shows the general layout of a telescope pair in a long-baseline near-infrared interferometer. Designs of these interferometers can vary substantially, but all follow the same general principles:

- Light is collected at individual telescopes and transported via beam relays (usually vacuum tubes e.g. ten Brummelaar et al. 2005) to a central location to be processed;
- The light from each telescope is put through delay lines, or path compensators, to ensure coherence;
- The coherent light is sent through optical fibres to be interfered in a beam combiner, producing fringes and measuring the observables (visibility amplitude and phase).

1. Available at: http://www.jmmc.fr/apps/beta/LITpro/
2. Available at: https://github.com/bkloppenborg/simtoi
3. Available at: https://github.com/amerand/PMOIRED

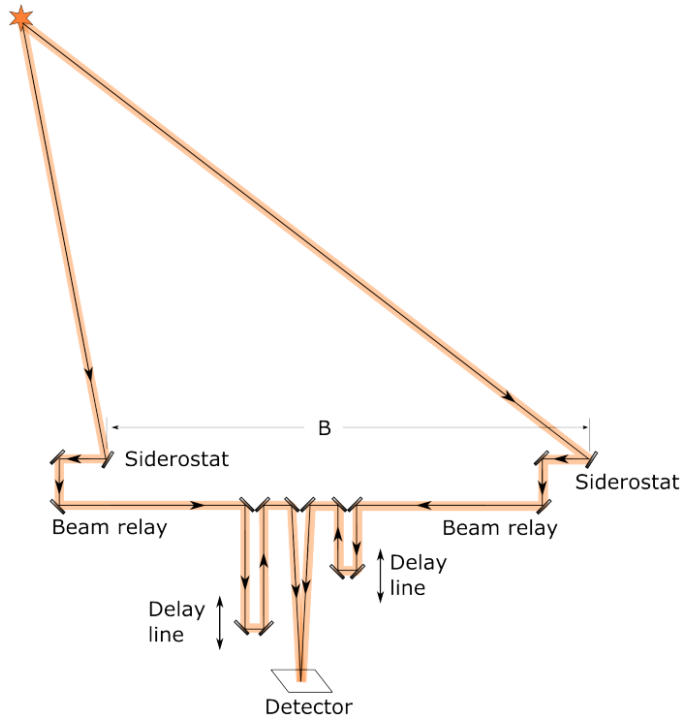

Figure 3.7: Sketch of a two-element long-baseline interferometer. The delay lines are mobile and can be moved in real time in order to ensure coherence. Figure taken from (Buscher 2015).

Therefore, an interferometer can be subdivided into two main parts – the facility itself, including the telescopes and delay lines, and the 'instruments', which usually refer to the beam combiners. Below I briefly describe some of the most widely-used and state-of-the-art long-baseline interferometers.

3.5.1 VLTI

The Very Large Telescope Interferometer (VLTI) is the main infrared interferometric facility of the European Southern Observatory (ESO). Located at Cerro Paranal in Northern Chile, it consists of four 8.2 m unit telescopes (UTs), which can also be used individually as traditional telescopes, and four 1.8 m auxiliary telescopes (ATs). The large mirror diameter and state-of-the-art adaptive optics system of the UTs (known as MACAO) allows for observation of targets fainter than any other interferometer, up to $V_{\rm mag} \sim 17$ in extreme cases (Arsenault et al. 2003). The UTs have baseline lengths ranging from 47 m to 130 m.

The ATs are entirely dedicated to interferometry, unlike the UTs. Despite their much smaller mirror size, each telescope is mounted on railway tracks and can be moved

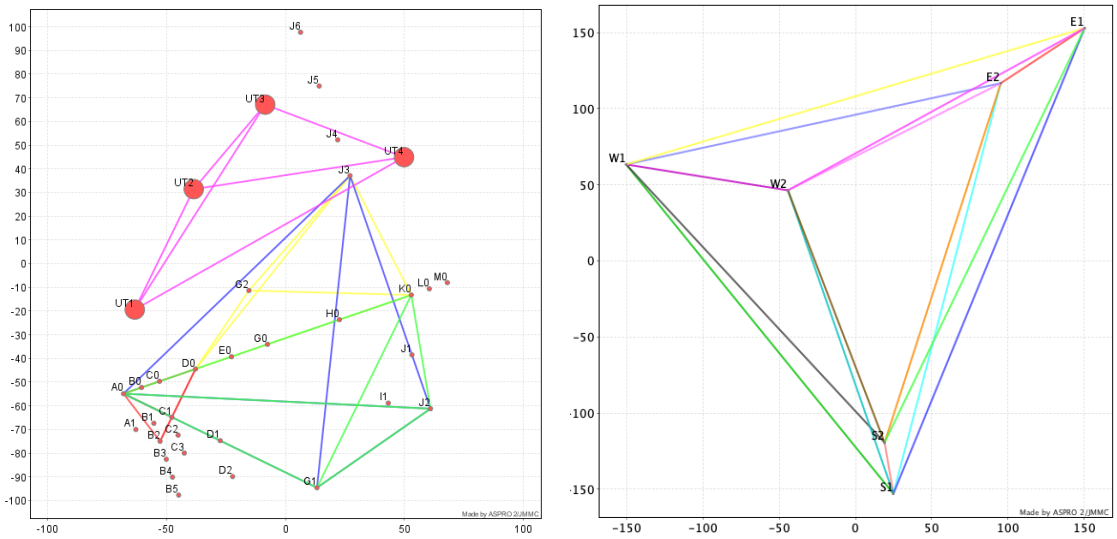

(a) Diagram of VLTI baselines. The UT baselines are shown in purple, and the four different AT configurations for P are shown in red (small), yellow (medium), blue (large), and green (astrometric).

(b) Diagram of CHARA baselines.

Figure 3.8: Baselines for the two most commonly used NIR interferometers. The axes have units of metres.

between multiple stations. Therefore, observations can be taken with the ATs in four different configurations: small (11-34 m), medium (40-104 m), large (58-132 m) and astrometric (49-129 m), as shown on Figure 3.8a. In addition, only two telescopes can be moved per day, so in practice some observations will be taken on intermediate configurations, increasing the potential baselines even further (Arsenault et al. 2003). Therefore, the ATs offer significant control over the spatial frequencies probed and if multiple configurations are used to observe and object, AT observations can give a very well-sampled (u, v)-coverage. The ATs also have an adaptive optics system (NAOMI), which allows observations of objects as faint as 9 magnitudes in the near-infrared (Woillez et al. 2019).

As of the time of writing, there are three main instruments operational at the VLTI, all of which are four-telescope combiners. The oldest instrument in active use at the VLTI, as well as the simplest, is PIONIER, with first light in November 2010 (Le Bouquin et al. 2011). It observes in the H band (centred on 1.65 µm), and observations with PIONIER are generally taken using the 'GRISM' spectral setup, which provides six spectral channels (equivalent to a resolution of $\mathcal{R} \sim 40$). This allows modelling of the dust continuum, but not spectral lines. PIONIER has been used to push the boundaries of high-

resolution astronomy for many years. For example, it has fully resolved a symbiotic binary undergoing mass transfer (Blind et al. 2011), detected exozodiacal light around nearby sun-like stars (Ertel et al. 2014) and, perhaps most impressively, observed granulation on a stellar surface other than that of the Sun for the first time (Paladini et al. 2018).

The GRAVITY instrument is the VLTI's first second-generation instrument, having begun operations in January 2016, and operates in the K band (centred on 2.2 µm). GRAVITY is able to provide spectrally-dispersed observations to a very high level of precision due to its in-built fringe tracker (FT), which uses a low-resolution ($\mathcal{R} \sim 22$) channel to 'lock on' to fringes and keep them focused by modulating mirrors mounted within the instrument. This allows GRAVITY to correct for atmospheric and instrumental effects in real time, increasing the potential integration times of the observation. The science camera (SC) simultaneously then allows data to be recorded either in medium ($\mathcal{R} \sim 500$) or high ($\mathcal{R} \sim 4000$) resolution, the latter of which is large enough to resolve spectral lines (see Chapters 4 and 5). GRAVITY was conceived as a platform to observe objects at a very small angular resolution, and has been responsible for some of the VLTI's most celebrated accomplishments in recent years, such as the detection of gravitational redshift (GRAVITY Collaboration et al. 2018) and relativistic Schwarzschild precession around Sgr A* (GRAVITY Collaboration et al. 2020). The GRAVITY beam combiner is shown on Figure 3.9. The newest instrument at the VLTI is MATISSE, which had its first light in March 2018. This is a mid-infrared instrument which observes in the L, M and N bands (centred around 3.5, 4.7 and 10 µm respectively). Like GRAVITY, it offers spectrally dispersed fringes, with the L- and M-bands offering a range of spectral resolutions up to $\mathcal{R} \sim 3500$ – while the N-band has spectral resolutions up to $\mathcal{R} \sim 220$ (Lopez et al. 2022). An interesting feature of MATISSE is the ability to record observations in L/M- and N-band simultaneously, in low or medium spectral resolution. The suite of near-infrared instruments at the VLTI allows for probing of a variety of length scales and regions in protoplanetary discs, from the pure gaseous disc with PIONIER up to the area just beyond the inner rim of the dusty disc with MATISSE, making it an invaluable telescope for studying these objects.

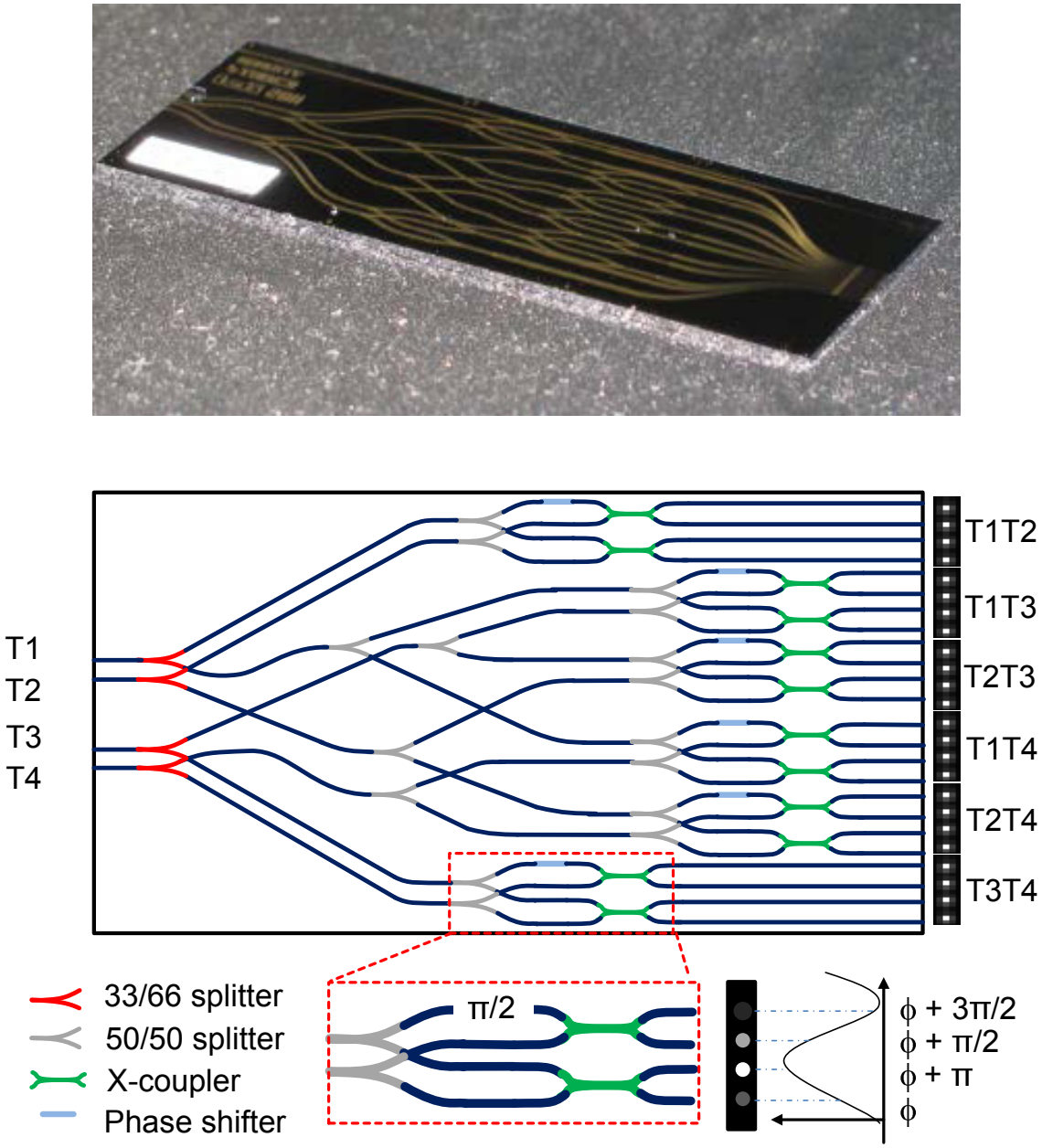

Figure 3.9: A photograph of the integrated optics chip of the GRAVITY instrument at the VLTI (top panel), and a schematic of the chip (bottom panel). Taken from Gravity Collaboration et al. (2017).

3.5.2 CHARA

The Centre for High Angular Resolution Astrophysics (CHARA) is located on Mt. Wilson, California, and is comprised of six 1 m telescopes arrayed in a Y shape, the most of any optical interferometer worldwide at the time of writing. While the telescopes are fixed, unlike the VLTI ATs, their arrangement allows for very long baselines (> 330 m, see Figure 3.8b). The primary instruments at CHARA are MIRC-X (J, H bands, Anugu et al. 2020) and MYSTIC (K band, Monnier et al. 2018). These instruments are at the cutting edge of interferometry of binary YSOs, and have been used in the landmark GW Ori study already mentioned in Chapter 2 (Kraus et al. 2020), as well as many other programmes such as the highly-ambitious ARMADA project, which analyses dozens of previously-unresolved binaries (Gardner et al. 2022).

3.5.3 Other facilities

There are many other long-baseline interferometers operational or soon to be inaugurated. The Naval Precision Optical Interferometer (NPOI) has 6 collectors with mirror size 12 cm. Despite this being much smaller than other interferometers, the maximum baseline of NPOI is ~ 450 m, the largest of any facility. This allows bright targets to be observed at very high resolution. The VISION instrument can provide spectrally dispersed observations with resolution up to $\mathcal{R} \sim 1200$ in visible and very near-infrared wavelengths (570-900 nm). The Magdalena Ridge Observatory Interferometer (MROI) also has its telescopes, 1.4 m in size, arranged in a Y shape. The MROI is still under construction at the time of writing, but eventually is planned to incorporate ten unit telescopes, more than any other near-infrared interferometer. A unique feature of MROI is the equal spacing between telescopes, allowing the technique of 'baseline bootstrapping'. This approach involves separating telescopes by a distance smaller than the size of the main lobe of the visibility of an object to allow a self-calibration of the atmospheric piston error (Buscher et al. 2013).

In the following chapters, I will show how all of the ideas contained in these initial chapters can be used to study young binary systems, by looking at two specific objects.

Chapter 4

Characterising the orbit and circumstellar environment of the high-mass YSO binary MWC 166 A

4.1 Introduction

The masses and ages of young stellar objects (YSOs) are commonly derived from a comparison of observed positions on a colour-magnitude diagram (CMD) with theoretical models (e.g. Siess et al. 2000; Baraffe et al. 2015; Choi et al. 2016). Evolutionary tracks of YSOs are very sensitive to mass and as such need to be calibrated from observed systems with well-constrained masses. The relative paucity of higher-mass Herbig Be YSOs ($\gtrsim 5M_{\odot}$) compared with their lower-mass T Tauri counterparts means that models of higher-mass stars are less thoroughly calibrated. The high effective temperature of Herbig Be stars ($\gtrsim$ 15000 K), as well as their often-uncertain ages due to mass loss from stellar winds, makes it much less straightforward to calculate their masses (Massey et al. 2012). Stassun et al. (2014) found that predicted and measured masses can differ by $\sim$ 10%. The gold standard for deriving model-independent masses is to take advantage of the orbital

mechanics of binary systems. If both astrometric and radial velocity (RV) data are used, the derived orbital parameters can be combined with reliable distance estimates (if any exist) to extract dynamical masses for the individual objects. This requires observation of a binary system at multiple epochs spread over a substantial fraction of the orbit, so targets with relatively short orbits and small separations are the best candidates. The need for precise astrometry on very small angular scales ($\sim$ 1 mas) has hugely benefitted from the relatively recent development of optical and near-infrared (NIR) interferometry, which has 'unlocked' a larger tranche of suitable systems compared to even 15 years ago.

The focus of this study is the multiple system MWC 166 (also known as HD 53367, HIP 34116, and V750 Mon). This is a hierarchical triple system, with a close spectroscopic binary (MWC 166 A) orbited by a wide companion (MWC 166 B) at a separation of 0.6″ (Fabricius et al. 2002). The RV variations of the spectroscopic binary were first reported by Finkenzeller and Mundt (1984), and tentative spectroscopic orbit solutions have been presented by Corporon and Lagrange (1999) and Pogodin et al. (2006). In this paper I focus on this inner spectroscopic binary, the components of which have been labelled MWC 166 Aa and MWC 166 Ab throughout. The object also features significant mid-infrared to millimetre excess, which is indicative of a disc around MWC 166 A. Here, I present NIR interferometric observations obtained with the Very Large Telescope Interferometer (VLTI) and the Center for High Angular Resolution Astronomy (CHARA; ten Brummelaar et al. 2005) Array, which have allowed me to derive a first astrometric orbital solution of the system. I present my observations in Section 4.2, which is followed by a discussion of my modelling approach (Section 4.3). I derive the orbit solution and dynamical mass constraints in Section 4.4, and spectral line analysis results are presented in Section 4.5. A discussion on the distribution of circumstellar material – both in the dust continuum and in prominent K band emission lines – is presented in Section 4.6.

4.2 Observations

Near-infrared interferometric observations were taken over a period of 8 years, mainly using the PIONIER (Le Bouquin et al. 2011) and GRAVITY (Gravity Collaboration et al. 2017) four-beam combiners at the VLTI. All VLTI observations employed the 1.8-metre

Auxiliary Telescopes. Longer baselines were provided by four-telescope observations using the CHARA Array instrument MIRC-X (Kraus et al. 2018; Anugu et al. 2020).

The GRAVITY observations were taken in the K band (1.99-2.45 µm) as part of ESO programme 098.C-0910(A). GRAVITY observations include data from the fringe tracker, which operates at a spectral resolution of $\mathcal{R} = \Delta\lambda/\lambda \sim 22$, as well as the science combiner either in medium ($\mathcal{R} \sim 500$) or high ($\mathcal{R} \sim 4000$) resolution (Gravity Collaboration et al. 2017). The observations achieved an angular resolution up to $(\lambda/2B_{\max}) = 1.6$ milliarcseconds (mas) on the longest baselines ($B_{\max} = 130$ m in length), sufficient to spatially resolve the components of MWC 166 A (Gravity Collaboration et al. 2017). The reduction pipeline used was the GRAVITY data reduction pipeline[1] running in the `ESOreflex v2.9.1` environment (Freudling et al. 2013). Besides the statistical uncertainties computed by the GRAVITY pipeline, I include 5% and 1° errors, for the visibility and closure phase, respectively, to account for calibration uncertainties.

The PIONIER observations covered the H band (1.59-1.75 µm) and were obtained as part of multiple ESO programmes: 102.C-0701, 104.C-0737, and 106.21JU. These data were recorded over 6 channels at spectral resolution $\mathcal{R} \sim 40$. The reduction pipeline used was `pndrs v3.52` (Le Bouquin et al. 2011). I also included published data from the large programme 190.C-0963[2] (e.g. Lazareff et al. 2017; Kluska et al. 2016), over 3 spectral channels and with a resolution of $\mathcal{R} \sim 15$.

MIRC-X was used in its H band mode as part of the programme 2020B-M7, using four of the six CHARA Array telescopes. CHARA's much longer maximum baseline of 330 m allowed probing of the object geometry at a nearly three-times higher resolution than possible with VLTI. The `MIRC-X v0.9.5` pipeline[3] (Anugu et al. 2020, § 4) was used to reduce the data.

A full description of the observations is provided in Table 4.1. Each observation was calibrated by observing suitable calibrator stars with known uniform disc diameters (taken from Bourgès et al. 2017), to account for atmospheric absorption and instrument

1. Available at: https://ftp.eso.org/pub/dfs/pipelines/instruments/gravity/gravity-pipeline-manual-1.5.4.pdf
2. Taken from the Optical interferometry DataBase (OiDB), available at: http://oidb.jmmc.fr.
3. Available at: https://gitlab.chara.gsu.edu/lebouquj/mircx_pipeline

Table 4.1: All interferometric observations of MWC 166. Data from programme 190.C-0963 are lacking calibrator information due to being taken pre-calibrated from the JMMC OiDB. Dates are given in the format YYYY-MM-DD.

Date	Programme ID	Array Config	Instrument	$\mathcal{R} \sim \Delta\lambda/\lambda$	Calibrator(s) used
2013-01-27	190.C-0963(A)	K0-A1-G1-J3	PIONIER	15	-
2013-02-20	190.C-0963(B)	D0-G1-H0-I1		15	-
2017-03-14	098.C-0910(A)	A0-G1-J2-J3	GRAVITY	22 & 4000	HD 49647
2017-04-27	098.C-0910(A)	A0-G1-J2-J3		22 & 4000	HD 57087
2017-04-28	098.C-0910(A)	A0-G1-J2-J3		22 & 500	HD 49647
2018-01-11	098.C-0910(A)	A0-G1-J2-J3		22 & 4000	HD 49647
2018-02-06	098.C-0910(A)	A0-G1-J2-J3		22 & 4000	HD 38117
”	098.C-0910(A)	A0-G1-J2-J3		22 & 500	HD 55137
2018-11-29	102.C-0701(B)	A0-G1-J2-K0	PIONIER	40	HD 51914
2018-11-30	102.C-0701(B)	A0-G1-J2-K0		40	HD 51914
2019-12-15	104.C-0737(C)	A0-B2-C1-D0	PIONIER	40	HD 51914
2019-12-16	104.C-0737(C)	A0-B2-C1-D0		40	HD 49741
2019-12-23	104.C-0737(A)	D0-G2-J3-K0		40	HD 51914
2019-12-24	104.C-0737(A)	D0-G2-J3-K0		40	HD 51914
2019-12-29	104.C-0737(B)	A0-G1-J2-J3		40	HD 51914
2020-11-18	2020B-M7	W1-S2-S1-E2	MIRC-X	102	HD 58457
2020-11-19	2020B-M7	W2-W1-S2-S1		50	HD 54930
2020-12-13	106.21JU.002	A0-G1-J2-J3	PIONIER	40	HD 45694, HD 54438, HD 51914
2020-12-19	106.21JU.001	D0-G2-J3-K0		40	HD 45694, HD 54438, HD 51914
2020-12-28	106.21JU.003	A0-B2-C1-D0		40	HD 45694, HD 54438, HD 51914

response. The calibrators were also inspected for signatures of binarity to ensure only single stars were observed. In order to improve the (u, v)-coverage, I grouped the individual measurements into epochs. However, this proved to be difficult due to the rapidly changing orbit of the system. Based on the literature RV orbital period of $\sim$ 183 days (Pogodin et al. 2006), a variation of about one degree in position angle (PA) per day is to be expected. Considering that the PA uncertainties in my binary model fits are on the same order of magnitude as this (see Table 4.3), each epoch should include data from at most two consecutive nights, ensuring that the relative positions of the two components do not change significantly during each epoch. The observations for which this consolidation was performed are marked accordingly in Table 4.1.

4.3 Modelling

4.3.1 Continuum modelling of the system

I fitted the interferometric visibility and closure phase data at each epoch using the Exeter in-house geometric modelling pipeline (e.g. Kreplin et al. 2018). As the stellar radii of MWC 166 Aa and Ab are expected to be $\sim$ 0.04 mas at the distance calculated by Kaltcheva

and Hilditch 2000, I assume that the stellar photospheres can be modelled as point sources.

Initially, the visibilities and closure phases of MWC 166 A were fitted with the following free parameters: separation (ρ); PA[4] of the secondary component from the primary (θ); and the flux contribution of the secondary to the total flux in the model ($f_2/f_{\rm tot}$). The primary flux contribution was kept fixed

Due to the changes in the $f_2/f_{\rm tot}$ flux ratio, the secondary is at some epochs brighter than the primary in my NIR wavelength bands. While there is some variability to the system as a whole over year-length timescales (Pogodin et al. 2006), the relative brightness of the two stars has not been previously recorded, so this was an unexpected finding. In light of this, I restricted θ either to the [0°, 180°] or [180°, 360°] range, where the quadrant was chosen for each epoch to achieve an astrometric orbit that is consistent with the spectroscopic orbit of Pogodin et al. (2006). This was done to ensure that the primary and secondary components of the system were correctly identified at each epoch.

Initially, I did not account for contributions from possible dust emission, consistent with the low measured infrared excess emission in the K band (Tjin A Djie et al. 2001). The two-point-source model fits allow derivation of the astrometry of the two components of the system, but yield a flux ratio that changes significantly between epochs, both in the H and K band. These models also consistently over-predicted the visibilities, as can be seen from the red points in Figure 4.1, leading to large reduced χ^2 values, in particular on the visibilities (e.g. $\chi^2_{\rm vis} > 16$ for the MIRC-X data). In order to reduce this systematic error, I also conducted fits that include extended emission.

4.3.1.1 Evidence for extended circumbinary disc emission

I tried modelling the extended flux assuming three different geometries: a Gaussian with full width at half maximum (FWHM) σ, seen under inclination i and a major axis (east of north) PA $\Theta_{\rm ext}$; a ring with radius R and a thickness of $0.2R$, seen under inclination i and a PA $\Theta_{\rm ext}$; and as over-resolved flux 'background' (modelled as a circular Gaussian with $\sigma = 1000$ mas, i.e. filling the field-of-view). The integrated flux contribution of the extended emission component to the total flux in the model is $f_{\rm ext}/f_{\rm tot}$, where I define

4. Defined as east of north

$f_{\rm tot} \equiv f_1 + f_2 + f_{\rm ext}$.

For the VLTI epochs, the different geometries for the extended emission returned improved χ^2 values over the two-point-source model, but no one extended model had consistently smaller χ^2 values over all epochs. Adopting a Gaussian geometry for the extended emission component results in $\chi^2_{\rm vis}$ values ranging from 0.34 to 2.24, while adapting a ring geometry results in $\chi^2_{\rm vis} = 0.49...4.65$, and over-resolved flux results in $\chi^2_{\rm vis} = 0.57...6.81$. For comparison, the pure point-source model has $\chi^2_{\rm vis}$ between 0.94 and 31.86. Closure phase χ^2 values were found to be almost completely model-independent, with the models returning $\chi^2_{\rm CP} < 2.84$ (point-sources), $\chi^2_{\rm CP} < 1.62$ (background), $\chi^2_{\rm CP} < 1.13$ (Gaussian), $\chi^2_{\rm CP} < 1.43$ (ring).

The MIRC-X data probes roughly three-times higher spatial frequencies than the VLTI data. Data taken over a larger range of spatial frequencies allows me to probe farther lobes of the visibility curve, which helps to more reliably distinguish the effects of the extended emission from the sinusoidal binary modulation. Figures 4.1 and 4.2 respectively show the resultant model visibilities and closure phases obtained from my geometric models described above, overlaid over the data. While the closure phases are well described by the original two-point-source model independently of any extended flux or lack thereof, for the visibilities this is not the case. The two-point-source model, represented by the red points in Figure 4.1, clearly overpredicts the visibility compared to the other models, especially in the high-visibility regime (where $V \gtrsim 0.6$). The model parameters corresponding to Figs. 4.1 and 4.2 are shown in Table 4.2.

By examining the χ^2 values both for visibility and closure phase in Table 4.2, it can be seen that the background model provides a significant improvement on the two-point-source model. A ring profile provides a similar, or even slightly better fit (see Table 4.2), but introduces three additional free parameters while providing only a marginal improvement in the goodness of the fit. I also conducted a fit for a Gaussian model $(\sigma, i, \Theta_{\rm ext})$, which returned similar χ^2 values as the ring model, but I found that the parameters i and $\Theta_{\rm ext}$ did not converge to a value independent of the boundary conditions chosen, while the flux parameters $f_2/f_{\rm tot}$ and $f_{\rm ext}/f_{\rm tot}$ were found to be consistent with the background model. As such, I favour the background model over the Gaussian model.

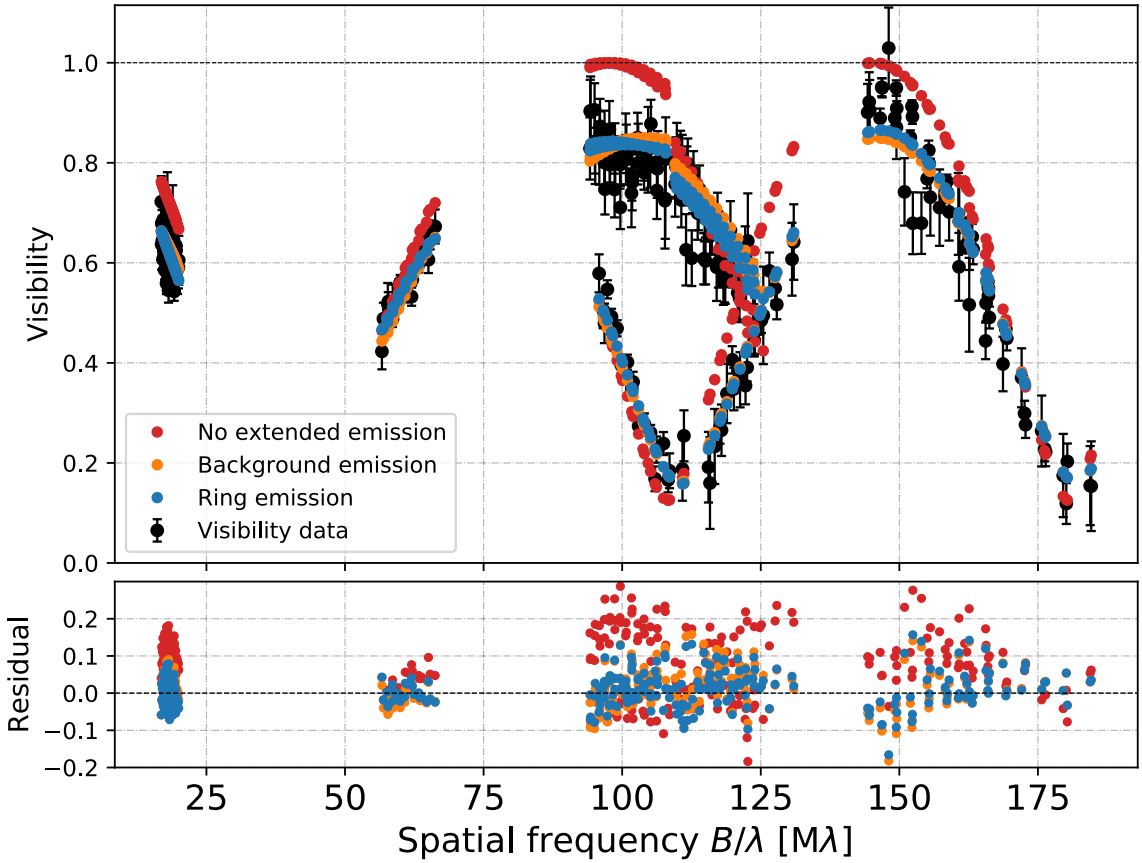

Figure 4.1: Visibilities (and associated residuals) of MIRC-X models. At $V \gtrsim 0.6$, the purely point-source model overshoots the observed data points substantially.

Table 4.2: MIRC-X extended emission model comparison.

Model:	No ext. emission	Background	Ring
ρ [mas]	2.87 ± 0.01	2.84 ± 0.01	2.84 ± 0.01
θ [°]	134.3 ± 0.4	131.1 ± 0.3	131.7 ± 0.3
f_2/f_{tot}	0.437 ± 0.012	0.345 ± 0.004	0.344 ± 0.006
R [mas]	-	-	$4.55^{+0.22}_{-0.19}$
i [°]	-	-	55.2 ± 4.0
Θ_{ext} [°]	-	-	$100.6^{+13.1}_{-9.8}$
$f_{\mathrm{ext}}/f_{\mathrm{tot}}$	-	0.150 ± 0.004	0.150 ± 0.005
χ^2_{Vis}	16.47	3.27	2.63
χ^2_{CP}	4.28	1.95	2.07

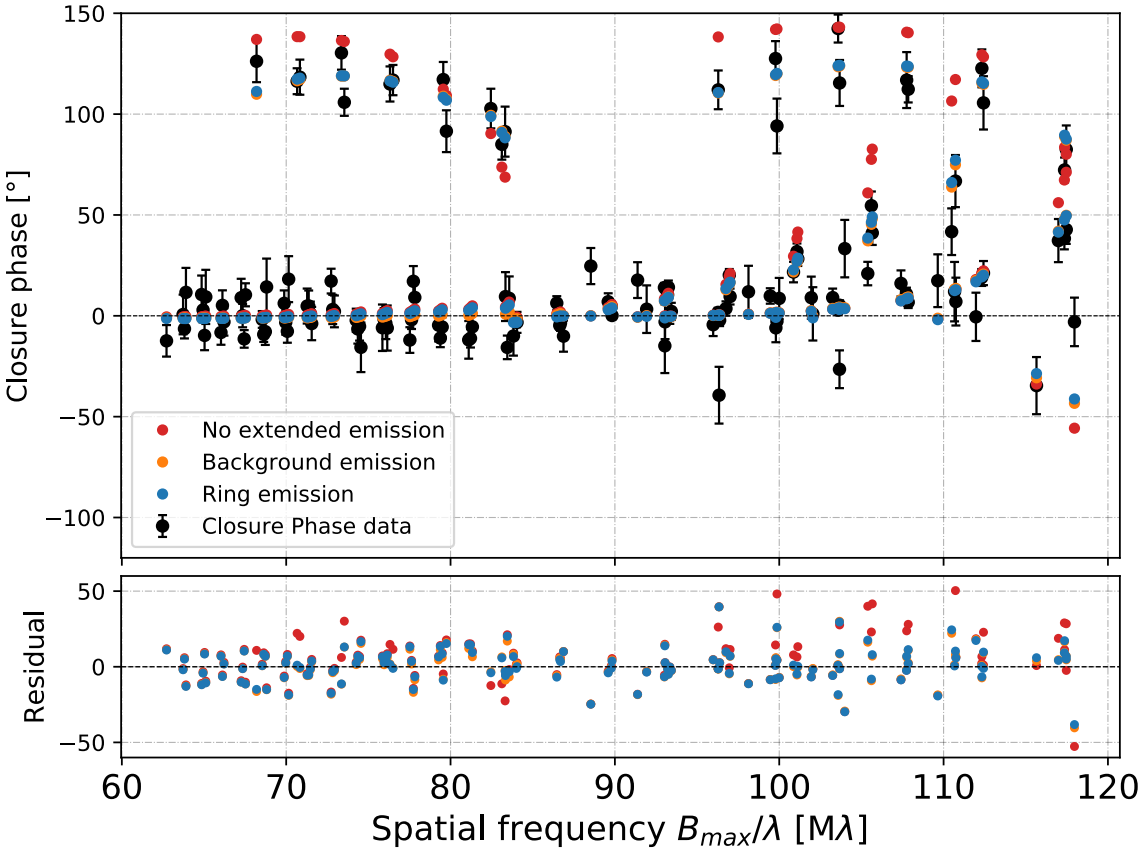

Figure 4.2: Closure phases (and associated residuals) of MIRC-X models.

Therefore, I adopt the over-resolved background model as geometry for the extended emission for all epochs and instruments, likely representing scattered light from the disc. This minimised the model complexity and degrees of freedom. The relative astrometry was therefore fitted with four free parameters: separation (ρ); PA of the secondary component from the primary (θ); secondary flux as fraction of the total flux ($f_2/f_{\rm tot}$) and extended flux as fraction of the total flux ($f_{\rm ext}/f_{\rm tot}$).

It is apparent that the relative astrometry of the binary (ρ, θ) does not depend much on whether extended flux is included in the fit. The value of $f_2/f_{\rm tot}$ and $f_{\rm ext}/f_{\rm tot}$ change depended on whether extended emission is included in the fit, but is rather independent of the geometry of the emission.

4.3.2 Modelling of the K band He i and Br γ lines

For the GRAVITY data, I simultaneously recorded high-resolution data ($\Delta\lambda/\lambda = 4000$) for all epochs, in addition to the low-resolution data used to establish the relative astrom-

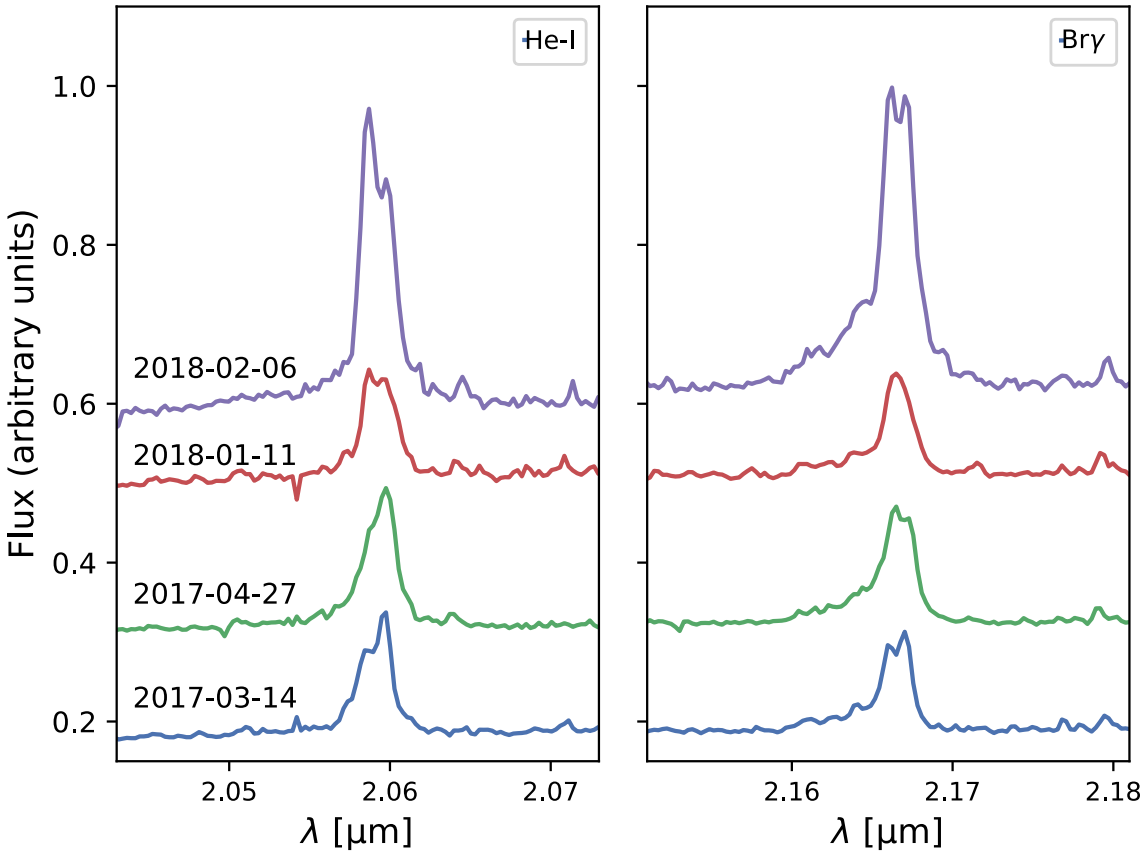

Figure 4.3: Continuum-normalised spectra around the He I and Brγ lines. The different epochs have been offset for clarity. Epoch-dependent variations are visible. Dates are given in the format YYYY-MM-DD.

Table 4.3: Relative astrometry for MWC 166 Aa and Ab, derived from H and K band continuum visibility and closure phase modelling. The model includes two point sources and extended background emission, for a total of four free parameters: separation ρ, position of the secondary component θ (east of north), secondary flux $f_2/f_{\rm tot}$, and extended flux $f_{\rm ext}/f_{\rm tot}$. Dates are given in the format YYYY-MM-DD.

Epoch	Inst.	ρ [mas]	θ [°]	$f_2/f_{\rm tot}$	$f_{\rm ext}/f_{\rm tot}$	$\chi^2_{\rm vis}$	$\chi^2_{\rm CP}$
2013-01-27	PIONIER	1.50 ± 0.09	309.8 ± 0.3	0.223 ± 0.015	0.021 ± 0.005	0.81	0.88
2013-02-20	”	1.68 ± 0.12	343.5 ± 1.1	0.189 ± 0.021	0.002 ± 0.001	1.88	0.90
2017-03-14	GRAVITY	1.59 ± 0.08	358.7 ± 0.4	0.289 ± 0.003	0.051 ± 0.004	2.11	1.07
2017-04-28[a]	”	1.90 ± 0.10	47.4 ± 0.2	0.268 ± 0.003	0.116 ± 0.005	10.76	2.53
2018-01-11	”	0.89 ± 0.05	233.3 ± 1.0	0.295 ± 0.013	0.015 ± 0.003	0.71	1.04
2018-02-06	”	1.54 ± 0.08	306.2 ± 0.2	0.274 ± 0.003	0.023 ± 0.002	0.62	0.48
2018-11-30[a]	PIONIER	2.43 ± 0.12	138.2 ± 0.1	0.271 ± 0.001	0.013 ± 0.002	2.17	1.62
2019-12-16[a]	”	2.03 ± 0.11	148.1 ± 0.8	0.508 ± 0.005	0.011 ± 0.002	1.02	0.71
2019-12-24[a]	”	1.34 ± 0.07	154.2 ± 0.6	0.456 ± 0.002	0.087 ± 0.004	6.81	0.92
2019-12-29	”	1.34 ± 0.07	167.5 ± 0.1	0.429 ± 0.001	0.023 ± 0.002	2.43	0.72
2020-11-19[a]	MIRC-X	2.84 ± 0.14	131.1 ± 0.3	0.345 ± 0.004	0.150 ± 0.004	3.27	1.95
2020-12-13	PIONIER	2.09 ± 0.10	144.6 ± 0.1	0.410 ± 0.001	0.013 ± 0.002	0.86	0.89
2020-12-19	”	1.85 ± 0.09	149.7 ± 0.2	0.422 ± 0.008	0.035 ± 0.002	0.72	1.03
2020-12-28	”	1.53 ± 0.11	162.4 ± 1.3	0.675 ± 0.058	0.018 ± 0.005	0.57	0.39

[a] Data combines two days of observation modelled simultaneously, as defined in table 4.1.

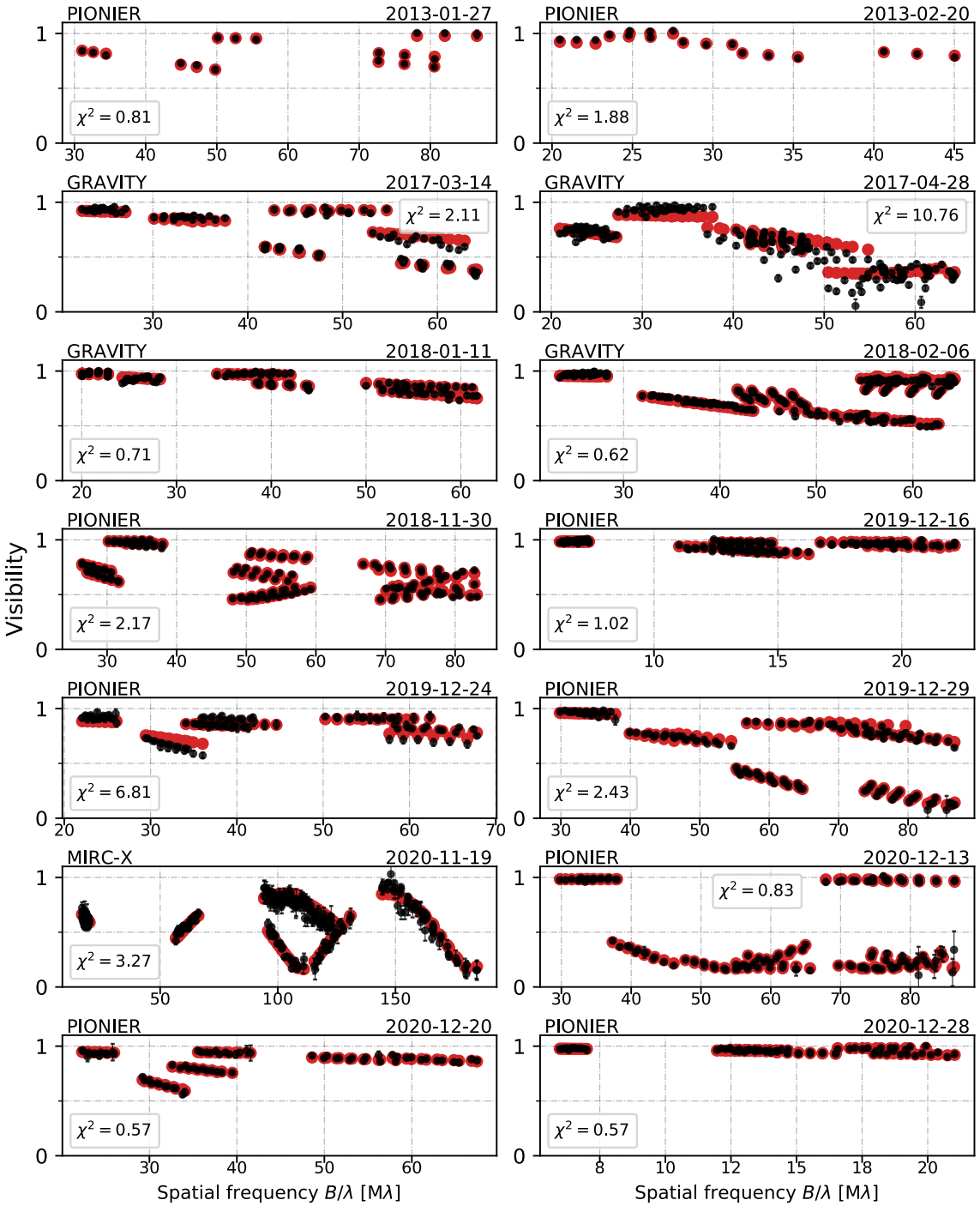

Figure 4.4: Observed continuum visibilities (black) and corresponding models (red) plotted against spatial frequency for all epochs. The model fit includes extended background emission. Dates are given in the format YYYY-MM-DD.

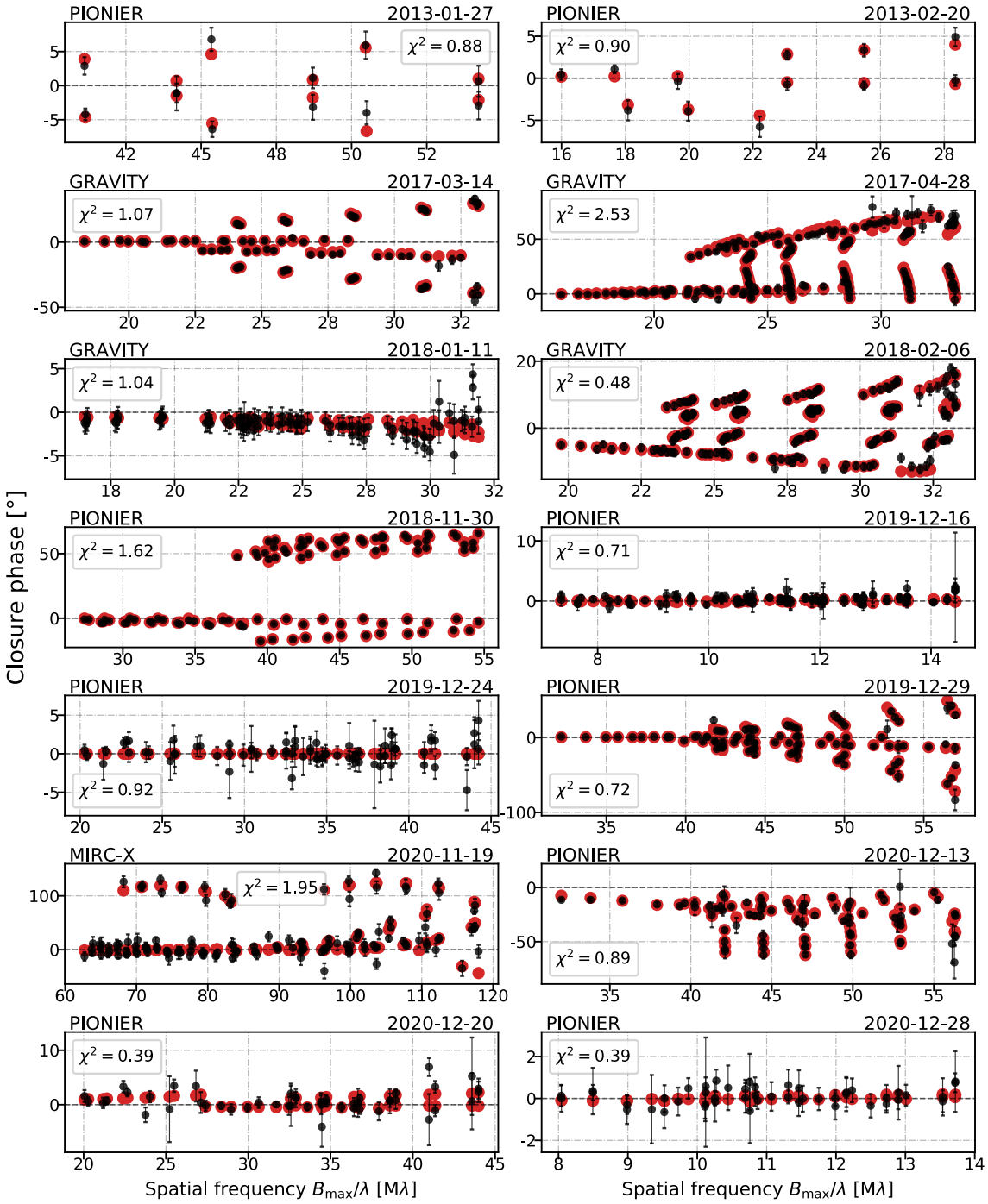

Figure 4.5: Observed continuum closure phases (black) and corresponding models (red) plotted against spatial frequency for all epochs. The model fit includes extended background emission. The scaling on the vertical axis was adjusted for each epoch. Dates are given in the format YYYY-MM-DD.

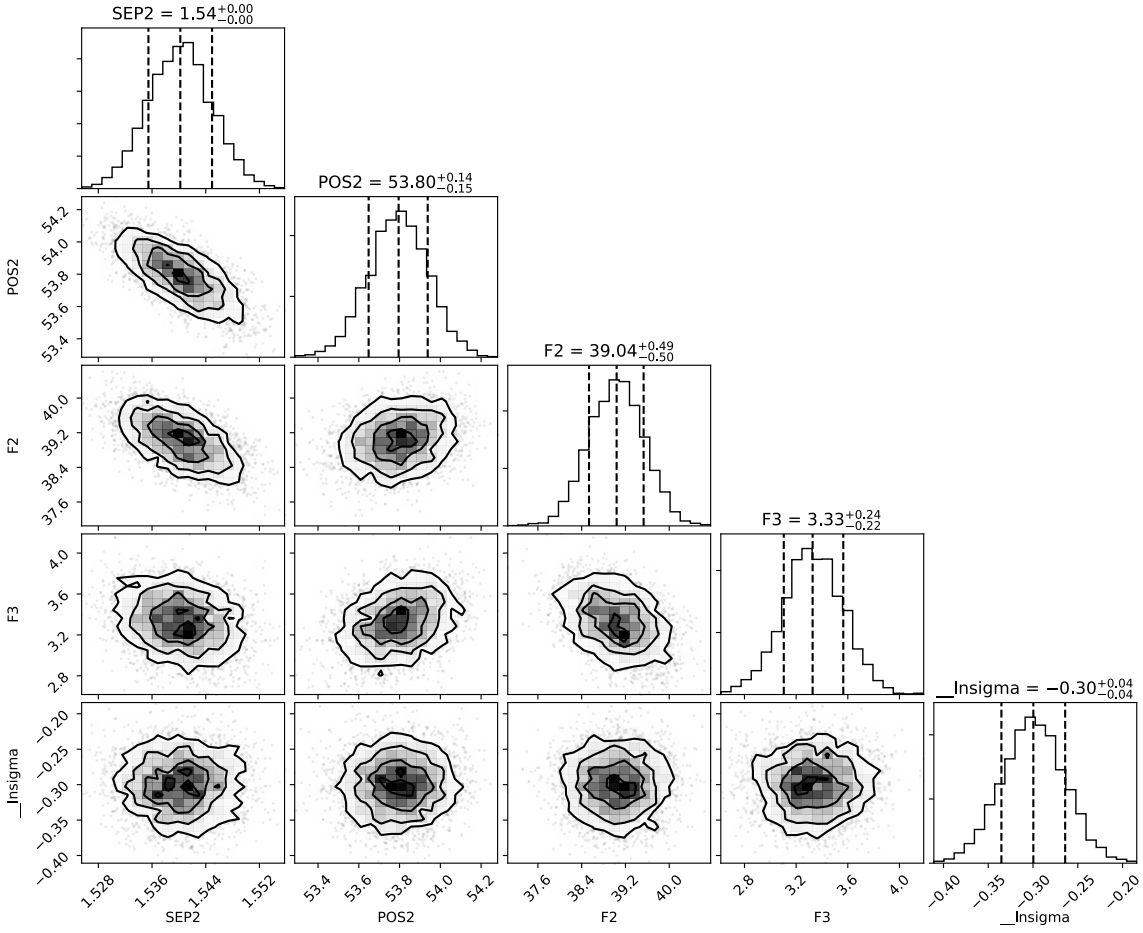

Figure 4.6: Corner plot showing the possible correlations between free parameters (ρ, θ, $F_2 = 100 \cdot f_2/f_{\rm tot}$ and $F_3 = 100 \cdot f_{\rm ext}/f_{\rm tot}$, respectively) for epoch 6 February 2018 of the continuum GRAVITY data, where the model fit includes extended background emission.

etry. As can be seen from MWC 166 A's K band spectrum, there are strong line features at 2.058 and 2.166 µm (Figure 4.3), corresponding to helium-I and Brackett-γ emission, respectively.

In order to model the spectral lines, I used the fitting tool PMOIRED[5], which is capable of fitting closure phases, differential phases, differential visibilities, and line spectra simultaneously, both over the continuum and over specific spectral windows. After finding the continuum geometry of the system for each epoch (Section 4.3.1.1), I introduced new model components to fit the He I and Br γ lines individually, using geometries of varying complexity. I initially used a single Gaussian of FWHM $\sigma = 0.1$ mas and left the position of the line-emitting region as a free parameter. At all epochs, this resulted in only very small spatial displacements from the origin, suggesting the primary component is responsible for the majority of the emission in the system. However, this singular emission zone near the primary is perhaps too simplistic a model. If I examine the flux intensity of the two lines (Figure 4.3), there are indications of time-dependent variability, as well as signs of double-peaked lines at several epochs. This could imply that the emission originates from both stars, or it could a signature of the gas kinematics. Furthermore, the differential phases over the spectral lines show signatures of rotating emission that are not accurately modelled by the single-Gaussian model. These features would be most naturally explained by a circumprimary disc.

4.3.2.1 Circumprimary gas disc model

The circumprimary disc model I used is based on the model described in Frost et al. (2022), which was used to model the binary system HR 6819. The model comprises several components and has 12 free parameters that describe the entirety of the system.

Firstly, the stars themselves are modelled as uniform discs with diameters corresponding to twice the stellar radii I obtained from my continuum fit (see Section 4.4.4), and the secondary component is given a displacement from the primary's position at the origin, as well as a continuum flux f_2/f_1, while the primary flux is fixed to $f_1 \equiv 1$.

The line emission is subsequently modelled to be originating from two regions, one

5. Reference: https://github.com/amerand/PMOIRED

blueshifted and the other redshifted, to represent the approaching and receding part of a rotating disc (labelled B and R, respectively). Each of these components was given its own spatial displacement (x_i, y_i), with the size of the emitting region following a Gaussian profile with FWHM $\sigma_i = \frac{1}{2}\sqrt{x_i^2 + y_i^2}$. I additionally modelled the line components in the spectral domain. Each component is given a flux profile f_i accounting for the differences in line strength between the components (which can be seen to vary by epoch in Figure 4.3), and a Lorentzian shape with FWHM kept equal for both wings. Each line wing is centred on a wavelength that is displaced from the central line wavelength λ_0, such that $\lambda_\mathrm{B} = (\lambda_0 - \Delta\lambda)$ and $\lambda_\mathrm{R} = (\lambda_0 + \Delta\lambda)$.

The resultant fitted parameters of the model described above are presented for all GRAVITY epochs in Section 4.5. The model is fitted simultaneously to the telluric-corrected spectrum, closure phase, differential phase, and differential visibility.

4.4 Results: Orbital solution and mass–distance constraints

4.4.1 Binary astrometry and orbital fit

The parameters of the best-fit continuum model with background component are listed in Table 4.3. The model visibilities that correspond to the best-fit model are shown in Figure 4.4, while closure phases are shown in Figure 4.5. My modelling script makes use of Markov chain Monte Carlo module `emcee` (Foreman-Mackey 2016) to explore the parameter space and obtain error estimates from the posterior probability distribution. I show the corner plot for a representative epoch (2 February 2018) in Figure 4.6. An important source of systematic uncertainty that affects primarily the derived separations is the wavelength calibration, and I account for this by including a systematic uncertainty of 5% for the separations listed in Table 4.3.

Using the relative astrometry for each epoch, I fitted a Keplerian orbit using the standard Campbell elements defined in Section 2.4.1: P = orbital period; T_0 = epoch of periastron passage; a_1 = semi-major axis of primary component; i = orbital inclination (to the line of sight); e = eccentricity; Ω = longitude of ascending node; ω = longitude of periastron; K_1 = orbital curve semi-amplitude of primary component; V_0 = RV of the

system's centre of mass.

I used two fitting approaches: **ORBITX code:** This code[6] (Tokovinin 1992) fits orbits using both astrometric and RV data simultaneously. I modified the ORBITX code to account for uncertainties in both ρ and θ, a feature absent from the original code, which only uses uncertainties on ρ.

Grid-search algorithm: I used the grid-search algorithm developed by Kraus et al. (2009) to construct a grid of orbital solutions in the P, T_0, and e parameter space, where the remaining elements a, i, Ω, ω are determined from the Thiele-Innes elements. I explored the parameter space around $P = 0.480...1.100\,\mathrm{yr}$, $T_0 = 2019.5...2020.5\,\mathrm{yr}$ (step sizes of $0.001\,\mathrm{yr}$), and $e = 0.100...0.600$ with a step size of 0.001, and selected the solution with the lowest combined residuals in RV and astrometry. I then repeated the process with smaller step-sizes around the initial solution (a factor of ten for all parameters, $= 0.0001\,\mathrm{yr}, 0.0001\,\mathrm{yr}, 0.0001$, respectively, for P, T, e), in order to increase precision. Uncertainties were calculated by examining the χ^2 curve for each parameter.

The best-fit orbit solutions found with these methods are listed in columns (3), (4) of Table 4.4, and are overplotted on the data in Figs. 4.7 and 4.8. Both the orbits provide a very good fit to the existing data, and provide similar results for all parameters. This is despite a substantial portion of the orbit still lacking astrometric observations. I adopt the orbit from column (3) when discussing derived quantities in the subsequent sections.

4.4.2 Comparison to RV orbit

Corporon and Lagrange (1999) and Pogodin et al. (2006) derived orbits for MWC 166 A from the RV data, with the more recent of the two being a refinement including additional RV points. The orbital parameters for this RV orbit are shown in column (2) of Table 4.4. My spectroscopic and astrometric orbital solutions differ substantially from the earlier RV-only orbit. The most notable difference is in the orbital period, which I calculated as almost exactly twice the length of the Pogodin et al. (2006) orbit. This doubling of the period was only discernible thanks to the astrometric data, as using the RVs alone provides

6. Available at: https://zenodo.org/record/61119

Table 4.4: Orbital parameters for MWC 166 A. Column (2) gives the RV fit obtained by Pogodin et al. (2006). Columns (3) and (4) give the best-fit orbital solution including both RV data and the astrometry data, using the ORBITX and the grid-search methods, respectively. These solutions were derived using the background geometric model described in Section 4.3.1.1.

Parameter (1)	RV only (2)	ORBITX orbit (3)	Grid-search orbit (4)
P [yr]	0.50296 ± 0.00027	1.0067 ± 0.0001	1.0066 ± 0.0002
P [days]	*183.70 ± 0.10*	*367.69 ± 0.04*	*367.65 ± 0.07*
T_0 [yr]	1993.3581 ± 0.0078	2020.0722 ± 0.0003	2020.0713 ± 0.0010
a_1 [mas]	-	2.6122 ± 0.0385	2.684 ± 0.008
i [°]	-	53.62 ± 0.32	55.27 ± 0.11
$a_1 \sin i$ [mas]	2.15 ± 0.07^a	-	-
e	0.28 ± 0.03	0.498 ± 0.001	0.492 ± 0.003
Ω [°]	-	306.3 ± 0.2	304.9 ± 0.2
ω [°]	263.8 ± 6.6	313.8 ± 0.2	315.6 ± 0.5
K_1 [km s^{-1}]	18.6 ± 0.7	20.3 ± 0.4	20.3 ± 0.4
V_0 [km s^{-1}]	44.2 ± 0.5	35.3 ± 0.3	34.7 ± 0.3
$M_{\rm tot}$ [$M_\odot$]^b	-	17.05 ± 2.70	18.52 ± 2.81

[a] Pogodin et al. (2006) returns $a \sin i = 60 \pm 2\ R_\odot$. A conversion to milliarcseconds has been made to allow a better comparison with the calculated semi-major axis and inclination. The distance used was 990 pc.
[b] Mass calculated for $d = (990 \pm 50)$ pc.

an equally good fit to both orbits. I also found the orbit to be much more elliptical than previously thought, with its eccentricity of 0.498 ± 0.003 being much larger than that of the RV orbit ($e = 0.28 \pm 0.03$). A newly determined parameter from my orbit is the inclination, with a value of $i = 53.6 \pm 0.3°$.

4.4.3 Dynamical system mass

According to Kepler's third law, the period of an orbit P is proportional to the cube of the semi-major axis of the orbit a (see Section 2.5.1.1). Unfortunately, there are several conflicting distance estimates for this system in the literature. As mentioned in Section 4.1, photometrically calculated distances have placed MWC 166 at a distance of roughly one kiloparsec. Parallax observations have corroborated the photometric distances for a majority of the other individual members of CMa OB1, but are not consistent in the case of MWC 166. Hipparcos (ESA 1997) measured a distance of 247 ± 82 pc, while Gaia Data Release 2 (DR2) parallaxes correspond to an even shorter distance of 131^{+16}_{-13} pc (Bailer-Jones et al. 2018) – roughly ten times closer than the ~ 1 kpc to its parent association. This

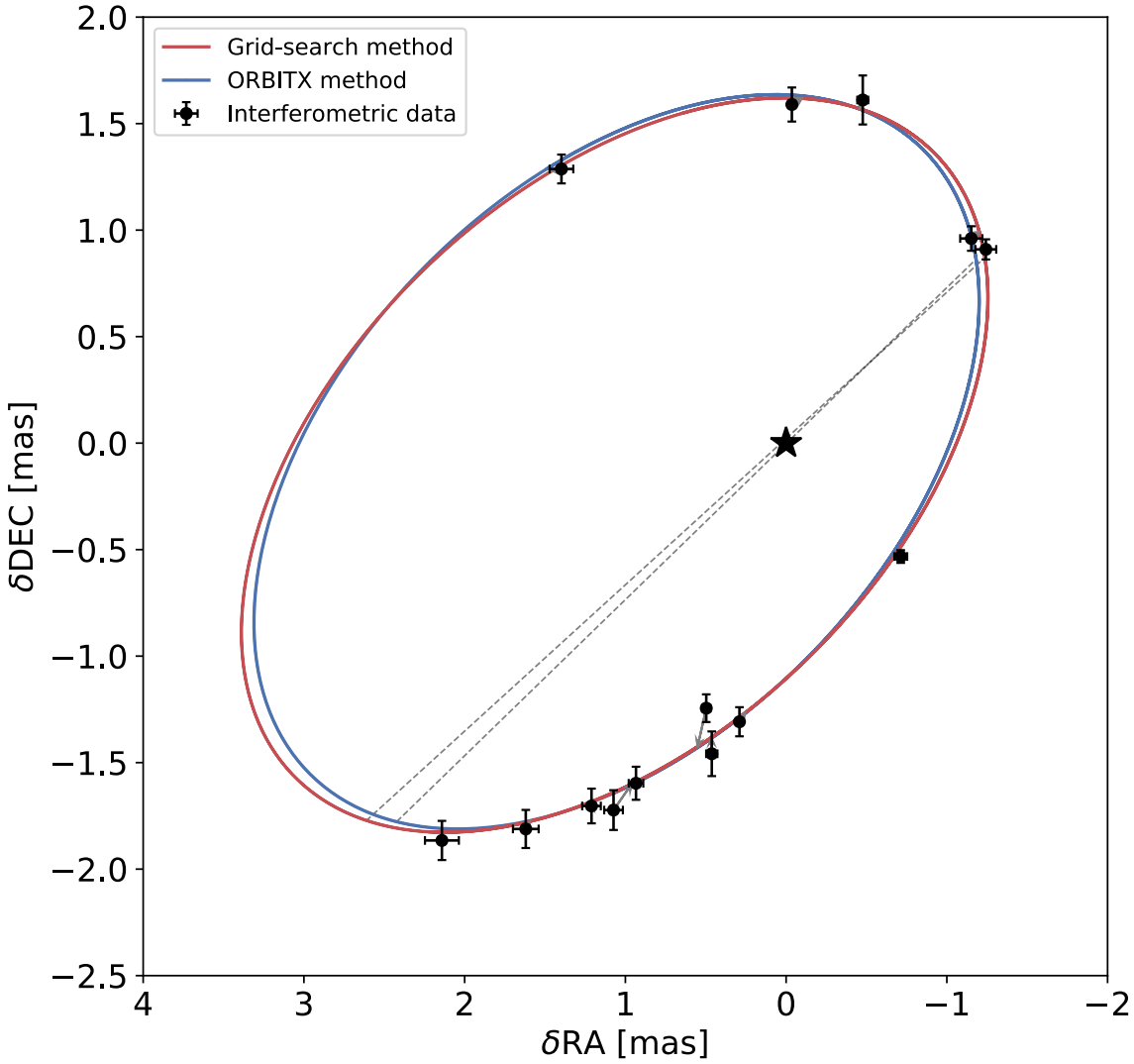

Figure 4.7: Astrometric orbit solutions derived using both the ORBITX code (blue line) and the grid-search code (red line). The primary star is kept fixed at the origin, and the x and y axes show displacement in right ascension and declination, respectively. The dotted lines connect the ascending and descending nodes of each orbit.

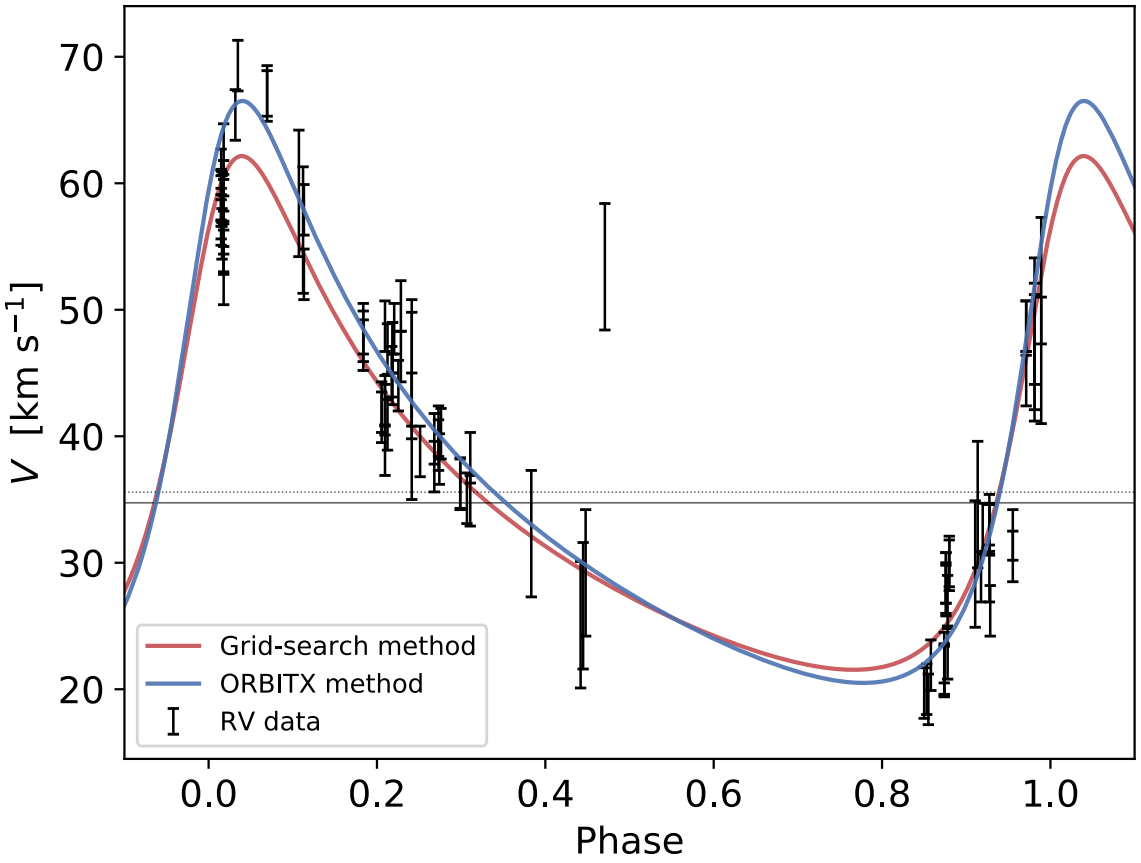

Figure 4.8: Radial velocity measurements of MWC 166 A taken in the period 1994–2005 plotted against orbital phase. The blue and red fitted curves correspond to the orbits specified in Cols. (3) and (4) of Table 4.4, respectively. The dotted black line shows the velocity of the system's centre of mass (V_0) for the grid-search method, and the solid grey line shows V_0 for the ORBITX orbit.

discrepancy can likely be explained by the binarity of the system, as DR2 does not solve for source multiplicity. Indeed, the recent release of preliminary results from Gaia Early Data Release 3 has brought the parallax distance to MWC 166 closer to the photometric distance values, albeit with very large uncertainties ($d \sim 1600 \pm 700$ pc, Bailer-Jones et al. 2021). The Keplerian mass-distance relation (Eq. 2.4) shows that distances of $\lesssim 650$ pc correspond to masses of $M_{\rm tot} < 5\,M_{\odot}$, clearly below the mass threshold for MWC 166 Aa's spectral type of B0III (Fairlamb et al. 2015). Conversely, the photometric distances offer more physically realistic values – the most recent distance estimate of 990 ± 50 pc returns a system mass of $M_{\rm tot} = 17.1 \pm 2.7\ M_{\odot}$, which is also in agreement with the prediction of 20-25 $M_{\odot}$ by Pogodin et al. (2006). Additionally, any parallax distances are unreliable due to having been calculated with the assumption of a six-month orbit, which I have shown is too short by a factor of two. In light of these points, in this work I have treated the photometric distances preferentially. I have therefore taken the literature distance to MWC 166 to be the most recent photometric distance, 990 ± 50 pc (Kaltcheva and Hilditch 2000).

4.4.4 From combined mass to individual masses and other properties

My full orbital solution allows me to constrain model-independent individual masses for the first time. Using this method I determined the masses of MWC 166 Aa and MWC 166 Ab as $M_1 = (12.19 \pm 2.18)\,M_{\odot}$ and $M_2 = (4.90 \pm 0.52)\,M_{\odot}$, respectively. Our $M_{\rm dyn}$ measurements for both components were used to derive the remaining stellar parameters, and their respective confidence bounds, from theoretical evolution tracks. I used CMD 3.6[7] to generate a solar metallicity ($Z = 0.0152$) isochrone table from PARSEC 1.2S (Bressan et al. 2012; Chen et al. 2014; Chen et al. 2015; Tang et al. 2014; Marigo et al. 2017; Pastorelli et al. 2019).

The evolutionary status of MWC 166 A has not been conclusively established. Analysis of the spatial distribution of O- and B-type stars in its parent OB association, CMa OB1-R1, resulted in an estimate for its age of $\sim 3 \times 10^6$ yr (Clariá 1974b). At this age, MWC 166 Aa is likely already onto the main sequence, while MWC 166 Ab might still be in its pre-main-sequence stage (Tjin A Djie et al. 2001). Later work by Herbst

7. http://stev.oapd.inaf.it/cgi-bin/cmd

and Assousa (1977) showed that CMa OB1-R1's main stars are located on the rim of an expanding shell of neutral hydrogen, consistent with star formation being triggered by a supernova within the last $\sim 500\,\mathrm{kyr}$. Due to the uncertain age of the system, I selected these two potential ages, as well as a reasonable intermediate age ($1 \times 10^6\,\mathrm{yr}$), upper bound ($1 \times 10^7\,\mathrm{yr}$), and lower bound ($1 \times 10^5\,\mathrm{yr}$). Then, for each of the estimated ages, I drew an isochrone of an appropriate age from the CMD table and performed a quadratic interpolation over the mass points within it to find the value for each parameter that corresponds to M_{dyn} at the given age. This process was repeated for the upper and lower bounds on M_{dyn} to find the confidence bounds for each parameter at the given age. My estimates for the stellar parameters using this method are presented in Table 4.5. Figure 4.9 shows the isochrones for each age estimate plotted on a Hertzsprung-Russell diagram of $\log(L)$ versus $\log(T_{\mathrm{eff}})$, as well as the interpolated values for the primary and secondary components as large circles and triangles, respectively. From Figure 4.9, it can be seen that, at the ages of 500 kyr, 1 Myr, and 3 Myr, the primary star is on the main sequence, with negligible variations in parameters between these ages. At the upper bound age of 10 Myr, the primary is in the process of beginning to evolve beyond the main sequence. Conversely, it is clear from the Hertzsprung-Russell diagram that the secondary component is predicted to be on the main sequence for all ages save the youngest, where it is still in its protostellar stage. Also in Figure 4.9 is shown the location of the primary as calculated by Fairlamb et al. (2015), which appears to agree with all ages except the upper bound of 10 Myr. In Section 4.6.4, I generalise this process to all generated isochrones to attempt to constrain the age of the system.

4.5 Results: Modelling the gas distribution and kinematics in the He i and Br γ lines

The circumprimary disc model described in Section 4.3.2 produces an excellent fit to the data at all epochs. Figure 4.10 shows the results of the fit for the epoch 14 March 2017, where panel (a) shows the spectra, closure phases, differential phases, and visibilities measured with GRAVITY overplotted with prediction from the best-fit model. The three left-most plots in panel (b) show synthetic images computed from the best-fit model for

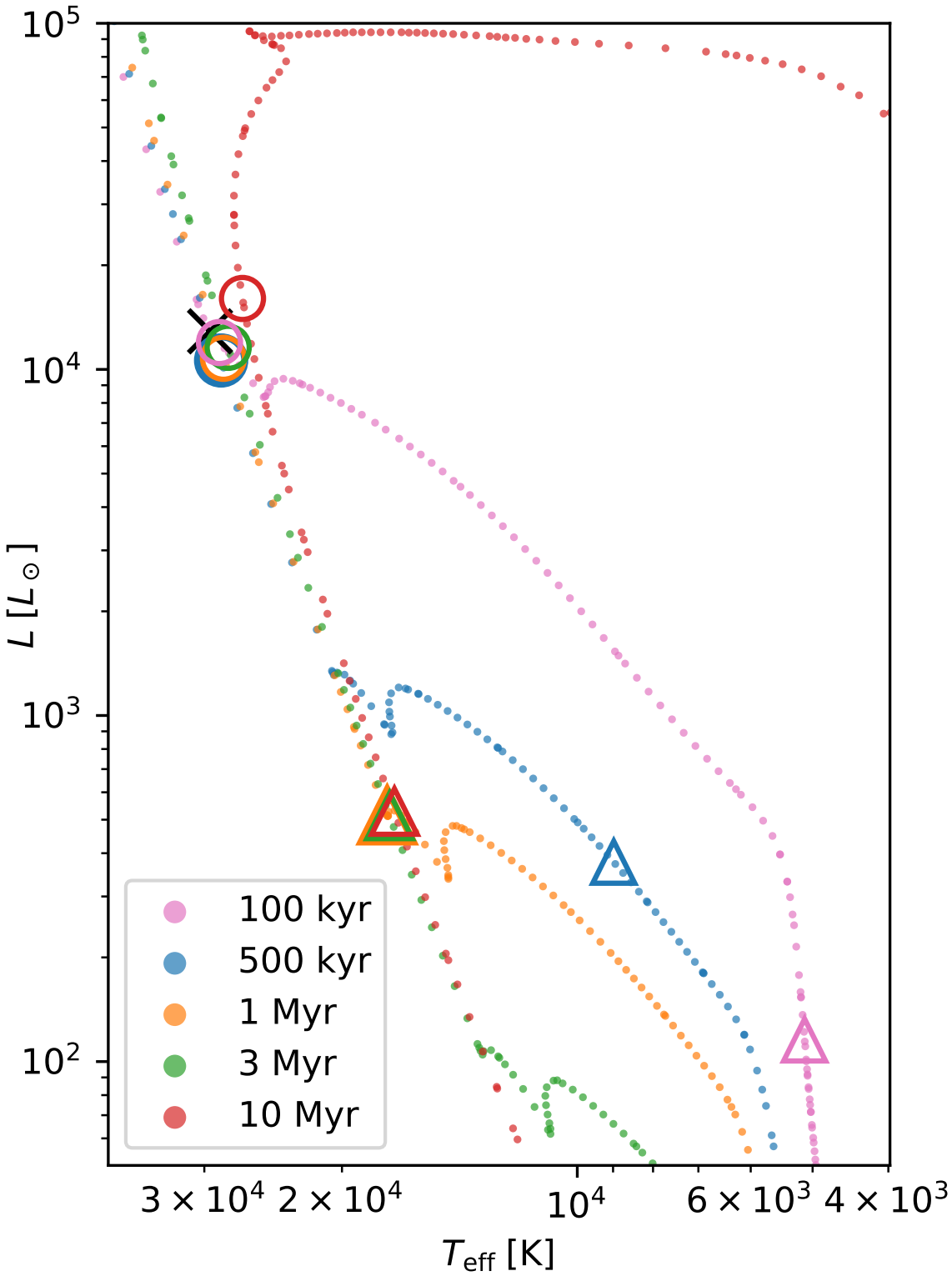

Figure 4.9: Hertzsprung-Russell diagram showing PARSEC 1.2S isochrone tracks for each age. Superimposed are the interpolated L, $T_{\rm eff}$ values for the primary star (large circles) and secondary star (triangles), for all ages. The black cross shows the location of the primary's parameters as determined by Fairlamb et al. (2015).

Table 4.5: `PARSEC 1.2S and COLIBRI S_37` models of each component of MWC 166 A. Isochrones were selected at five representative ages including reasonable lower and upper bounds, with stellar parameters corresponding to the dynamical masses of each component. The isochrones assume solar metallicities and that the stars are coeval.

Parameter	MWC 166 Aa	MWC 166 Ab
$M_{\rm dyn}$ $[M_\odot]$	12.19 ± 2.18	4.90 ± 0.52
Age [yr]	1.0×10^5	
L $[L_\odot]$	$\left(1.20^{+0.53}_{-0.31}\right) \times 10^4$	$\left(1.15^{+0.39}_{-0.24}\right) \times 10^2$
R $[R_\odot]$	$4.43^{+0.11}_{-2.03}$	$13.66^{+1.80}_{-1.31}$
$T_{\rm eff}$ [K]	$28\ 700^{+2400}_{-6600}$	$5\ 120^{+60}_{-40}$
$\log(g)$	$4.23^{+0.02}_{-0.41}$	$2.85^{+0.04}_{-0.06}$
Age [yr]	5.0×10^5	
L $[L_\odot]$	$\left(1.06^{+0.67}_{-0.49}\right) \times 10^4$	$\left(3.77^{+8.01}_{-2.72}\right) \times 10^2$
R $[R_\odot]$	$4.21^{+0.44}_{-0.48}$	$8.02^{+3.70}_{-1.17}$
$T_{\rm eff}$ [K]	$28\ 600^{+2200}_{-2500}$	$9\ 000^{+7300}_{-2900}$
$\log(g)$	4.27 ± 0.02	$3.32^{+0.58}_{-0.21}$
Age [yr]	1.0×10^6	
L $[L_\odot]$	$\left(1.08^{+0.70}_{-0.50}\right) \times 10^4$	$\left(5.13^{+2.23}_{-1.72}\right) \times 10^2$
R $[R_\odot]$	$4.30^{+0.48}_{-0.50}$	$2.46^{+0.44}_{-0.15}$
$T_{\rm eff}$ [K]	$28\ 400^{+2100}_{-2500}$	$17\ 500^{+1100}_{-2900}$
$\log(g)$	4.25 ± 0.02	$4.34^{+0.19}_{-0.01}$
Age [yr]	3.0×10^6	
L $[L_\odot]$	$\left(1.16^{+0.80}_{-0.55}\right) \times 10^4$	$\left(5.13^{+2.23}_{-1.72}\right) \times 10^2$
R $[R_\odot]$	$4.59^{+0.58}_{-0.59}$	2.50 ± 0.16
$T_{\rm eff}$ [K]	$28\ 000^{+2100}_{-2500}$	$17\ 400^{+1000}_{-1100}$
$\log(g)$	4.20 ± 0.03	4.33 ± 0.01
Age [yr]	1.0×10^7	
L $[L_\odot]$	$\left(1.60^{+1.51}_{-0.86}\right) \times 10^4$	$\left(5.28^{+2.39}_{-1.79}\right) \times 10^2$
R $[R_\odot]$	$5.87^{+1.91}_{-1.22}$	$2.61^{+0.20}_{-0.19}$
$T_{\rm eff}$ [K]	$26\ 800^{+700}_{-1900}$	$17\ 100^{+1000}_{-1100}$
$\log(g)$	$3.98^{+0.12}_{-0.17}$	4.29 ± 0.02

three representative wavelengths. The central panel shows the brightness distribution at λ_0, while to the left and right of this the wavelength is redshifted and blueshifted respectively by a factor of $\lambda_0 \pm 3\Delta\lambda$. The right-most panel of the figure shows the flux contribution of each synthetic model component. The line modelling results for all epochs (analogously to Figure 4.10) are shown in Appendix A, and the findings are summarised in Table 4.6, for both spectral lines of interest.

The results show substantial evidence of line emission being localised around the primary star, consistent throughout all four GRAVITY epochs. The redshifted component (R) is displaced consistently towards the north-west of the primary star, while the blueshifted component (B) is located south-east of the primary. The displacement of the two components from the star is generally (~ 0.25 mas). The average displacement for He I was found to be $(10.5 \pm 0.4)\,R_1$, and for the Br γ this was $(11.5 \pm 0.4)\,R_1$. The derived values for each epoch can be seen in column (5) of Table 4.7. The relative intensities of the B and R components also seem to be variable by epoch and by spectral line. From columns (3) and (4) of Table 4.7, it can be seen that, for the He I line, the red wing contributes 60% of the flux for the first two epochs, a similar level of intensity as the blue wing during the latter two epochs. On the other hand, the Br γ line flux tends to be more equally distributed between the two components, apart from in the epoch 6 February 2018, where the blue component is substantially stronger. The emission of the redshifted and blueshifted line wing are displaced along an average PA of $134.0 \pm 1.1°$, indicating that this is the sky-projected PA of the major axis of the rotating disc. Accordingly, the rotation axis of the discs, and likely also the primary star, is oriented along PA $44.0 \pm 1.1°$ on sky.

4.6 Discussion

4.6.1 Evidence for circumbinary dust

The interferometric observations in the continuum allow me to quantify the excess emission through the visibility fit (Section 4.3.1.1), where I find that $\sim 2\%$ and $\sim 5\%$ of the excess emission are associated with extended flux in the H band and K band, respectively. The H band observations also show 'spikes' in the extended flux contribution in the epochs 24 December 2019 and 19 November 2020, with $f_{\rm ext}/f_{\rm tot}$ contributing up to 15% of the total

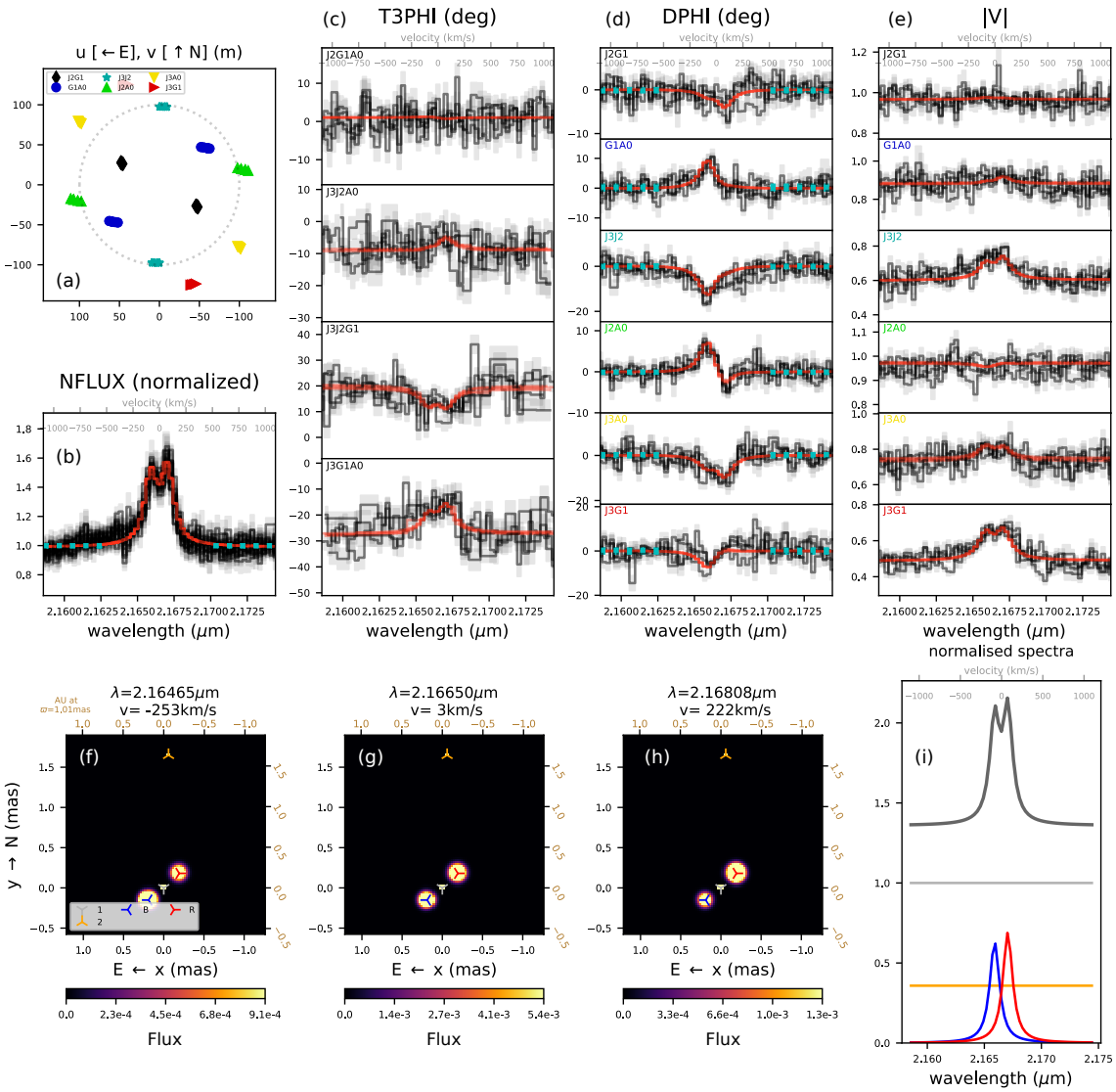

Figure 4.10: Results of the Br γ line modelling, for the epoch 14 March 2017. **(a)**: (u, v)-coverage for the observations associated with the epoch, coloured by baseline pair. **(b)**: Telluric-corrected normalised flux (labelled NFLUX, black lines), overplotted with flux in the best-fit model (red line). **(c)**, **(d)**, **(e)**: Data from each GRAVITY exposure (black lines), overplotted with quantities computed from best-fit model (red lines). The observables are closure phase for each telescope triplet (T3PHI), differential phase for each baseline (DPHI), and visibility for each baseline (|V|), respectively. **(f)**, **(g)**, **(h)**: Brightness distribution corresponding to the best fit, for three representative wavelengths. **(i)**: Synthetic line strengths and profiles for the two spectral components in the model (red and blue), in addition to the monochromatic continuum flux associated with the primary component (silver) and the secondary component (gold). The parameters corresponding to the fits can be found in Table 4.6.

Table 4.6: Model parameters corresponding to the best-fit PMOIRED circumprimary disc line models, for both spectral lines of interest, for each GRAVITY epoch (Section 4.5). Dates are given in the format YYYY-MM-DD.

Epoch	2017-03-14		2017-04-27	
Spec. Line	He I	Br γ	He I	Br γ
ρ [mas]	1.67 ± 0.01	1.65 ± 0.01	1.98 ± 0.01	1.98 ± 0.01
θ [°]	357.4 ± 0.3	357.8 ± 0.3	42.3 ± 0.3	42.0 ± 0.2
f_2	0.414 ± 0.004	0.359 ± 0.003	0.457 ± 0.004	0.402 ± 0.002
x_B [mas]	0.212 ± 0.017	0.192 ± 0.015	0.242 ± 0.034	0.255 ± 0.031
y_B [mas]	-0.118 ± 0.017	-0.184 ± 0.012	-0.226 ± 0.028	-0.118 ± 0.024
σ_B [mas]	0.121	0.133	0.166	0.141
f_B	0.712 ± 0.015	0.633 ± 0.015	0.668 ± 0.026	0.497 ± 0.023
x_R [mas]	-0.155 ± 0.011	-0.190 ± 0.013	-0.168 ± 0.021	-0.208 ± 0.021
y_R [mas]	0.168 ± 0.009	0.135 ± 0.011	0.188 ± 0.017	0.202 ± 0.017
σ_R [mas]	0.114	0.117	0.126	0.145
f_R	1.074 ± 0.014	0.688 ± 0.013	1.009 ± 0.021	0.664 ± 0.017
FWHM [nm]	1.045 ± 0.016	1.046 ± 0.022	1.231 ± 0.031	1.340 ± 0.041
λ_0 [µm]	2.0590	2.1665	2.0593	2.1667
$\Delta\lambda$ [µm]	0.617 ± 0.005	0.577 ± 0.006	0.568 ± 0.009	0.558 ± 0.011
χ^2	2.55	2.37	4.18	3.07

Epoch	2018-01-11		2018-02-06	
Spec. Line	He I	Br γ	He I	Br γ
ρ [mas]	0.86 ± 0.02	0.90 ± 0.02	1.59 ± 0.01	1.56 ± 0.01
θ [°]	238.1 ± 1.1	238.9 ± 1.0	307.8 ± 0.2	307.3 ± 0.2
f_2	0.318 ± 0.025	0.240 ± 0.016	0.440 ± 0.007	0.399 ± 0.006
x_B [mas]	0.114 ± 0.016	0.223 ± 0.022	0.175 ± 0.013	0.161 ± 0.013
y_B [mas]	-0.091 ± 0.023	-0.076 ± 0.036	-0.052 ± 0.011	-0.123 ± 0.011
σ_B [mas]	0.073	0.118	0.091	0.102
f_B	0.533 ± 0.016	0.289 ± 0.020	0.945 ± 0.016	0.643 ± 0.015
x_R [mas]	-0.048 ± 0.017	0.040 ± 0.020	-0.130 ± 0.015	-0.053 ± 0.020
y_R [mas]	0.184 ± 0.026	0.244 ± 0.032	0.241 ± 0.014	0.243 ± 0.019
σ_R [mas]	0.095	0.124	0.137	0.124
f_R	0.425 ± 0.014	0.309 ± 0.016	0.603 ± 0.014	0.326 ± 0.012
FWHM [nm]	1.150 ± 0.026	1.386 ± 0.048	1.051 ± 0.018	1.330 ± 0.030
λ_0 [µm]	2.0593	2.1667	2.0592	2.1667
$\Delta\lambda$ [µm]	0.578 ± 0.008	0.422 ± 0.016	0.606 ± 0.006	0.576 ± 0.011
χ^2	2.22	1.95	3.53	3.04

Table 4.7: Line wing comparison per epoch. Columns (3) and (4): Relative strengths of the red and blue wings of the respective spectral line. Uncertainties are 0.01 for all values in these columns. Columns (5) and (6): radius of line emission centre, averaged from the red and blue wings, given respectively in units of milli-arcseconds, and the primary star's radius at 3 Myr (see Table 4.5). Column (7) shows the estimated rotational axis of the primary star. Dates are given in the format YYYY-MM-DD.

Epoch (1)	Line (2)	f_R/f_{R+B} (3)	f_B/f_{R+B} (4)	$\bar{\rho}_{\rm line}$ [mas] (5)	$\bar{\rho}_{\rm line}\,[R_1]$ (6)	$\theta_{\rm rot}$ [°] (7)
2017-03-14	He I	0.60	0.40	0.24 ± 0.02	11.2 ± 0.9	37.9 ± 2.4
	Br γ	0.52	0.48	0.25 ± 0.01	11.6 ± 0.5	39.9 ± 2.1
2017-04-27	He I	0.60	0.40	0.29 ± 0.03	13.5 ± 1.4	45.0 ± 4.0
	Br γ	0.57	0.43	0.29 ± 0.03	13.5 ± 1.4	34.7 ± 3.3
2018-01-11	He I	0.44	0.56	0.17 ± 0.02	7.9 ± 0.9	59.0 ± 5.0
	Br γ	0.52	0.48	0.24 ± 0.03	11.2 ± 1.4	60.0 ± 5.0
2018-02-06	He I	0.39	0.61	0.23 ± 0.01	10.7 ± 0.5	43.9 ± 2.5
	Br γ	0.34	0.66	0.23 ± 0.02	10.7 ± 0.9	59.7 ± 3.2

flux for these epochs. The geometry of the extended dust is still poorly constrained, but my modelling shows the emission originates from scales at least twice larger than the binary separation vector (for a ring model), but likely even larger (for a Gaussian or background flux model; Table 4.2 and Section 4.3.1.1). This is comparable to the dynamical truncation radius predicted by Artymowicz and Lubow (1994) for circular binaries ($\sim 1.7a$).

The expected Silicate dust sublimation radius ($R_{\rm s}$) can be estimated with

$$R_{\rm s} = 1.1\sqrt{\epsilon}\left(\frac{L}{1000\,L_\odot}\right)^{1/2}\left(\frac{T_{\rm s}}{1500\,{\rm K}}\right)^{-2}\ {\rm au}, \tag{4.1}$$

where L is the bolometric luminosity of the star(s) irradiating the disc and T_s is the dust sublimation temperature (Monnier and Millan-Gabet 2002). In the above equation, ϵ is the ratio of dust absorption efficiencies for radiation for the incident and re-emitted field, as defined in Section 1.4.2.1. I fix this value to $\epsilon = 1$ in order to estimate the rim location for large micron-sized dust grains. The above equation has several simplifications compared to the physical system, chief among which is the assumption of a single star rather than a binary. While dust sublimation radii have been calculated for binary systems (e.g. Nagel et al. 2010), dynamical interactions cause the inner dust rim to be at a larger radius than R_s. A detailed calculation is therefore outside the scope of this work, but Eq. 4.1 can still give an order-of-magnitude estimate for the minimum dust inner rim radius

of the circumbinary disc, assuming a luminosity equivalent to that of the two components combined. Substituting the sum of the luminosity values from the central age estimate of 1 Myr in Table 4.5 gives $R_s = 2.6$ au, 4.6 au and 7.1 au for dust sublimation temperatures of 2000 K, 1500 K and 1200 K, respectively. This suggests that individual dusty circumstellar discs are likely not present in the MWC 166 A system. Due to the calculated semi-major axis of the orbit being comparable to the smallest of the above estimates ($a_1 = 2.61$ au at $d = 990$ pc), it is expected that substantial individual dusty discs around each of the components are not capable of surviving for extended periods of time due to dynamical interactions (e.g. Mathieu 1994). Accordingly, I associate the extended continuum emission with a circumbinary disc component instead of circumstellar disc component.

4.6.2 Evidence for variable extinction or circumstellar material

The relative flux contribution of the two point sources in my model was found to be variable, especially in the H band continuum. The flux associated with the secondary appears to increase around phase ~ 0.9, and was found to be as bright as the primary at one epoch (24 December 2019) and even brighter than the primary at two epochs (16 December 2019 and 28 December 2020). These last two epochs were both taken on the compact AT configuration, and returned visibilities very close to unity – as well as closure phases close to zero – at all probed baselines (see Figs. 4.4 and 4.5). This, and the more limited (u, v)-coverage caused by the shorter baselines, can result in ambiguities in the model (Anthonioz et al. 2015). To rule this out, I repeated the modelling for these two epochs while restricting the secondary to a maximum brightness of 100% of the primary. I then repeated the astrometric fit, and found it to be incompatible with any physical orbit when considered with the other points. This means that the secondary's increase in relative H band brightness to outshine the primary at the epochs 16 December 2019 and 28 December 2020 is the only solution that agrees with the Keplerian orbit of the objects.

Since these two points are at very similar orbital phases (0.88 and 0.91, respectively), I argue that this variability could be a result of the dynamical interaction of the secondary with the circumbinary disc, possibly through variable extinction, where the line-of-sight extinction changes towards one of the stars due to rearrangements in the circumbinary disc. In addition, the point-source flux estimate (f_2/f_1) might contain emission contributions

from circumstellar gas or dust, in particular as the binary separation is still comparable to the interferometric beam size. Therefore, the observed f_2/f_1 brightness increase might correspond to an increase in excess emission near the location of the secondary as it approaches periastron, either through an accretion burst onto the secondary or from a hot spot at the inner edge of the circumbinary disc caused by the additional heating from the secondary. Indeed, smoothed particle hydrodynamics simulations of young, eccentric close binaries with circumbinary discs, such as those by Dunhill et al. (2015, for HD 104237) and Muzerolle et al. (2019, for DQ Tau), have suggested that dynamical interactions can cause a differential rate of accretion depending on the orbital phase, with the highest accretion peak occurring during the $10 - 20\%$ of the orbit preceding periastron. The observed brightening, around orbital phase ~ 0.9, could be consistent with this prediction.

4.6.3 Nature of the line-emitting region

As shown in Section 4.5, the geometry in the K band emission lines is substantially different from what I see in the continuum. The best fit to the circumstellar environment in the He I and Br γ lines indicates a strongly emitting Keplerian disc around the primary component. In this section I present three possible interpretations for the physical origin of the line emission: emission from the accretion region, an ionised gas accretion disc channelling circumstellar material to the star, or a decretion disc tracing material from the star being lost through stellar winds.

4.6.3.1 Accretion onto the primary

Brackett-γ emission is a common marker of magnetospheric accretion in YSOs and is especially useful for accretion rate determination, since the luminosity of the line ($L_{\mathrm{Br}\gamma}$) has been shown to be directly related to the accretion luminosity (L_{acc}, see Section 1.4.3) over a wide mass range from brown dwarfs to Herbig Ae stars (e.g. Muzerolle et al. 1998; Calvet et al. 2004). This relation follows a power law that is strongly dependent on stellar mass (Fairlamb et al. 2017). For Herbig Ae objects, Donehew and Brittain (2011) derived the following relation:

$$\log(L_{\mathrm{acc}}/L_{\odot}) = (0.9 \pm 0.2)\log(L_{\mathrm{Br}\gamma}/L_{\odot}) + (3.3 \pm 0.7), \tag{4.2}$$

with similar values obtained by Mendigutía et al. (2011). Using the Br γ luminosity for MWC 166 A calculated by Donehew and Brittain (2011) of $L_{\mathrm{Br}\gamma} = (11\pm5)\times10^{-3}\,L_{\odot}$, I can estimate the accretion luminosity and hence the mass accretion rate from Equation 1.10. This results in $L_{\mathrm{acc}} \sim 35\pm65 L_{\odot}$ and subsequently $\dot{M} \sim (3.9 \pm 7.4) \times 10^{-7}\,M_{\odot}\,\mathrm{yr}^{-1}$, which is in line with the typical mass accretion rate of $2 \times 10^{-7}\,M_{\odot}\,\mathrm{yr}^{-1}$ found by Mendigutía et al. (2011).

However, it must be noted that, with a mass of 12 $M_{\odot}$, MWC 166 Aa is a Be star, leaving it outside of the regime where the $L_{\mathrm{Br}\gamma}$ – L_{acc} relation has been calibrated. Indeed, Eq. 4.2 provides a systematic overestimate of L_{acc} for Be stars, according to Donehew and Brittain (2011). Furthermore, the large uncertainties inherent to the estimate of $L_{\mathrm{Br}\gamma}$ by Donehew and Brittain (2011) result in very large errors on the propagated quantities. As a result, the above value for $\dot{M}$ should be taken to be an order-of-magnitude estimate.

The strong Br γ signal is consistent with accretion, as is the youth of the system. However, the geometry of the line emission does not appear to be consistent with direct stellar accretion. The radius of the emission originates from a region farther from the stellar surface than the $\sim 5R_{\star}$ that would be expected from accretion in Herbig Ae and Be stars (Bouvier et al. 2020). Furthermore, the geometry of the line emission is also stable over all epochs, with the red and blue lobes consistently located north-west and south-east of MWC 166 Aa, and with velocities consistent with Keplerian rotation, which is not expected of material being funnelled onto a stellar surface (Bouvier et al. 2007). As a result, the line emission does not appear to be tracing direct stellar accretion, but rather a process that is more spatially extended.

4.6.3.2 Inner gas accretion disc

The line emission might trace ionised gas in the inner region of the circumprimary gas disc. Based on hydrodynamic simulations, I expect that a stable circumprimary gas disc can exist out to one-third of the binary separation (Artymowicz and Lubow 1994). This disc could accommodate the mass transport from the large-scale mass reservoir seen in far-infrared excess emission, over a circumbinary disc to the star. For MWC 166 A, the upper limit on the radius is ~ 0.9 au or $\sim 15\,R_1$, which is in agreement with the observed location

of the Br γ emission ($\sim 11.5\,R_1$). These discs are often found around Herbig Ae and Be systems, which would be consistent with the age of the system (see Section 4.6.4). The emission would then be tracing ionised gas in Keplerian rotation around the star, rather than direct accretion onto the star. Kraus et al. (2012) found an example of such a disc around another young B-type close binary system, V921 Sco, using similar techniques. The Br γ line profiles were found to be similarly strong and narrow to those presented in this study for MWC 166 Aa. They also were similarly variable in intensity and wing strength, while still being consistent with a Keplerian disc.

However, the lack of evidence of direct accretion in my observations means that this scenario cannot be confirmed. Further observations at shorter wavelengths may show evidence of accretion, for example by showing emission closer to the stellar surface.

4.6.3.3 Be decretion disc

As a third scenario, I consider that the observed circumprimary emission might be associated with a decretion disc, as observed around classical Be stars. Classical Be stars are defined as non-supergiant B stars that have shown Balmer line emission at some point in time (Collins 1987). Generally very fast rotators, they typically host gaseous circumstellar discs characterised by a viscous decretion model (e.g. Lee et al. 1991; Carciofi 2011), with material ejected by radiation pressure from the star forming a Keplerian disc. This disc is sustained by periodic outbursts from the star (Grundstrom et al. 2011), which leads to variability on a range of timescales from days to years (Labadie-Bartz et al. 2017).

Variability in the emission line profile is also common in decretion discs, with violet-to-red (V/R) variations meaning the redshifted and blueshifted wings of the line are commonly found at different relative strengths at different epochs (Rivinius et al. 2013) – Figure 4.3 shows that such variations are indeed present in the spectrum of MWC 166 A, and the results in columns (3) and (4) of Table 4.7 quantify this. In the simplest of Keplerian models, the flux intensities of each wing should be equal. The observed deviation from this profile is due to the flux intensity of the disc being azimuthally asymmetrical (Porter and Rivinius 2003), which is most likely due to temperature or gas density enhancements in specific regions of the disc. My observations, comprising only four epochs, are insufficient

to characterise the observed variations in V/R ratio as being periodic or quasi-periodic, but previous studies (Hanuschik et al. 1995) indicate that, in general, these variations are cyclic in the long term. Hummel and Hanuschik (1997) modelled a one-armed density wave precessing around the star as an explanation for these variations.

The rapidly changing V/R ratio is characteristic of Classical Be stars observed at intermediate inclinations (Catanzaro 2013). Such variations are generally not found in Herbig Be objects. Furthermore, the line-emitting region around the primary is rather extended, which is more consistent with decretion than accretion. I would assume Br γ emission from magnetospheric accretion to originate no more than $5R_\star$ from the star (Bouvier et al. 2020). However, I find that at all epochs, it is located well beyond the stellar surface. I estimated the radius of the emission by averaging the angular displacement in the blue and red wings of each line, with the results shown in column (5) of Table 4.7. These values do agree with each other in almost all circumstances, despite some slight variation between the two lines and epochs, with a general separation from the primary of ~ 0.25 mas, or $\sim 11R_1$. Comparing this value to other spectro-interferometric Be studies shows that it is consistent with that of a Classical Be disc, with the VLTI/AMBER survey by Cochetti et al. (2019) showing Br γ radii ranging between $3 - 13\,R_\star$. The lack of dust in Be discs also correlates with my findings from the continuum fit, where I found no evidence for circumprimary dust.

In light of the above points, the decretion disc model cannot be excluded for the circumprimary emission. Previous photometric studies of MWC 166 A found evidence for periodic dissipation and regeneration of the circumstellar envelope around the primary star over a period of months (Pogodin et al. 2006), which is consistent with models and observations of Be stars and adds weight to this interpretation of the line emission.

This would be in contrast to previous characterisations of MWC 166 Aa as a Herbig Be star (Fairlamb et al. 2015), and is also supported by my isochrone interpolation: from Figure 4.9, it can be seen that the large mass of the primary means that it is evolved beyond the protostellar stage at all age estimates. This is further supported by the relatively small NIR excess in the spectral energy distribution of MWC 166 A, suggesting that the circumstellar environment has been at least partially cleared of material. The observed

far-infrared excess of the system at $\sim 100\,\mu$m, however, is more supportive of the accretion disc scenario outlined in Section 4.6.3.2.

As a result, I can characterise the K band line emission as originating in a Keplerian or quasi-Keplerian circumprimary gas disc, as opposed to direct stellar accretion. Whether this is an accretion disc or a decretion disc is to be confirmed by future observations.

4.6.4 Constraining the age of the system

4.6.4.1 Previous distance estimates for MWC 166

MWC 166 is located in the nearby OB association Canis Major OB1. Markarian (1952) was the first to estimate the distance to CMa OB1, identifying 11 probable members of the association and deriving a distance of 960 pc (Gregorio-Hetem 2008). Clariá (1974a) confirmed the physical association of the CMa OB1 association with the nearby reflection nebula CMa R1, and placed an upper bound on the age of the complex of ~ 3 Myr. The distance to MWC 166 and to the CMa OB1/R1 association is still poorly constrained. Clariá 1974b identified 44 members of CMa OB1/R1, including MWC 166, and calculated its distance as 1150 ± 140 pc based on UBV photometry. Further study of the region was undertaken by Tovmasyan et al. (1993), who observed 43 early-type stars associated with CMa OB1. It was concluded that stars were divided into three regions – with late B-type stars clustered at 320 pc and 570 pc, and early B-type and O-type stars at 1100 pc. Shevchenko et al. (1999) subsequently took photometry for 88 stars found to be probable members of CMa R1, deriving a most probable distance of 1050 ± 150 pc.

All of these photometric estimates give a value for the distance to CMa R1 on the order of 1 kpc, but do not attempt to calculate distances to individual stars within the association. Tjin A Djie et al. (2001) was the first to study the individual members of CMa R1 collectively, and calculated photometric distances. Parallax observations have corroborated the photometric distance calculations for a majority of individual members of CMa OB1/R1, but are not consistent in the case of MWC 166. HIPPARCOS (ESA 1997) measured a distance of 247 ± 82 pc, about a quarter of the distance of CMa R1, while GAIA DR2 parallaxes correspond to an even shorter distance of 131^{+16}_{-13} pc (Bailer-Jones et al. 2018) – roughly ten times closer than its parent association. It should in addition

be noted that the distance estimate to MWC 166 provided by Bailer-Jones et al. (2018) is closer than 99% of all sources in the catalogue – a further indication of the unrealistically close distance reported by parallax. The discrepancy between these parallax measurements and photometric distance to its containing cluster can likely be explained by the binarity of the system. Bailer-Jones et al. (2018) indeed states that all parallaxes are assumed to be for single stars, ignoring multiplicity. Additionally, other identified members of CMa R1 largely have parallaxes consistent with the distance to the region. Therefore, I discount in this work the parallax measurements, and take the 'canonical' distance to MWC 166 to be the photometric distance most recently calibrated by Kaltcheva and Hilditch (2000), 990 ± 50 pc.

As Table 4.5 and Figure 4.9 show, the primary star has already reached the main-sequence for all plausible age estimates, while the secondary is still in its pre-main-sequence stage at the youngest age estimates. By comparing the luminosities of the two stars at different ages to the flux ratios found from the interferometric observations, I can place some constraints on the age of the system.

I first performed the process described in Section 4.4.4 for every age isochrone in the CMD table between 100 kyr and 10 Myr. I then used the derived parameters to generate spectral energy distributions for both stars, using model atmospheres from Kurucz (1993). I then calculated values of f_2/f_1 at the central wavelengths of both the H and K bands, 1.65 µm and 2.2 µm, respectively, to enable a comparison with the corresponding values from the continuum interferometry (see Figure 4.11).

The H band flux ratio measurements show significant scatter between epochs, which might be due to scattered light contributions that are are important towards shorter wavelengths. As described in Section 4.6.2, PIONIER will likely be more strongly affected by these contributions, while MIRC-X and the long CHARA baselines should be able to resolve out extended flux and separate the components more reliably. Therefore, I adopt the MIRC-X value of $f_2/f_1 = 0.484 \pm 0.014$ as the most reliable H-band flux ratio measurements, and mark this value with the blue line in the lower panel of Figure 4.11.

The K band continuum GRAVITY data shows much less variability, and therefore

I chose to take the weighted average of the GRAVITY flux ratios is plotted on the lower panel of Figure 4.11, corresponding to an average flux ratio of $f_2/f_1 = 0.399 \pm 0.021$.

Comparing the measured H and K band flux ratio with the model values, I can exclude ages for the system of $\lesssim 500\,\mathrm{kyr}$. In the K band, this is well beyond the 3σ significance level. For the H band, this is only 2σ, but the range of ages $< 500\,\mathrm{kyr}$ for which this is the case is very small, and only due to the relatively large mass uncertainties – which are themselves large because of the uncertainty on the system's distance.

At such young ages, the NIR brightness of the secondary would exceed the primary, due to the low temperature of the secondary component, which is not supported by the interferometric observations. The upper age of the system is less well constrained, as the stars evolve very slowly once they reach the main-sequence (see Figure 4.9). This can be seen in Figure 4.11, where the models predict consistently $f_2/f_1 \sim 0.2$ for ages beyond 1 Myr. The average continuum K band flux ratio is larger than this, suggesting that the secondary component of the system is still in its pre-main-sequence stage. From the combined H and K band constraints, I estimate the system age to $(7 \pm 2) \times 10^5\,\mathrm{yr}$. This young age is also consistent with the presence of circumstellar material (see Section 4.6.1). Such an age is also consistent with either the accretion or decretion disc models described in Sections 4.6.3.2 and 4.6.3.3.

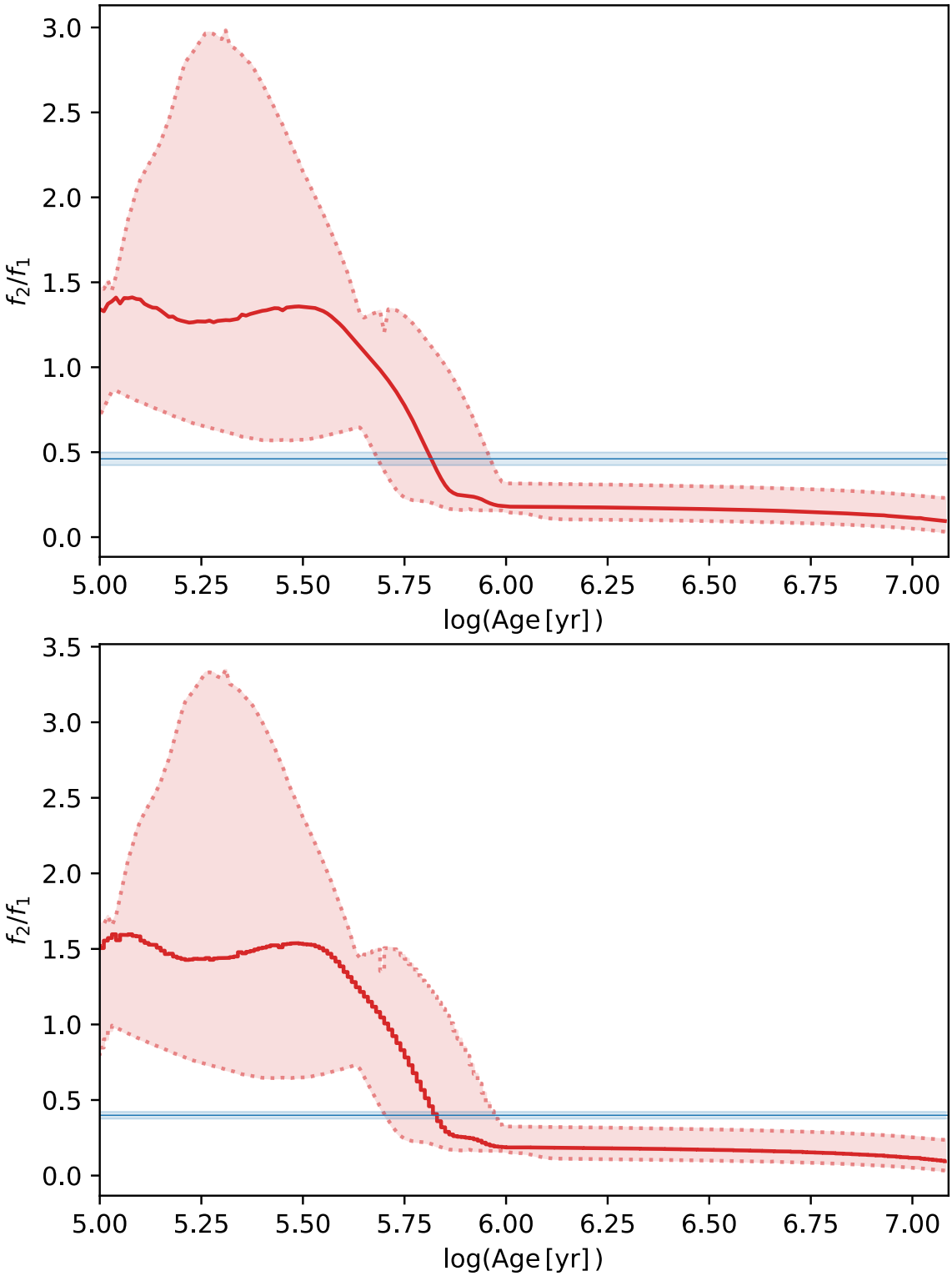

Figure 4.11: Flux ratio f_2/f_1 plotted against log(Age), for all isochrones (red lines), compared to interferometric flux ratios at the same wavelength (blue lines). The upper panel shows the flux ratio at 1.65 µm, while the lower panel shows the flux ratio at 2.2 µm – the central wavelengths for the H and K bands, respectively. The lighter-shaded areas illustrate the uncertainty on each quantity.

Chapter 5

The inner region of the YSO binary HD 104237 A

5.1 Introduction

HD 104237 A is a Herbig Ae system located at a distance of $d = 106.5^{+0.6}_{-0.5}$ pc (Bailer-Jones et al. 2021). The system is a member of the ϵ Cha association of co-moving objects, and comprises a primary star (HD 104237 A) and four associated companions within 15" (Feigelson et al. 2003). The spectrum of the primary star presents as a single-lined spectroscopic binary, due to the influence of a companion, HD 104237 Ab, on a very tight orbit (Böhm et al. 2004). HD 104237 A has been widely studied both spectroscopically and interferometrically due to its proximity and brightness.

Böhm et al. (2004) derived a spectroscopic orbit of the inner single-lined binary which was refined by Garcia et al. (2013), who observed the system with medium and high spectral resolution AMBER data and incorporated Br γ astrometry at four epochs into the orbit. The parameters of this orbit can be found in Column (2) of Table 5.7. Despite the relatively few astrometric points, the large number of RV observations did allow the precise constraint of certain parameters of the orbit, including the period. This was found to be very short, at $P = 19.856 \pm 0.002$ d, implying a very small semi-major axis of $a = 1.9 \pm 0.6$ mas. Therefore, a more precise specification of the orbit requires

astrometry of very high precision, an ideal task for NIR interferometry.

5.1.1 Circumbinary disc

HD 104237 A is known to host a circumbinary disc. Early photometric and spectroscopic studies showed strong H α emission, as well as a substantial near-infrared (NIR) excess (Meeus et al. 2001), which was suggested to be the result of re-radiation of dust grains in the circumstellar environment (Hu et al. 1989). Subsequent photometric observations found the H α emission to be highly variable (Baines et al. 2006). Garcia Lopez et al. (2006) derived an accretion rate of $\dot{M}_{\rm acc} \sim 4 \times 10^{-8}\, M_{\odot}\, {\rm yr}^{-1}$ by analysing the Brackett γ line (see Section 1.4.3.1).

However, the extent of this disc has not been fully constrained. Observations by Hales et al. (2014) detected CO emission originating from the circumbinary disc, and simultaneously fitted the SED of the system and the observed CO disc with radiative transfer modelling. They found a total dust mass of $4 \times 10^{-4}\, M_{\odot}$ and a best-fit radius of ~ 90 au, comparable to the estimate by Grady et al. (2004) of $\sim$ 70au. However, the more recent Gemini-LIGHTS study (Rich et al. 2022) studied the outer disc region in the J and H bands with polarised light observations, finding no evidence of disc material at radii > 21 au from the stars.

The inner region of the circumbinary disc has been studied extensively using VLTI/AMBER observations, by Tatulli et al. (2007), Kraus et al. (2008), and Garcia et al. (2013). Kraus et al. (2008) found the two components of HD 104237 A to be located inside the inner radius of the circumbinary K-band emission, adding weight to the hypothesis of the circumstellar environment taking the form of a circumbinary disc of material, responsible for the substantial NIR excess observed in its SED. Dunhill et al. (2015) conducted smoothed particle hydrodynamics (SPH) simulations of HD 104237 A and its circumstellar environment, the results of which were consistent with an inner cavity of the circumbinary disc having a diameter of ~ 4 mas. The geometry of the cavity was also predicted to not be stable over time, precessing with a timescale on the order of decades, and with streamers of material spiralling from the inner rim of the disc onto the stars (see Figure 5.1).

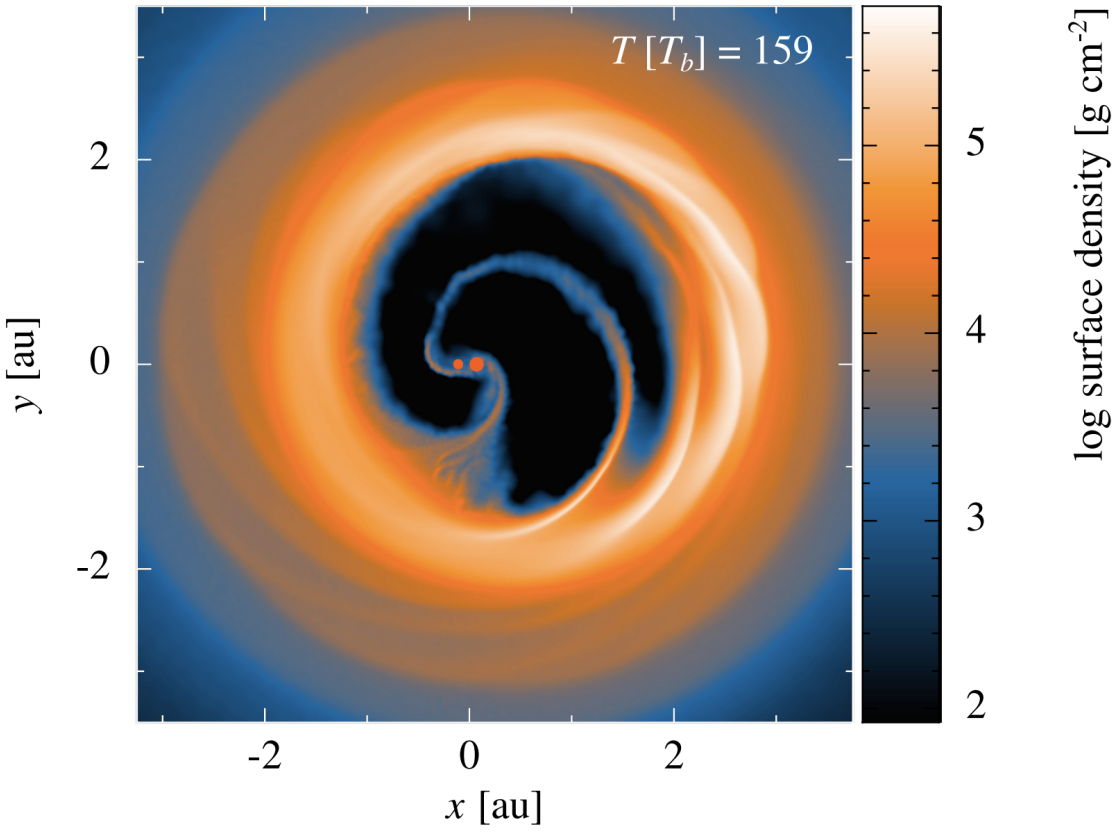

Figure 5.1: Snapshot from SPH model of HD 104237, taken from Dunhill et al. (2015). The dynamical interactions between stars and disc are clearly represented, with streamers of material crossing the cavity to accrete onto the stars.

5.1.2 Jet

The system is also associated with a series of knots of material which have been observed to comprise a collimated micro-jet, the Herbig-Haro object HH 669, which was detected in Lyman α at a speed of $\sim 340\,\mathrm{km\,s^{-1}}$ (Grady et al. 2004). This implies that HD 104237 is still a dynamically active system, with the two central objects interacting with the circumstellar material to drive this outflow. The region from which this jet is launched has been suggested to be the inner rim of the circumbinary disc (Garcia et al. 2013), which would result in an estimated mass loss of $\dot{M}_{\mathrm{wind}} \sim 2\times10^{-9}\,M_{\odot}\,\mathrm{yr}^{-1}$, an order of magnitude less than the predicted accretion onto the stars. In this chapter I will present near-infrared interferometric observations taken at the Very Large Telescope Interferometer (VLTI), covering multiple orbits of the system.

Table 5.1: Literature parameters of the HD 104237 A system. **References:** [1] Bailer-Jones et al. (2021), [2] Böhm et al. (2004), [3] van den Ancker et al. (1998), [4] Garcia et al. (2013), [5] Fumel and Böhm (2012), [6] Grady et al. (2004).

Parameter	Value	Reference
d [pc]	$106.5^{+0.6}_{-0.5}$	1
M_1 $[M_\odot]$	2.2 ± 0.2	2
L_1 $[L_\odot]$	35^{+5}_{-4}	3
R_1 $[R_\odot]$	2.7 ± 0.2	4
$\log(g)_1$	3.9 ± 0.3	5
$T_{\rm eff,1}$ [K]	8550 ± 150	5
M_2 $[M_\odot]$	1.7 ± 0.1	2
L_2 $[L_\odot]$	2.6	6
R_2 $[R_\odot]$	2.5	5
$\log(g)_2$	3.9	5
$T_{\rm eff,2}$ [K]	4730	6

5.2 Observations

HD 104237 A was observed at 14 epochs using the GRAVITY (Gravity Collaboration et al. 2017) 4-beam combiner at the VLTI, as part of programme 0102.C-0949. The observations were taken with the Auxiliary Telescopes (ATs) in their Small, Medium, and Large configurations, and using GRAVITY's high spectral resolution mode of $\mathcal{R} = \Delta\lambda/\lambda \sim 4000$. The data were reduced using the GRAVITY data reduction pipeline as part of the `ESOreflex v2.9.1` environment (Freudling et al. 2013). Observations were also taken with VLTI/PIONIER (Le Bouquin et al. 2011) as part of programme 106.21JU, subsequently reduced with the `pndrs v3.5.2` pipeline (Le Bouquin et al. 2011). Due to the extremely short orbital period of the system (Garcia et al. 2013), more astrometric measurements were needed to obtain a robust orbital fit. I obtained 61 individual calibrated observations taken with PIONIER from the Jean-Marie Mariotti Centre Optical interferometry DataBase (JMMC OiDB) [1], and included them in the geometric modelling analysis. The observations are listed in full in Table 5.2. Observations taken during the same night were analysed as a single epoch in order to increase the signal-to-noise ratio, with the number of pointings in each epoch shown in the final column of Table 5.2. I also included the RV observations from Böhm et al. (2004), comprising $\sim$ 1400 points with an uncertainty of $\pm 0.2\,\mathrm{km\,s^{-1}}$, in order to build a three-dimensional orbital picture of the system.

1. Available at: http://oidb.jmmc.fr.

Table 5.2: Full list of interferometric observations of HD 104237 A. Observations with $\mathcal{R} = 4201$ were taken with the GRAVITY instrument, and the remainder are PIONIER observations.
PIONIER data not observed as part of project 106.21JU were taken from OiDB. Observations of HD 104237 A from programmes 088.C-0613, 089.C-0211, 093.C-0844, 091.C-0504 were published in Kobus et al. (2020). Observations from programme 190.C-0963 were published in Kobus et al. (2020) and Lazareff et al. (2017).
The column labelled 'Phase' shows the orbital phase of each observation, derived from the solution in Table 5.7.

Date	MJD ($+2.4 \times 10^6$)	Phase	Programme ID	Array Config	Baseline range (m)	$\mathcal{R}$ ($\Delta\lambda/\lambda$)	Pointings
2012-02-29	55986.1819	0.509	088.C-0613(A)	A1-G1-I1-K0	46.64 – 129.00	41	5
2012-06-14	56092.9651	0.886	089.C-0211(A)	A1-G1-I1-K0	46.64 – 129.00	18	2
2012-12-21	56282.3732	0.425	190.C-0963(C)	A1-B2-C1-D0	11.31 – 35.79	18	1
2012-12-22	56283.3444	0.474	190.C-0963(C)	A1-B2-C1-D0	11.31 – 35.79	18	1
2013-02-18	56341.3791	0.397	190.C-0963(B)	D0-G1-H0-I1	40.78 – 82.35	18	1
2013-02-19	56342.1778	0.437	190.C-0963(B)	D0-G1-H0-I1	40.78 – 82.35	18	2
2013-04-11	56393.0033	0.997	091.C-0504(A)	D0-G1-H0-I1	40.78 – 82.35	18	21
2014-02-27	56715.2844	0.227	092.D-0590(B)	D0-G1-H0-I1	40.78 – 82.35	18	1
2014-03-01	56717.1101	0.319	092.C-0243(A)	D0-G1-H0-I1	40.78 – 82.35	18	2
2014-03-02	56718.1952	0.374	092.C-0243(A)	D0-G1-H0-I1	40.78 – 82.35	18	7
2014-05-28	56805.9810	0.795	093.C-0844(A)	D0-G1-H0-I1	40.78 – 82.35	18	4
2014-06-02	56810.9945	0.047	093.C-0844(A)	B2-C1-D0	11.31 – 33.94	18	4
2018-12-23	58475.3022	0.864	102.C-0949(A)	A0-B2-C1-D0	11.31 – 33.94	4201	3
2019-01-14	58497.3267	0.973	102.C-0949(B)	D0-G2-J3-K0	39.99 – 104.32	4201	5
2019-01-15	58498.3229	0.023	102.C-0949(B)	D0-G2-J3-K0	39.99 – 104.32	4201	6
2019-02-22	58536.2214	0.932	102.C-0949(C)	A0-G1-J2-J3	58.24 – 132.44	4201	5
2019-02-23	58537.1893	0.981	102.C-0949(C)	A0-G1-J2-J3	58.24 – 132.44	4201	6
2019-02-24	58538.2405	0.034	102.C-0949(C)	A0-G1-J2-J3	58.24 – 132.44	4201	3
2019-02-26	58540.2784	0.136	102.C-0949(C)	A0-G1-J2-J3	58.24 – 132.44	4201	15
2019-03-08	58550.1472	0.633	102.C-0949(C)	A0-G1-J2-J3	58.24 – 132.44	4201	9
2019-03-10	58552.2638	0.740	102.C-0949(A)	A0-B2-J2-J3	58.24 – 132.44	4201	15
2019-03-11	58553.2111	0.788	102.C-0949(A)	A0-B2-C1-D0	11.31 – 33.94	4201	3
2019-03-12	58554.2019	0.838	102.C-0949(A)	A0-B2-C1-D0	11.31 – 33.94	4201	4
2019-03-15	58557.1607	0.987	102.C-0949(A)	A0-B2-C1-D0	11.31 – 33.94	4201	4
2019-03-16	58558.0548	0.032	102.C-0949(A)	A0-B2-C1-D0	11.31 – 33.94	4201	4
2019-03-22	58564.3256	0.347	102.C-0949(A)	A0-B2-C1-D0	11.31 – 33.94	4201	3
2020-12-19	59202.2892	0.476	106.21JU.002	D0-G2-J3-K0	39.99 – 104.32	34	3
2020-12-20	59203.1877	0.521	106.21JU.001	D0-G2-J3-K0	39.99 – 104.32	34	2
2020-12-28	59211.2789	0.929	106.21JU.003	A0-B2-C1-D0	11.31 – 33.94	34	2

5.3 Geometric modelling of the dust continuum

5.3.1 Initial fit to constrain astrometry

From the interferometric observations, I geometrically modelled the system using the modelling tool PMOIRED[2] (Mérand 2022). Each epoch was modelled individually due to the rapid orbit of the two components. This was then used to construct a three-dimensional orbit of the system, which is presented in Section 5.4. The separation of the two components of the system is known from the literature to be very small, with a semi-major axis of $a \sim 2$ mas. This is close to the resolution limit for the PIONIER and GRAVITY instruments and, considering that at periastron the separation will be as little as ~ 0.5 mas, the binary may not be resolved at certain epochs with an orbital phase close to zero, especially on short baselines. From Table 5.2, it can be seen that the majority of the GRAVITY observations were either taken very close to periastron, on the small AT configuration, or both. It was not possible to obtain reliable astrometry for these observations, and therefore the orbit described in Section 5.4 was calculated based solely on the PIONIER models. I modelled the system using a relatively simple geometry – two uniform discs of size 0.1 mas representing each component, as well as circumstellar emission, modelled with a variety of geometries which are outlined below.

5.3.1.1 Gaussian model

I initially conducted the modelling using a Gaussian to represent circumstellar emission. This model included six free parameters: the displacement of the secondary from the primary to the North (x) and East (y); the relative flux contribution of the secondary (f_2); the extended flux contribution taking the form of a power-law with amplitude $f_{\mathrm{ext},0}$ and index $f_{\mathrm{ext,P}}$; and the full-width at half maximum (FWHM) of the Gaussian representing the extended flux (σ_{ext}). The flux components are relative to the primary $f_1 \equiv 1$. The centre of the extended emission was set to be located at the centre of mass of the two components, using the masses from Table 5.1. The model described above provides a relatively robust fit for the astrometry at most PIONIER epochs, despite its simplicity. However, the comparatively large χ^2 values (see Table 5.3) show that this model is too

2. Available at: https://github.com/amerand/PMOIRED

simplistic for further analysis, and indeed previous studies of the object have indicated that the circumbinary emission has a central cavity, as described in Section 5.1.1.

5.3.1.2 Ring model

A more physical model would treat the NIR dust continuum emission as a ring, with an inner cavity where the temperatures are too high for optically-thick dust to survive. I therefore implemented an alternative model for the circumstellar emission with the following free parameters: disc inclination ($i_{\rm ext}$); disc PA ($\Theta_{\rm ext}$); disc azimuthal amplitude ($A_{\rm ext,az}$); disc azimuthal PA ($\Theta_{\rm ext,az}$); disc inner diameter ($D_{\rm ext,in}$) and outer diameter ($D_{\rm ext,out}$); density power-law index $\rho_{\rm ext}$; disc flux amplitude ($f_{\rm ext,0}$); disc flux power-law index ($f_{\rm ext,P}$).

The PIONIER models were first executed for the epoch 2012-02-29. This epoch has the largest baseline range, maximum baseline, and number of pointings of any of the PIONIER epochs (see Table 5.2). In addition, it has very large closure phases and also captures the first null of the visibility curve, so is ideal for exploring the circumstellar environment of the system. For this initial model of epoch 2012-02-29, the disc centre location parameters ($x_{\rm ext}, y_{\rm ext}$) were also set to be free parameters. This was done in order to ensure that the remaining disc parameters were as reliable as possible, for use in the remaining observations. Once the disc parameters were established, they were fixed and used for the remaining PIONIER epochs, which were fitted with the disc centre at the centre of mass of the two components, as in the Gaussian model.

5.3.2 Combining observations of similar orbital phase

The models described above correspond to a single epoch of observation due to the short period of the binary orbit. Since the period has been robustly determined from the RV orbit (Grady et al. 2004; Garcia et al. 2013), it is possible to combine observations which occur at similar orbital phase in order to improve the (u, v)-coverage of the geometric model. For the GRAVITY data, the epochs used were: 2019-01-14, 2019-01-15, 2019-02-22, 2019-02-23, 2019-02-24, 2019-03-15, 2019-03-16. These epochs, when taken together, provide the widest range of baselines at the VLTI, offering a substantial (u, v)-coverage. They have an orbital phase ranging between $\sim 0.93 - 0.03$, and were chosen such that the

location of the stellar components would be similar across the epochs used. Furthermore, the positions of the stars were fixed based on the orbit derived in Section 5.4. I took the mean orbital phase value of the observations to be used, and fixed the values of (x_2, y_2) to the corresponding ephemeris. This was especially important because of the separation between the components being too small to be fully resolved near periastron, which is where most GRAVITY epochs were taken, as shown in Table 5.2.

The modelling was executed with PMOIRED, modelling squared visibilities (V2) and closure phases (T3PHI) in the dust continuum simultaneously. In order to model the dust continuum, the Science Camera data was binned by a factor of 100, to achieve a spectral resolution of $\mathcal{R} \sim 42$. I excluded visibilities with a relative error of $> 8\%$, as well as closure phases with errors larger than 3°, in order to eliminate datapoints with a large scatter from the fit. The fit was then bootstrapped ($N = 1000$) to increase the confidence of the error estimation. The results of the GRAVITY multi-epoch fit are found in Section 5.4.2.1.

5.4 Results: Dust continuum modelling and orbital solution

5.4.1 Derivation of relative astrometry

5.4.1.1 Constraining disc parameters in the PIONIER data

The PIONIER models were first executed for the epoch 2012-02-29. This epoch has the largest number of pointings of any of the PIONIER epochs (see Table 5.2). In addition, it has very large closure phases and also captures the first null of the visibility curve, so is ideal for exploring the circumstellar environment of the system.

My initial Gaussian models show a region of extended continuum emission, which has a FWHM of $\sim$ 7 mas, corresponding to $\sim$ 0.75 au for the distance to the system calculated by Bailer-Jones et al. (2021) ($d = 106.5^{+0.6}_{-0.5}$ pc). The results of the Gaussian model fit for the epoch 2012-02-29 are shown in Columns (2) and (3) of Table 5.3, for uniform diameters (UDs) of 0.1 and 1.0 mas, representing the stars being unresolved and resolved respectively. These values were kept fixed due to a lack of conversion in the fit when they were allowed to be fitted. The Gaussian models show a worse fit to the data

Table 5.3: Model comparison for the epoch 2012-02-29.

Parameter	Gaussian		Ring	
(1)	(2)	(3)	(4)	(5)
UD_1 [mas]	0.1	1.0	0.1	0.984 ± 0.096
UD_2 [mas]	0.1	1.0	0.1	1.12 ± 0.12
x_2 [mas]	-1.208 ± 0.039	-1.219 ± 0.044	-1.165 ± 0.011	-1.175 ± 0.008
y_2 [mas]	-3.348 ± 0.048	-3.328 ± 0.052	-3.085 ± 0.026	-3.101 ± 0.020
f_2	0.725 ± 0.028	0.734 ± 0.027	0.595 ± 0.009	0.634 ± 0.020
x_{ext} [mas]	-0.82 ± 0.32	-0.98 ± 0.42	0.002 ± 0.037	-0.047 ± 0.025
y_{ext} [mas]	-0.32 ± 0.32	0.06 ± 0.42	-1.097 ± 0.077	-1.081 ± 0.063
σ_{ext} [mas]	6.84 ± 0.17	7.16 ± 0.23	-	-
$D_{ext,in}$ [mas]	-	-	5.33 ± 0.28	6.09 ± 0.20
$D_{ext,out}$ [mas]	-	-	12.31 ± 0.52	14.3 ± 1.3
i_{ext} [°]	-	-	33.1 ± 3.3	29.9 ± 3.5
Θ_{ext} [°]	-	-	154.5 ± 4.6	167.7 ± 9.6
$A_{ext,az}$	-	-	0.264 ± 0.059	0.269 ± 0.061
$\Theta_{ext,az}$	-	-	152.7 ± 8.9	161.4 ± 6.5
ρ_{ext}	-	-	1.89 ± 0.47	3.90 ± 0.44
$f_{ext,0}$	1.133 ± 0.055	0.881 ± 0.063	1.051 ± 0.027	0.832 ± 0.034
$f_{ext,P}$	3.71 ± 0.34	4.84 ± 0.47	2.89 ± 0.13	3.63 ± 0.15
χ^2	12.75	14.71	2.57	1.34

compared to the ring models, and therefore to model the astrometry of the system, a ring model was chosen. The ring models tested for 2012-02-29 are shown on Columns (4) and (5) of Table 5.3. The fit corresponding to Column (5) is also shown in Figure 5.2. As can be seen from the relative χ^2 values, the ring models offer a substantially-improved fit compared to the Gaussian models. Column (4) shows the results of the fit which kept the UDs of the stars fixed to 0.1 mas, while Column (5) shows the results for the fit when the UDs were allowed to vary. The two ring models have very similar disc parameters, with the model listed in Column (5) having a slightly better χ^2. The larger diameters associated with that model are however not consistent with the literature value for the primary (UD_H=0.335 mas, Bourgès et al. 2017). Additionally, the angular size of the component UDs is roughly a factor of three too large for the stars based on the results in Table 5.8. Therefore, in all subsequent modelling, the stars were assumed to be unresolved and kept fixed to 0.1 mas, to represent point sources.

In the models presented in Table 5.3, the central location of the extended emission, (x_{ext}, y_{ext}) was allowed to be fitted, rather than being fixed at the centre of mass of the components, although in practice the disc centre was close to the centre of mass. In

subsequent modelling, this was fixed to the centre of mass of the two stars, to ensure consistency between epochs and to reduce the number of free parameters in the model.

5.4.1.2 Analysis of remaining PIONIER epochs with fixed disc parameters

The disc parameters from Column (4) of Table 5.3 were fixed and used for the remaining PIONIER epochs. The model produced good agreement with the data for the majority of PIONIER epochs (see Table 5.4), and the derived (x_2, y_2) points were used to calculate a three-dimensional orbital solution for the orbit of the system, presented in Table 5.7 and Figure 5.5. The PIONIER epochs 2013-04-11, 2014-06-02 and 2020-12-28 were excluded from the orbital fit due to their proximity to periastron, a problem exacerbated by the short baseline lengths (see Table 5.2). Additionally, the PIONIER data my team and I collected in 2020 returned very large residuals when fitted with the disc parameters from 2012-02-29, and so all these observations were also excluded from the orbital fit. This is explained in more detail in Section 5.4.2.1.

As mentioned in Section, 5.3.1, most of the GRAVITY observations were also taken at binary separations which were too small to resolve without very large residuals, and as such these epochs were also excluded from the orbital fit. Furthermore, the disc parameters from the PIONIER model were found to produce very large χ^2 values in the continuum GRAVITY data, leading to the separate analysis of the GRAVITY observations, the results of which are presented below.

5.4.2 Continuum modelling of the GRAVITY data

5.4.2.1 Multi-epoch model to derive disc parameters

The results of the multi-epoch continuum GRAVITY model described in Section 5.3.2 are shown on Figure 5.4, and the corresponding parameters are presented in Table 5.5. The geometry is slightly different to that found from the PIONIER model, but the majority of the parameters are in agreement regardless.

The inner diameter of the disc from the GRAVITY multi-epoch model was found to be smaller than the PIONIER model, with $D_{\rm ext,in} = 4.6$ mas, compared to 5.3 mas. Tatulli et al. (2007) derived a diameter of 3.9 mas, while Kraus et al. (2008) found a value

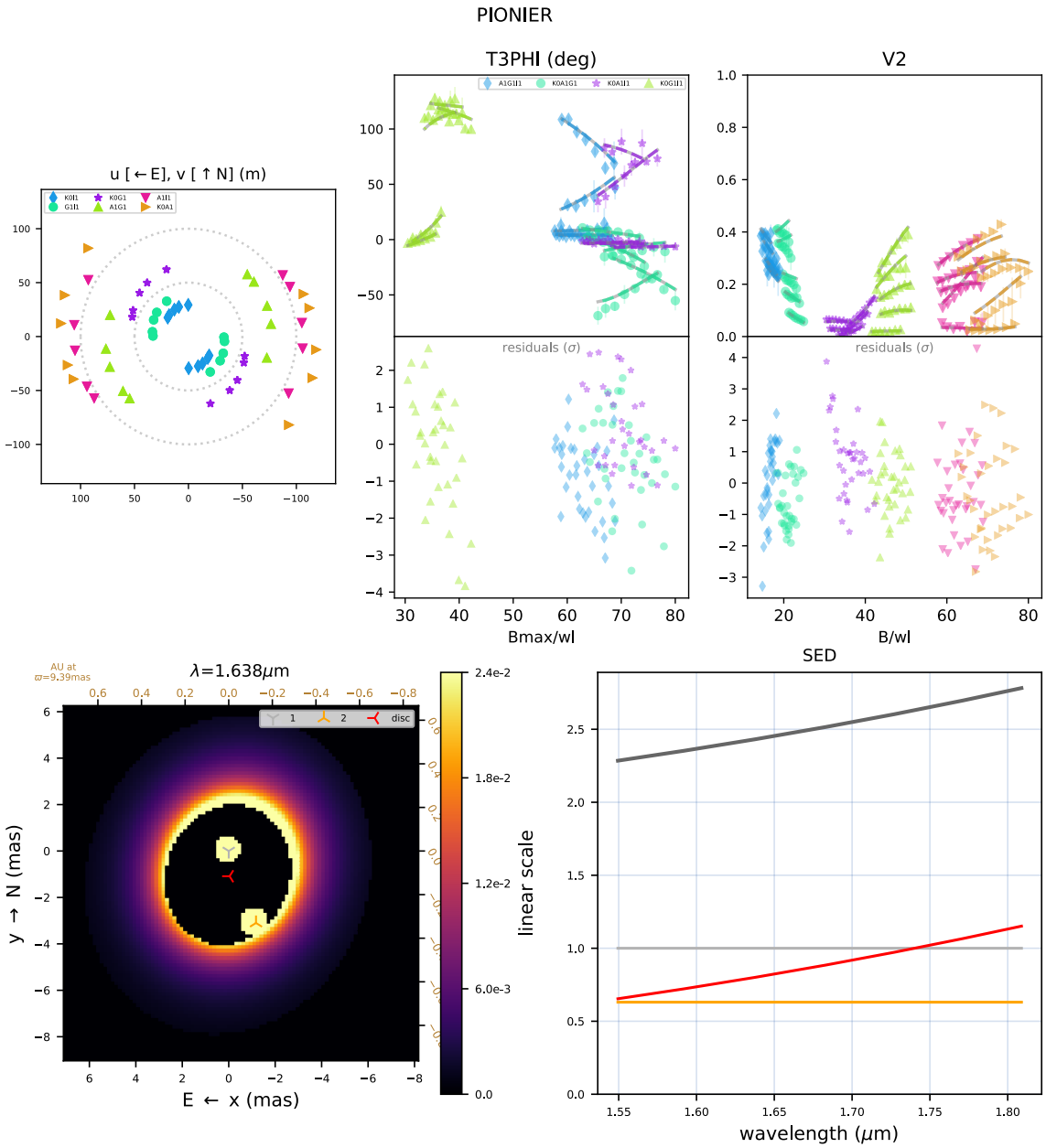

Figure 5.2: Results of the continuum modelling for the PIONIER epoch 2012-02-29. **Top row, left to right**: (u, v)-coverage for the observations associated with the epoch, coloured by baseline pair; Closure phase, coloured by telescope triplet (T3PHI); squared visibility, coloured by baseline (V2). The data are represented by the points, with the best fit shown by the solid lines. **Bottom row, left to right**: Brightness distribution corresponding to the best fit; wavelength dependence of each component. The parameters corresponding to the fit can be found in Column (5) of Table 5.3.

Table 5.4: Relative astrometry for HD 104237 A, derived from continuum visibility and closure phase modelling. The model included two point-sources and circumstellar emission in the form of a ring, the parameters of which were kept fixed to the values calculated from epoch 2012-02-29 (Column (4) in Table 5.3). The parameters E_{maj}, E_{min} and E_θ are respectively the semi-major axis, semi-minor axis and PA of the error ellipse for each epoch. This astrometry is plotted on Figure 5.5.

Epoch	Phase	x_2	y_2	E_{maj}	E_{min}	E_θ [°]	χ^2_ν
	[mas]	[mas]	[mas]	[mas]	[°]		
2012-02-29	0.509	-1.17 ± 0.01	-3.09 ± 0.03	0.024	0.053	-36.6	2.57
2012-06-14	0.886	1.35 ± 0.042	-1.45 ± 0.06	0.021	0.067	-34.2	4.35
2012-12-21	0.425	-2.09 ± 0.48	-3.39 ± 0.47	0.154	0.605	-45.5	0.40
2012-12-22	0.474	-1.58 ± 0.50	-3.64 ± 0.24	0.204	0.492	-81.0	0.53
2013-02-18	0.397	-1.82 ± 0.14	-2.79 ± 0.12	0.112	0.143	59.8	5.47
2013-02-19	0.437	-1.78 ± 0.04	-2.94 ± 0.04	0.031	0.048	-37.8	17.71
2014-02-27	0.227	-2.20 ± 0.03	-1.45 ± 0.06	0.073	0.023	18.6	1.51
2014-03-01	0.319	-2.19 ± 0.04	-2.36 ± 0.03	0.023	0.043	-49.5	4.29
2014-03-02	0.374	-1.99 ± 0.01	-2.86 ± 0.02	0.010	0.020	29.0	2.12
2014-05-28	0.795	0.59 ± 0.02	-2.54 ± 0.02	0.019	0.025	75.0	1.64

of 5.0 mas. Additionally, the AMBER modelling by Garcia et al. (2013) used a diameter of 4 mas. All these values are in good agreement with the results of the continuum fit.

The outer radius of the emission is a degenerate parameter with $f_{ext,0}$ and $f_{ext,P}$, which explains the discrepancies in these parameters between the two models. The disc inclinations of the two models are in agreement with each other and with the orbital inclination, however this may be due to the relatively large uncertainties compared to the other orbital parameters. This co-planarity is the assumption made by Garcia et al. (2013), and is in keeping with theoretical models of circumbinary discs at small radii (Martin and Lubow 2017; Zanazzi and Lai 2018).

The PA of the disc, Θ_{ext}, does however not agree with the value derived from the PIONIER fit. This could be due to the time elapsed between the observations – since the system has a very short orbital period, it is possible that the disc has physically changed in the almost seven years between the epoch used for the PIONIER model and the GRAVITY multi-epoch model. Dunhill et al. (2015) found from SPH simulations that the disc cavity is expected to precess over decadal timescales, although it is unclear if this will have a noticeable effect in the ~ 7 year gap between observations. Furthermore, such a change would also be reflected in the PIONIER data taken in 2020. In order to verify this, the

Table 5.5: Model parameters for the circumstellar emission, as calculated from the GRAVITY multi-epoch dataset. These parameters were then used as a basis for the line analysis in Section 5.5, apart from $A_{\rm ext,az}$ and $\Theta_{\rm ext,az}$, which were allowed to vary per each epoch.

Param	Value
$D_{\rm ext,in}$ [mas]	4.62 ± 0.12
$D_{\rm ext,out}$ [mas]	26.6 ± 1.0
$i_{\rm ext}$ [°]	27.8 ± 2.0
$\Theta_{\rm ext}$ [°]	133.9 ± 4.5
$A_{\rm ext,az}$	0.264 ± 0.059
$\Theta_{\rm ext,az}$	152.7 ± 8.9
$\rho_{\rm ext}$	3.360 ± 0.092
$f_{\rm ext,0}$	2.380 ± 0.054
$f_{\rm ext,P}$	2.387 ± 0.094
χ^2	6.97

2020 PIONIER data were fitted with the disc parameters being left free. This did result in a better fit to the disc (see Figure 5.3), although with a $\chi^2 = 49$. The associated PA of the disc was found to be distinct from both the 2012-12-29 and GRAVITY multi-epoch fits, at $\Theta_{\rm ext} = (228 \pm 15)°$, suggesting that the disc geometry evolves over timescales on the order of years.

5.4.2.2 Modelling individual epochs using the multi-epoch disc parameters

The multi-epoch fit was then used to fit the parameters f_2, $A_{\rm ext}$ and $\Theta_{\rm ext}$ on an epoch-by-epoch basis, since these parameters are likely to change on a very short timescale. The epochs 2019-02-24 and 2019-03-08 were excluded from the modelling. This is because of incompatibility with the orbit, with the epoch 2019-02-24 resulting in a value of $f_2 = 0$, and the epoch 2019-03-08 returning a very large χ^2 due to poorly-constrained closure phases. The results for the continuum fits are presented in Table 5.6. The multi-epoch model provided excellent fits to the continuum data at most epochs, indicating that the binary positions from the orbit are robust.

5.4.3 Orbital fit

The orbit of HD 104237 A was fitted from the relative astrometry (Table 5.4) and the RV measurements taken by Böhm et al. (2004) using the python package `spinOS`[3] (Fabry et al. 2021b). The parameters for the orbit are listed in Table 5.7, as are the parameters

3. Available at: https://github.com/matthiasfabry/spinOS.

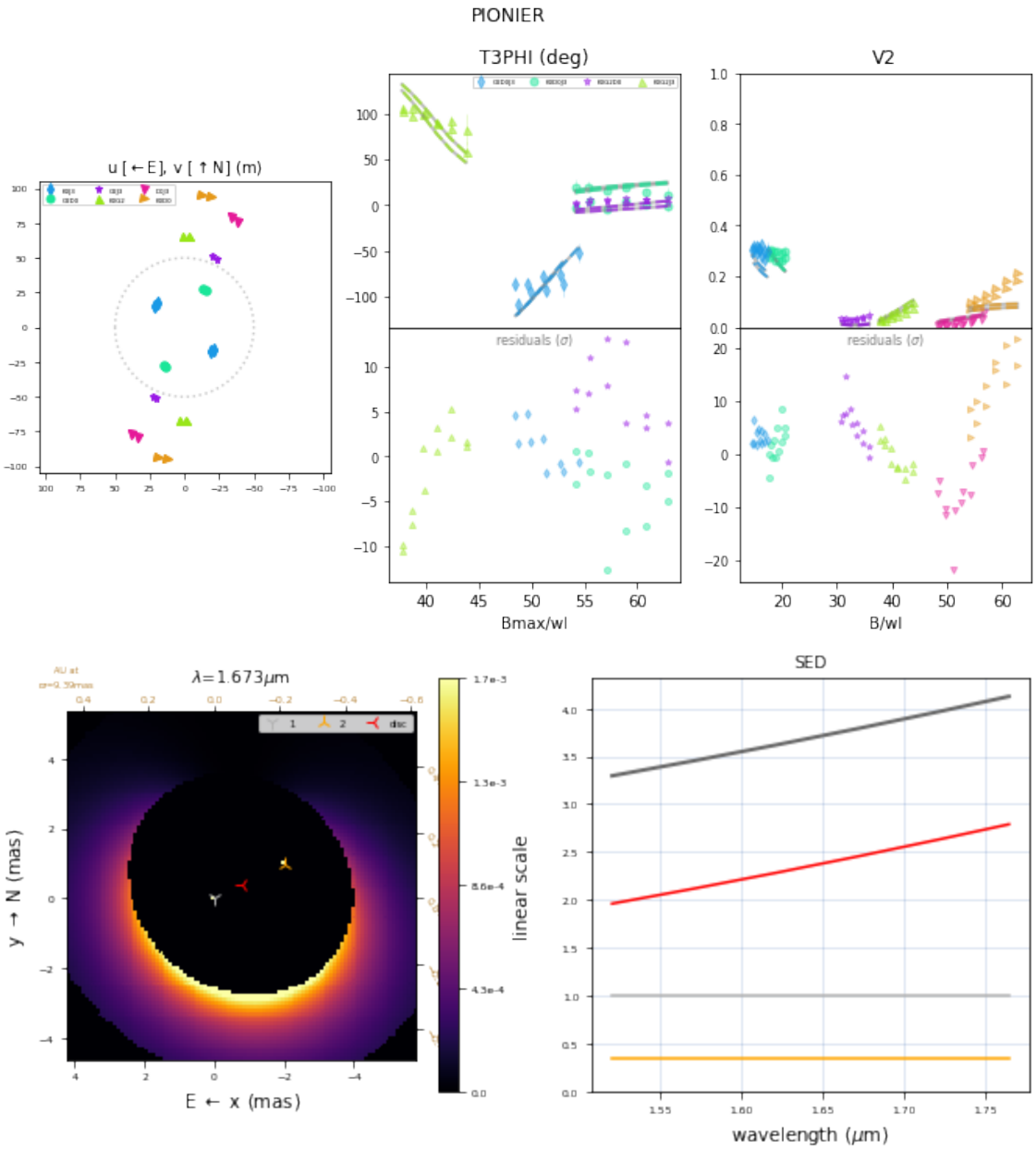

Figure 5.3: Fit to the epoch 2020-12-20, showing the different geometry compared to the fit for 2012-12-29.

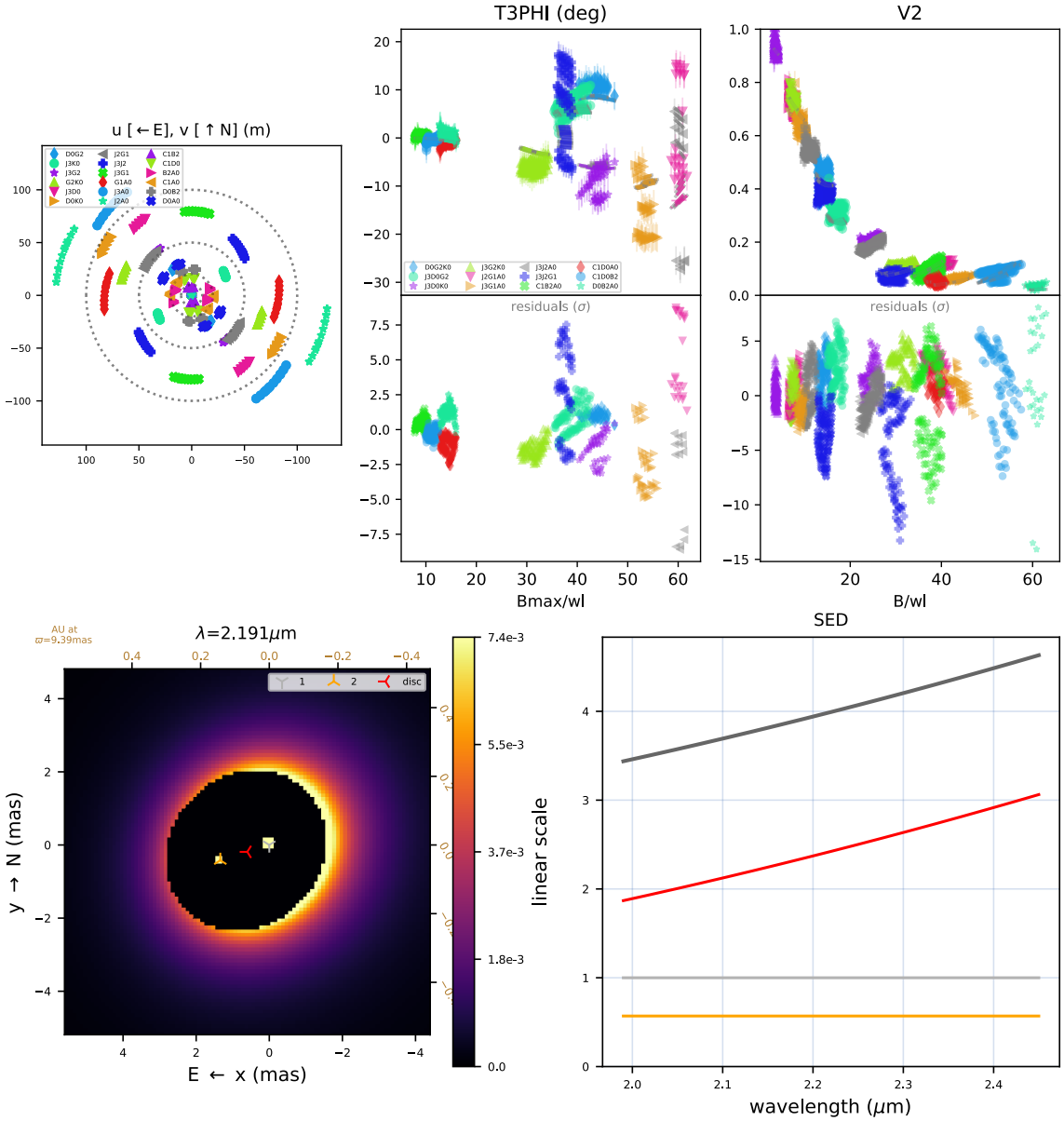

Figure 5.4: Results of the dust continuum fit performed on the GRAVITY multi-epoch dataset.

Table 5.6: Model parameters corresponding to the bootstrapped best-fit continuum GRAVITY models, fixing (x_2, y_2) to the positions predicted by the orbit in Table 5.7, and the remaining disc parameters to the values in Table 5.5.

Epoch	Phase	f_2	$A_{\rm ext}$	$\Theta_{\rm ext}$ [°]	χ^2
2018-12-23	0.864	0.463 ± 0.038	0.633 ± 0.092	193 ± 14	0.58
2019-01-14	0.973	0.682 ± 0.026	0.524 ± 0.027	147 ± 2	1.26
2019-01-15	0.023	0.509 ± 0.038	0.366 ± 0.025	103 ± 10	8.38
2019-02-22	0.932	0.496 ± 0.014	0.228 ± 0.042	140 ± 21	14.43
2019-02-23	0.981	0.494 ± 0.022	0.188 ± 0.058	132 ± 28	9.50
2019-02-26	0.136	0.242 ± 0.019	1.000 ± 0.001	209 ± 3	0.94
2019-03-10	0.740	0.83 ± 0.11	1.000 ± 0.001	125 ± 8	0.56
2019-03-11	0.788	0.382 ± 0.023	0.514 ± 0.049	198 ± 5	0.99
2019-03-12	0.838	0.388 ± 0.017	0.787 ± 0.030	199 ± 2	0.98
2019-03-15	0.987	0.150 ± 0.021	0.973 ± 0.021	189 ± 1	0.70
2019-03-16	0.032	0.432 ± 0.046	0.924 ± 0.094	179 ± 3	1.20
2019-03-22	0.347	0.370 ± 0.038	1.000 ± 0.001	38 ± 1	2.33

corresponding to the fit by Garcia et al. (2013). Comparing the calculated orbit with the fit by Garcia et al. (2013), there is good agreement for all orbital parameters, with P, a, e, Ω, K_1 and V_0 being more tightly constrained than previously and the remaining parameters evaluated to a similar degree of precision as those by Garcia et al. (2013). The derived value of T_0 is also in excellent agreement, with $\mod_1([T_{0,\rm Garcia} - T_0]/P) = 0.009 \pm 0.010\,\rm d$. The dynamical mass of the system does appear larger than the value from Garcia et al. (2013), but several other estimates for the mass of the individual components are in closer agreement with the values I derived from the orbit, for the primary ranging from $2.1\,M_\odot$ (Grady et al. 2004) to $2.5 \pm 0.1\,M_\odot$ (van den Ancker et al. 1998). There are few mass estimates of the secondary component. Böhm et al. (2004) derived masses of $M_1 = 2.2 \pm 0.1\,M_\odot$, $M_2 = 1.7 \pm 0.1\,M_\odot$.

5.4.4 Determining stellar parameters for each component

Finding a full orbital solution for the orbit of HD 104237 A allowed us to determine the mass of the individual components by using the binary mass function (Curé et al. 2015), which can be used to express the mass of the secondary component purely as a function of P, K_1, i, and $M_{\rm tot}$ (see Equation 2.7 and Zarrilli et al. 2022). I determined the masses of HD 104237 Aa and Ab to respectively be $M_1 = (2.37 \pm 0.28)\,M_\odot$ and $M_2 = (1.93 \pm 0.29)\,M_\odot$. I derived the remaining fundamental stellar parameters for the two components of HD 104237 A from interpolating stellar evolution tracks based on these

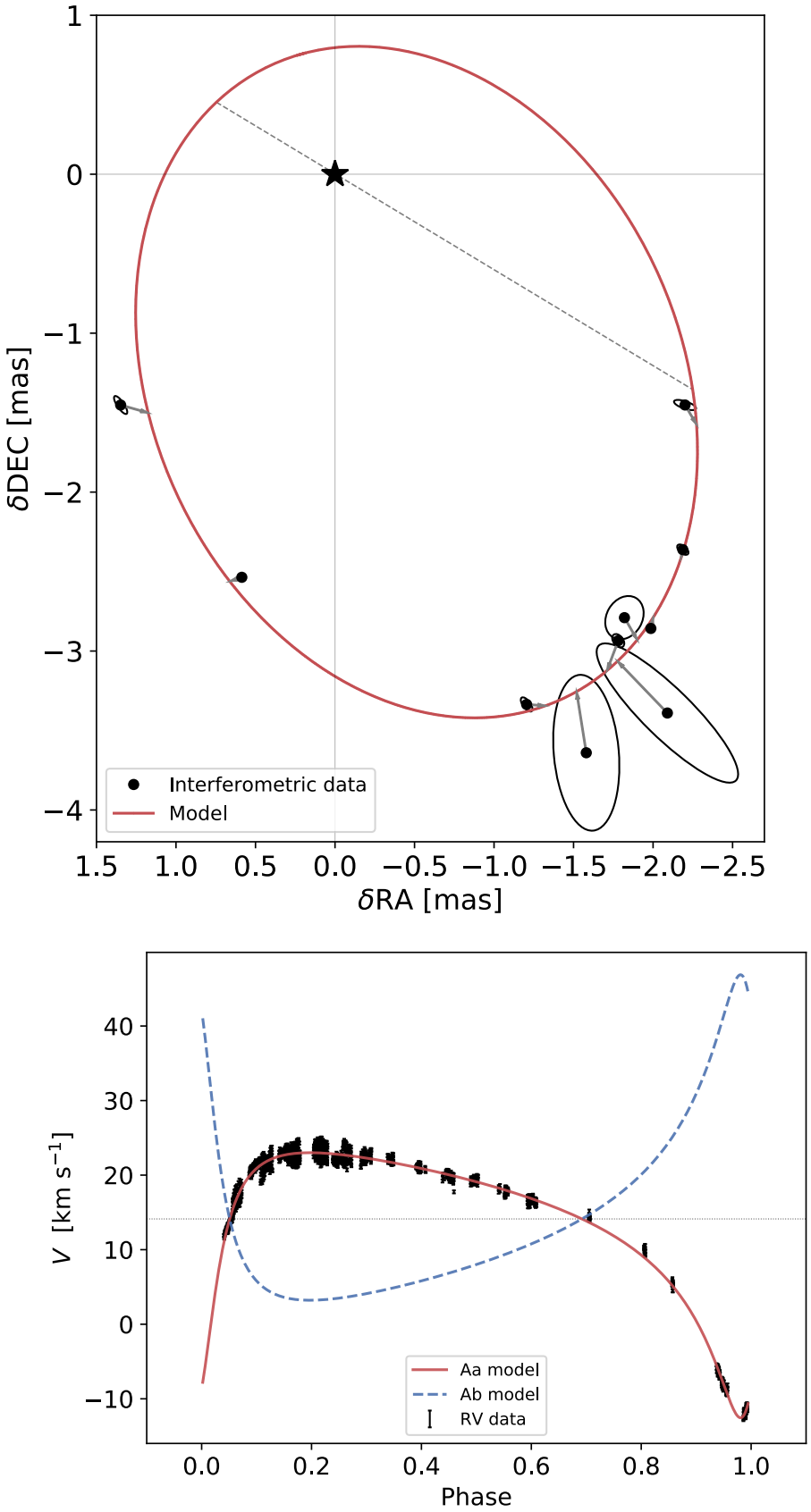

Figure 5.5: Astrometry (top) and radial velocities (bottom) corresponding to the best-fit orbital solution.

Table 5.7: Orbital parameters for HD 104237 A. The second column gives the fit obtained by Garcia et al. (2013). The third column shows my best-fit orbital solution including both RV data and the astrometry data, using the spinOS code. This solution was derived using the astrometry found in Table 5.4.

Parameter	Garcia et al. (2013)	This work
(1)	(2)	(3)
P [d]	19.856 ± 0.002	19.8565 ± 0.0006
T_0 [MJD]	51647.539 ± 0.003	58557.4276 ± 0.0073
a [mas]	1.9 ± 0.6	2.225 ± 0.011
i [°]	163^{+12}_{-9} *	163.87 ± 10.98
e	0.643 ± 0.006	0.6410 ± 0.0016
Ω [°]	234 ± 8	238.98 ± 0.25
ω [°]	218.2 ± 0.9	218.69 ± 2.13
K_1 [km s^{-1}]	17.8 ± 0.2	17.78 ± 0.05
V_0 [km s^{-1}]	14.1 ± 0.1	14.13 ± 0.03
$M_{\rm tot}$ [$M_\odot$]	3.6	4.30 ± 0.02

* The value from Garcia et al. (2013) is 17^{+12}_{-9} °, but for a retrograde orbit. I have changed this to $(180 - i)$° to enable better comparison to the value in this work.

masses. I used the CMD 3.6 tool[4] to generate isochrone tables using PARSEC 1.2S models (e.g Bressan et al. 2012; Chen et al. 2014), with an extinction of $A_V = 0.31$ (Gontcharov and Mosenkov 2017) and assuming Solar metallicity (Cowley et al. 2013). These were calculated for ages ranging between 10^6 and 10^7 yr, with isochrones corresponding to a selection of ages in this range plotted on Figure 5.6.

5.4.5 Evolutionary status of the system

From the isochrone fit, it can be seen that the two components are at different stages in their evolution depending on the age taken for the system, which has not been conclusively established. van den Ancker et al. (1998) estimated the age of the system as 2 Myr, which is plotted as the brown points on Figure 5.6. At this age, both components are clearly in the pre-main-sequence (PMS) stage of evolution. A more recent estimate by Vioque et al. (2018) gives an age of $5.48^{+0.27}_{-0.40}$ Myr (plotted as the blue, red and green tracks on Figure 5.6), corresponding to a scenario where the primary is just reaching the main sequence, while the secondary is still contracting. This has implications for the NIR excesses of the two stars, and therefore their relative H and K band luminosity.

In order to investigate the relationship between the observed flux ratios for the two

4. Available at: http://stev.oapd.inaf.it/cgi-bin/cmd

stars and their stellar parameters in more detail, I used the method described in Zarrilli et al. (2022) and Chapter 4. I generated SEDs for both stars using atmospheric models from Kurucz (1993), based on the derived masses from the orbital fit. This was done for all PARSEC isochrones with ages ranging from 10^6 yr to 10^7 yr, with a step size of 10^5 yr. I subsequently generated an additional set of isochrones with a step size of 2×10^4 yr between the ages of $2 - 8 \times 10^6$ yr, due to the rapidly-changing values of f_2/f_1 at these ages. The results are plotted on Figure 5.7, and show an age dependence that appears at first unusual. Due to the different masses of the two components, the primary will evolve more rapidly than the secondary. This initially causes the flux ratio to decrease to a minimum of $f_2/f_1 = 0.30$, which occurs at an age of 3.4 Myr. As the primary brightens and contracts, it emits more radiation in ultraviolet and blue bands, and less in infrared bands compared to the secondary. This results in a steadily increasing f_2/f_1 in the NIR as the system ages, This continues until the secondary begins the same process, causing the flux ratio to peak at $f_2/f_1 = 1.82$ (at ~ 6.1 Myr), and subsequently start decreasing to the point where both stars are on the main sequence. This stable equilibrium of $f_2/f_1 \sim 0.88$ is reached at an age of ~ 7.8 Myr, at which point further evolution has a very small effect on the stars' flux ratio. The flux ratio from the geometric modelling is variable, but generally $f_2/f_1 \sim 0.6$, with the value corresponding to Column (5) in Table 5.3 marked as the solid black line on Figure 5.7, which intersects the f_2/f_1 curve in two locations. The first of these is very close to the age value of 2 Myr from van den Ancker et al. (1998), while the second is at 4.3 Myr. The corresponding isochrone tracks are marked with brown points and orange points on Figure 4.9 respectively. The orbital solution presented in Section 5.4 is compatible with a flux ratio of $f_2/f_1 < 1$, which implies that the system is younger than the estimate by Vioque et al. (2018). The stellar parameters for both components of the system are presented in Table 5.8, for both best-fit age estimates from the flux ratio, and the values from Vioque et al. (2018).

The parameters for HD 104237 Aa (Table 5.8) agree with the literature values from Table 5.1 at the youngest age estimate from Vioque et al. (2018), as well as the age of 4.28 Myr which is favoured by the flux ratio fit. The value of 2 Myr substantially underestimates the luminosity of the system, and as such the age of the system is likely to be ~ 4.3 Myr. This is consistent with our findings above, supporting the hypothesis of

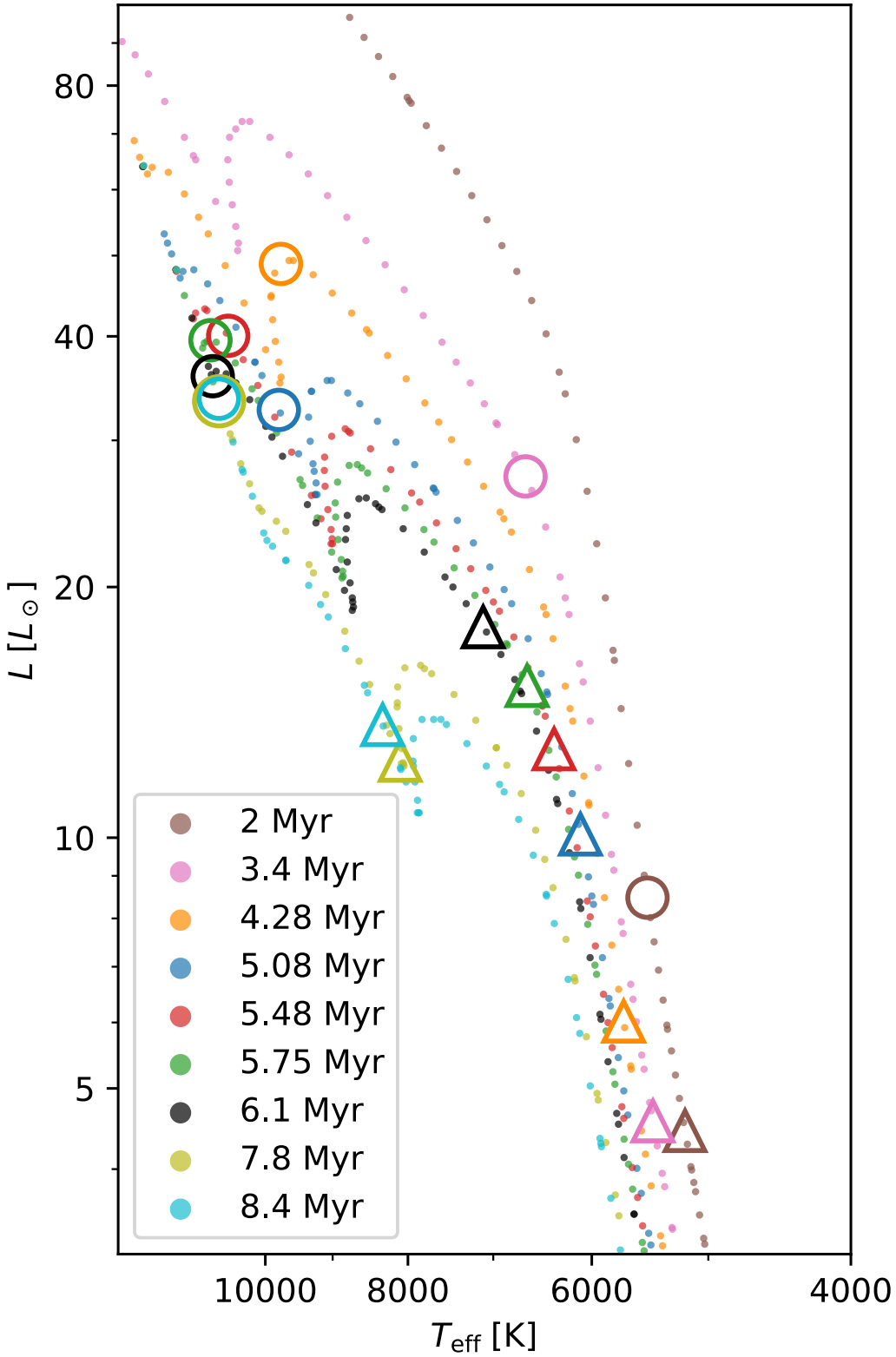

Figure 5.6: Hertzsprung-Russell diagram showing the evolutionary status of HD 104237 Aa (circles) and HD 104237 Ab (triangles). Both stars are in the process of evolving onto the main sequence, as can be seen from their different locations on the tracks at the different ages.

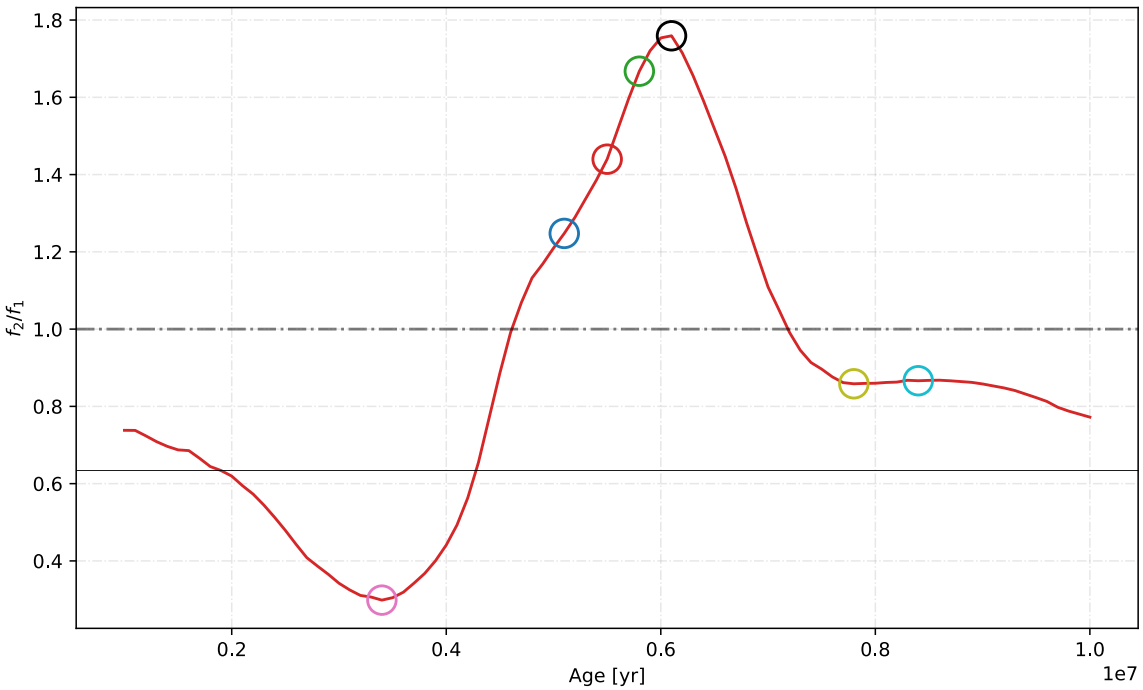

Figure 5.7: HD 104237 A flux ratio vs. age, for the H band central wavelength, 1.65 µm. The coloured circles correspond to the ages on Figure 4.9, and the solid black line shows the flux ratio according to the model in Column (5) of Table 5.3. This intersects with the flux ratio curve at two points.

Vioque et al. (2018) overestimating the age of the system.

5.5 Geometric modelling of the Brackett γ line

The GRAVITY data which I collected was taken in the high spectral resolution mode ($\mathcal{R} = 4201$), allowing the modelling of K band spectral lines. The K band spectrum for HD 104237 A shows very prominent peaks in the Brackett γ line, a feature found in many T Tauri stars and often associated with magnetospheric accretion (e.g. GRAVITY Collaboration et al. 2017, discussed in Sections 1.4.3.1 and 2.6). In order to characterise the nature of the Br γ emission, I modelled it on an epoch-by-epoch basis. The continuum parameters for each epoch were fixed to those of the multi-epoch model described in Section 5.3.2, apart from the flux of the secondary component f_2, and the azimuthal parameters of the disc, $A_{\rm ext,az}$ and $\Theta_{\rm ext}$. These parameters are likely to change within the timescale covered by the observations, as they are proportional to the relative positions of the components at any given epoch (Garcia et al. 2013). For each epoch, I excluded the noisiest datapoints – all visibilities and fluxes with a relative error of greater than 10%,

Table 5.8: Parameters of the HD 104237 A system for the age given by (Vioque et al. 2018), as well as its lower and upper bounds, calculated from the orbit listed in Column (5) of Table 5.7.

Parameter	HD 104237 Aa	HD 104237 Ab
M $[M_\odot]$	2.37 ± 0.28	1.93 ± 0.29
Age [yr]	2×10^6 (van den Ancker et al. 1998)	
L $[L_\odot]$	$8.47^{+11.23}_{-3.00}$	$4.45^{+2.16}_{-1.36}$
R $[R_\odot]$	$3.21^{+1.07}_{-0.86}$	$2.61^{+0.34}_{-0.27}$
$T_{\rm eff}$ [K]	5500^{+380}_{-210}	5200^{+200}_{-190}
$\log(g)$	$3.80^{+0.07}_{-0.20}$	$3.89^{+0.02}_{-0.05}$
Age [yr]	4.28×10^6 (Column (3), Table 5.3)	
L $[L_\odot]$	$47.2^{+15.9}_{-33.3}$	$6.14^{+21.67}_{-3.57}$
R $[R_\odot]$	$2.38^{+0.49}_{-0.86}$	$2.52^{+0.80}_{-0.57}$
$T_{\rm eff}$ [K]	9800^{+2010}_{-3610}	5720^{+1550}_{-490}
$\log(g)$	$4.06^{+0.25}_{-0.32}$	$3.92^{+0.15}_{-0.18}$
Age [yr]	5.08×10^6 (Vioque et al. 2018, lower bound)	
L $[L_\odot]$	$32.6^{+19.6}_{-7.9}$	$10.1^{+21.6}_{-7.3}$
R $[R_\odot]$	$1.99^{+0.96}_{-0.22}$	$2.84^{+0.91}_{-0.69}$
$T_{\rm eff}$ [K]	9800^{+1890}_{-2290}	6110^{+3240}_{-730}
$\log(g)$	$4.21^{+0.15}_{-0.40}$	$3.81^{+0.30}_{-0.27}$
Age [yr]	5.48×10^6 (Vioque et al. 2018)	
L $[L_\odot]$	$40.1^{+11.7}_{-10.1}$	$12.8^{+9.6}_{-9.8}$
R $[R_\odot]$	$1.88^{+0.10}_{-0.58}$	$2.94^{+1.00}_{-1.02}$
$T_{\rm eff}$ [K]	10600^{+1040}_{-1990}	6360^{+2640}_{-910}
$\log(g)$	$4.26^{+0.11}_{-0.29}$	$3.78^{+0.30}_{-0.42}$
Age [yr]	5.75×10^6 (Vioque et al. 2018, upper bound)	
L $[L_\odot]$	$39.6^{+12.2}_{-13.2}$	$15.2^{+8.3}_{-12.1}$
R $[R_\odot]$	$1.77^{+0.37}_{-0.01}$	$2.95^{+1.00}_{-1.02}$
$T_{\rm eff}$ [K]	10900^{+760}_{-1950}	6640^{+2520}_{-1120}
$\log(g)$	$4.32^{+0.05}_{-0.22}$	$3.78^{+0.29}_{-0.42}$

as well as all closure phases and differential phases with an error of greater than 5°.

The Br γ line appears single-peaked at the GRAVITY high resolution, as indeed it did in the even higher-resolution AMBER data ($\mathcal{R} \sim 10000$) collected by Garcia et al. (2013). However, attempting to fit a single component to the Br γ results in a poor fit to the data at several epochs, especially the differential phases, which exhibit features which are not modelled by a single-component line model, such as S-shapes across the line (see Figure B.3 for an example). Much higher-resolution H α spectra ($\mathcal{R} > 30000$) did show a double-peaked profile (Acke et al. 2005), and since these two spectral lines are known to trace similar processes, it is reasonable to assume that there are at least two components of emission. Therefore, my initial models for the Br γ emission comprised two components. For all models, the Br γ fitting was performed on all epochs in Table 5.6, with the exception of 2019-02-26 and 2019-03-22, which had poor-quality flux data preventing reliable determination of $f_{\mathrm{Br}\gamma,\mathrm{i}}$.

5.5.1 Model 1: Science-agnostic, or 'Free' model

The first model was chosen to be agnostic in its treatment of the Br γ emission's origin. I included two closely-spaced components with wavelength ($\lambda_0 \pm \Delta\lambda$), where $\lambda_0 \equiv 2.1666\mu$m and $\Delta\lambda$ was a free parameter in the model. Each Br γ component was given its own spatial displacement ($x_{\mathrm{Br}\gamma,i}$, $y_{\mathrm{Br}\gamma,i}$), and their size was fixed to a Gaussian with FWHM 0.1 mas. The flux components were allowed to be fitted, $f_{\mathrm{Br}\gamma,i}$, as well as the Lorentzian FWHM, which was kept equal for both line components.

Results

The Br γ emission in the circumstellar region of HD 104237 A was found to be highly variable in both intensity and geometry between epochs. The model parameters corresponding to the best fit per epoch are shown in Table B.1, and the model fits and brightness distributions for each epoch can be found in Appendix B.1. The size of the Br γ-emitting regions was found to be unresolved, but their locations were spatially resolved at every epoch. The rapidly-changing orbit of the system results in the location of this emission changing on an epoch-by-epoch basis throughout the period.

I will summarise below the main characteristics of the emission at each epoch under Model 1. Multiple epochs show a characteristic signature of accretion onto the primary object. 2018-12-23 has two Br γ components emitting in the vicinity of the primary. 2019-01-14/15 show the clearest signs of all epochs of a two-component emission model. The spatial locations of the emissions are in the vicinity of the two stars, but not as close to them as in other epochs, especially that of 2019-01-15 (see Figure B.3). Since these two epochs are either side of periastron, the stars move extremely rapidly over a short space of time. However, the emission originates from similar locations regardless of this movement, implying that the emission is not necessarily entirely associated with the stars at these epochs.

2019-02-22/23 show Br γ emission originating near the primary star (from radii of $\lesssim$ 0.1 au), but also show emission originating from the location of the secondary component, suggesting that at these epochs both stars are accreting material from the disc.

The epoch 2019-03-10 shows two components located either side of the primary, similarly to the emission location in MWC 166 Aa (see Section 4.5), although the data is of poor quality.

The latter four epochs in Table B.1 were best fit by a single component. For 2019-03-11/12, the emission is associated with the primary component, while for 2019-03-15/16 it is located near the disc rim but not associated with either component.

5.5.2 Model 2: Fixing the Br γ emission to each component

A second model for the Br γ emission associated each component of the line emission with one of the stars. If there is emission associated with each component, the expected deviation from the line centre for each wing of the line will be:

$$\frac{\Delta\lambda}{\lambda} = \frac{v}{c}, \tag{5.1}$$

where v is the velocity of each component at the epoch in question. This can be easily calculated from the RV fit, since both masses $M_{1,2}$, the RV of the primary v_1, and the

Epoch	Phase	v_1 [km s^{-1}]	v_2 [km s^{-1}]	$\Delta\lambda_1$ [µm]	$\Delta\lambda_2$ [µm]
2018-12-23	0.864	9.2	20.2	6.65×10^{-5}	1.46×10^{-4}
2019-01-14	0.973	-0.8	32.5	-5.78×10^{-6}	2.35×10^{-4}
2019-01-15	0.023	-9.7	43.4	-7.01×10^{-5}	3.14×10^{-4}
2019-02-22	0.932	4.2	26.3	3.04×10^{-5}	1.90×10^{-4}
2019-02-23	0.982	-1.8	33.7	-1.30×10^{-5}	2.43×10^{-4}
2019-02-26	0.136	18.2	9.1	1.32×10^{-4}	6.60×10^{-5}
2019-03-10	0.740	14.7	13.4	1.06×10^{-4}	9.71×10^{-5}
2019-03-11	0.788	13.7	14.7	9.90×10^{-5}	1.06×10^{-4}
2019-03-12	0.838	10.8	18.2	7.81×10^{-5}	1.32×10^{-4}
2019-03-15	0.987	-2.9	35.0	-2.10×10^{-5}	2.53×10^{-4}
2019-03-16	0.032	-11.3	45.4	-8.17×10^{-5}	3.28×10^{-4}
2019-03-22	0.347	22.5	3.9	1.63×10^{-4}	2.78×10^{-5}

Table 5.9: Radial velocity and associated wavelength shift for each component of HD 104237 A.

velocity of the system's centre of mass V_0 are known:

$$v_2 = -\frac{M_1}{M_2}(v_1 - V_0) + V_0. \tag{5.2}$$

The wavelength shifts for each of the stars at each GRAVITY epoch are shown in Table 5.9. In order to investigate the relative contribution of each component to the Br γ emission, I fitted the data to a model which spatially fixed the position of each Br γ component to that of the stars, while also fixing the spectral location of the centre of each peak to $\lambda_0 + \Delta\lambda_i$, where $\lambda_0 \equiv 2.1666$ µm.

Results

The model described above had only three free parameters: the Br γ flux associated with each component, $f_{\mathrm{Br}\gamma,i}$, and the Lorentzian component FWHM, which was kept equal for both wings of the line. The results are shown in Table B.2, and a comparison of the Br γ fluxes of each model is plotted on Figure 5.8. A limitation of this model is in the interpretation that all Br γ flux is associated with accretion onto one of the two components, which is not necessarily the case, as previous work has highlighted the jet and magnetospheric interaction as other possible contributors to the observed Br γ. In comparison with the free model, the fixed model offers a worse fit at most epochs, as evidenced by the consistently larger χ^2 values. However, the relatively-unconstrained

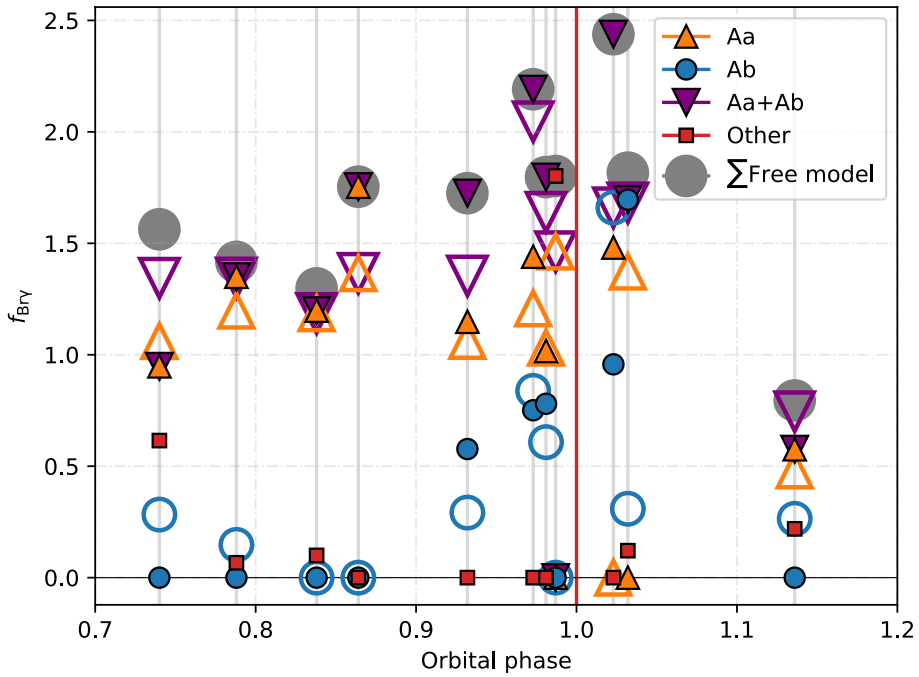

Figure 5.8: Comparison of Br γ flux for the two two-component models described in Section 5.5. The filled markers correspond to the Free model (Model 1), which included primary, secondary, and other emission. The grey points represent the sum of all emission in this model. The hollow points correspond to the Fixed model (Model 2), which only included primary and secondary emission. The red line shows the epoch of periastron passage.

nature of the free model can result in some difficulty in interpreting results, as mentioned in the previous section.

A comparison of the relative Br γ fluxes between Models 1 and 2 can be found in Figure 5.8, which shows that the two models generally agree with each other away from periastron, but have a larger difference close to it. The total line flux is very similar at all epochs in both models, but the distribution is different at certain epochs. It can be seen from the bottom panel that, in the 'free' model (Model 1), the secondary component is only associated with Br γ emission around periastron, with no emission otherwise. The epochs close to periastron where $f_{\mathrm{Br}\,\gamma,2} = 0$, 2019-03-15 and 2019-03-16, also have $f_{\mathrm{Br}\,\gamma,1} = 0$ for those epochs, while in the 'fixed' model, some of this flux was reassigned to the primary component.

Considering that the 'free' model is a better fit to the data, it can be reasoned that at these epochs the emission originates near to neither of the stars. That the two epochs are separated by just one day could support the idea that a different physical process is

responsible for the Br γ emission at those epochs.

5.5.3 Model 3: Three-component model

In light of the limitations of the models described above, I also constructed a third model combining them: two Br γ components fixed on the stars and with the appropriate $\Delta\lambda_{1,2}$, and one additional component free-floating both spatially and spectrally around the line with a wavelength $\lambda_0 + \Delta\lambda_3$. The flux of the spectral lines was constructed in the same way to the previous two models. The three-component model aimed to integrate both models described above into a flexible, yet physically sound description of the circumstellar environment.

Results

The results of the three-component fit are shown in Appendix B.3, and the relative Br γ flux ratios are plotted on the top panel of Figure B.23. A summary of the findings per epoch are given below.

It can be seen that the flux, $\Delta\lambda$ and spatial displacement of the third Br γ component can be degenerate in cases where it is $< 0.2\ f_1$, i.e. in the epochs 2019-01-14, 2019-03-11 and 2019-03-12, where both the spatial displacement and $\Delta\lambda_3$ are large. This is clearly a spurious result, and as such the position of the third component should not be seen as well-constrained in these epochs, which are marked with a (*) in Table B.4. These epochs are fit just as well by the fixed model.

2018-12-23: This epoch has the third Br γ component positioned such that it is equidistant with the secondary from the primary, in the opposite direction (see Figure B.13). Considering that there was no detected emission from the secondary in either Models 1 or 2, it is a fair assumption that this is an artefact arising from the code's attempt to fit the photocentre onto the primary component while forcing some emission from the secondary component. The relative fluxes of the emissive components support this hypothesis, and as such Model 3 was discounted for this epoch.

The differential phases in epoch 2019-01-15 are poorly fit by Model 3 (see Figure B.15), indicating that the emission has at least two components not associated with either star. The equivalent epoch under Model 1 (Figure B.3) shows this by locating the

emission components to regions separated from both stars by $\sim 90°$. Further modelling which included a fourth component returned results very similar to those of Model 1, with both stars having their flux component zero-weighted.

The third component in the epochs 2019-02-22, 2019-03-15, 2019-03-16, is located at a similar position in the inner rim, and provides a good fit to the data without appearing to be an artefact of the code, since emission originating from roughly the same area was seen in Model 1. In these epochs, the third emissive component has a larger fraction of the flux than the stars.

5.5.4 Comparison of Br γ emission models

The main results of the three models can be found in Table 5.10. Each of the three models provided the best fit to the data at certain epochs, with the best model indicated by parentheses in the second column of the table. This suggests that HD 104237 Aa is the sole source of the Br γ emission in the epochs 2018-12-23, 2019-01-14, 2019-03-11, 2019-03-12. The emission originates from both stars in the epoch 2019-03-10, without any circumstellar emission. The epoch 2019-02-23 has the secondary emitting as well as a circumstellar component. In the epochs 2019-02-22, 2019-03-15, 2019-03-16, both stars emit as well as a third component not associated with either object . For the epoch 2019-01-15 there is emission only associated with circumstellar components at more than one location, and no emission from the stars. Due to the difficulty in interpreting this, I have excluded this epoch from Table 5.10 and Figure 5.9. In the following section, I will discuss potential origins for the Br γ emission.

5.6 Nature of the Br γ emission

5.6.1 Jet

Garcia et al. (2013) posited two scenarios for the origin of the Br γ emission in HD 104237 A. The first was a common origin with the observed Ly α jet oriented at a PA of $\theta_{\rm jet} = 332°$ (Grady et al. 2004). In this scenario, the Br γ emission would be tracing a knot of material ejected from the inner regions of the system along the jet axis. However, while this model fitted the data well, the knot was found to have zero proper motion, incompatible

Table 5.10: Model comparison for all epochs. I have listed the components of emission as associated with either the primary, secondary, or extended. The flux of extended emission which was poorly-constrained spatially in Model 3 is listed, but not its separation or position angle. Models which provide a much worse fit or lack a physical justification are not included in this table.

Epoch	Model	$f_{\mathrm{Br}\gamma,\mathrm{Aa}}$	$f_{\mathrm{Br}\gamma,\mathrm{Ab}}$	$f_{\mathrm{Br}\gamma,\mathrm{ext}}$	$\rho_{\mathrm{Br}\gamma,\mathrm{ext}}$ [mas]	$\theta_{\mathrm{Br}\gamma,\mathrm{ext}}$ [°]	FWHM [nm]	χ^2
2018-12-23	(1)	1.75 ± 0.12	-	-	-	-	0.73 ± 0.02	3.21
	2	1.38 ± 0.03	-	-	-	-	1.01 ± 0.02	3.61
2019-01-14	(1)	1.11 ± 0.05	1.05 ± 0.05	-	-	-	0.89 ± 0.02	3.58
	2	1.23 ± 0.02	0.83 ± 0.02	-	-	-	0.86 ± 0.01	3.69
	3	1.23 ± 0.02	0.78 ± 0.02	0.16 ± 0.01	-	-	0.91 ± 0.01	4.27
2019-02-22	1	1.09 ± 0.04	0.58 ± 0.05	-	-	-	1.07 ± 0.02	18.37
	2	1.06 ± 0.03	0.29 ± 0.02	-	-	-	0.84 ± 0.03	22.72
	(3)	0.40 ± 0.09	0.54 ± 0.03	0.79 ± 0.07	1.18 ± 0.07	319.1 ± 3.1	1.01 ± 0.03	18.71
2019-02-23	(1)	1.07 ± 0.03	0.80 ± 0.02	-	-	-	1.18 ± 0.04	18.89
	2	1.03 ± 0.05	0.61 ± 0.04	-	-	-	0.84 ± 0.04	36.20
	3	-	0.80 ± 0.03	1.00 ± 0.03	0.92 ± 0.03	289.6 ± 2.4	1.26 ± 0.04	31.08
2019-03-10	(2)	1.06 ± 0.04	0.28 ± 0.03	-	-	-	1.12 ± 0.04	3.33
	3	1.04 ± 2.23	0.38 ± 0.05	-	-	-	1.10 ± 0.01	3.48
2019-03-11	1	1.37 ± 0.01	-	-	-	-	1.16 ± 0.01	2.63
	2	1.20 ± 0.03	0.15 ± 0.02	-	-	-	1.14 ± 0.03	2.72
	(3)	1.33 ± 0.04	-	0.16 ± 0.03	-	-	1.16 ± 0.03	2.55
2019-03-12	1	1.22 ± 0.01	-	-	-	-	1.15 ± 0.01	3.69
	2	1.19 ± 0.03	-	-	-	-	1.14 ± 0.03	3.55
	(3)	1.19 ± 0.02	-	0.08 ± 0.01	-	-	1.08 ± 0.02	3.31
2019-03-15	1	-	-	1.52 ± 0.01	1.40 ± 0.02	335.5 ± 1.5	1.27 ± 0.01	4.46
	2	1.46 ± 0.03	-	-	-	-	1.27 ± 0.02	5.40
	(3)	0.21 ± 0.09	0.52 ± 0.05	1.02 ± 0.06	2.28 ± 0.11	324.8 ± 2.3	1.08 ± 0.02	3.71
2019-03-16	1	-	-	1.72 ± 0.01	1.45 ± 0.03	320.6 ± 1.4	1.13 ± 0.01	5.69
	2	1.37 ± 0.03	9.31 ± 0.03	-	-	-	1.05 ± 0.02	6.39
	(3)	0.15 ± 0.10	0.46 ± 0.04	1.38 ± 0.08	2.05 ± 0.10	311.4 ± 2.8	0.91 ± 0.02	4.13

with both theory and the measurements made by Grady et al. (2004), who reported a proper motion in the hundreds of kilometres per second. The jet scenario was therefore rejected despite its low χ^2 due to a lack of physical justification for its properties (Garcia et al. 2013).

There were few epochs in the GRAVITY data which provided a potential signature of such jet emission. When modelled with Model 3, the epochs 2019-02-22, 2019-03-15, 2019-03-16 do show tentative signs of emission originating from the dust inner rim and in a direction which is consistent with previous observations of the jet in Ly α, as shown in Table 5.10. These epochs are all also very close to periastron, which is where the jet is predicted to be at its strongest. However, there is a lack of relative movement of this emission between the latter two epochs, observed on two consecutive days. This is similar to the finding by Garcia et al. (2013), and therefore I cannot confidently say that this emission is associated with the jet.

5.6.2 Magnetospheric accretion

The second scenario for the Br γ in HD 104237 A was emission originating from accretion shocks on the two stars, which Garcia et al. (2013) concluded was a more likely origin. The results in Section 5.5 support this hypothesis at most epochs, given the very small displacement from the primary of at least one component of the Br γ emission. Looking at the epochs individually, it is clear that the emission is highly variable by orbital phase, as was also found by Garcia et al. (2013).

My results can be used to estimate the relative fraction of Br γ emitted by each component. The accretion luminosity for HD 104237 A was estimated by Garcia Lopez et al. (2006) to be $L_{\rm acc} \sim 2.7\,L_\odot$ using the relation between $L_{\rm Br\gamma}$ and $L_{\rm acc}$ developed by Calvet et al. (2004):

$$\log(L_{\rm acc}/L_\odot) = -0.7 + 0.9(\log L_{\rm Br\gamma}/L_\odot + 4), \tag{5.3}$$

furthermore determining its accretion rate to be $\dot{M} \sim 3.55 \times 10^{-8}\,M_\odot$. According to the above equation, $L_{\rm Br\gamma} \sim 1.82 \times 10^{-3}\,L_\odot$. However, it is clear from my data that the total Br γ flux, $\sum f_{\rm Br\gamma}$, is also variable by epoch. I therefore took the weighted average of the total flux from the best-fit models corresponding to the values in Table 5.10, $\langle \sum f_{\rm Br\gamma} \rangle = 1.49 \pm 0.02$, and weighted the Br γ luminosities at each epoch t by this mean flux, such that:

$$L_{{\rm Br\gamma},t} = L_{\rm Br\gamma} \frac{\sum f_{{\rm Br\gamma},t}}{\langle \sum f_{\rm Br\gamma} \rangle}. \tag{5.4}$$

I then estimated a mass accretion rate for each component of HD 104237 A by using Equation 1.10 ($L_{\rm acc} = GM_*\dot{M}/R_*$), and the stellar parameters corresponding to the 4.28×10^6 yr model in Table 5.8. The full results for the individual models are given in Apperndix B, while the results for the best models at each epoch are found in Table 5.11, which I will discuss below.

As can be seen on Figure 5.9, the accretion rates of the two objects can be divided into two main sections. At orbital phases < 0.90, the primary appears to be responsible for the vast majority of the Br γ emission, and consequently dominates the accretion. In this 'quiescent' part of the orbit, the weighted mean of the primary component's accretion rate is $\dot{M}_1 = (7.6 \pm 1.1) \times 10^{-8}\,M_\odot\,{\rm yr}^{-1}$. The secondary component has a visible

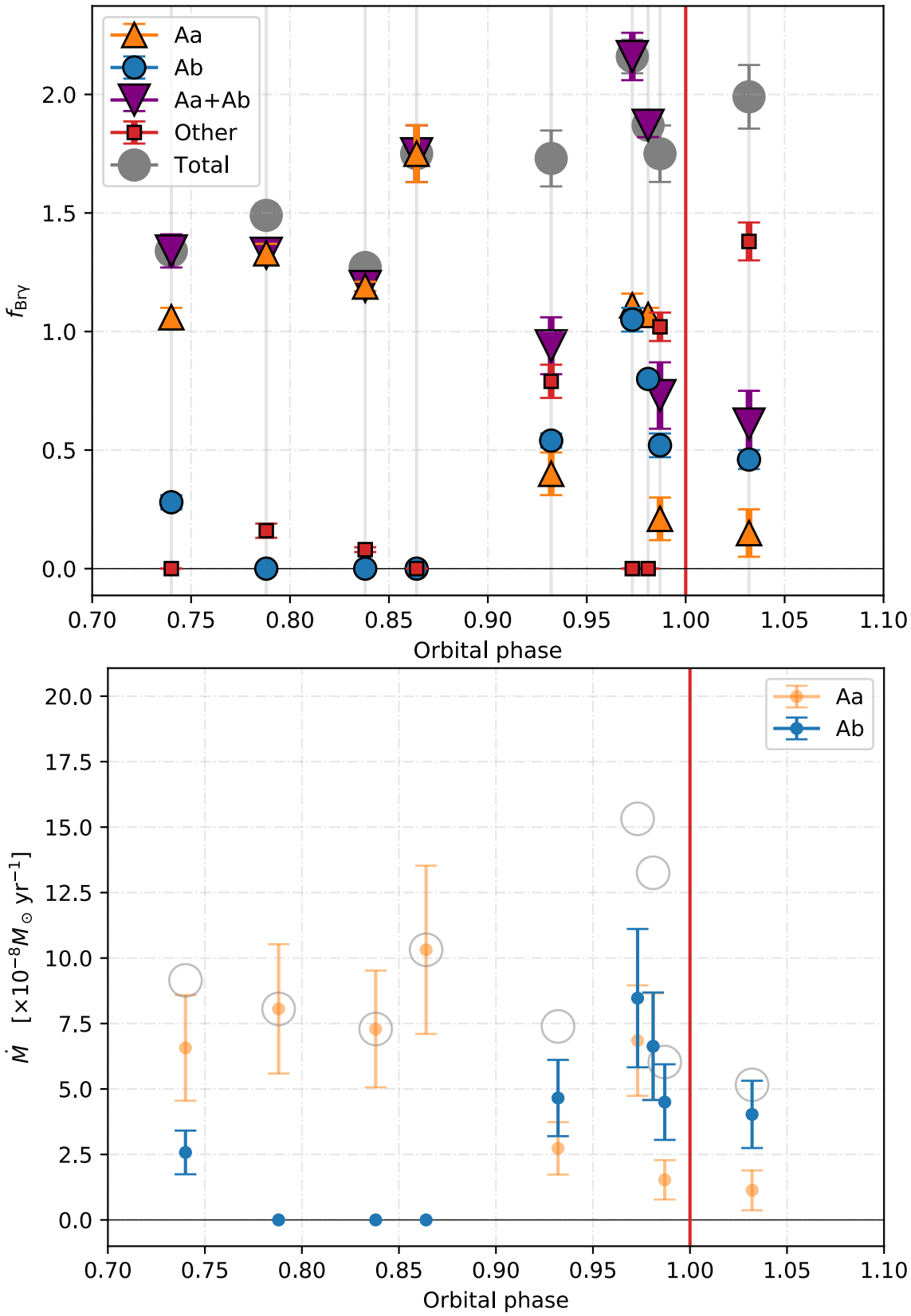

Figure 5.9: Graphical representation of Table 5.11. **Top panel**: Br γ flux for the best-fit models at each epoch, for each component and in total, as a fraction of f_1. **Bottom panel**: Associated accretion rates for each component of HD 104237 A, with the total represented by the grey circles. The red line shows the epoch of periastron passage.

Table 5.11: Relative Br γ luminosities and accretion rates for each component, based on the best-fit model per epoch from Table 5.10.

Epoch	$L_{\mathrm{Br}\gamma,1}$ $[10^{-4}\,L_\odot]$	$L_{\mathrm{Br}\gamma,2}$ $[10^{-4}\,L_\odot]$	$L_{\mathrm{Br}\gamma,\mathrm{ext}}$ $[10^{-4}\,L_\odot]$	$L_{\mathrm{acc},1}$ $[L_\odot]$	$L_{\mathrm{acc},2}$ $[L_\odot]$	$\dot{M}_1$ $[10^{-8}\,M_\odot/\mathrm{yr}]$	$\dot{M}_2$ $[10^{-8}\,M_\odot/\mathrm{yr}]$
2018-12-23	21.9 ± 1.5	-	-	3.21 ± 0.20	-	10.3 ± 3.2	-
2019-01-14	13.9 ± 0.6	13.2 ± 0.6	-	2.13 ± 0.09	2.03 ± 0.09	6.85 ± 2.11	8.47 ± 2.64
2019-02-22	5.01 ± 1.13	6.77 ± 0.38	9.90 ± 0.88	0.85 ± 0.17	1.12 ± 0.06	2.73 ± 1.00	4.66 ± 1.46
2019-02-23	13.4 ± 0.4	10.0 ± 0.3	-	2.06 ± 0.05	1.59 ± 0.04	6.63 ± 2.03	6.63 ± 2.05
2019-03-10	13.3 ± 0.5	3.51 ± 0.38	-	2.05 ± 0.07	0.62 ± 0.06	6.57 ± 2.02	2.58 ± 0.83
2019-03-11	16.7 ± 0.5	-	2.01 ± 0.38	2.51 ± 0.07	-	8.06 ± 2.47	-
2019-03-12	14.9 ± 0.3	-	1.00 ± 0.13	2.27 ± 0.03	-	7.29 ± 2.23	-
2019-03-15	2.63 ± 1.13	6.52 ± 0.63	12.8 ± 0.8	0.48 ± 0.19	1.08 ± 0.09	1.53 ± 0.75	4.50 ± 1.44
2019-03-16	1.88 ± 1.25	5.77 ± 0.50	17.3 ± 1.0	0.35 ± 0.21	0.97 ± 0.08	1.13 ± 0.76	4.03 ± 1.28

spike in accretion rate around periastron, accreting at a rate exceeding the primary. The weighted mean of the accretion rates of the two components in this part of the orbit are $\dot{M}_1 = (2.1 \pm 0.4) \times 10^{-8}\,M_\odot\,\mathrm{yr}^{-1}$ and $\dot{M}_2 = (4.9 \pm 0.7) \times 10^{-8}\,M_\odot\,\mathrm{yr}^{-1}$. The accretion rate calculated by Garcia Lopez et al. (2006) lies roughly halfway between that of the primary and the secondary around periastron. The discrepancies are largely due to the different stellar parameters used – the literature value used $L_* = 6\,L_\odot$, $M_* = 2\,M_\odot$, which are much closer to my derived values for the secondary component. Fairlamb et al. (2015) used measurements of HD 104237 A's UV Balmer excess to find a value of $\dot{M} \sim 2.1 \times 10^{-7}\,M_\odot$, an order of magnitude larger than that found by Garcia Lopez et al. (2006) and more similar to the total accretion rate which I derived.

This spike in the accretion onto the secondary component around periastron passage is predicted by theory (Dunhill et al. 2015). Garcia et al. (2013) observed an increase in the overall Br γ emission at periastron passage and, under the assumption that Br γ emission localised on the stars is directly caused by magnetospheric accretion, I have shown that this increase is primarily associated with the secondary component.

5.7 Future work and outlook

The continuum and line fitting described in this chapter both use relatively simple models for the system. For the continuum modelling, this was because of the difficulty in combining epochs to increase the available baselines. A future goal for the continuum modelling of this system is to incorporate dynamic fitting of data with positions (x_2, y_2) dependent on the derived orbital fit, in order to increase SNR by modelling multiple epochs simulta-

neously. However, due to the rapidly-changing circumstellar environment, as well as the variability of the stars, this would only have limited success without a model of how the circumstellar emission changes over time.

The Br γ modelling undertaken in this chapter shows that the emission is variable both in intensity and spatial extent. Whilst modelling magnetospheric accretion was relatively straightforward, for certain epochs the modelling under this assumption was not reflected in the data, as seen in Figure B.15. A potential source of Br γ emission for these epochs is material in the process of being channelled through field lines onto the stars, as the simulation in Figure 5.1 shows. In such a case, the emission could be coming from a region large enough to be spatially-resolved, and as such difficult to fit with the small Gaussians which I have used in all my line models. The epoch for which this is most likely is 2019-01-15, but at many other epochs emission appears to be originating in the vicinity of the stars but outside the radius where magnetospheric accretion is likely. Future work will attempt to fit these epochs with spatially-resolved accretion streamers to test this hypothesis.

This is clearly a fascinating system which merits much more observation throughout the entire orbit. The rapid evolution of the circumbinary environment, as well as the variability of the stars, would make this system an excellent candidate for continuous observation at high spectral resolution over at least a month on a variety of baseline lengths.

Chapter 6

Conclusions

In this thesis I have described some of the challenges inherent in the study of close binary YSOs, as well as the recent and ongoing advances which are helping us to pull back the curtain. The aim of my PhD was to demonstrate the power of near-infrared interferometry to push our understanding of close binary YSOs beyond the current paradigm. The two objects which I studied in detail over the course of my PhD are very different and yet show striking similarities. I will present the conclusions I have drawn from each, and then place them in the broader context of the field.

6.1 MWC 166 A

In Chapter 4 I presented GRAVITY, PIONIER, and MIRC-X observations of MWC 166 A that resolve the system in the NIR H band and K band with milliarcsecond resolution. I derived the astrometry of the system at 13 epochs and calculated a first fully three-dimensional orbital solution for the system. This orbit differs substantially from the RV-only orbits of Corporon and Lagrange (1999) and Pogodin et al. (2006), having a period twice as long. I have subsequently constrained the dynamical system mass ($17.1 \pm 2.7\,M_{\odot}$ for the photometric distance of 990 ± 50 pc found by Kaltcheva and Hilditch 2000) and the distance of the system, with my results excluding previous parallax measurements of the distance where $d < 500$ pc. Furthermore, I have calculated, for the first time, the individual masses of the primary and secondary components of the system, which I find to

be $M_1 = (12.19 \pm 2.18)\,M_\odot$ and $M_2 = (4.90 \pm 0.52)\,M_\odot$, respectively. I also find estimates for the other fundamental stellar parameters based on quadratic isochrone interpolation.

Furthermore, I found evidence for circumstellar emission, both in the dust continuum and in the He I and Br γ spectral lines, although they have different geometries. The geometry of the extended emission in the continuum is not well constrained, with the best fit corresponding to an over-resolved background halo. The variability in the continuum emission between epochs may be an indication of physical variability in the quantity of circumstellar dust, or it might indicate that the geometry is more complex than assumed in my model. Characterising it in more detail will require additional interferometric observations, ideally at mid-infrared wavelengths.

On the other hand, the geometry of the He I and Br γ line emission is well constrained by my observations. My models show emission in these lines to be localised around the primary, where the redshifted and blueshifted wings are spatially displaced, consistent with gas in a circumprimary disc. The large spatial extent of the line-emitting regions ($11.5\,R_1$ for Brγ, $10.5\,R_1$ for He I) and stable PA orientation are inconsistent with an origin in magnetospheric accretion or boundary-layer accretion, but support the hypothesis that the line emission is tracing an ionised gas disc. This gas disc might either be fed by mass infall from outside the binary or represent a decretion disc forming through mass loss from the primary.

Finally, I constrain the age of the system to $(7 \pm 2) \times 10^5$ yr, based on the measured flux ratio of the components. I find that the primary is a main-sequence Be star, while the secondary is a Herbig Be object still in the process of gravitational contraction onto the main sequence.

6.2 HD 104237 A

In this chapter, GRAVITY and PIONIER observations of HD 104237 A were presented. Archival PIONIER observations were used to find a three-dimensional orbital solution, in agreement with the existing solution by Garcia et al. (2013). Using the most recent distance estimate of $d = 106.5^{+0.6}_{-0.5}$ pc, I constrained the masses of the individual components, $M_1 = (2.37 \pm 0.28)\,M_\odot$, $M_2 = (1.93 \pm 0.29)\,M_\odot$. Stellar parameters were then calculated for a variety of ages, with an age of ~ 4.3 Myr being the best fit to the flux ratio of the components as derived from the interferometry. This corresponds to both objects being in the final stage of pre-main-sequence evolution.

I subsequently used the orbital fit to model the circumstellar environment in the GRAVITY observations by allowing the stellar positions to be fixed, when they otherwise would not have been resolved. The circumstellar continuum emission was found to take the form of a circumbinary disc with $D_{\rm in} \sim 5$ mas, in agreement with the findings of Tatulli et al. (2007), Kraus et al. (2008) and Garcia et al. (2013). The Br γ line emission originating from the system was found to be variable both in intensity and spatial location, with signs of accretion onto both the primary and secondary star, depending on the epoch of observation, with the secondary component increasing in relative flux close to periastron, in line with the predictions of SPH simulations (e.g. Dunhill et al. 2015). I have consequently demonstrated that the increase in Br γ flux at periastron is associated with the secondary component. There is also tentative evidence of emission not associated with either star at several epochs, although the origin is unclear from the observations presented. There is a possibility of the emission being linked with the Ly α jet found by Grady et al. (2004) at several epochs, although the emission could also be tracing accretion streamers within the cavity of the continuum emission.

6.3 Final conclusions

There still are many mysteries inherent in our understanding of the birth and evolution of stars which can be solved with long-baseline interferometry. In Chapters 4 and 5 I have shown that binary YSOs are very dynamic objects over a range of masses, and that geometric modelling with near-infrared interferometry is able to spatially resolve the

regions closest to the stars in young binary systems, both in the continuum and across spectral lines. Thanks to the resolving power of long-baseline interferometers, even simple models can reveal secrets about stellar formation and evolution unattainable with single dish telescopes, and provide ways of calibrating and testing models of stellar formation and evolution. As new and exciting facilities open worldwide which can provide observations simultaneously in multiple spectral bands, at higher spectral resolutions and on longer baselines, the techniques described in this thesis will come to be used for more and more discoveries.

The Appendices

Appendix A

Full set of PMOIRED line models for MWC 166 A

Presented below are the full set of He I and Br γ line models for the four GRAVITY epochs, discussed in Sections 4.3.2 and 4.5. The figures comprise nine panels, laid out equivalently to those in Figure 4.10.

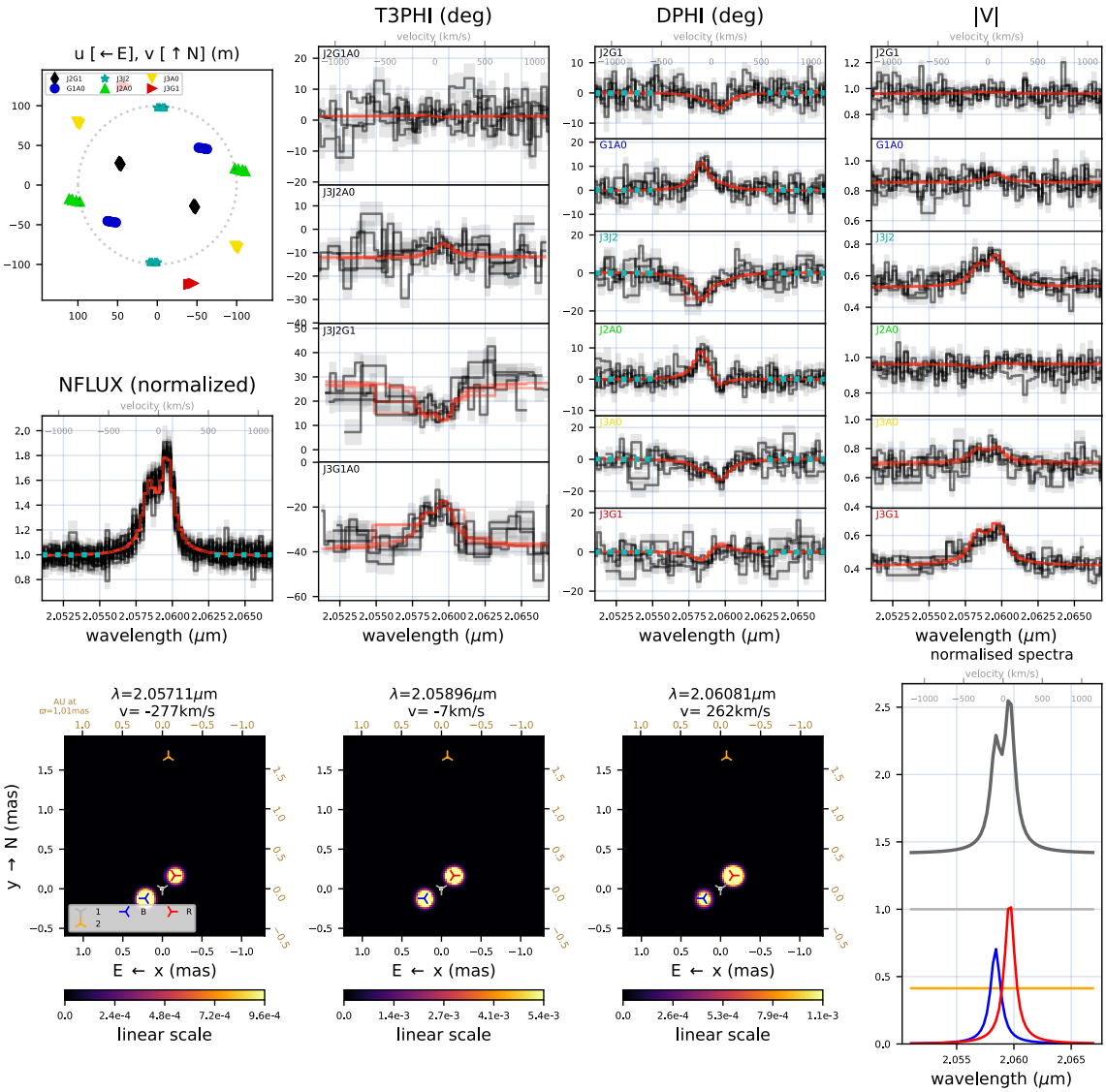

Figure A.1: 2017-03-14, He I

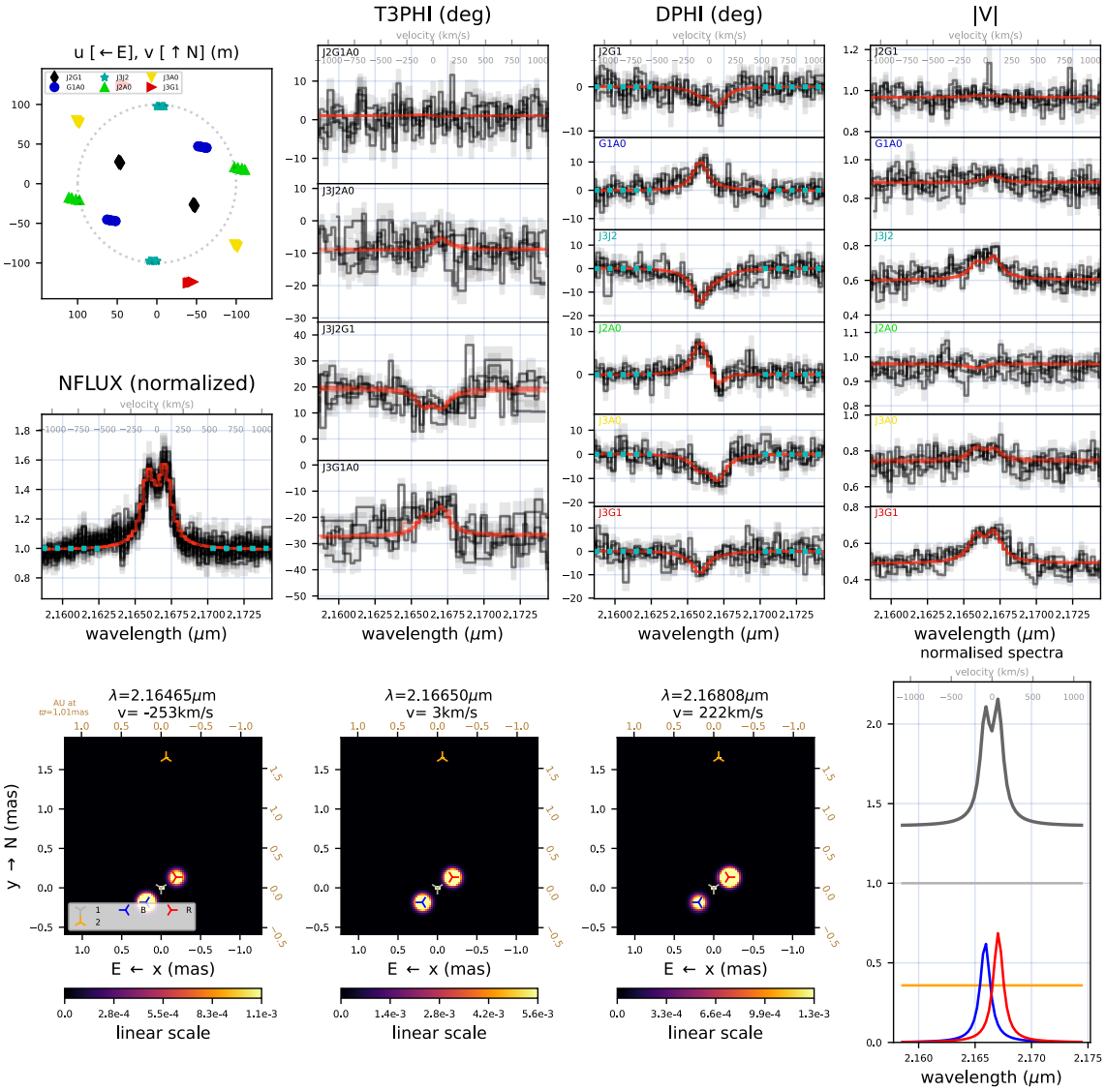

Figure A.2: 2017-03-14, Br γ

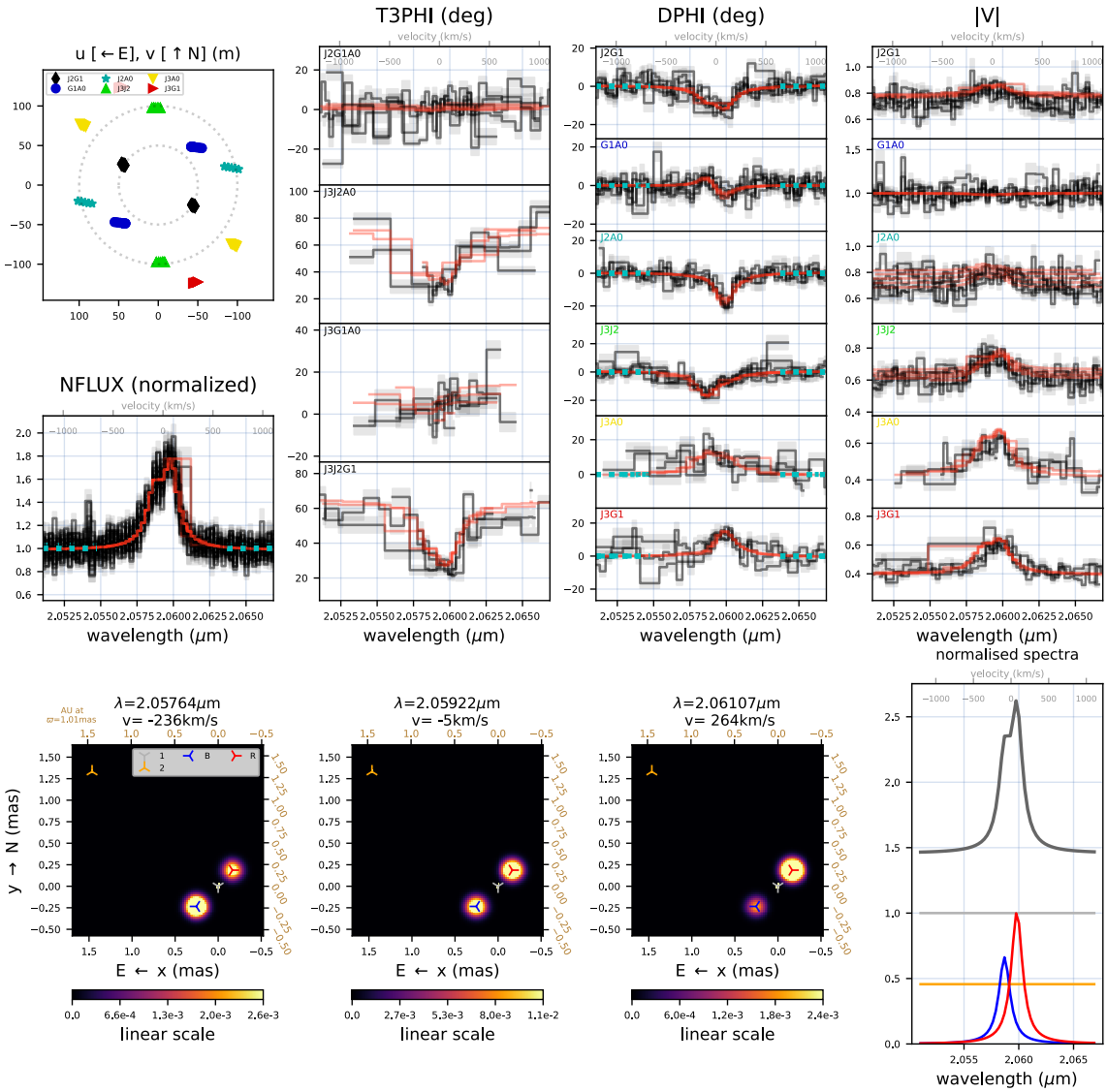

Figure A.3: 2017-04-27, He I

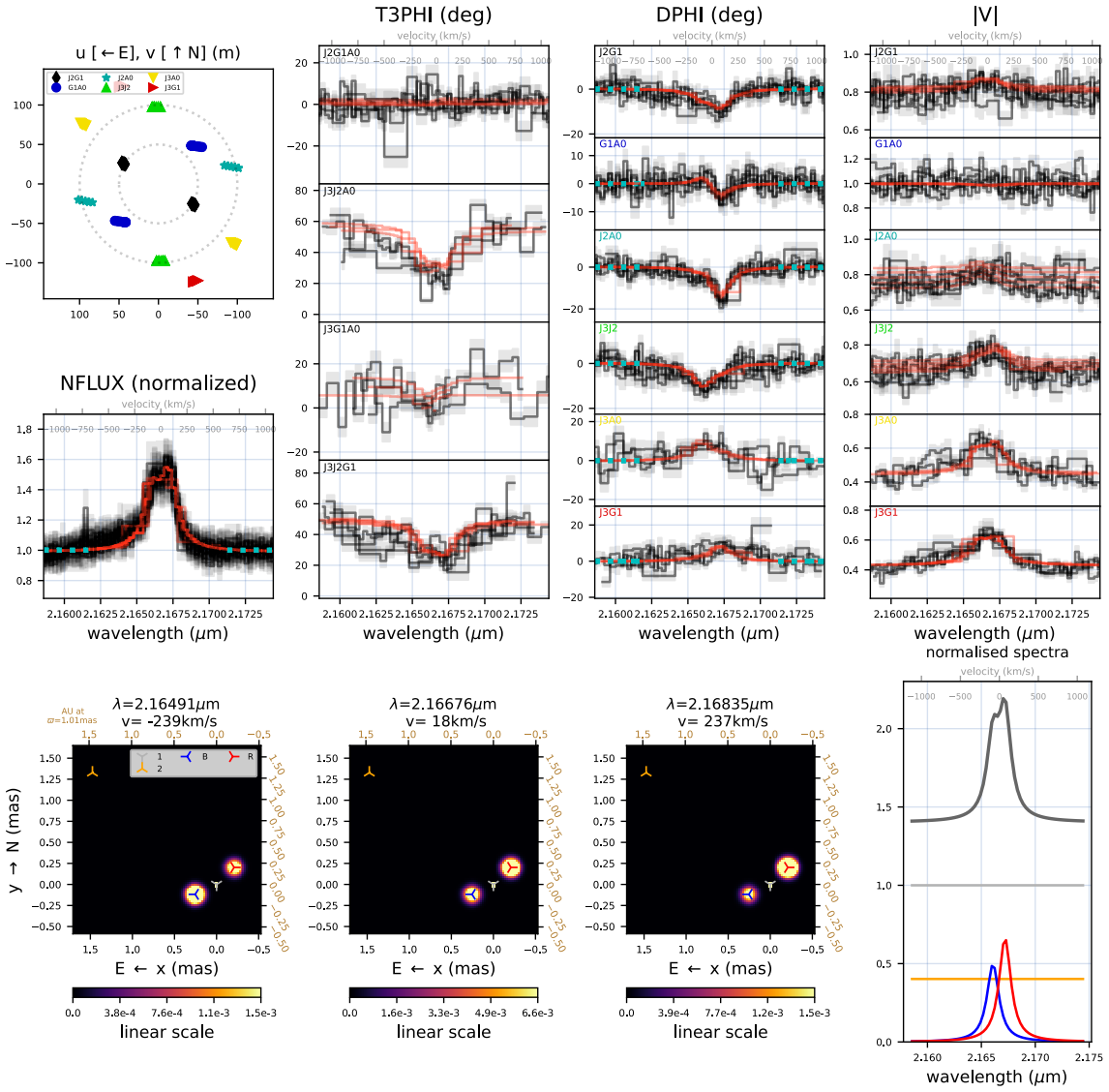

Figure A.4: 2017-04-27, Br γ

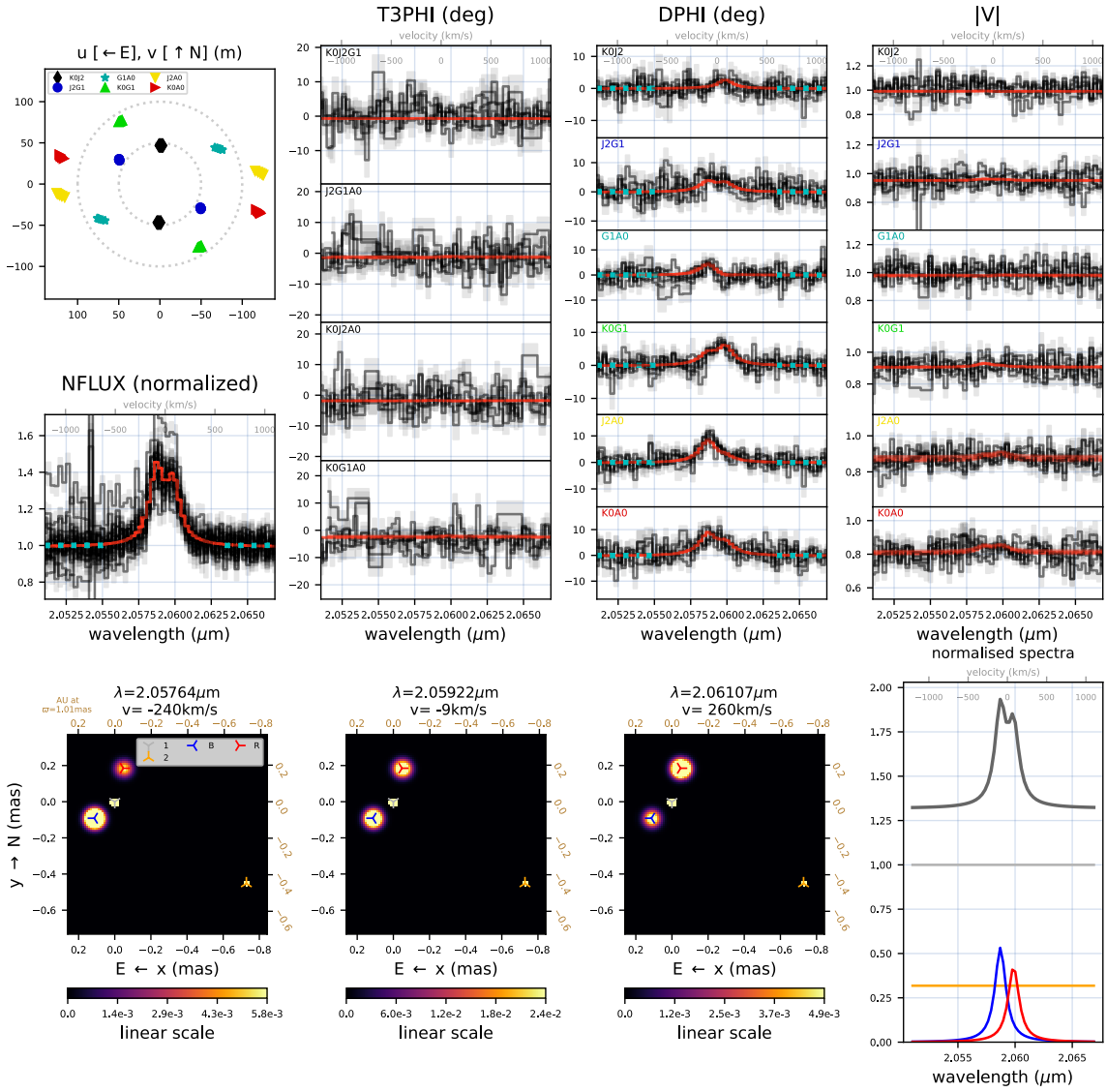

Figure A.5: 2018-01-11, He I

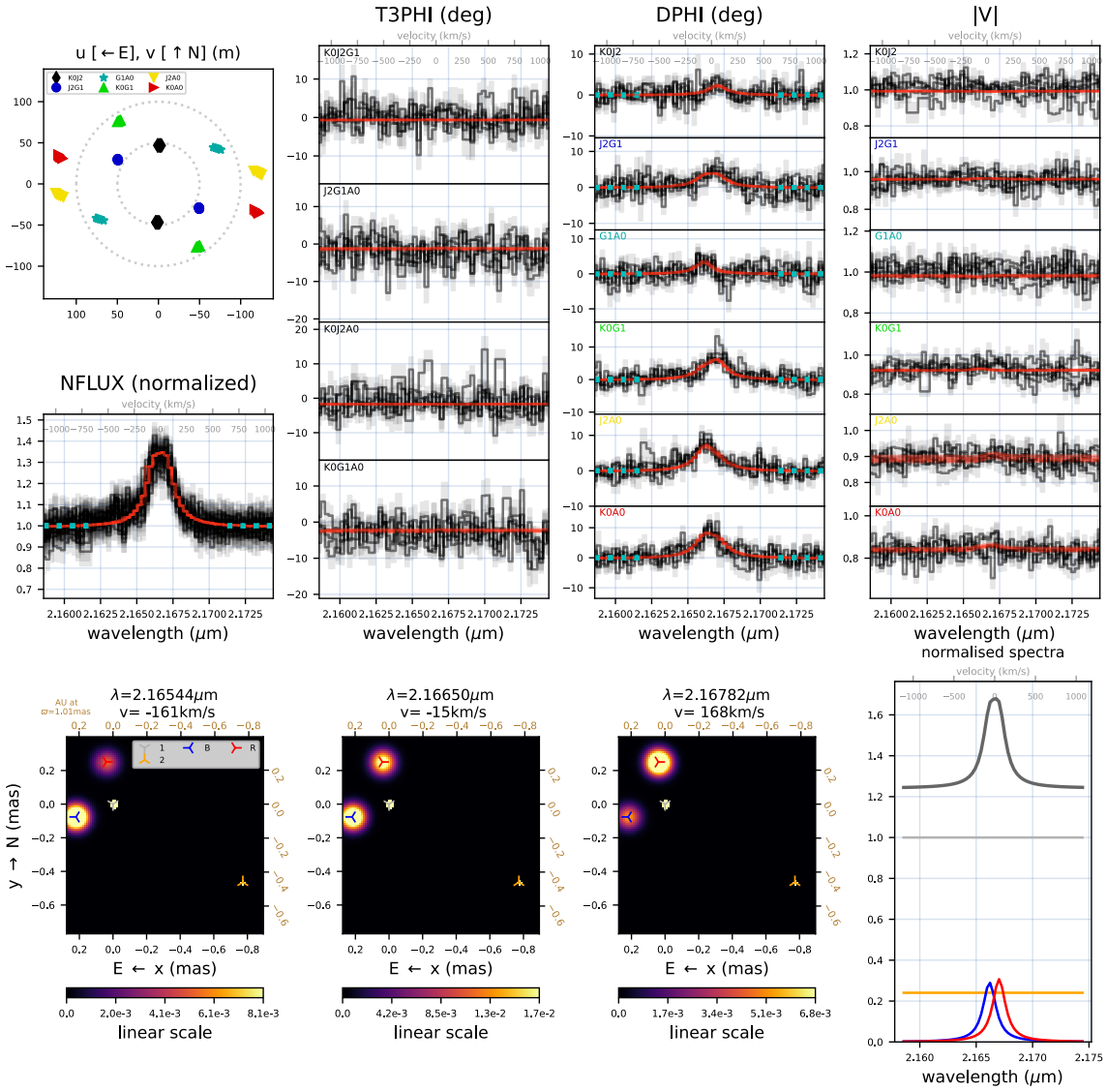

Figure A.6: 2018-01-11, Br γ

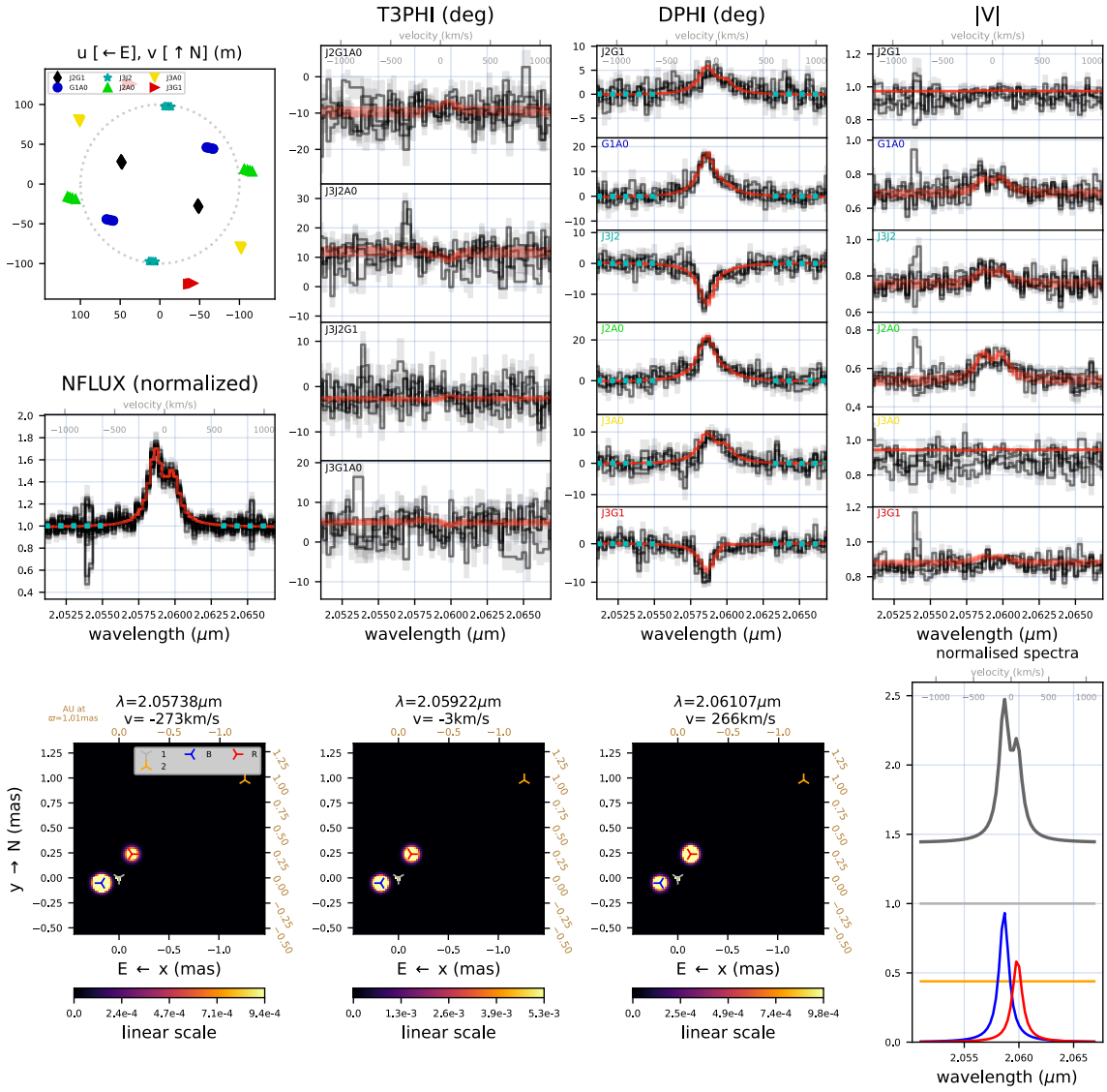

Figure A.7: 2018-02-06, He I

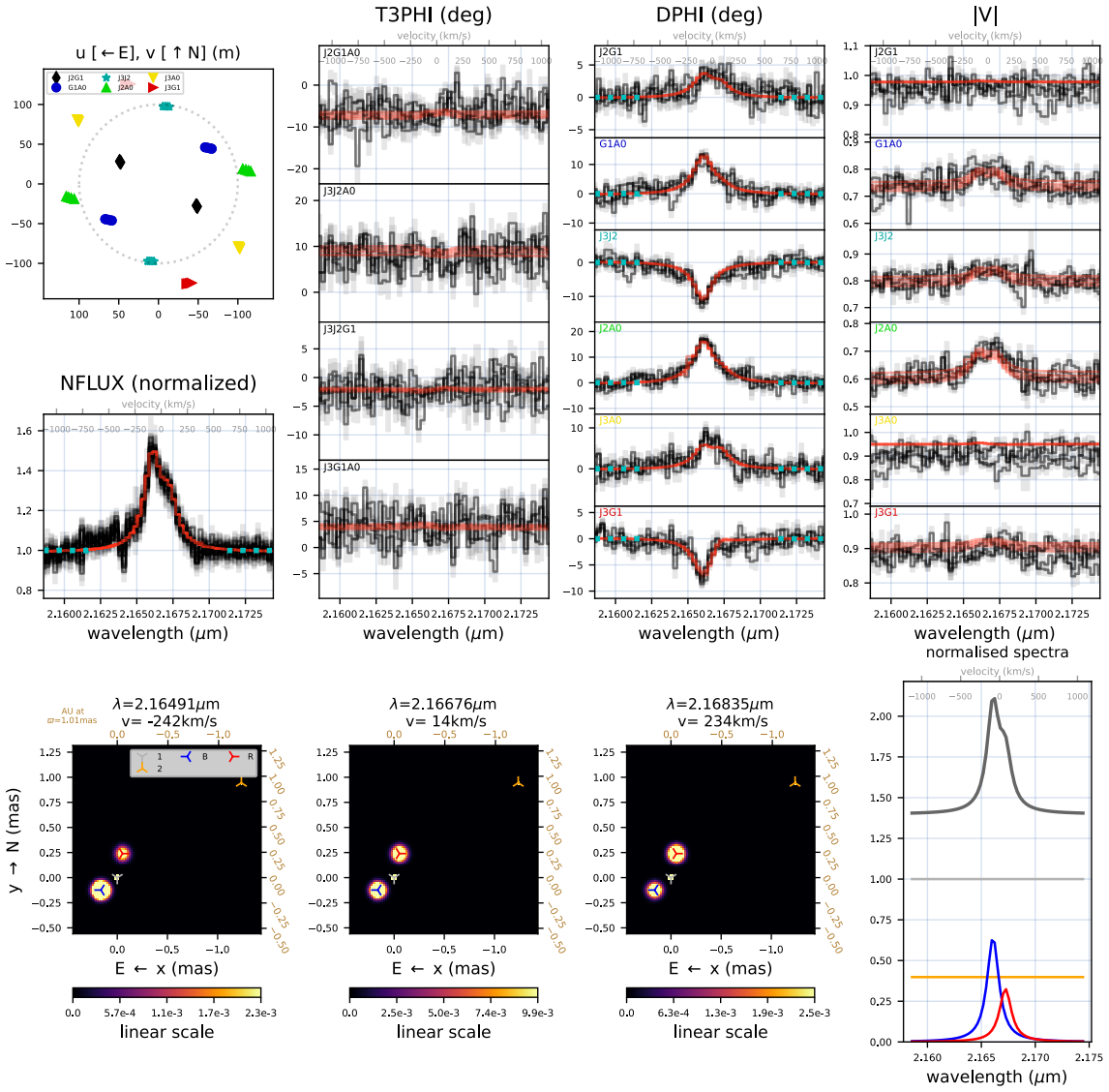

Figure A.8: 2018-02-06, Br γ

Appendix B

PMOIRED line models for HD 104237 A

B.1 Model 1: 'Free' model

Presented below are the set of Br γ line models for the HD 104237 A described in Section 5.5.1, as well as associated results. The figures comprise seven panels, laid out equivalently to those in Section A.

B.1.1 Models

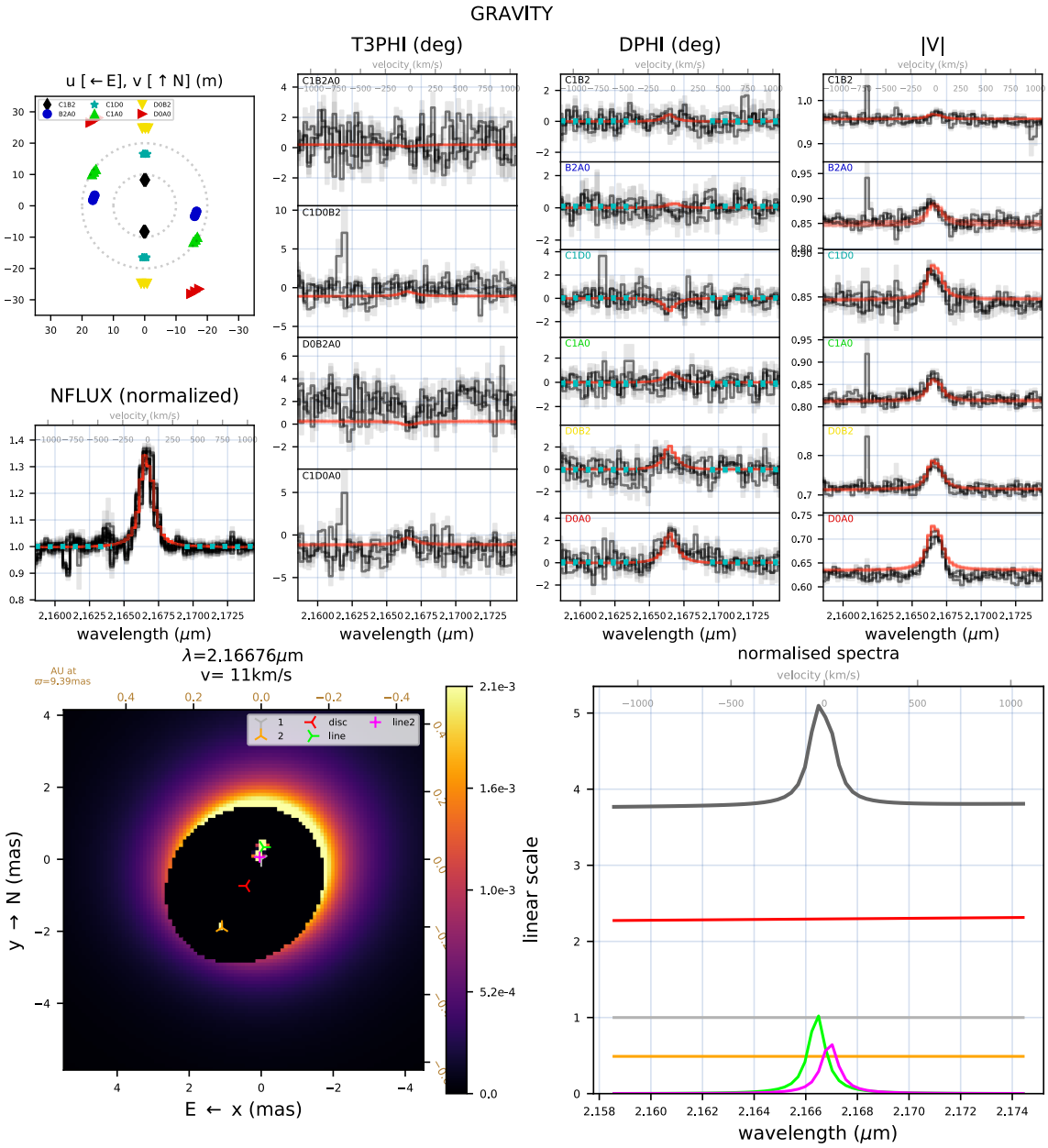

Figure B.1: 2018-12-23.

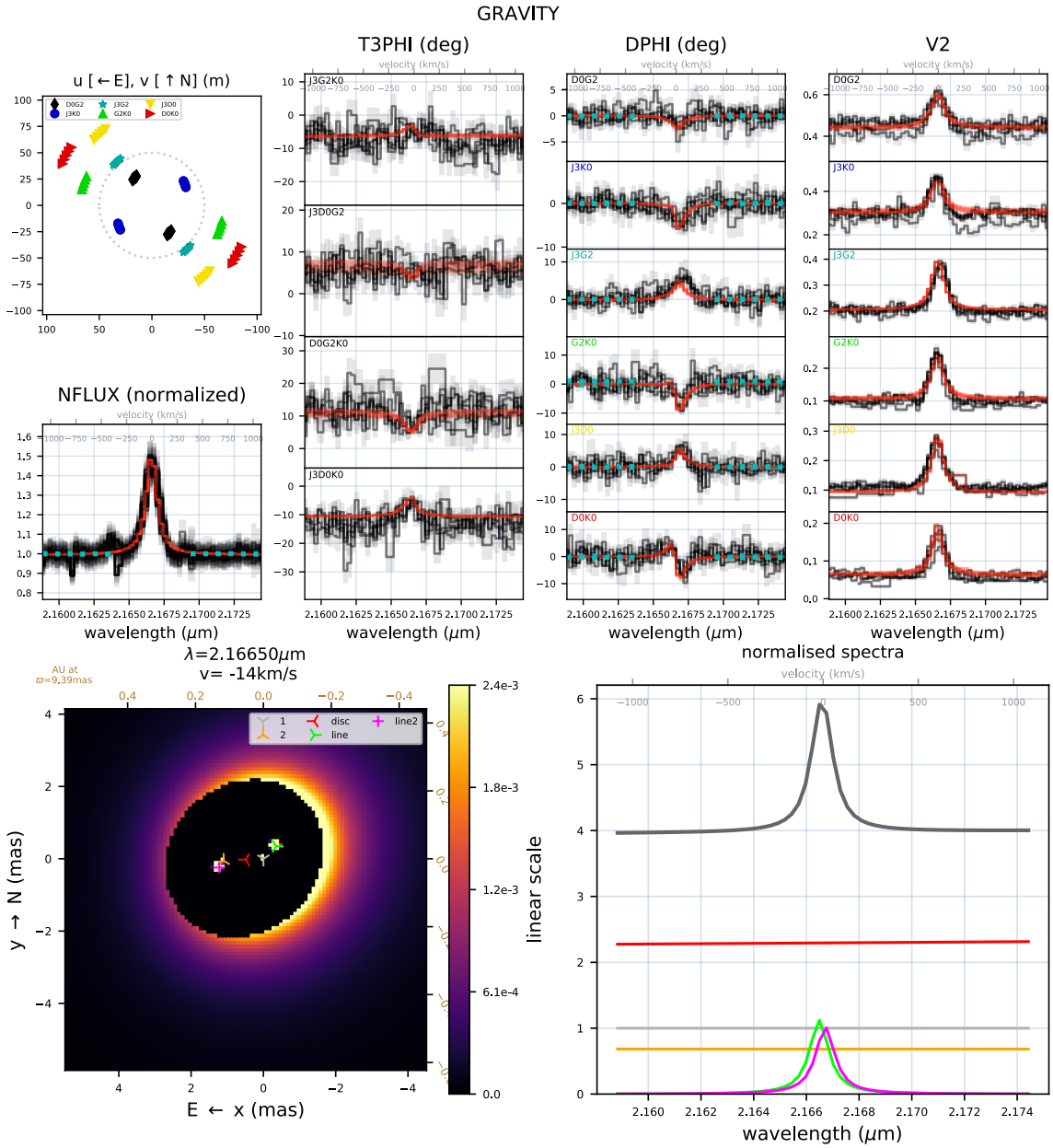

Figure B.2: 2019-01-14.

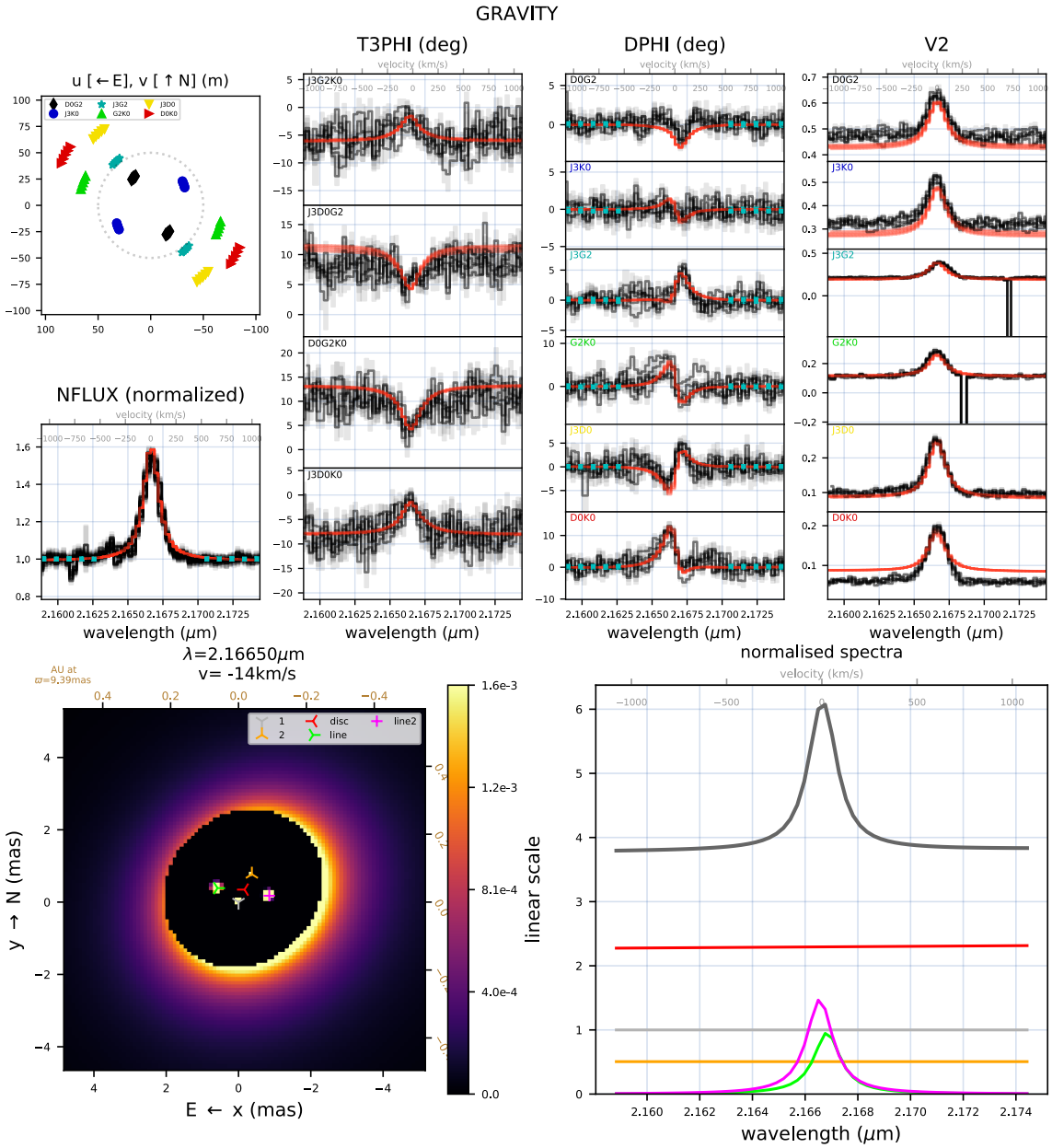

Figure B.3: 2019-01-15.

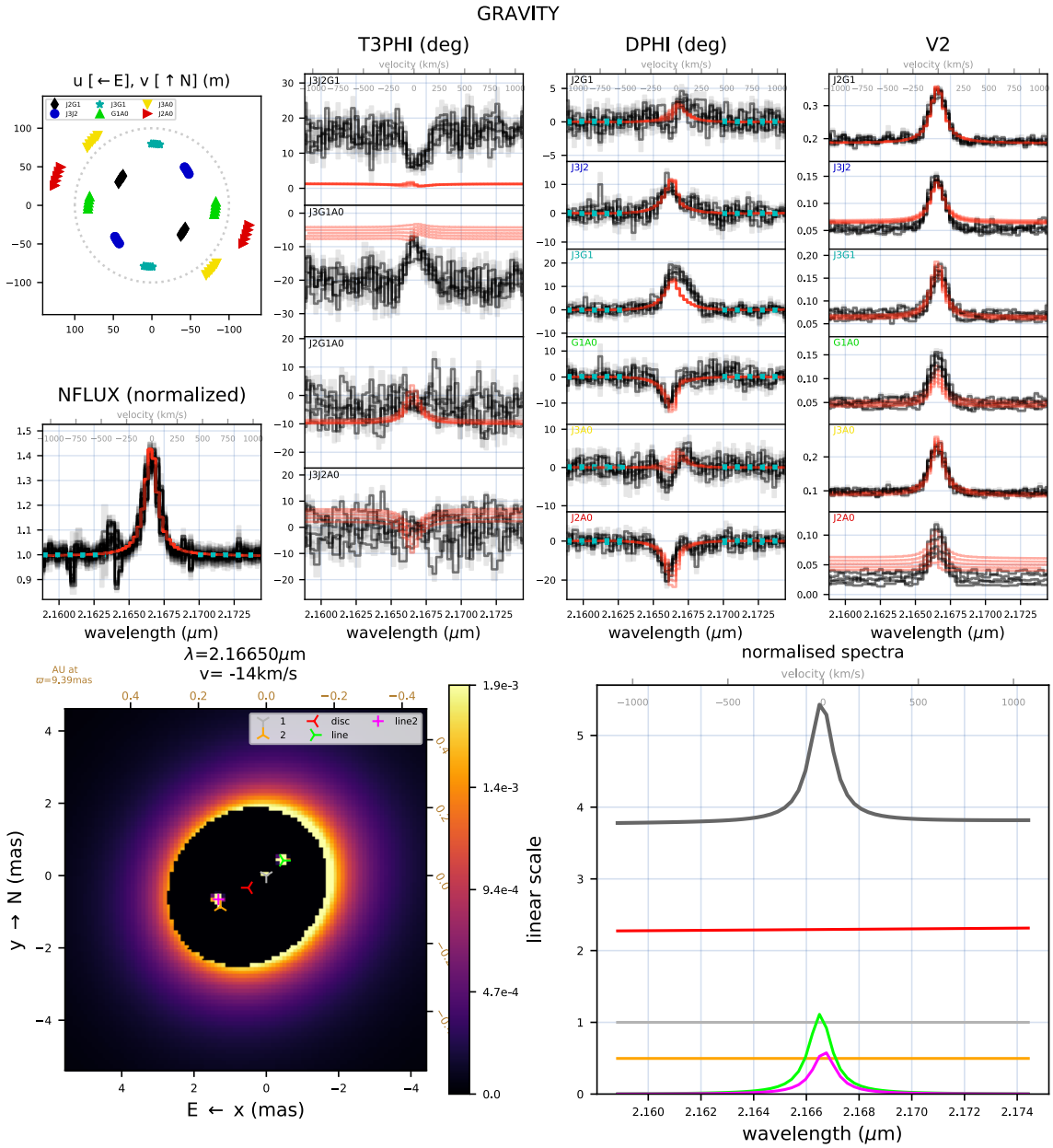

Figure B.4: 2019-02-22.

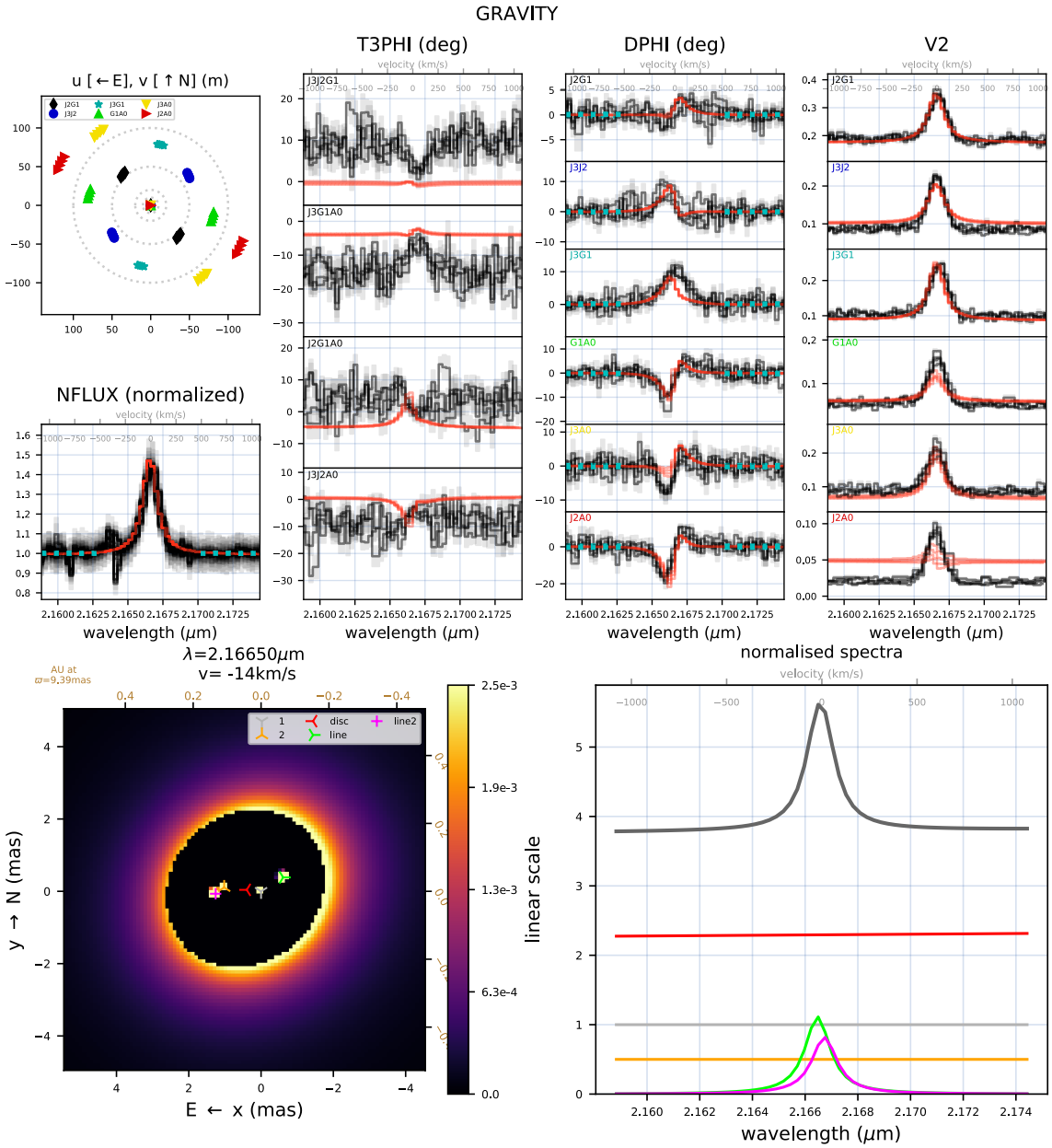

Figure B.5: 2019-02-23.

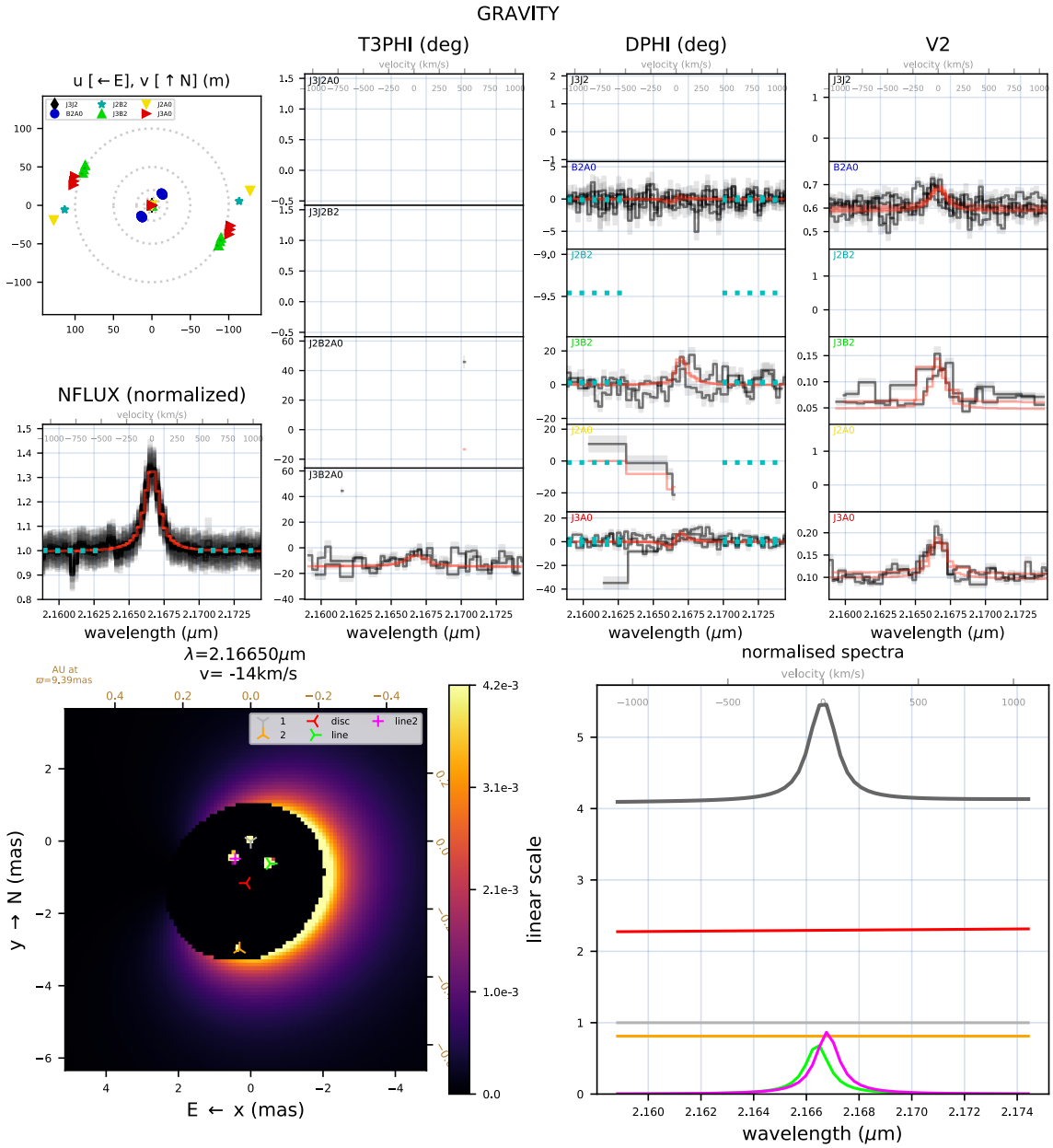

Figure B.6: 2019-03-10.

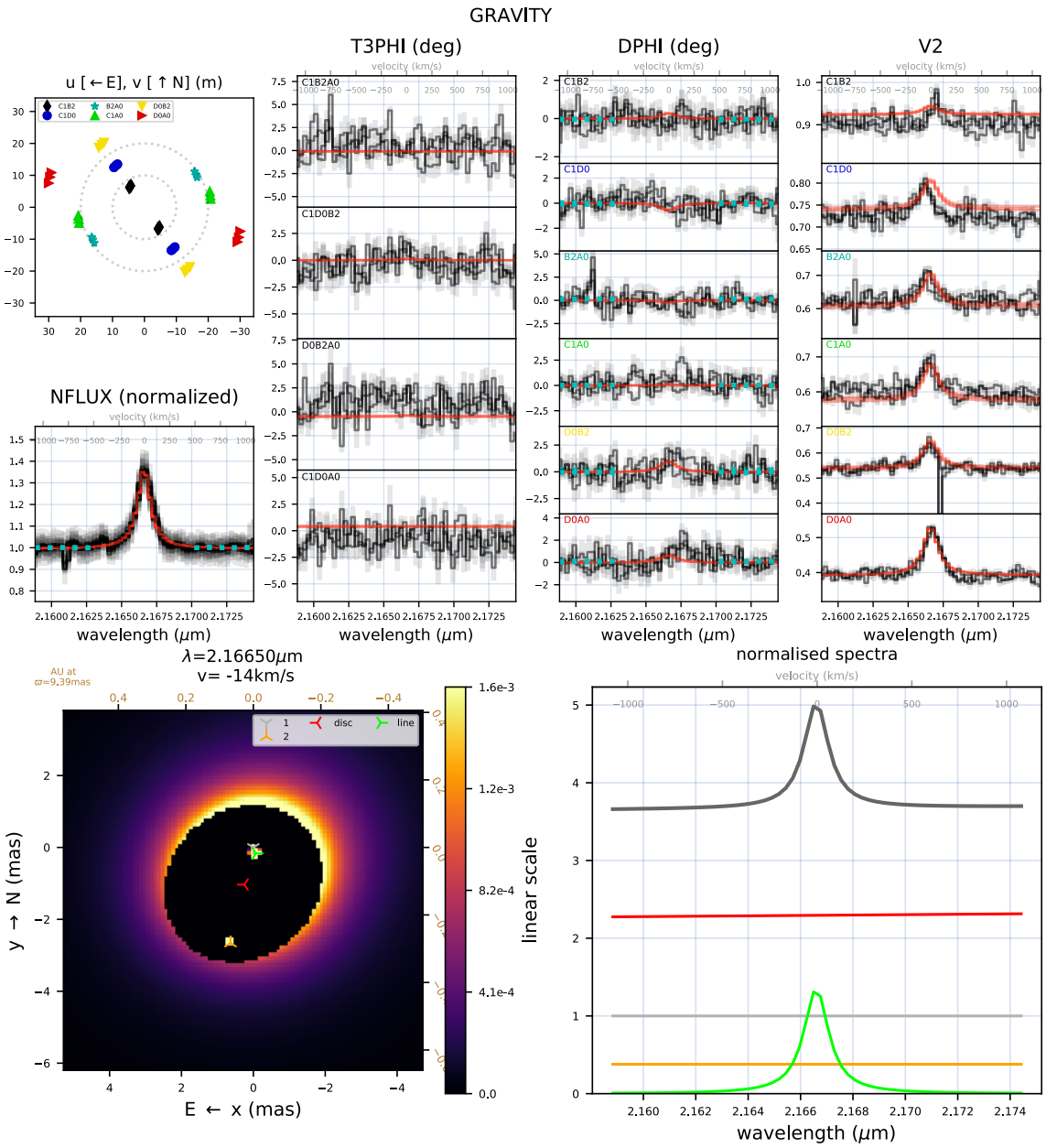

Figure B.7: 2019-03-11.

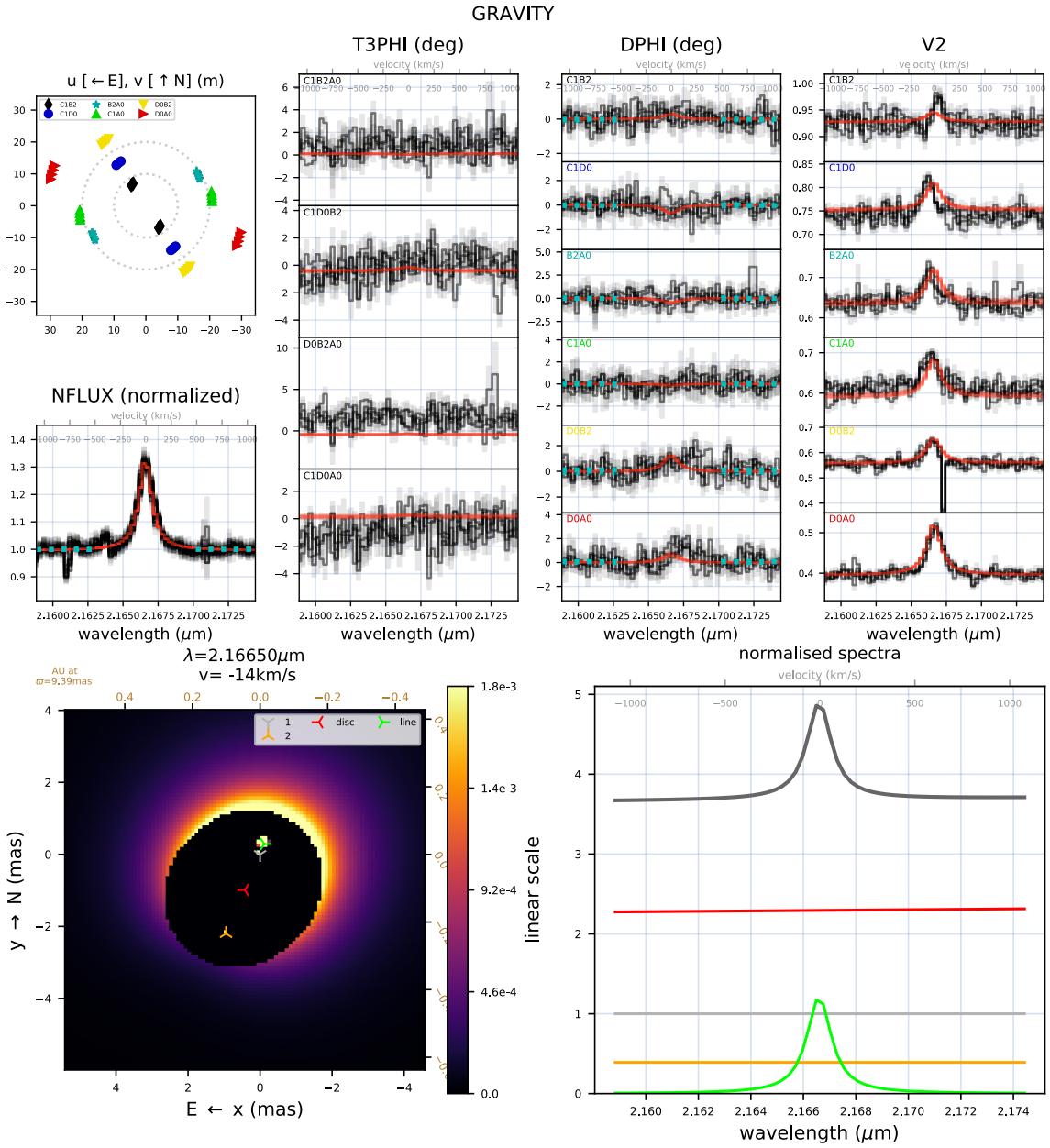

Figure B.8: 2019-03-12.

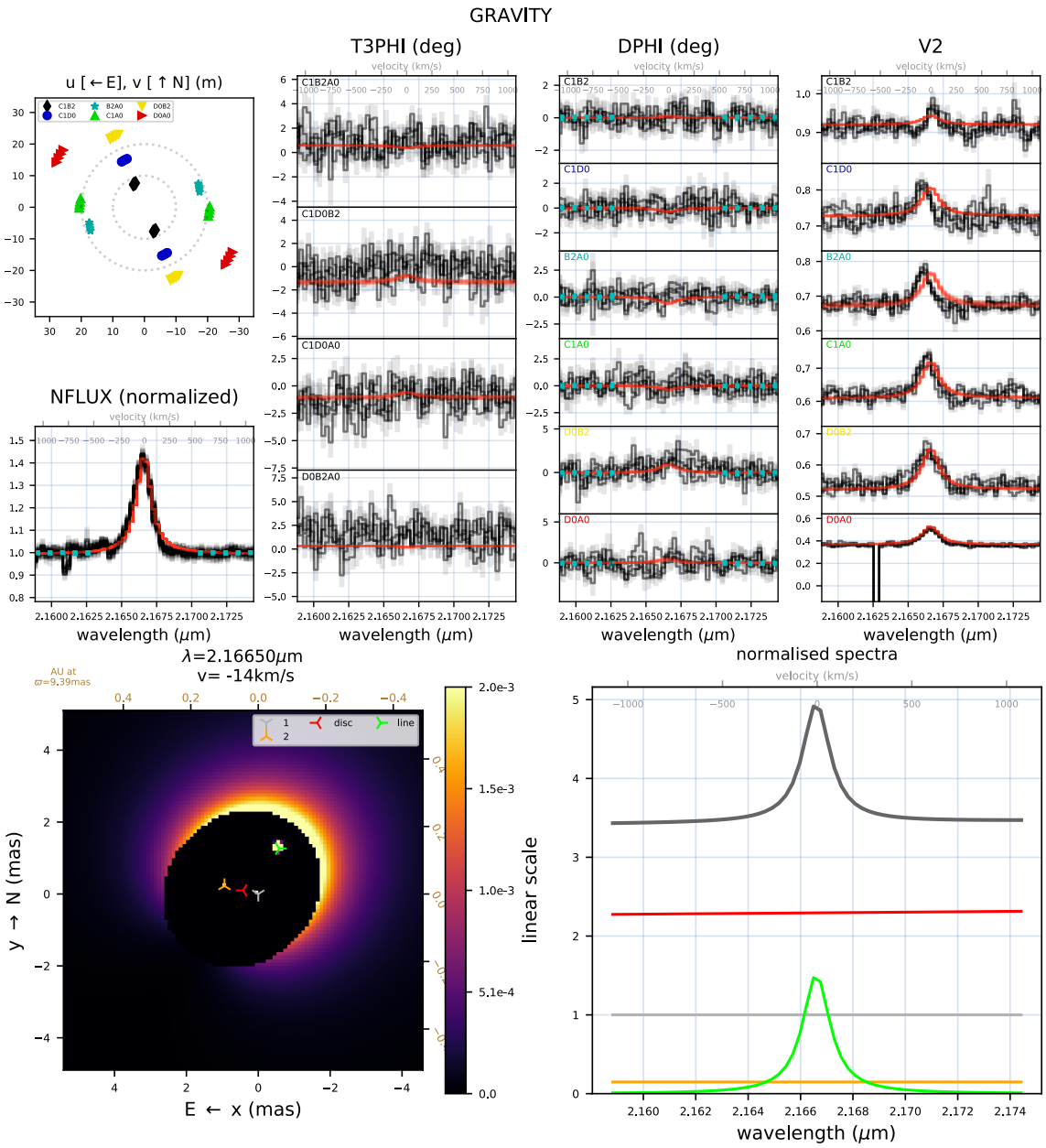

Figure B.9: 2019-03-15.

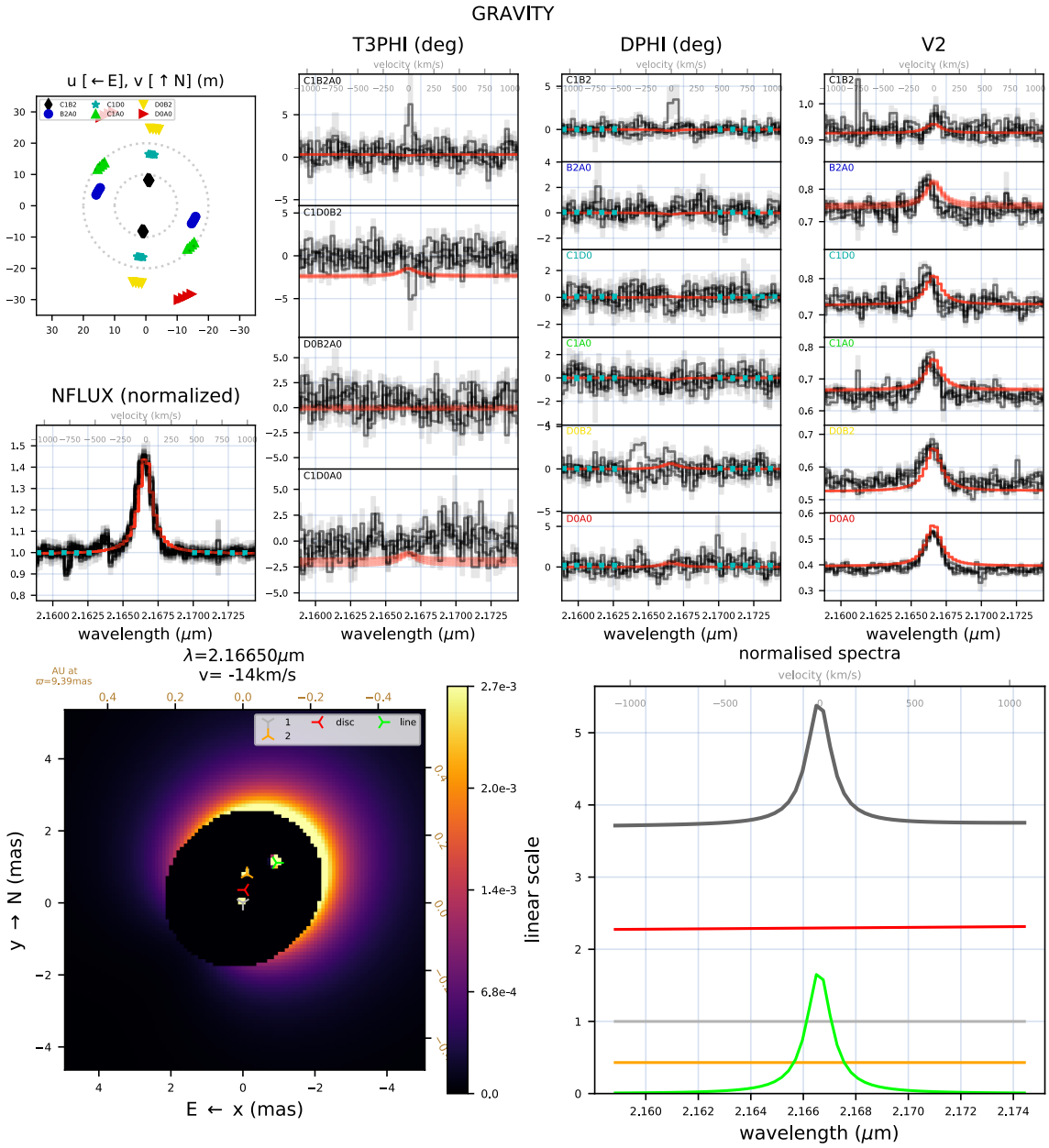

Figure B.10: 2019-03-16.

B.1.2 Results

Table B.1: Model parameters corresponding to the best-fit free Br γ line model (Model 1). NB the components of emission are not necessarily associated with a stellar component in this model.

Epoch	$x_{\mathrm{Br}\gamma,1}$ [mas]	$y_{\mathrm{Br}\gamma,1}$ [mas]	$f_{\mathrm{Br}\gamma,1}$	$x_{\mathrm{Br}\gamma,2}$ [mas]	$y_{\mathrm{Br}\gamma,2}$ [mas]	$f_{\mathrm{Br}\gamma,2}$	$\Delta\lambda$ [$10^{-4}\mu$m]	FWHM [nm]	χ^2
2018-12-23	-0.08 ± 0.11	0.25 ± 0.08	0.85 ± 0.02	0.13 ± 0.11	0.03 ± 0.08	0.90 ± 0.02	2.43 ± 0.06	0.73 ± 0.02	3.21
2019-01-14	-0.37 ± 0.05	0.34 ± 0.05	1.11 ± 0.05	1.21 ± 0.07	-0.23 ± 0.07	1.05 ± 0.05	1.26 ± 0.17	0.89 ± 0.02	3.58
2019-01-15	0.53 ± 0.05	0.42 ± 0.04	0.96 ± 0.04	-0.84 ± 0.03	0.16 ± 0.03	1.45 ± 0.05	-1.39 ± 0.07	1.24 ± 0.02	13.87
2019-02-22	-0.47 ± 0.05	0.42 ± 0.04	1.09 ± 0.04	1.34 ± 0.10	-0.66 ± 0.09	0.58 ± 0.05	0.70 ± 0.13	1.07 ± 0.02	18.37
2019-02-23	-0.61 ± 0.04	0.37 ± 0.02	1.07 ± 0.03	1.25 ± 0.06	-0.08 ± 0.06	0.80 ± 0.02	1.34 ± 0.01	1.18 ± 0.04	13.90
2019-03-10	-0.44 ± 0.15	-0.77 ± 0.27	0.75 ± 0.03	0.39 ± 0.10	-0.37 ± 0.23	0.86 ± 0.03	1.93 ± 0.21	1.01 ± 0.03	3.02
2019-03-11	-0.07 ± 0.03	-0.18 ± 0.04	1.37 ± 0.01	-	-	-	-	1.16 ± 0.01	2.63
2019-03-12	-0.12 ± 0.04	0.30 ± 0.07	1.22 ± 0.01	-	-	-	-	1.15 ± 0.01	3.69
2019-03-15	-0.58 ± 0.04	1.27 ± 0.01	1.52 ± 0.01	-	-	-	-	1.27 ± 0.01	4.46
2019-03-16	-0.92 ± 0.04	1.12 ± 0.03	1.72 ± 0.01	-	-	-	-	1.13 ± 0.01	5.69

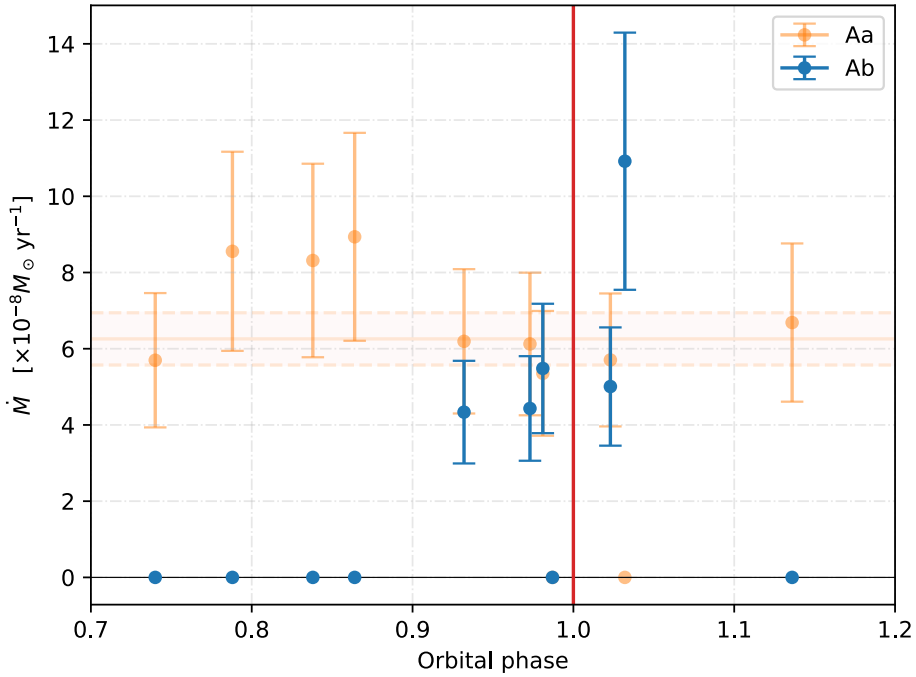

Figure B.11: Accretion rates of each component of HD 104237 A, for the in Model 1. The weighted averages for each component are shown as the shaded areas. In this model, the secondary component only accretes around periastron, and is too variable for an average to be reliably calculated. The red line shows the epoch of periastron passage.

B.2 Model 2: Spatially- and spectrally-fixed Br γ emission

In this section are results associated with the fixed Br γ models described in Section 5.5.2.

Table B.2: Model parameters corresponding to the fixed Br γ line model (Model 2).

Epoch	Phase	$\Delta\lambda_1$ [µm]	$\Delta\lambda_2$ [µm]	$f_{\mathrm{Br}\gamma,1}$	$f_{\mathrm{Br}\gamma,2}$	FWHM [nm]	χ^2
2018-12-23	0.864	6.65×10^{-5}	1.46×10^{-4}	1.38 ± 0.03	-	1.01 ± 0.02	3.61
2019-01-14	0.973	-5.78×10^{-6}	2.35×10^{-4}	1.23 ± 0.02	0.83 ± 0.02	0.86 ± 0.01	3.69
2019-01-15	0.023	-7.01×10^{-5}	3.14×10^{-4}	-	1.66 ± 0.04	1.37 ± 0.03	25.00
2019-02-22	0.932	3.04×10^{-5}	1.90×10^{-4}	1.06 ± 0.03	0.29 ± 0.02	0.84 ± 0.03	22.72
2019-02-23	0.981	-1.30×10^{-5}	2.43×10^{-4}	1.03 ± 0.05	0.61 ± 0.04	0.84 ± 0.04	36.20
2019-03-10	0.740	1.06×10^{-4}	9.71×10^{-5}	1.06 ± 0.04	0.28 ± 0.03	1.12 ± 0.04	3.33
2019-03-11	0.788	9.90×10^{-5}	1.06×10^{-4}	1.20 ± 0.03	0.15 ± 0.02	1.14 ± 0.03	2.72
2019-03-12	0.838	7.81×10^{-5}	1.32×10^{-4}	1.19 ± 0.03	-	1.14 ± 0.02	3.55
2019-03-15	0.987	-2.10×10^{-5}	2.53×10^{-4}	1.46 ± 0.03	-	1.27 ± 0.02	5.40
2019-03-16	0.032	-8.17×10^{-5}	3.28×10^{-4}	1.37 ± 0.03	0.31 ± 0.03	1.05 ± 0.02	6.39

Table B.3: Relative Br γ luminosities for each component, based on the models from Table B.2 (Model 2). The values for L_{acc} and $\dot{M}$ are given assuming all Br γ emission is associated with magnetospheric accretion.

Epoch	$\frac{f_{\mathrm{Br}\gamma,1}}{f_{\mathrm{Br}\gamma,\mathrm{tot}}}$	$L_{\mathrm{acc},1}$ $[L_\odot]$	$L_{\mathrm{acc},2}$ $[L_\odot]$	$\dot{M}_1$ $[10^{-8}\,M_\odot/\mathrm{yr}]$	$\dot{M}_2$ $[10^{-8}\,M_\odot/\mathrm{yr}]$
2018-12-23	1	2.78	-	8.9 ± 2.7	-
2019-01-14	0.59	1.73 ± 0.02	1.25 ± 0.02	5.6 ± 1.7	5.2 ± 1.6
2019-01-15	-	-	2.78	-	11.6 ± 3.6
2019-02-22	0.78	2.24 ± 0.03	0.70 ± 0.04	7.2 ± 2.2	2.9 ± 0.9
2019-02-23	0.63	1.83 ± 0.05	1.14 ± 0.06	5.9 ± 1.8	4.8 ± 1.5
2019-03-10	0.79	2.25 ± 0.05	0.69 ± 0.06	7.2 ± 2.2	2.9 ± 0.9
2019-03-11	0.89	2.51 ± 0.04	0.38 ± 0.05	8.1 ± 2.5	1.6 ± 0.5
2019-03-12	1	2.78	-	8.9 ± 2.7	-
2019-03-15	1	2.78	-	8.9 ± 2.7	-
2019-03-16	0.82	2.32 ± 0.04	0.61 ± 0.05	7.4 ± 2.3	2.5 ± 0.8

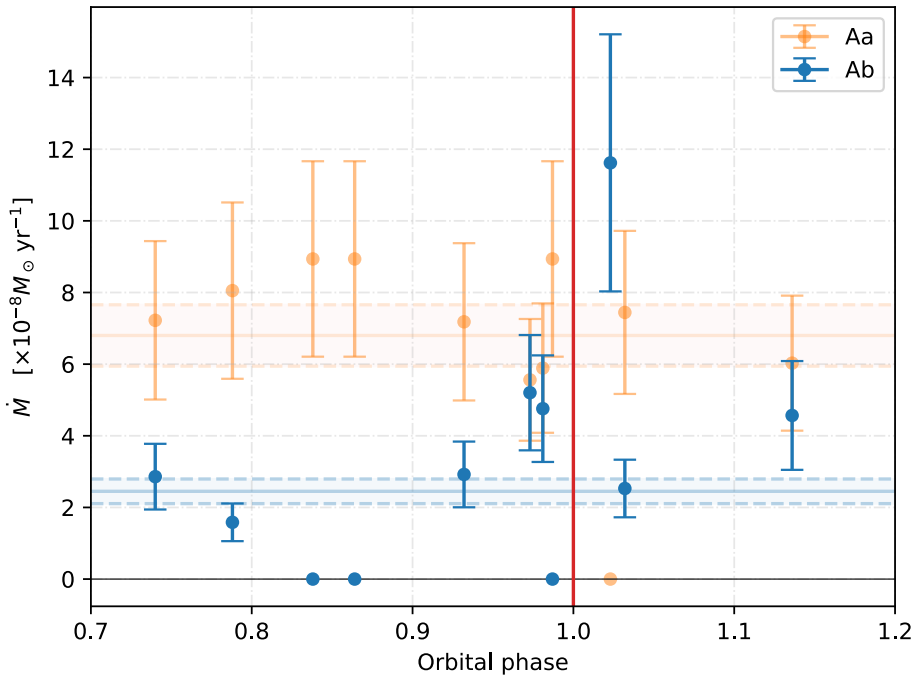

Figure B.12: Accretion rates of each component of HD 104237 A for Model 2. The weighted averages for each component are shown as the shaded areas. The red line shows the epoch of periastron passage.

B.3 Model 3: Three-component model

In this section are the full set of three-component Br γ models described in Section 5.5.3, as well as associated results.

B.3.1 Models

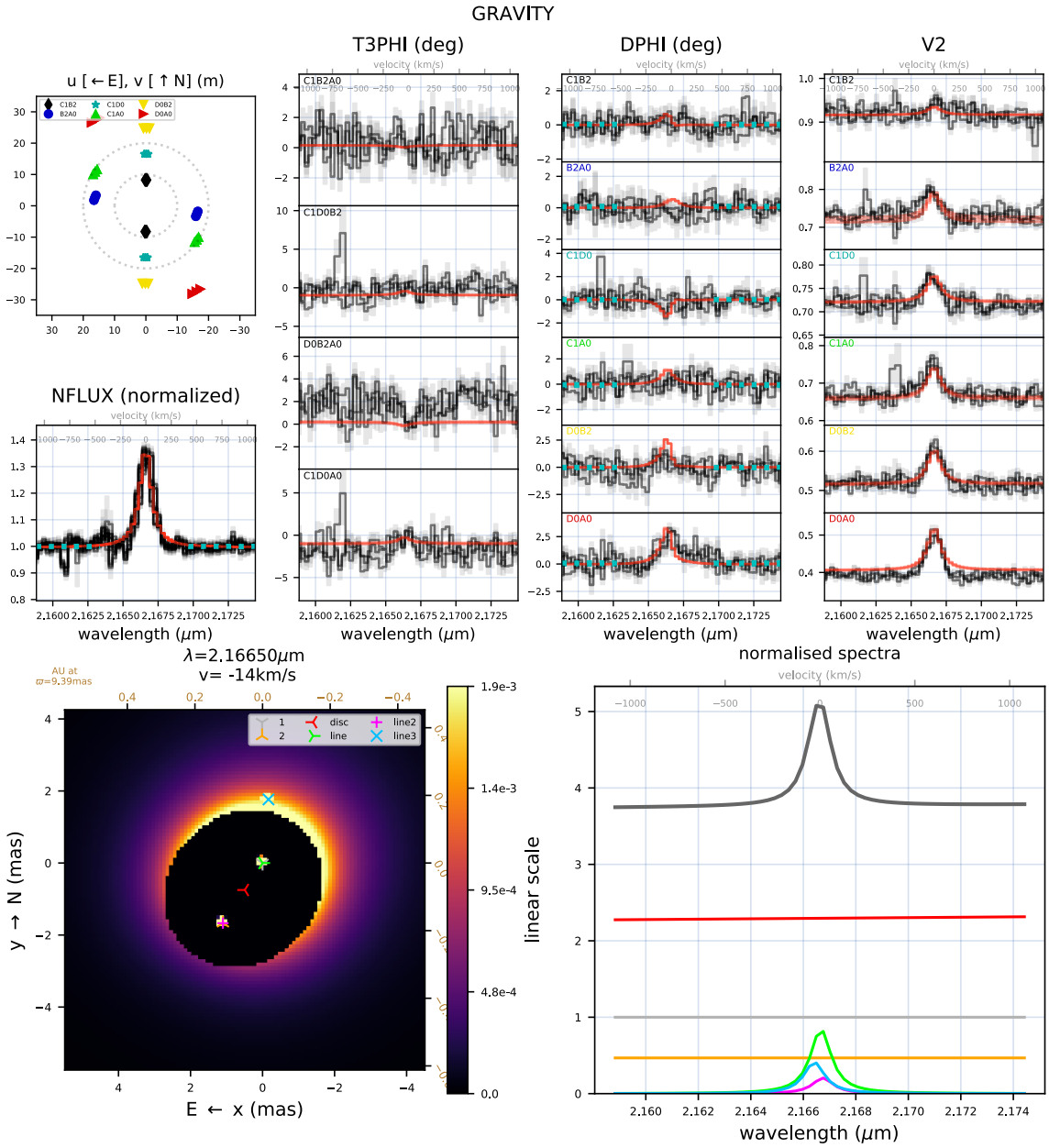

Figure B.13: 2018-12-23, three-component model.

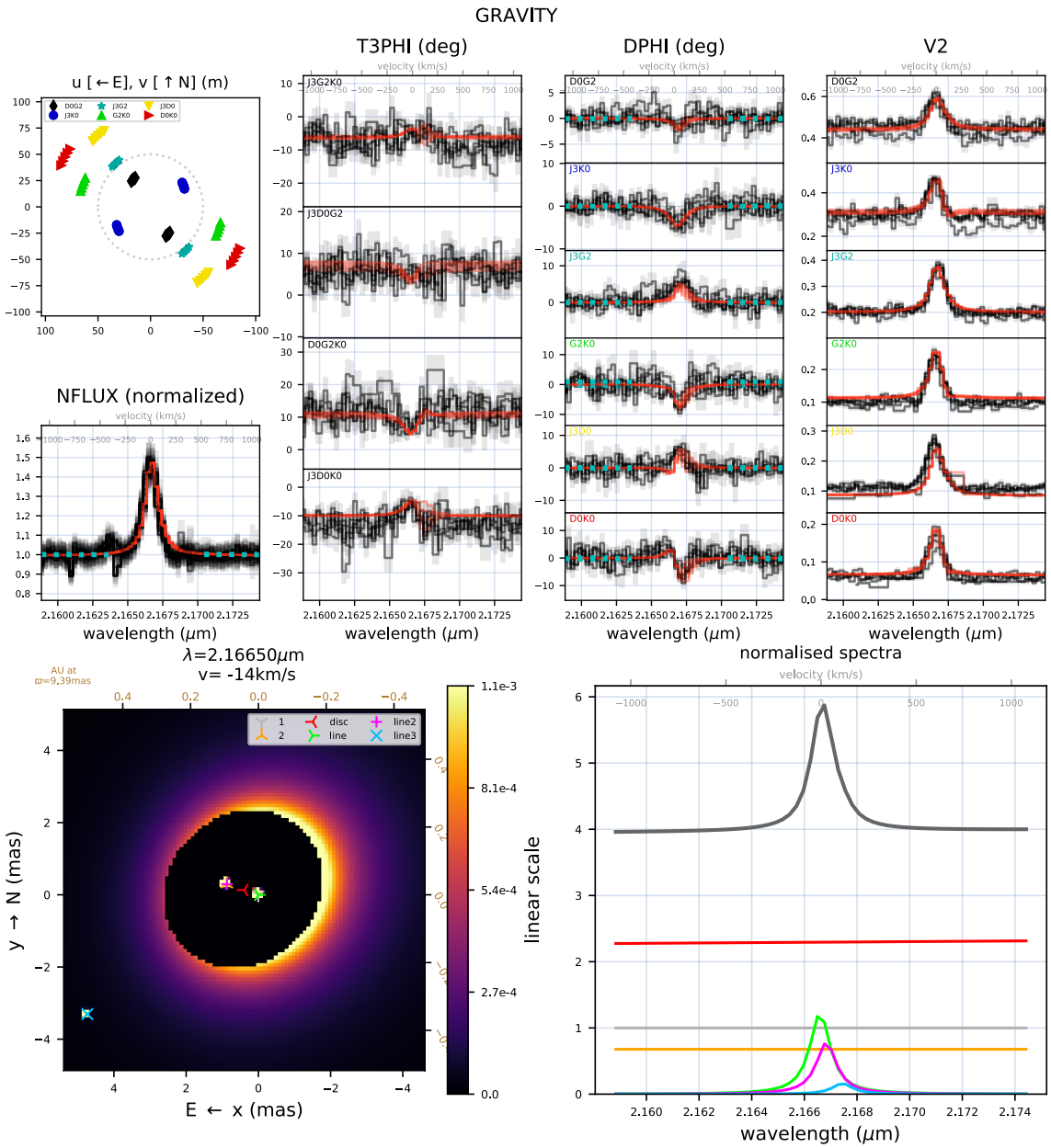

Figure B.14: 2019-01-14, three-component model.

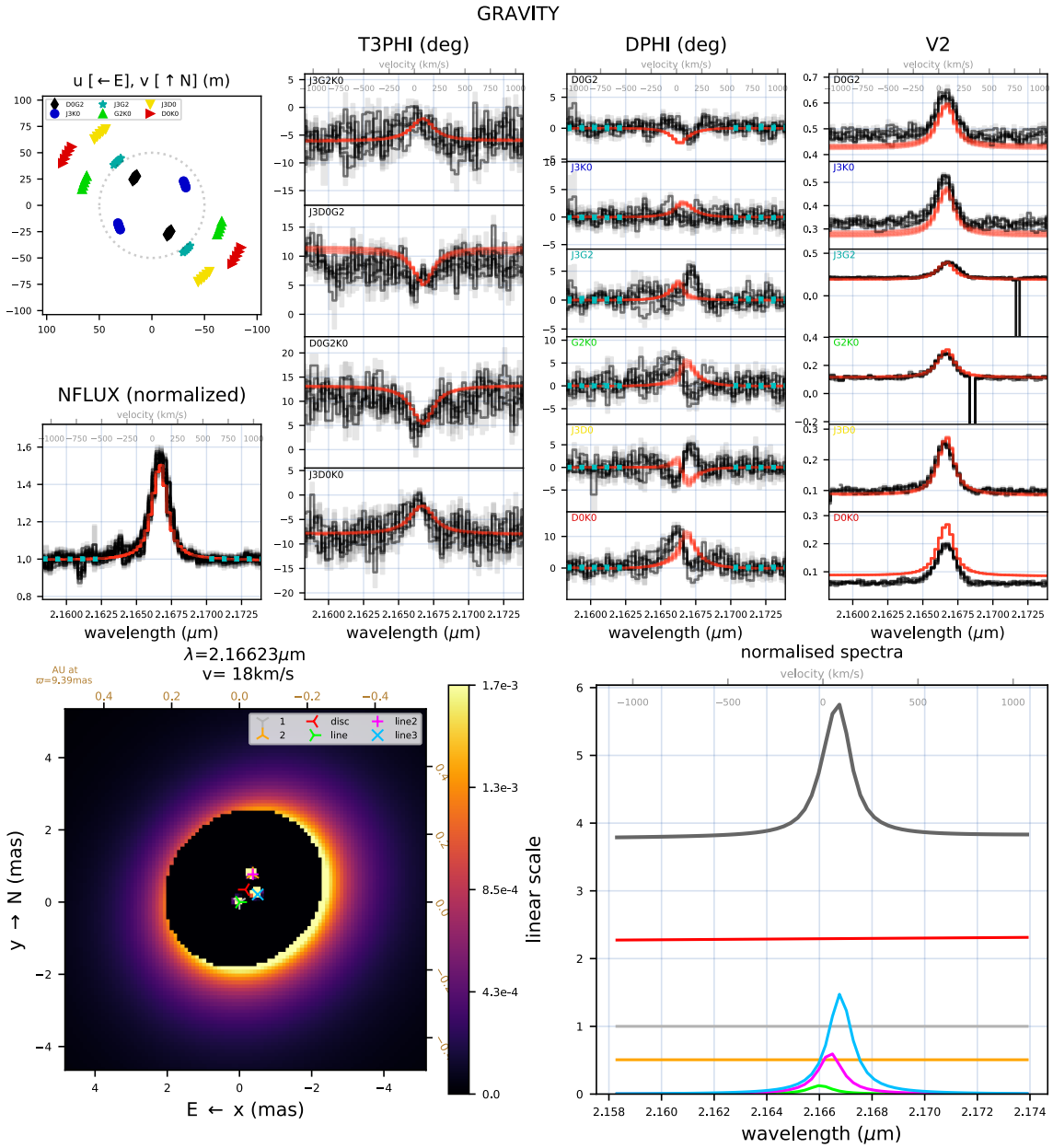

Figure B.15: 2019-01-15, three-component model.

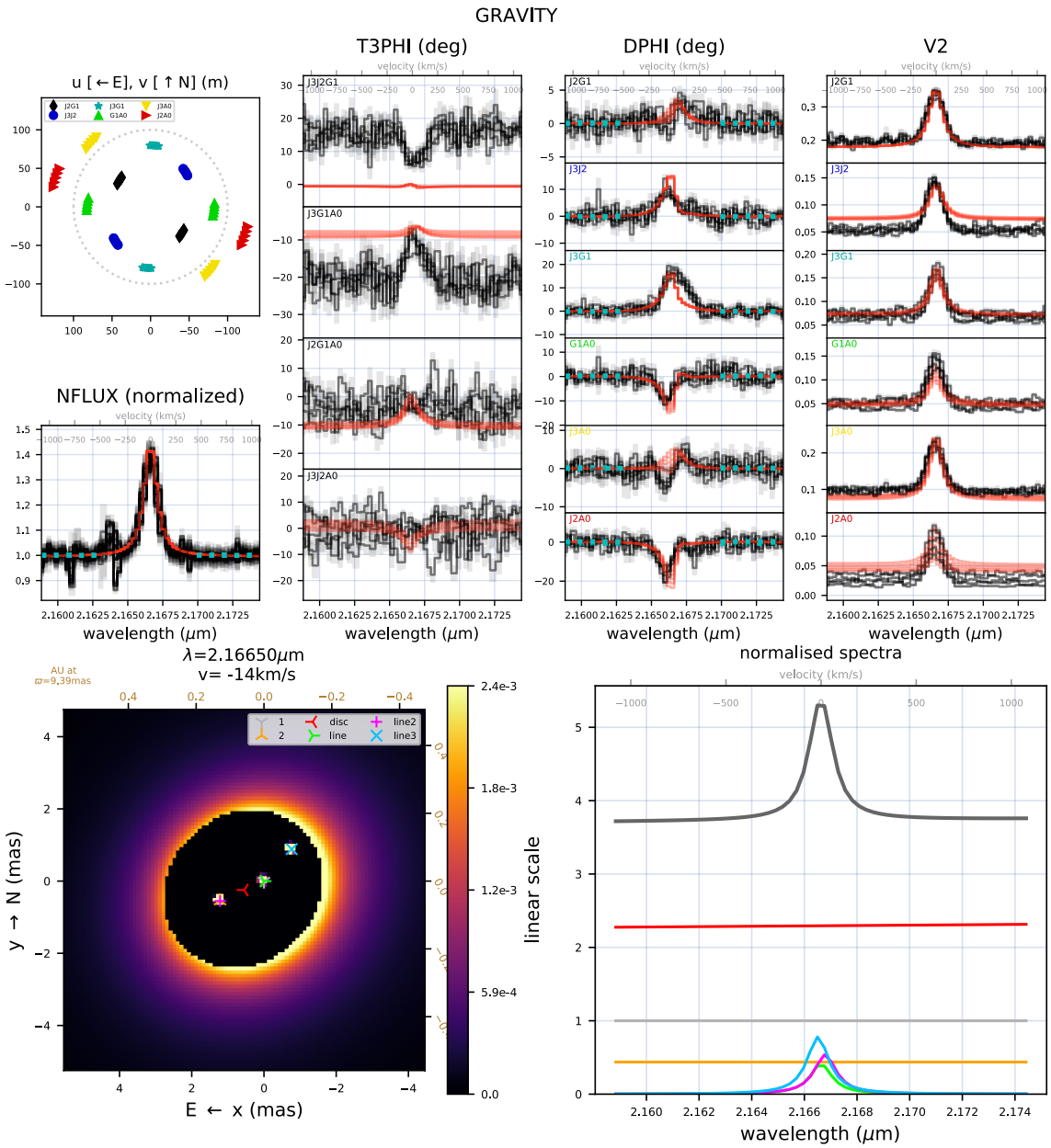

Figure B.16: 2019-02-22, three-component model.

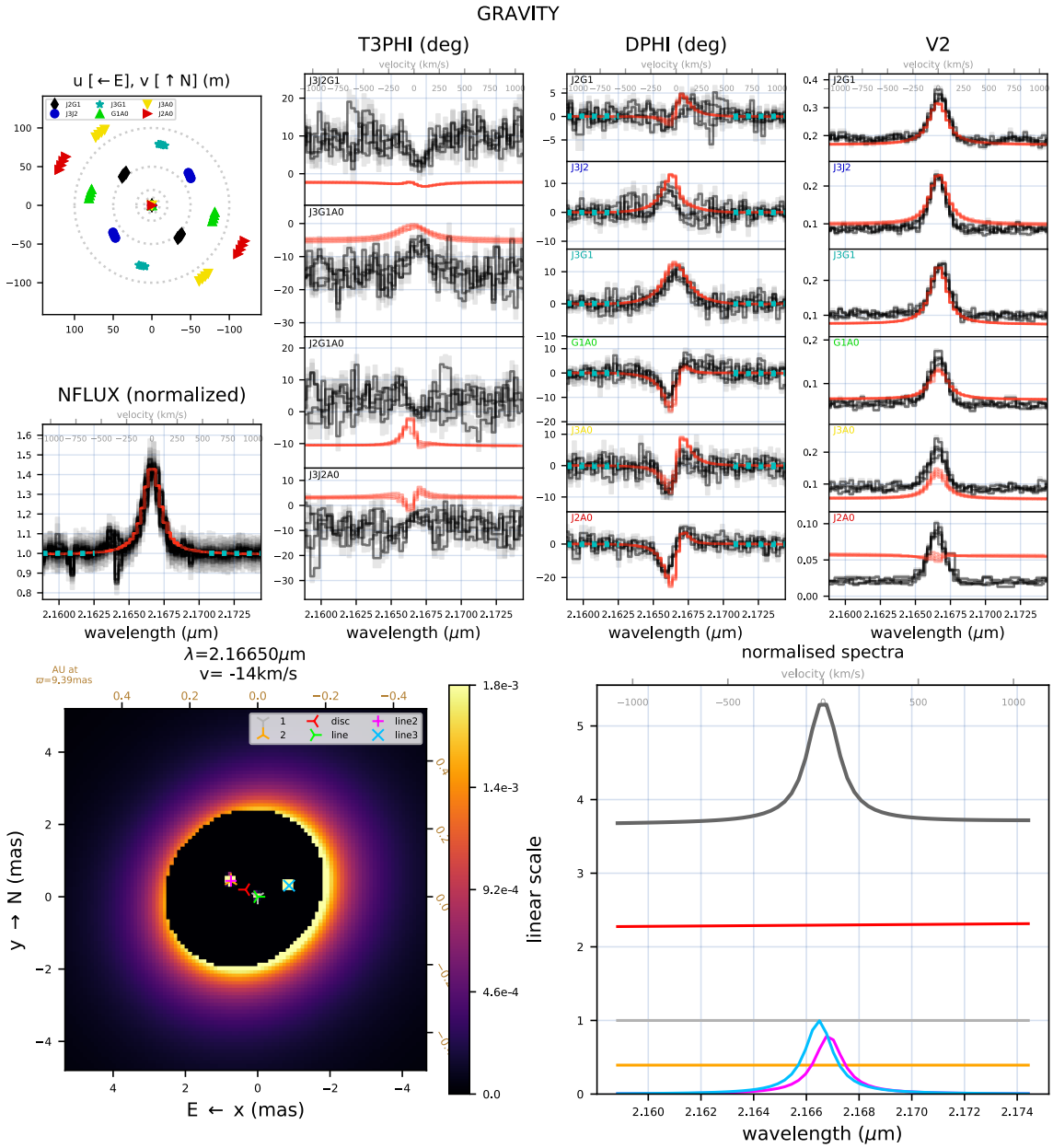

Figure B.17: 2019-02-23, three-component model.

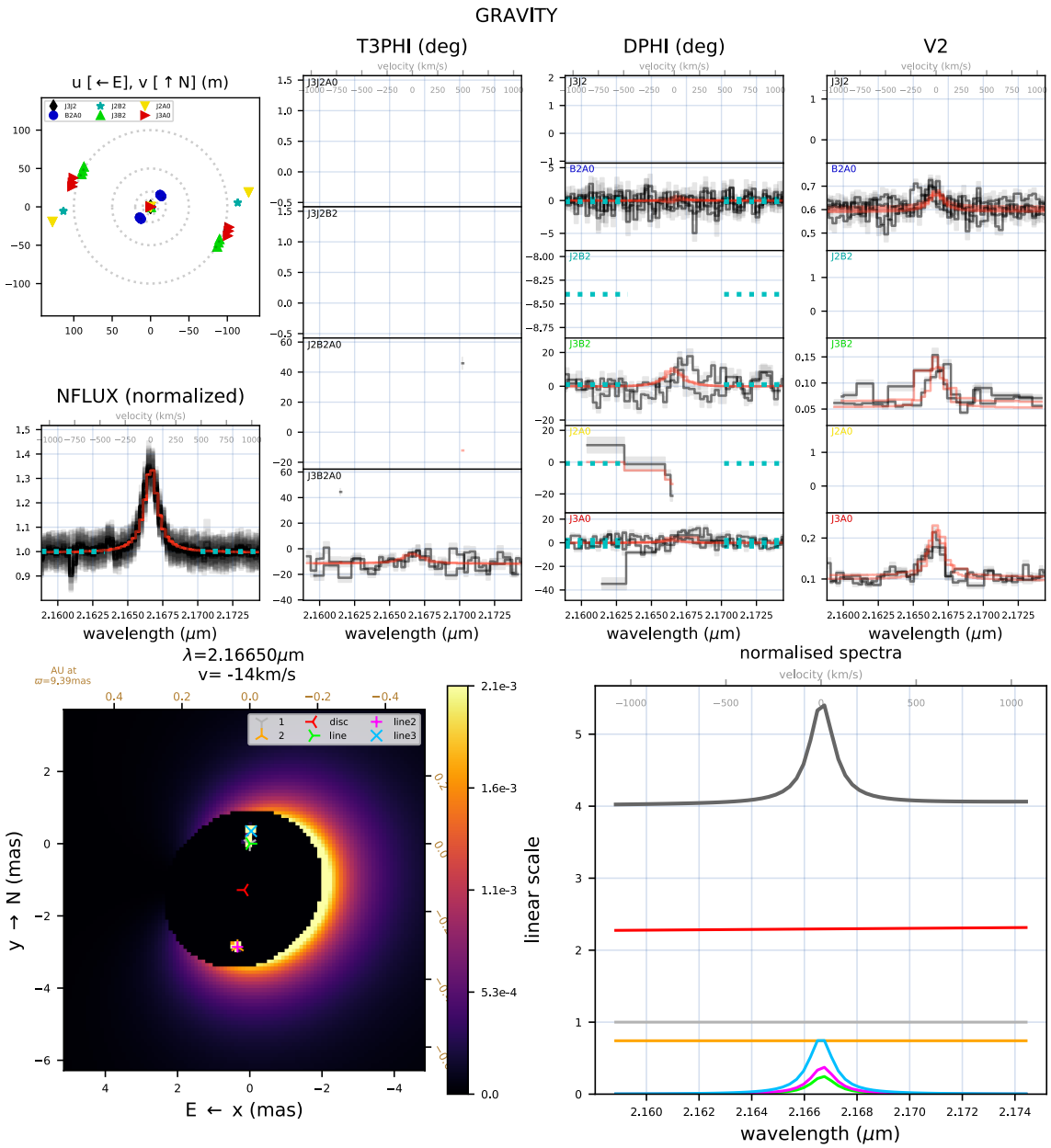

Figure B.18: 2019-03-10, three-component model.

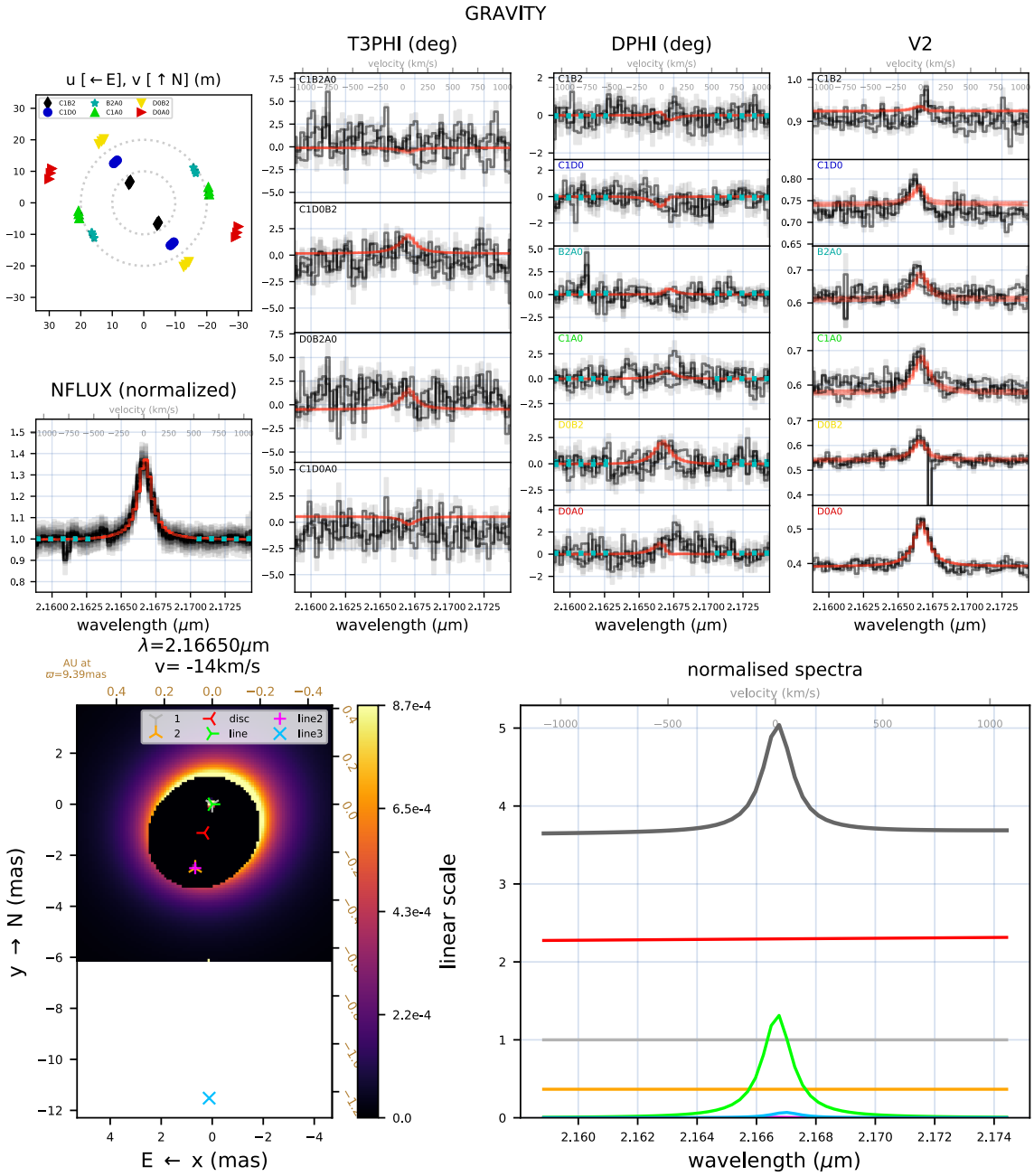

Figure B.19: 2019-03-11, three-component model.

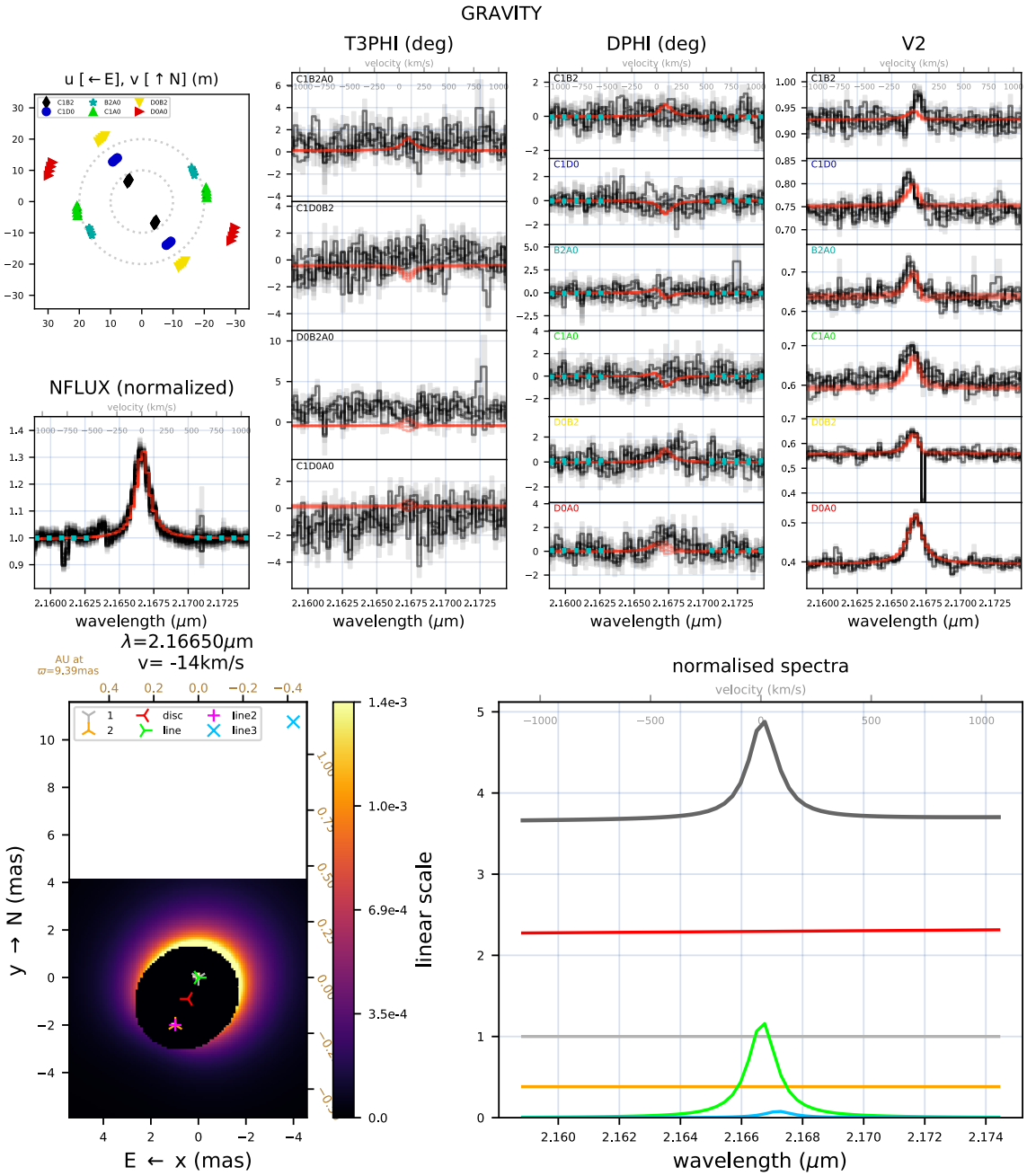

Figure B.20: 2019-03-12, three-component model.

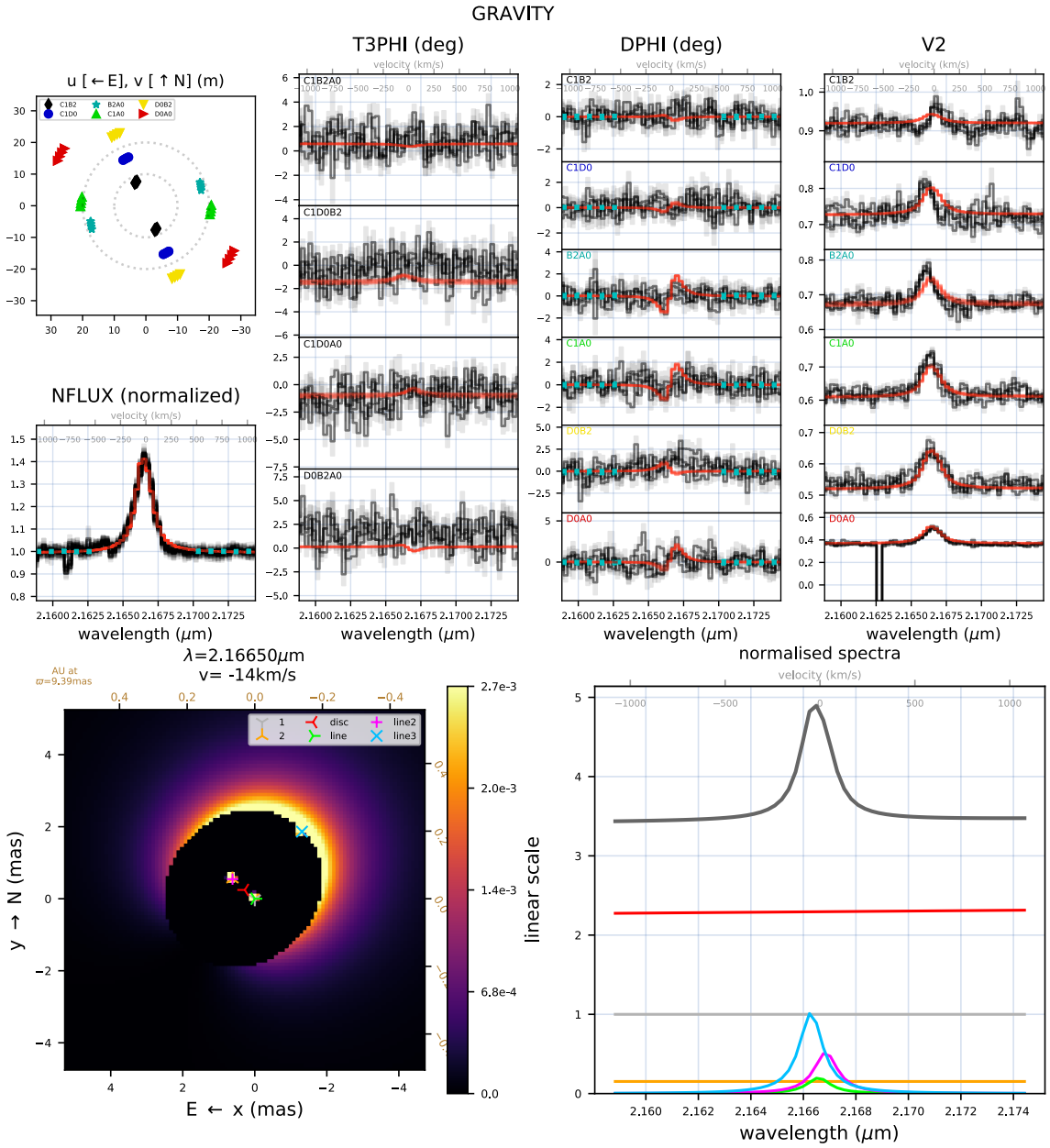

Figure B.21: 2019-03-15, three-component model.

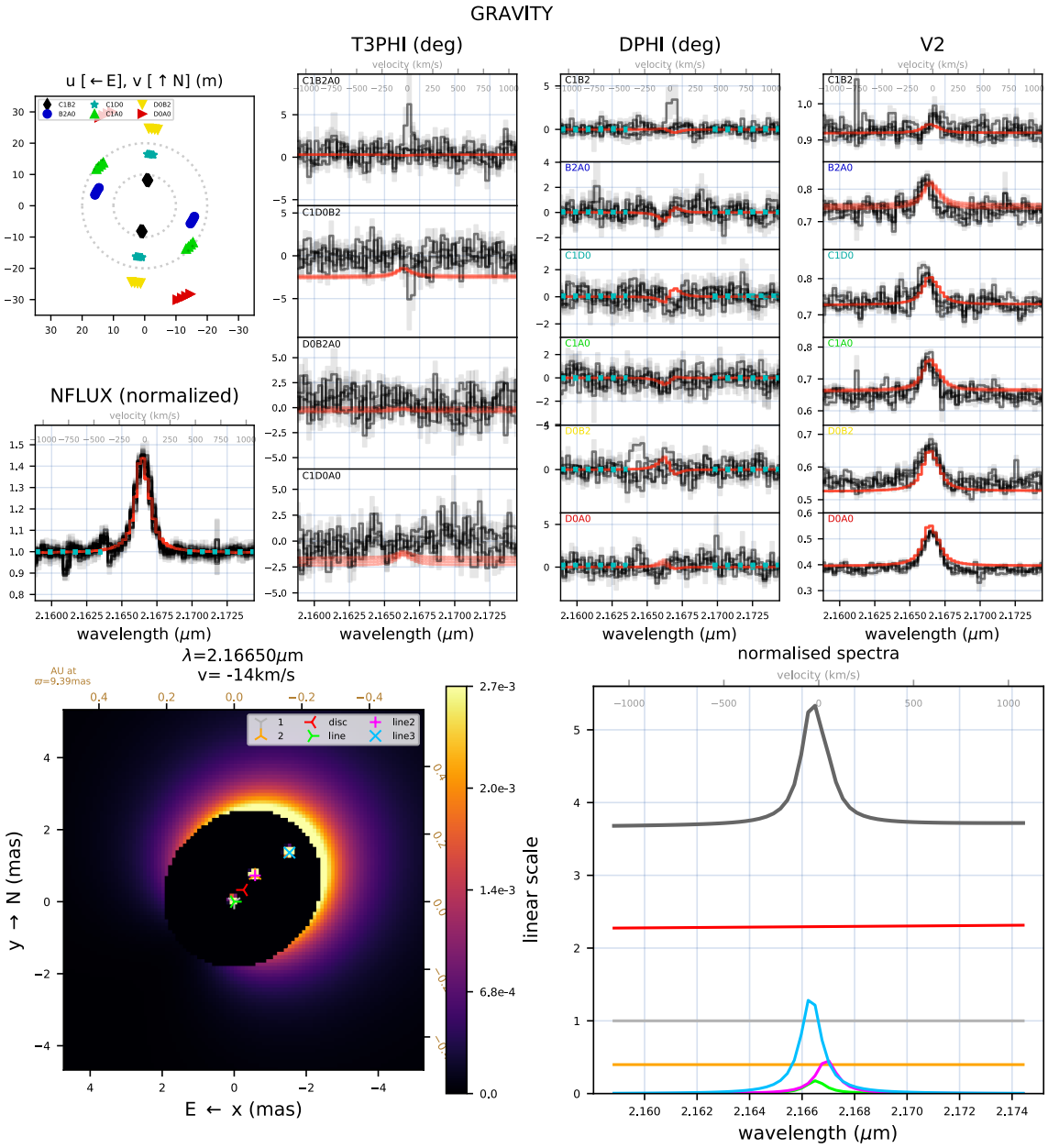

Figure B.22: 2019-03-16, three-component model.

B.3.2 Results

Table B.4: Model parameters corresponding to the three-component Br γ line model (Model 3). The values of $\Delta\lambda_{1,2}$ were kept fixed to those in the corresponding column of Table 5.9. Positions marked with a (*) are unreliable due to the weak flux associated with the third component at these epochs.

Epoch	$f_{\mathrm{Br}\gamma,1}$	$f_{\mathrm{Br}\gamma,2}$	$f_{\mathrm{Br}\gamma,3}$	$x_{\mathrm{Br}\gamma,3}$ [mas]	$y_{\mathrm{Br}\gamma,3}$ [mas]	$\Delta\lambda_3$ [10^{-4}µm]	FWHM [nm]	χ^2
2018-12-23	0.85 ± 0.12	0.21 ± 0.05	0.41 ± 0.07	-0.16 ± 0.16	1.76 ± 0.19	-1.83 ± 0.35	0.95 ± 0.02	3.33
2019-01-14*	1.23 ± 0.02	0.78 ± 0.02	0.16 ± 0.01	4.74 ± 0.17	-3.30 ± 0.19	8.44 ± 0.32	0.91 ± 0.01	4.27
2019-01-15	0.15 ± 0.05	0.54 ± 0.09	1.52 ± 0.06	-0.49 ± 0.03	0.22 ± 0.05	6.80 ± 0.17	1.08 ± 0.03	17.50
2019-02-22	0.41 ± 0.09	0.54 ± 0.03	0.78 ± 0.07	-0.77 ± 0.06	0.89 ± 0.07	-0.82 ± 0.17	1.01 ± 0.03	18.74
2019-02-23	-	0.80 ± 0.03	1.00 ± 0.03	-0.87 ± 0.03	0.31 ± 0.04	-1.27 ± 0.20	1.26 ± 0.04	31.11
2019-03-10	0.25 ± 1.59	0.38 ± 0.05	0.79 ± 1.57	-0.04 ± 0.09	0.35 ± 0.64	0.3 ± 1.5	1.10 ± 0.01	3.48
2019-03-1(1)	1.33 ± 0.04	-	0.07 ± 0.01	0.12 ± 0.39	-11.5 ± 0.9	3.80 ± 0.52	3.80 ± 0.51	2.55
2019-03-1(2)	1.19 ± 0.02	-	0.08 ± 0.01	-3.99 ± 0.32	10.8 ± 0.6	6.06 ± 0.42	1.08 ± 0.02	3.31
2019-03-15	0.20 ± 0.09	0.52 ± 0.05	1.02 ± 0.06	-1.31 ± 0.07	1.86 ± 0.12	-3.10 ± 0.16	1.08 ± 0.02	3.71
2019-03-16	0.18 ± 0.09	0.47 ± 0.04	1.36 ± 0.08	-1.54 ± 0.11	1.36 ± 0.09	-2.59 ± 0.12	0.91 ± 0.02	4.11

Table B.5: Relative Br γ luminosities for each component, based on the three-component model from Table B.4 (Model 3). The values in the second and third column are given as a fraction of the total flux, including flux not associated with either star.

Epoch	$\frac{f_{\mathrm{Br}\gamma,1}}{f_{\mathrm{Br}\gamma,\mathrm{tot}}}$	$\frac{f_{\mathrm{Br}\gamma,2}}{f_{\mathrm{Br}\gamma,\mathrm{tot}}}$	$L_{\mathrm{acc},1}$ [$L_\odot$]	$L_{\mathrm{acc},2}$ [$L_\odot$]	$\dot{M}_1$ [$10^{-8}\,M_\odot$/yr]	$\dot{M}_2$ [$10^{-8}\,M_\odot$/yr]
2018-12-23	0.58 ± 0.05	0.14 ± 0.03	1.71 ± 0.13	0.47 ± 0.10	5.5 ± 1.7	2.0 ± 0.7
2019-01-14	0.56 ± 0.01	0.36 ± 0.01	1.65 ± 0.02	1.12 ± 0.02	5.3 ± 1.6	4.7 ± 1.5
2019-01-15	0.07 ± 0.02	0.24 ± 0.03	0.25 ± 0.07	0.78 ± 0.09	0.8 ± 0.3	3.3 ± 1.1
2019-02-22	0.23 ± 0.04	0.31 ± 0.02	0.75 ± 0.12	0.98 ± 0.07	7.3 ± 2.2	2.8 ± 0.9
2019-02-23	-	0.44 ± 0.01	-	1.34 ± 0.03	-	5.6 ± 1.7
2019-03-10	0.77 ± 0.03	-	2.20 ± 0.08	-	7.1 ± 2.2	-
2019-03-11	0.95 ± 0.01	-	2.66 ± 0.06	-	8.5 ± 2.6	< 0.1
2019-03-12	0.93 ± 0.05	-	2.61 ± 0.14	-	8.4 ± 2.6	-
2019-03-15	0.12 ± 0.04	0.30 ± 0.03	0.41 ± 0.14	0.94 ± 0.07	1.3 ± 0.6	3.9 ± 1.2
2019-03-16	0.08 ± 0.04	0.23 ± 0.02	0.28 ± 0.14	0.75 ± 0.06	8.9 ± 5.3	3.1 ± 1.0

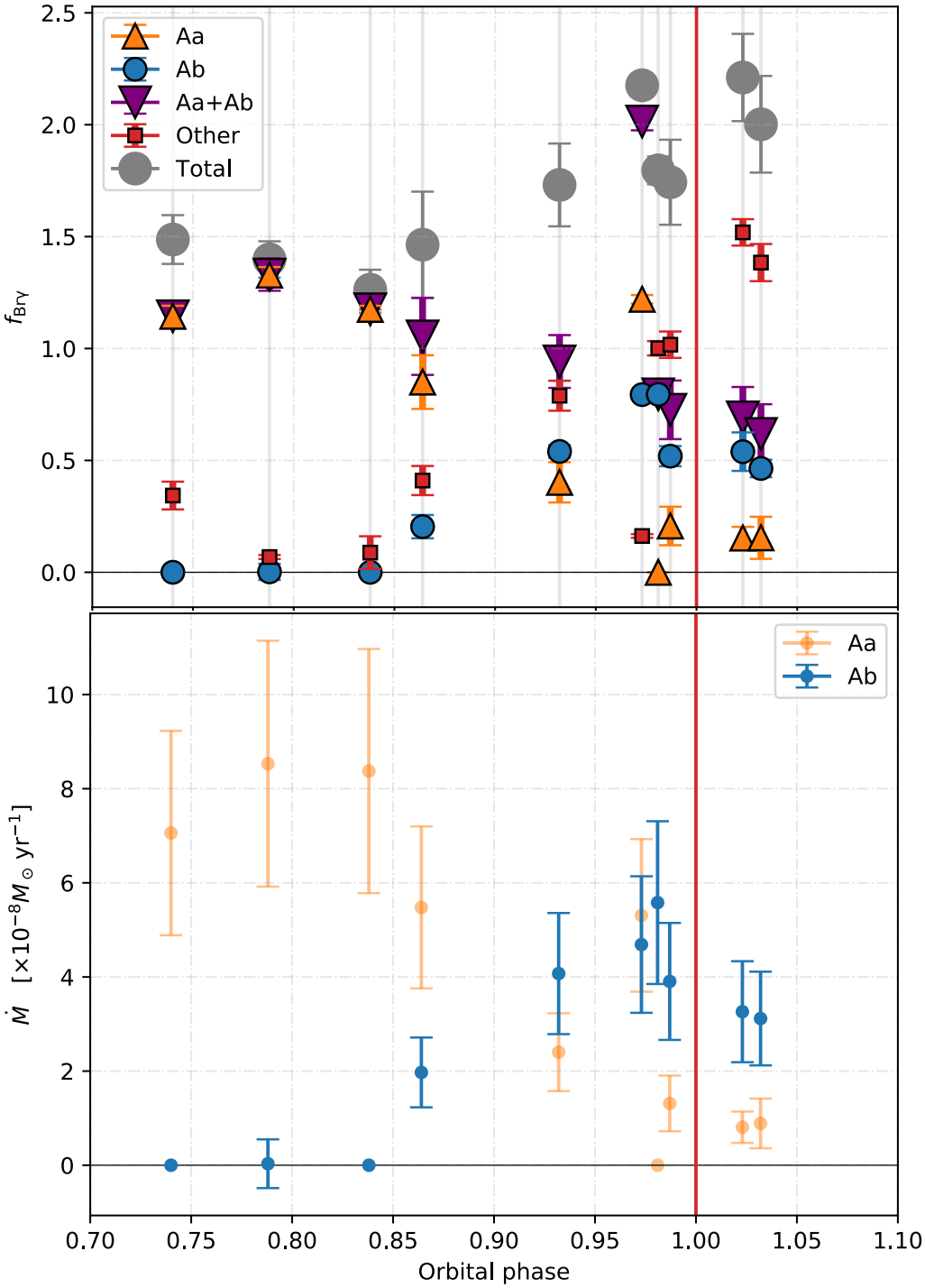

Figure B.23: Br γ flux for the three-component model (top panel) and the associated accretion rates of the two stars (bottom panel) at each epoch. The red line indicates the epoch of periastron passage.

Bibliography

Accadia, T., F. Acernese, M. Alshourbagy, et al. 2012. 'Virgo: a laser interferometer to detect gravitational waves.' *Journal of Instrumentation* 7, no. 3 (March): 3012.

Acke, B., M. E. van den Ancker, and C. P. Dullemond. 2005. '[O I] 6300 Å emission in Herbig Ae/Be systems: Signature of Keplerian rotation.' A&A 436, no. 1 (June): 209–230.

Alexander, R., I. Pascucci, S. Andrews, et al. 2014. 'The Dispersal of Protoplanetary Disks.' In *Protostars and Planets VI,* edited by Henrik Beuther, Ralf S. Klessen, Cornelis P. Dullemond, et al., 475. January.

Alexander, Richard D., and Philip J. Armitage. 2009. 'Giant Planet Migration, Disk Evolution, and the Origin of Transitional Disks.' ApJ 704, no. 2 (October): 989–1001.

ALMA Partnership, C. L. Brogan, L. M. Pérez, et al. 2015. 'The 2014 ALMA Long Baseline Campaign: First Results from High Angular Resolution Observations toward the HL Tau Region.' ApJL 808, no. 1 (July): L3.

André, Philippe, Derek Ward-Thompson, and Mary Barsony. 1993. 'Submillimetre continuum observations of Rho Ophiuchi A – the candidate protostar VLA 1623 and prestellar clumps.' *The Astrophysical Journal, Part 1* 406, no. 1 (March): 122–141.

Anthonioz, F., F. Ménard, C. Pinte, et al. 2015. 'The VLTI/PIONIER near-infrared interferometric survey of southern T Tauri stars. I. First results.' A&A 574 (January): A41.

Anugu, Narsireddy, Jean-Baptiste Le Bouquin, John D. Monnier, et al. 2020. 'MIRC-X: A Highly Sensitive Six-telescope Interferometric Imager at the CHARA Array.' AJ 160, no. 4 (October): 158.

Arsenault, Robin, Jaime Alonso, Henri Bonnet, et al. 2003. 'MACAO-VLTI: an adaptive optics system for the ESO interferometer.' *Wizinowich, Peter L.; Bonaccini, Domenico: Adaptive optical system technologies II, SPIE, 174-185 (2003)* (February).

Artymowicz, P., C. J. Clarke, S. H. Lubow, et al. 1991. 'The Effect of an External Disk on the Orbital Elements of a Central Binary.' ApJL 370 (March): L35.

Artymowicz, Pawel, and Stephen H. Lubow. 1994. 'Dynamics of Binary-Disk Interaction. I. Resonances and Disk Gap Sizes.' ApJ 421 (February): 651.

Audard, M., P. Ábrahám, M. M. Dunham, et al. 2014. 'Episodic Accretion in Young Stars.' In *Protostars and Planets VI,* edited by Henrik Beuther, Ralf S. Klessen, Cornelis P. Dullemond, et al., 387. January.

El-Badry, Kareem, Hans-Walter Rix, and Tyler M. Heintz. 2021. 'A million binaries from Gaia eDR3: sample selection and validation of Gaia parallax uncertainties.' MNRAS 506, no. 2 (September): 2269–2295.

El-Badry, Kareem, Yuan-Sen Ting, Hans-Walter Rix, et al. 2018. 'Discovery and characterization of 3000+ main-sequence binaries from APOGEE spectra.' MNRAS 476, no. 1 (May): 528–553.

Bailer-Jones, C. A. L., J. Rybizki, M. Fouesneau, et al. 2018. 'Estimating Distance from Parallaxes. IV. Distances to 1.33 Billion Stars in Gaia Data Release 2.' AJ 156, no. 2 (August): 58.

Bailer-Jones, C. A. L., J. Rybizki, M. Fouesneau, et al. 2021. 'Estimating Distances from Parallaxes. V. Geometric and Photogeometric Distances to 1.47 Billion Stars in Gaia Early Data Release 3.' AJ 161, no. 3 (March): 147.

Baines, Deborah, René D. Oudmaijer, John M. Porter, et al. 2006. 'On the binarity of Herbig Ae/Be stars.' MNRAS 367, no. 2 (April): 737–753.

Balega, Iu., A. Blazit, D. Bonneau, et al. 1982. 'The angular diameter of Betelgeuse.' A&A 115 (November): 253–256.

Ball, R. S. 1872. 'Binary Stars: ξ Ursæ Majoris.' MNRAS 32 (June): 336.

Baraffe, I., G. Chabrier, F. Allard, et al. 1995. 'New Evolutionary Tracks for Very Low Mass Stars.' ApJL 446 (June): L35.

Baraffe, Isabelle, Derek Homeier, France Allard, et al. 2015. 'New evolutionary models for pre-main sequence and main sequence low-mass stars down to the hydrogen-burning limit.' A&A 577 (May): A42.

Bate, M. R., S. H. Lubow, G. I. Ogilvie, et al. 2003. 'Three-dimensional calculations of high- and low-mass planets embedded in protoplanetary discs.' MNRAS 341 (May): 213–229.

Bate, Matthew R. 1998. 'Collapse of a Molecular Cloud Core to Stellar Densities: The First Three-dimensional Calculations.' ApJL 508, no. 1 (November): L95–L98.

Beck, Tracy L., Jeffery S. Bary, and Peter J. McGregor. 2010. 'Spatially Extended Brackett Gamma Emission in the Environments of Young Stars.' ApJ 722, no. 2 (October): 1360–1372.

Belyaev, Mikhail A., and Roman R. Rafikov. 2012. 'Supersonic Shear Instabilities in Astrophysical Boundary Layers.' ApJ 752, no. 2 (June): 115.

Belyaev, Mikhail A., Roman R. Rafikov, and James M. Stone. 2013. 'Angular Momentum Transport by Acoustic Modes Generated in the Boundary Layer. II. Magnetohydrodynamic Simulations.' ApJ 770, no. 1 (June): 68.

Benisty, M., C. Dominik, K. Follette, et al. 2022. 'Optical and Near-infrared View of Planet-forming Disks and Protoplanets.' *arXiv e-prints* (March): arXiv:2203.09991.

Benisty, M., A. Juhasz, A. Boccaletti, et al. 2015. 'Asymmetric features in the protoplanetary disk MWC 758.' A&A 578 (June): L6.

Benisty, Myriam, Jaehan Bae, Stefano Facchini, et al. 2021. 'A Circumplanetary Disk around PDS70c.' ApJL 916, no. 1 (July): L2.

Berger, Jean Philippe, and Damien Segransan. 2007. 'An introduction to visibility modeling.' *New Astronomy Reviews* 51, nos. 8-9 (October): 576–582.

Bergin, Edwin A., and Mario Tafalla. 2007. 'Cold Dark Clouds: The Initial Conditions for Star Formation.' ARA&A 45, no. 1 (September): 339–396.

Biller, Beth, Sylvestre Lacour, Attila Juhász, et al. 2012. 'A Likely Close-in Low-mass Stellar Companion to the Transitional Disk Star HD 142527.' ApJL 753, no. 2 (July): L38.

Birko, Danijela, Tomaž Zwitter, Eva K. Grebel, et al. 2019. 'Single-lined Spectroscopic Binary Star Candidates from a Combination of the RAVE and Gaia DR2 Surveys.' AJ 158, no. 4 (October): 155.

Blind, N., H. M. J. Boffin, J. -P. Berger, et al. 2011. 'An incisive look at the symbiotic star ¡ASTROBJ¿SS Leporis¡/ASTROBJ¿. Milli-arcsecond imaging with PIONIER/VLTI.' A&A 536 (December): A55.

Blum, Edward, and Sergei Lototsky. 2006. *Mathematics of Physics and Engineering.* 98. July.

Boehler, Y., E. Weaver, A. Isella, et al. 2017. 'A Close-up View of the Young Circumbinary Disk HD 142527.' ApJ 840, no. 1 (May): 60.

Boffin, H. M. J. 2012. 'The mass-ratio distribution of spectroscopic binaries.' In *Orbital Couples: Pas de Deux in the Solar System and the Milky Way,* edited by F. Arenou and D. Hestroffer, 41–44. May.

Böhm, T., C. Catala, L. Balona, et al. 2004. 'Spectroscopic monitoring of the Herbig Ae star HD 104237. I. Multiperiodic stellar oscillations.' A&A 427 (December): 907–922.

Boissier, J., T. Alonso-Albi, A. Fuente, et al. 2011. 'Massive young disks around Herbig Ae stars.' A&A 531 (July): A50.

Bonneau, D., J.-M. Clausse, X. Delfosse, et al. 2006. 'SearchCal: a virtual observatory tool for searching calibrators in optical long baseline interferometry. I. The bright object case.' A&A 456 (September): 789–789.

Bonnell, I. A., M. R. Bate, C. J. Clarke, et al. 2001. 'Competitive accretion in embedded stellar clusters.' MNRAS 323, no. 4 (May): 785–794.

Bonnell, Ian A., Matthew R. Bate, and Stephen G. Vine. 2003. 'The hierarchical formation of a stellar cluster.' MNRAS 343, no. 2 (August): 413–418.

Bordier, E., A. J. Frost, H. Sana, et al. 2022. 'The origin of close massive binaries in the M17 star-forming region.' A&A 663 (July): A26.

Born, Max, and Emil Wolf. 1999. *Principles of Optics.*

Bourgès, L., G. Mella, S. Lafrasse, et al. 2017. 'VizieR Online Data Catalog: JMMC Stellar Diameters Catalogue - JSDC. Version 2 (Bourges+, 2017).' *VizieR Online Data Catalog* 2346 (January).

Bouvier, J., S. H. P. Alencar, T. J. Harries, et al. 2007. 'Magnetospheric Accretion in Classical T Tauri Stars.' In *Protostars and Planets V,* edited by Bo Reipurth, David Jewitt, and Klaus Keil, 479. January.

Bouvier, J., K. Perraut, J. -B. Le Bouquin, et al. 2020. 'Probing the magnetospheric accretion region of the young pre-transitional disk system DoAr 44 using VLTI/GRAVITY.' A&A 636 (April): A108.

Bressan, Alessandro, Paola Marigo, Léo. Girardi, et al. 2012. 'PARSEC: stellar tracks and isochrones with the PAdova and TRieste Stellar Evolution Code.' ADS Bibcode: 2012MNRAS.427..127B, *Monthly Notices of the Royal Astronomical Society* 427 (November): 127–145. Accessed March 11, 2022.

Buscher, D. F., M. Creech-Eakman, A. Farris, et al. 2013. 'The Conceptual Design Of The Magdalena Ridge Observatory Interferometer.' *Journal of Astronomical Instrumentation* 02 (02): 1340001.

Buscher, David F. 2015. *Practical Optical Interferometry.*

Busetti, F., H. Beust, and C. Harley. 2018. 'Stability of planets in triple star systems.' A&A 619 (November): A91.

Calvet, N., P. D'Alessio, L. Hartmann, et al. 2002. 'Evidence for a Developing Gap in a 10 Myr Old Protoplanetary Disk.' ApJ 568 (April): 1008–1016.

Calvet, Nuria, James Muzerolle, César Briceño, et al. 2004. 'The Mass Accretion Rates of Intermediate-Mass T Tauri Stars.' AJ 128, no. 3 (September): 1294–1318.

Camenzind, M. 1990. 'Magnetized Disk-Winds and the Origin of Bipolar Outflows.' *Reviews in Modern Astronomy* 3 (January): 234–265.

Carciofi, Alex C. 2011. 'The circumstellar discs of Be stars.' In *Active OB Stars: Structure, Evolution, Mass Loss, and Critical Limits,* edited by Coralie Neiner, Gregg Wade, Georges Meynet, et al., 272:325–336. July.

Catanzaro, G. 2013. 'Spectroscopic atlas of Hα and Hβ in a sample of northern Be stars.' A&A 550 (February): A79.

Chen, Cheng, Alessia Franchini, Stephen H. Lubow, et al. 2019. 'Orbital dynamics of circumbinary planets.' MNRAS 490, no. 4 (December): 5634–5646.

Chen, Yang, Alessandro Bressan, Léo Girardi, et al. 2015. 'PARSEC evolutionary tracks of massive stars up to 350 $M_{\odot}$ at metallicities $0.0001 \leq Z \leq 0.04$.' ADS Bibcode: 2015MNRAS.452.1068C, *Monthly Notices of the Royal Astronomical Society* 452 (September): 1068–1080. Accessed March 11, 2022.

Chen, Yang, Léo Girardi, Alessandro Bressan, et al. 2014. 'Improving PARSEC models for very low mass stars.' ADS Bibcode: 2014MNRAS.444.2525C, *Monthly Notices of the Royal Astronomical Society* 444 (November): 2525–2543. Accessed March 11, 2022.

Chiang, E. I., and P. Goldreich. 1997. 'Spectral Energy Distributions of T Tauri Stars with Passive Circumstellar Disks.' ApJ 490 (November): 368–376.

Chiang, E. I., M. K. Joung, M. J. Creech-Eakman, et al. 2001. 'Spectral Energy Distributions of Passive T Tauri and Herbig Ae Disks: Grain Mineralogy, Parameter Dependences, and Comparison with Infrared Space Observatory LWS Observations.' ApJ 547, no. 2 (February): 1077–1089.

Choi, Jieun, Aaron Dotter, Charlie Conroy, et al. 2016. 'Mesa Isochrones and Stellar Tracks (MIST). I. Solar-scaled Models.' ApJ 823, no. 2 (June): 102.

Cieza, Lucas A., Deborah L. Padgett, Lori E. Allen, et al. 2009. 'Primordial Circumstellar Disks in Binary Systems: Evidence for Reduced Lifetimes.' ApJL 696, no. 1 (May): L84–L88.

Clariá, J. J. 1974a. 'A study of the stellar association Canis Major OB 1.' A&A 37 (December): 229–236.

Clariá, J. J. 1974b. 'Investigation of a Milky Way region in Canis Majoris.' AJ 79 (October): 1022–1039.

Cochetti, Y. R., C. Arcos, S. Kanaan, et al. 2019. 'Spectro-interferometric observations of a sample of Be stars. Setting limits to the geometry and kinematics of stable Be disks.' A&A 621 (January): A123.

Coleman, Matthew S. B., Roman R. Rafikov, and Alexander A. Philippov. 2022. 'Boundary layers of accretion discs: Discovery of vortex-driven modes and other waves.' MNRAS 509, no. 1 (January): 440–462.

Collins, II, George W. 1987. 'The Use of Terms and Definitions in the Study of be Stars (review Paper).' In *IAU Colloq. 92: Physics of Be Stars,* edited by Arne Slettebak and Theodore P. Snow, 3. January.

Corporon, P., and A.-M. Lagrange. 1999. 'A search for spectroscopic binaries among Herbig Ae/Be stars.' A&AS 136 (May): 429–444.

Cowley, C. R., F. Castelli, and S. Hubrig. 2013. 'The Herbig Ae SB2 system HD 104237.' MNRAS 431, no. 4 (June): 3485–3493.

Curé, Michel, Diego F. Rial, Julia Cassetti, et al. 2015. 'A method to deconvolve mass ratio distribution of binary stars.' A&A 573 (January): A86.

Daemgen, S., S. Correia, and M. G. Petr-Gotzens. 2012. 'Protoplanetary disks of T Tauri binary systems in the Orion nebula cluster.' A&A 540 (April): A46.

Dobbs, C. L., M. R. Krumholz, J. Ballesteros-Paredes, et al. 2014. 'Formation of Molecular Clouds and Global Conditions for Star Formation.' In *Protostars and Planets VI,* edited by Henrik Beuther, Ralf S. Klessen, Cornelis P. Dullemond, et al., 3. January.

Dominik, C., C. P. Dullemond, L. B. F. M. Waters, et al. 2003. 'Understanding the spectra of isolated Herbig stars in the frame of a passive disk model.' A&A 398 (February): 607–619.

Donehew, Brian, and Sean Brittain. 2011. 'Measuring the Stellar Accretion Rates of Herbig Ae/Be Stars.' AJ 141, no. 2 (February): 46.

Doyle, Laurance R., Joshua A. Carter, Daniel C. Fabrycky, et al. 2011. 'Kepler-16: A Transiting Circumbinary Planet.' *Science* 333, no. 6049 (September): 1602.

Duchêne, G. 1999. 'Binary fraction in low-mass star forming regions: a reexamination of the possible excesses and implications.' A&A 341 (January): 547–552.

Duchêne, Gaspard, and Adam Kraus. 2013. 'Stellar Multiplicity.' ARA&A 51, no. 1 (August): 269–310.

Dullemond, C. P., A. Juhasz, A. Pohl, et al. 2012. *RADMC-3D: A multi-purpose radiative transfer tool.* Astrophysics Source Code Library, record ascl:1202.015, February.

Dullemond, C. P., and J. D. Monnier. 2010. 'The Inner Regions of Protoplanetary Disks.' ARA&A 48 (September): 205–239.

Dunham, M. M., A. M. Stutz, L. E. Allen, et al. 2014. 'The Evolution of Protostars: Insights from Ten Years of Infrared Surveys with Spitzer and Herschel.' In *Protostars and Planets VI,* edited by Henrik Beuther, Ralf S. Klessen, Cornelis P. Dullemond, et al., 195. January.

Dunham, Michael M., Lori E. Allen, II Evans Neal J., et al. 2015. 'Young Stellar Objects in the Gould Belt.' ApJS 220, no. 1 (September): 11.

Dunhill, A. C., J. Cuadra, and C. Dougados. 2015. 'Precession and accretion in circumbinary discs: the case of HD 104237.' MNRAS 448, no. 4 (April): 3545–3554.

Edwards, S., P. Hartigan, L. Ghandour, et al. 1994. 'Spectroscopic Evidence for Magnetospheric Accretion in Classical T Tauri Stars.' AJ 108 (September): 1056.

Eisner, J. A., J. D. Monnier, J. Woillez, et al. 2010. 'Spatially and Spectrally Resolved Hydrogen Gas within 0.1 AU of T Tauri and Herbig Ae/Be Stars.' ApJ 718, no. 2 (August): 774–794.

Ercolano, Barbara, and Giovanni Rosotti. 2015. 'The link between disc dispersal by photoevaporation and the semimajor axis distribution of exoplanets.' MNRAS 450, no. 3 (July): 3008–3014.

Ertel, S., O. Absil, D. Defrère, et al. 2014. 'A near-infrared interferometric survey of debris-disk stars. IV. An unbiased sample of 92 southern stars observed in H band with VLTI/PIONIER.' A&A 570 (October): A128.

ESA, ed. 1997. *The HIPPARCOS and TYCHO catalogues. Astrometric and photometric star catalogues derived from the ESA HIPPARCOS Space Astrometry Mission.* Vol. 1200. ESA Special Publication.

Espaillat, C., J. Muzerolle, J. Najita, et al. 2014. 'An Observational Perspective of Transitional Disks.' In *Protostars and Planets VI,* edited by Henrik Beuther, Ralf S. Klessen, Cornelis P. Dullemond, et al., 497. January.

Fabricius, C., E. Hög, V. V. Makarov, et al. 2002. 'The Tycho double star catalogue.' A&A 384 (March): 180–189.

Fabry, M., C. Hawcroft, A. J. Frost, et al. 2021a. 'Resolving the dynamical mass tension of the massive binary 9 Sagittarii.' A&A 651 (July): A119.

Fabry, Matthias, Calum Hawcroft, Laurent Mahy, et al. 2021b. *spinOS: SPectroscopic and INterferometric Orbital Solution finder.* Astrophysics Source Code Library, record ascl:2102.001, February.

Fairlamb, J. R., R. D. Oudmaijer, I. Mendigutia, et al. 2017. 'A spectroscopic survey of Herbig Ae/Be stars with X-Shooter - II. Accretion diagnostic lines.' MNRAS 464, no. 4 (February): 4721–4735.

Fairlamb, J. R., R. D. Oudmaijer, I. Mendigutía, et al. 2015. 'A spectroscopic survey of Herbig Ae/Be stars with X-shooter - I. Stellar parameters and accretion rates.' MNRAS 453, no. 1 (October): 976–1001.

Feigelson, Eric D., Warrick A. Lawson, and Gordon P. Garmire. 2003. 'The ϵ Chamaeleontis Young Stellar Group and the Characterization of Sparse Stellar Clusters.' ApJ 599, no. 2 (December): 1207–1222.

Feigelson, Eric D., and Thierry Montmerle. 1999. 'High-Energy Processes in Young Stellar Objects.' ARA&A 37 (January): 363–408.

Finkenzeller, U., and R. Mundt. 1984. 'The Herbig Ae/Be stars associated with nebulosity.' A&AS 55 (January): 109–141.

Fiorellino, Eleonora, Carlo F. Manara, Brunella Nisini, et al. 2021. 'KMOS study of the mass accretion rate from Class I to Class II in NGC 1333.' A&A 650 (June): A43.

Fizeau, Hippolyte. 1868. 'Prix Bordin: Rapport sur le concours de l'année 1867.' *Comptes Rendus de l'Académie des Sciences* 66:932–934.

Flock, M., S. Fromang, M. González, et al. 2013. 'Radiation magnetohydrodynamics in global simulations of protoplanetary discs.' A&A 560 (December): A43.

Foreman-Mackey, Daniel. 2016. 'corner.py: Scatterplot matrices in Python.' *The Journal of Open Source Software* 1, no. 2 (June): 24.

Francis, Logan, and Nienke van der Marel. 2020. 'Dust-depleted Inner Disks in a Large Sample of Transition Disks through Long-baseline ALMA Observations.' ApJ 892, no. 2 (April): 111.

Freudling, W., M. Romaniello, D. M. Bramich, et al. 2013. 'Automated data reduction workflows for astronomy. The ESO Reflex environment.' A&A 559 (November): A96.

Froebrich, D., S. Schmeja, M. D. Smith, et al. 2006. 'Evolution of Class 0 protostars: models versus observations.' *Monthly Notices of the Royal Astronomical Society* 368, no. 1 (March): 435–446.

Frost, A. J., J. Bodensteiner, Th. Rivinius, et al. 2022. 'HR 6819 is a binary system with no black hole. Revisiting the source with infrared interferometry and optical integral field spectroscopy.' A&A 659 (March): L3.

Fukagawa, Misato, Motohide Tamura, Yoichi Itoh, et al. 2006. 'Near-Infrared Images of Protoplanetary Disk Surrounding HD 142527.' ApJL 636, no. 2 (January): L153–L156.

Fumel, A., and T. Böhm. 2012. 'Spectroscopic monitoring of the Herbig Ae star HD 104237. II. Non-radial pulsations, mode analysis, and fundamental stellar parameters.' A&A 540 (April): A108.

Garcia, P. J. V., M. Benisty, C. Dougados, et al. 2013. 'Pre-main-sequence binaries with tidally disrupted discs: the Brγ in HD 104237.' MNRAS 430, no. 3 (April): 1839–1853.

Garcia Lopez, R., A. Natta, L. Testi, et al. 2006. 'Accretion rates in Herbig Ae stars.' A&A 459, no. 3 (December): 837–842.

Gardner, Tyler, John D. Monnier, Francis C. Fekel, et al. 2022. 'ARMADA. II. Further Detections of Inner Companions to Intermediate-mass Binaries with Microarcsecond Astrometry at CHARA and VLTI.' AJ 164, no. 5 (November): 184.

Getman, Konstantin V., Patrick S. Broos, Demerese M. Salter, et al. 2011. 'The Young Binary DQ Tau: A Hunt for X-ray Emission from Colliding Magnetospheres.' ApJ 730, no. 1 (March): 6.

Gomez de Castro, A. I., J. Lopez-Santiago, and A. Talavera. 2013. 'Evidence of accretion triggered oscillations in the pre-main-sequence interacting binary AK Sco.' MNRAS 429 (February): L1–L4.

Gontcharov, George A., and Aleksandr V. Mosenkov. 2017. 'Verifying reddening and extinction for Gaia DR1 TGAS main sequence stars.' MNRAS 472, no. 4 (December): 3805–3820.

Grady, C. A., B. Woodgate, Carlos A. O. Torres, et al. 2004. 'The Environment of the Optically Brightest Herbig Ae Star, HD 104237.' ApJ 608, no. 2 (June): 809–830.

Gravity Collaboration, R. Abuter, M. Accardo, et al. 2017. 'First light for GRAVITY: Phase referencing optical interferometry for the Very Large Telescope Interferometer.' A&A 602 (June): A94.

GRAVITY Collaboration, R. Abuter, A. Amorim, et al. 2018. 'Detection of the gravitational redshift in the orbit of the star S2 near the Galactic centre massive black hole.' A&A 615 (July): L15.

GRAVITY Collaboration, R. Abuter, A. Amorim, et al. 2020. 'Detection of the Schwarzschild precession in the orbit of the star S2 near the Galactic centre massive black hole.' A&A 636 (April): L5.

GRAVITY Collaboration, R. Garcia Lopez, K. Perraut, et al. 2017. 'The wind and the magnetospheric accretion onto the T Tauri star S Coronae Australis at sub-au resolution.' A&A 608 (December): A78.

Gregorio-Hetem, J. 2008. 'The Canis Major Star Forming Region.' In *Handbook of Star Forming Regions, Volume II,* edited by B. Reipurth, 5:1.

Grundstrom, Erika D., M. V. McSwain, C. Aragona, et al. 2011. 'Observations of Be Disk Building: Optical Spectra of NW Serpentis (HD 168797) over 35 days.' *Bulletin de la Societe Royale des Sciences de Liege* 80 (January): 371–375.

Hadjara, M., R. G. Petrov, S. Jankov, et al. 2022. 'Application limit of the photocentre displacement to fundamental stellar parameters of fast rotators - illustration on the edge-on fast rotator Regulus.' MNRAS 511, no. 4 (April): 4724–4740.

Haemmerlé, L., P. Eggenberger, S. Ekström, et al. 2019. 'Stellar models and isochrones from low-mass to massive stars including pre-main sequence phase with accretion.' A&A 624 (April): A137.

Haisch, Jr., Karl E., Elizabeth A. Lada, and Charles J. Lada. 2001. 'Disk Frequencies and Lifetimes in Young Clusters.' ApJL 553, no. 2 (June): L153–L156.

Hales, A. S., I. De Gregorio-Monsalvo, B. Montesinos, et al. 2014. 'A CO Survey in Planet-forming Disks: Characterizing the Gas Content in the Epoch of Planet Formation.' AJ 148, no. 3 (September): 47.

Hamers, Adrian S., and Simon F. Portegies Zwart. 2016. 'Secular dynamics of hierarchical multiple systems composed of nested binaries, with an arbitrary number of bodies and arbitrary hierarchical structure. First applications to multiplanet and multistar systems.' MNRAS 459, no. 3 (July): 2827–2874.

Hanbury Brown, R., and R. Q. Twiss. 1956a. 'A Test of a New Type of Stellar Interferometer on Sirius.' *Nature* 178 (4541): 1046–1048.

Hanbury Brown, R., and R. Q. Twiss. 1956b. 'The Question of Correlation between Photons in Coherent Light Rays.' *Nature* 178 (4548): 1447–1448.

Haniff, C. A., C. D. Mackay, D. J. Titterington, et al. 1987. 'The first images from optical aperture synthesis.' Nature 328, no. 6132 (August): 694–696.

Haniff, Chris. 2007. 'An introduction to the theory of interferometry.' *New Astronomy Reviews* 51, nos. 8-9 (October): 565–575.

Hanuschik, R. W., W. Hummel, O. Dietle, et al. 1995. 'V/R variability and global oscillations in Be star disks.' A&A 300 (August): 163.

Harries, T. J. 2000. 'Synthetic line profiles of rotationally distorted hot-star winds.' MNRAS 315 (July): 722–734.

Harris, Robert J., Sean M. Andrews, David J. Wilner, et al. 2012. 'A Resolved Census of Millimeter Emission from Taurus Multiple Star Systems.' ApJ 751, no. 2 (June): 115.

Hartmann, Lee. 2009. *Accretion Processes in Star Formation: Second Edition.*

Hartmann, Lee, Nuria Calvet, Erik Gullbring, et al. 1998. 'Accretion and the Evolution of T Tauri Disks.' ApJ 495, no. 1 (March): 385–400.

Hartmann, Lee, Gregory Herczeg, and Nuria Calvet. 2016. 'Accretion onto Pre-Main-Sequence Stars.' *Annual Review of Astronomy and Astrophysics* 54 (1): 135–180.

Hartmann, Lee, Robert Hewett, and Nuria Calvet. 1994. 'Magnetospheric Accretion Models for T Tauri Stars. I. Balmer Line Profiles without Rotation.' ApJ 426 (May): 669.

Hayashi, C. 1961. 'Stellar evolution in early phases of gravitational contraction.' PASJ 13 (January): 450–452.

Heath, R. M., and C. J. Nixon. 2020. 'On the orbital evolution of binaries with circumbinary discs.' A&A 641 (September): A64.

Henning, Thomas, and Dmitry Semenov. 2013. 'Chemistry in Protoplanetary Disks.' *Chemical Reviews* 113, no. 12 (December): 9016–9042.

Henyey, L. G., Robert Lelevier, and R. D. Levée. 1955. 'The Early Phases of Stellar Evolution.' PASP 67, no. 396 (June): 154.

Herbig, G. H. 1989. 'FU Orionis eruptions.' In *European Southern Observatory Conference and Workshop Proceedings,* 33:233–246. European Southern Observatory Conference and Workshop Proceedings. September.

Herbig, George H. 1960. 'The Spectra of Be- and Ae-Type Stars Associated with Nebulosity.' ApJS 4 (March): 337.

Herbst, W., and G. E. Assousa. 1977. 'Observational evidence for supernova-induced star formation - Canis Major R1.' ApJ 217 (October): 473–487.

Hillenbrand, Lynne A., and Lee W. Hartmann. 1998. 'A Preliminary Study of the Orion Nebula Cluster Structure and Dynamics.' ApJ 492, no. 2 (January): 540–553.

Hillenbrand, Lynne A., Stephen E. Strom, Frederick J. Vrba, et al. 1992. 'Herbig Ae/Be Stars: Intermediate-Mass Stars Surrounded by Massive Circumstellar Accretion Disks.' ApJ 397 (October): 613.

Hoyle, F. 1953. 'On the Fragmentation of Gas Clouds Into Galaxies and Stars.' ApJ 118 (November): 513.

Hu, J. Y., P. S. The, and D. de Winter. 1989. 'Photometric and spectroscopic study of three candidate Herbig Ae/Be stars : HD 37411, HD 100546 and HD 104237.' A&A 208 (January): 213–218.

Huang, Jane, Sean M. Andrews, Laura M. Pérez, et al. 2018. 'The Disk Substructures at High Angular Resolution Project (DSHARP). III. Spiral Structures in the Millimeter Continuum of the Elias 27, IM Lup, and WaOph 6 Disks.' ApJL 869, no. 2 (December): L43.

Hubrig, S., S. P. Järvinen, M. Schöller, et al. 2019. 'Observations of Magnetic Fields in Herbig Ae/Be Stars.' In *Physics of Magnetic Stars,* edited by D. O. Kudryavtsev, I. I. Romanyuk, and I. A. Yakunin, 518:18. Astronomical Society of the Pacific Conference Series. July.

Hummel, W., and R. W. Hanuschik. 1997. 'Line formation in Be star envelopes. II. Disk oscillations.' A&A 320 (April): 852–864.

Hunziker, S., H. M. Schmid, J. Ma, et al. 2021. 'HD 142527: quantitative disk polarimetry with SPHERE.' A&A 648 (April): A110.

Ireland, Michael J. 2016. 'Aperture Masking Imaging.' In *Astronomy at High Angular Resolution,* edited by Henri M. J. Boffin, Gaitee Hussain, Jean-Philippe Berger, et al., 439:43. Astrophysics and Space Science Library. January.

Isella, A., and A. Natta. 2005. 'The shape of the inner rim in proto-planetary disks.' A&A 438 (August): 899–907.

Järvinen, S P, T A Carroll, S Hubrig, et al. 2019. 'New evidence for weak magnetic fields in Herbig Ae/Be stars.' *Monthly Notices of the Royal Astronomical Society* 489, no. 1 (August): 886–890.

Jeans, J. H. 1902. 'The Stability of a Spherical Nebula.' *Philosophical Transactions of the Royal Society of London Series A* 199 (January): 1–53.

Johns-Krull, Christopher M. 2007. 'The Magnetic Fields of Classical T Tauri Stars.' ApJ 664, no. 2 (August): 975–985.

Johnston, Katharine G., Thomas P. Robitaille, Henrik Beuther, et al. 2015. 'A Keplerian-like Disk around the Forming O-type Star AFGL 4176.' ApJL 813, no. 1 (November): L19.

Johnstone, C. P., M. Jardine, S. G. Gregory, et al. 2013. 'Classical T Tauri stars: magnetic fields, coronae and star–disc interactions.' *Monthly Notices of the Royal Astronomical Society* 437, no. 4 (December): 3202–3220.

Joy, A. H., and G. van Biesbroeck. 1944. 'Five New Double Stars among Variables of the T Tauri Class.' PASP 56, no. 330 (June): 123–124.

Joy, Alfred H. 1945. 'T Tauri Variable Stars.' ApJ 102 (September): 168.

Kaltcheva, N. T., and R. W. Hilditch. 2000. 'The distribution of bright OB stars in the Canis Major-Puppis-Vela region of the Milky Way.' MNRAS 312, no. 4 (March): 753–768.

Kama, M., M. Min, and C. Dominik. 2009. 'The inner rim structures of protoplanetary discs.' A&A 506 (November): 1199–1213.

Kennedy, Grant M., Luca Matrà, Stefano Facchini, et al. 2019. 'A circumbinary protoplanetary disk in a polar configuration.' *Nature Astronomy* 3 (3): 230–235.

Kenyon, S. J., and L. Hartmann. 1987. 'Spectral Energy Distributions of T Tauri Stars: Disk Flaring and Limits on Accretion.' ApJ 323 (December): 714.

Kluska, J., M. Benisty, F. Soulez, et al. 2016. 'A disk asymmetry in motion around the B[e] star MWC158.' A&A 591 (June): A82.

Kobus, J., S. Wolf, T. Ratzka, et al. 2020. 'Interferometric study on the temporal variability of the brightness distributions of protoplanetary disks.' A&A 642 (October): A104.

Koenigl, Arieh. 1991. 'Disk Accretion onto Magnetic T Tauri Stars.' ApJL 370 (March): L39.

Königl, Arieh, and Raquel Salmeron. 2011. 'The Effects of Large-Scale Magnetic Fields on Disk Formation and Evolution.' In *Physical Processes in Circumstellar Disks around Young Stars,* edited by Paulo J. V. Garcia, 283–352.

Kozai, Yoshihide. 1962. 'Secular perturbations of asteroids with high inclination and eccentricity.' AJ 67 (November): 591–598.

Kraus, S., K.-H. Hofmann, M. Benisty, et al. 2008. 'The origin of hydrogen line emission for five Herbig Ae/Be stars spatially resolved by VLTI/AMBER spectro-interferometry.' A&A 489 (October): 1157–1173.

Kraus, S., G. Weigelt, Y. Y. Balega, et al. 2009. 'Tracing the young massive high-eccentricity binary system θ^1Orionis C through periastron passage.' A&A 497, no. 1 (April): 195–207.

Kraus, Stefan, Nuria Calvet, Lee Hartmann, et al. 2012. 'On the Nature of the Herbig B[e] Star Binary System V921 Scorpii: Geometry and Kinematics of the Circumprimary Disk on Sub-AU Scales.' ApJ 752, no. 1 (June): 11.

Kraus, Stefan, Karl-Heinz Hofmann, Karl M. Menten, et al. 2010. 'A hot compact dust disk around a massive young stellar object.' Nature 466, no. 7304 (July): 339–342.

Kraus, Stefan, Alexander Kreplin, Alison K. Young, et al. 2020. 'A triple-star system with a misaligned and warped circumstellar disk shaped by disk tearing.' *Science* 369, no. 6508 (September): 1233–1238.

Kraus, Stefan, John D. Monnier, Narsireddy Anugu, et al. 2018. 'The MIRC-X 6-telescope imager: key science drivers, instrument design and operation.' In *Optical and Infrared Interferometry and Imaging VI,* edited by Michelle J. Creech-Eakman, Peter G. Tuthill, and Antoine Mérand, 10701:1070123. Society of Photo-Optical Instrumentation Engineers (SPIE) Conference Series. July.

Kreplin, Alexander, Larisa Tambovtseva, Vladimir Grinin, et al. 2018. 'On the Brγ line emission of the Herbig Ae/Be star MWC 120.' MNRAS 476, no. 4 (June): 4520–4526.

Krumholz, Mark R., Richard I. Klein, Christopher F. McKee, et al. 2009. 'The Formation of Massive Star Systems by Accretion.' *Science* 323, no. 5915 (February): 754.

Kuiper, Rolf, Hubert Klahr, Henrik Beuther, et al. 2014. 'A Solution to the Radiation Pressure Problem in the Formation of Massive Stars.' In *The Labyrinth of Star Formation,* 36:379. Astrophysics and Space Science Proceedings. January.

Kurucz, R. L. 1993. 'VizieR Online Data Catalog: Model Atmospheres (Kurucz, 1979).' *VizieR Online Data Catalog* (October): VI/39.

Labadie-Bartz, Jonathan, Joshua Pepper, M. Virginia McSwain, et al. 2017. 'Photometric Variability of the Be Star Population.' AJ 153, no. 6 (June): 252.

Labeyrie, A. 1970. 'Attainment of Diffraction Limited Resolution in Large Telescopes by Fourier Analysing Speckle Patterns in Star Images.' A&A 6 (May): 85.

Labeyrie, A. 1975. 'Interference fringes obtained on Vega with two optical telescopes.' ApJL 196 (March): L71–L75.

Labeyrie, A., S. G. Lipson, and P. Nisenson. 2006. *An Introduction to Optical Stellar Interferometry.*

Lachaume, R. 2003. 'On marginally resolved objects in optical interferometry.' A&A 400 (March): 795–803.

Lacour, S., B. Biller, A. Cheetham, et al. 2016. 'An M-dwarf star in the transition disk of Herbig HD 142527. Physical parameters and orbital elements.' A&A 590 (May): A90.

Lada, C. J. 1987. 'Star formation - From OB associations to protostars.' In *Star Forming Regions,* edited by M. Peimbert and J. Jugaku, 115:1–17. IAU Symposium.

Lada, Charles J., and Frank H. Shu. 1990. 'The Formation of Sunlike Stars.' *Science* 248, no. 4955 (May): 564–572.

Lagrange, A. -M., A. Boccaletti, J. Milli, et al. 2012. 'The position of β Pictoris b position relative to the debris disk.' A&A 542 (June): A40.

Lakeland, Ben S., and Tim Naylor. 2022. 'Towards an understanding of YSO variability: a multiwavelength analysis of bursting, dipping, and symmetrically varying light curves of disc-bearing YSOs.' MNRAS 514, no. 2 (August): 2736–2755.

Laos, Stefan, Thomas P. Greene, Joan R. Najita, et al. 2021. 'The Near-stellar Environment of Class 0 Protostars: A First Look with Near-infrared Spectroscopy.' ApJ 921, no. 2 (November): 110.

Larson, Richard B. 2003. 'The physics of star formation.' *Reports on Progress in Physics* 66, no. 10 (October): 1651–1697.

Lazareff, B., J. -P. Berger, J. Kluska, et al. 2017. 'Structure of Herbig AeBe disks at the milliarcsecond scale . A statistical survey in the H band using PIONIER-VLTI.' A&A 599 (March): A85.

Le Bouquin, J. -B., O. Absil, M. Benisty, et al. 2009. 'The spin-orbit alignment of the Fomalhaut planetary system probed by optical long baseline interferometry.' A&A 498, no. 3 (May): L41–L44.

Le Bouquin, J. -B., J. -P. Berger, B. Lazareff, et al. 2011. 'PIONIER: a 4-telescope visitor instrument at VLTI.' A&A 535 (November): A67.

Lee, Umin, Yoji Osaki, and Hideyuki Saio. 1991. 'Viscous excretion discs around Be stars.' MNRAS 250 (May): 432–437.

Leinert, Ch., H. Zinnecker, N. Weitzel, et al. 1993. 'A systematic search for young binaries in Taurus.' A&A 278 (October): 129–149.

Li, Min, and Lin Xiao. 2016. 'Lifetimes and Accretion Rates of Protoplanetary Disks.' ApJ 820, no. 1 (March): 36.

Lidov, M. L. 1962. 'The evolution of orbits of artificial satellites of planets under the action of gravitational perturbations of external bodies.' Planet. Space Sci. 9, no. 10 (October): 719–759.

Lopez, B., S. Lagarde, R. G. Petrov, et al. 2022. 'MATISSE, the VLTI mid-infrared imaging spectro-interferometer.' A&A 659 (March): A192.

Low, C., and D. Lynden-Bell. 1976. 'The minimum Jeans mass or when fragmentation must stop.' MNRAS 176 (August): 367–390.

Lubow, S. H., and G. I. Ogilvie. 1998. 'Three-dimensional Waves Generated at Lindblad Resonances in Thermally Stratified Disks.' ApJ 504, no. 2 (September): 983–995.

Lynden-Bell, D., and A. J. Kalnajs. 1972. 'On the generating mechanism of spiral structure.' MNRAS 157 (January): 1.

Lynden-Bell, D., and J. E. Pringle. 1974. 'The evolution of viscous discs and the origin of the nebular variables.' MNRAS 168 (September): 603–637.

Manara, C. F., L. Testi, E. Rigliaco, et al. 2013. 'X-shooter spectroscopy of young stellar objects. II. Impact of chromospheric emission on accretion rate estimates.' A&A 551 (March): A107.

Marchand, Pierre, Kengo Tomida, Kei E. I. Tanaka, et al. 2020. 'Protostellar Collapse: Regulation of the Angular Momentum and Onset of an Ionic Precursor.' ApJ 900, no. 2 (September): 180.

Marigo, P., L. Girardi, A. Bressan, et al. 2017. 'A New Generation of PARSEC-COLIBRI Stellar Isochrones Including the TP-AGB Phase.' _Eprint: 1701.08510, ApJ 835 (January): 77.

Marino, S., S. Perez, and S. Casassus. 2015. 'Shadows Cast by a Warp in the HD 142527 Protoplanetary Disk.' ApJL 798, no. 2 (January): L44.

Markarian, B. E. 1952. 'A Revised List of Stellar Clusters of Type O.' *Proc. Acad. Sci. Armenian SSR* 15:13.

Martin, Rebecca G., Stephen Lepp, Stephen H. Lubow, et al. 2022. 'Circumbinary Disk Evolution in the Presence of an Outer Companion Star.' ApJL 927, no. 2 (March): L26.

Martin, Rebecca G., and Stephen H. Lubow. 2017. 'Polar Alignment of a Protoplanetary Disk around an Eccentric Binary.' ApJL 835, no. 2 (February): L28.

Martín, E. L. 1998. 'Weak and Post-T Tauri Stars around B-Type Members of the Scorpius-Centaurus OB Association.' AJ 115, no. 1 (January): 351–357.

Martinez, A. O., and F. Baron. 2020. 'Interferometric 3D imaging of lambda Andromedae.' In *American Astronomical Society Meeting Abstracts #235,* 235:377.03. American Astronomical Society Meeting Abstracts. January.

Massey, Philip, Nidia I. Morrell, Kathryn F. Neugent, et al. 2012. 'Photometric and Spectroscopic Studies of Massive Binaries in the Large Magellanic Cloud. I. Introduction and Orbits for Two Detached Systems: Evidence for a Mass Discrepancy?' ApJ 748, no. 2 (April): 96.

Mathieu, Robert D. 1994. 'Pre-Main-Sequence Binary Stars.' ARA&A 32 (January): 465–530.

Matsushita, Yuko, Masahiro N. Machida, Yuya Sakurai, et al. 2017. 'Massive outflows driven by magnetic effects in star-forming clouds with high mass accretion rates.' MNRAS 470, no. 1 (September): 1026–1049.

McKee, Christopher F., and Eve C. Ostriker. 2007. 'Theory of Star Formation.' ARA&A 45, no. 1 (September): 565–687.

McKee, Christopher F., and Jonathan C. Tan. 2003. 'The Formation of Massive Stars from Turbulent Cores.' ApJ 585, no. 2 (March): 850–871.

Meeus, G., L. B. F. M. Waters, J. Bouwman, et al. 2001. 'ISO spectroscopy of circumstellar dust in 14 Herbig Ae/Be systems: Towards an understanding of dust processing.' A&A 365 (January): 476–490.

Mendigutía, I., N. Calvet, B. Montesinos, et al. 2011. 'Accretion rates and accretion tracers of Herbig Ae/Be stars.' A&A 535 (November): A99.

Mérand, Antoine. 2022. 'Flexible spectro-interferometric modelling of OIFITS data with PMOIRED.' In *Optical and Infrared Interferometry and Imaging VIII,* edited by Antoine Mérand, Stephanie Sallum, and Joel Sanchez-Bermudez, vol. 12183, 121831N. Society of Photo-Optical Instrumentation Engineers (SPIE) Conference Series. August.

Michelson, A. A. 1891. 'Measurement of Jupiter's Satellites by Interference.' Nature 45, no. 1155 (December): 160–161.

Michelson, A. A., and E. W. Morley. 1887. 'On the relative motion of the Earth and the luminiferous ether.' *American Journal of Science* 34, no. 203 (November): 333–345.

Michelson, A. A., and F. G. Pease. 1921. 'Measurement of the Diameter of α Orionis with the Interferometer.' ApJ 53 (May): 249–259.

Michelson, Albert A. 1890. 'I. On the application of interference methods to astronomical measurements.' *The London, Edinburgh, and Dublin Philosophical Magazine and Journal of Science* 30 (182): 1–21.

Millan-Gabet, Rafael, F. Peter Schloerb, and Wesley A. Traub. 2001. 'Spatially Resolved Circumstellar Structure of Herbig AE/BE Stars in the Near-Infrared.' ApJ 546, no. 1 (January): 358–381.

Millour, F. 2014. 'Interferometry concepts.' In *EAS Publications Series,* 69-70:17–52. EAS Publications Series. September.

Miotello, A., S. Facchini, E. F. van Dishoeck, et al. 2018. 'Probing the protoplanetary disk gas surface density distribution with ^{13}CO emission.' A&A 619 (November): A113.

Monnier, J. D. 2007. 'Phases in interferometry.' *New Astronomy Reviews* 51 (October): 604–616.

Monnier, J. D., and R. Millan-Gabet. 2002. 'On the Interferometric Sizes of Young Stellar Objects.' ApJ 579, no. 2 (November): 694–698.

Monnier, John D., Jean-Baptiste Le Bouquin, Narsireddy Anugu, et al. 2018. 'MYSTIC: Michigan Young STar Imager at CHARA.' In *Optical and Infrared Interferometry and Imaging VI,* edited by Michelle J. Creech-Eakman, Peter G. Tuthill, and Antoine Mérand, 10701:1070122. Society of Photo-Optical Instrumentation Engineers (SPIE) Conference Series. July.

Mouillet, D., J. D. Larwood, J. C. B. Papaloizou, et al. 1997. 'A planet on an inclined orbit as an explanation of the warp in the beta Pictoris disc.' MNRAS 292, no. 4 (December): 896–904.

Mullally, F., Jeffrey L. Coughlin, Susan E. Thompson, et al. 2015. 'Planetary Candidates Observed by Kepler. VI. Planet Sample from Q1–Q16 (47 Months).' ApJS 217, no. 2 (April): 31.

Muzerolle, James, Kevin Flaherty, Zoltan Balog, et al. 2019. 'The Inner Disk and Accretion Flow of the Close Binary DQ Tau.' ApJ 877, no. 1 (May): 29.

Muzerolle, James, Lee Hartmann, and Nuria Calvet. 1998. 'Emission-Line Diagnostics of T Tauri Magnetospheric Accretion. I. Line Profile Observations.' AJ 116, no. 1 (July): 455–468.

Nagel, Erick, Paola D'Alessio, Nuria Calvet, et al. 2010. 'Wall Emission in Circumbinary Disks: the Case of Coku Tau/4.' ApJ 708, no. 1 (January): 38–50.

Najita, Joan, John S. Carr, and Alan T. Tokunaga. 1996. 'High-Resolution Spectroscopy of BR gamma Emission in Young Stellar Objects.' ApJ 456 (January): 292.

Natta, A., T. Prusti, R. Neri, et al. 2001. 'A reconsideration of disk properties in Herbig Ae stars.' A&A 371 (May): 186–197.

Niemela, V. 2001. 'A Short History and Other Stories of Binary Stars.' In *Revista Mexicana de Astronomia y Astrofisica Conference Series,* 11:23–26. Revista Mexicana de Astronomia y Astrofisica Conference Series. July.

Paladini, C., F. Baron, A. Jorissen, et al. 2018. 'Large granulation cells on the surface of the giant star π^1 Gruis.' Nature 553, no. 7688 (January): 310–312.

Pastorelli, Giada, Paola Marigo, Léo Girardi, et al. 2019. 'Constraining the thermally pulsing asymptotic giant branch phase with resolved stellar populations in the Small Magellanic Cloud.' ADS Bibcode: 2019MNRAS.485.5666P, *Monthly Notices of the Royal Astronomical Society* 485 (June): 5666–5692. Accessed March 11, 2022.

Pease, F. G. 1931. 'Interferometer Methods in Astronomy.' *Ergebnisse der exakten Naturwissenschaften* 10 (January): 84.

Pérez, Laura M., John M. Carpenter, Sean M. Andrews, et al. 2016. 'Spiral density waves in a young protoplanetary disk.' *Science* 353, no. 6307 (September): 1519–1521.

Perryman, Michael. 2011. *The Exoplanet Handbook.*

Pichardo, Barbara, Linda S. Sparke, and Luis A. Aguilar. 2005. 'Circumstellar and circumbinary discs in eccentric stellar binaries.' MNRAS 359, no. 2 (May): 521–530.

Picogna, Giovanni, Barbara Ercolano, James E. Owen, et al. 2019. 'The dispersal of protoplanetary discs - I. A new generation of X-ray photoevaporation models.' MNRAS 487, no. 1 (July): 691–701.

Piso, Ana-Maria A., Karin I. Öberg, Tilman Birnstiel, et al. 2015. 'C/O and Snowline Locations in Protoplanetary Disks: The Effect of Radial Drift and Viscous Gas Accretion.' ApJ 815, no. 2 (December): 109.

Pogodin, M. A., V. P. Malanushenko, O. V. Kozlova, et al. 2006. 'The Herbig B0e star HD 53367: circumstellar activity and evidence of binarity.' A&A 452, no. 2 (June): 551–559.

Porter, John M., and Thomas Rivinius. 2003. 'Classical Be Stars.' PASP 115, no. 812 (October): 1153–1170.

Ray, T. P., and J. Ferreira. 2021. 'Jets from young stars.' *New Astronomy Reviews* 93 (December): 101615.

Reipurth, Bo, and Hans Zinnecker. 1993. 'Visual binaries among pre-main sequence stars.' A&A 278 (October): 81–108.

Rice, Thomas S., Scott J. Wolk, and Colin Aspin. 2012. 'Near-infrared Variability in Young Stars in Cygnus OB7.' ApJ 755, no. 1 (August): 65.

Rich, Evan A., John D. Monnier, Alicia Aarnio, et al. 2022. 'Gemini-LIGHTS: Herbig Ae/Be and Massive T Tauri Protoplanetary Disks Imaged with Gemini Planet Imager.' AJ 164, no. 3 (September): 109.

Rivinius, Thomas, Alex C. Carciofi, and Christophe Martayan. 2013. 'Classical Be stars. Rapidly rotating B stars with viscous Keplerian decretion disks.' A&A Rev. 21 (October): 69.

Sana, H., S. E. de Mink, A. de Koter, et al. 2012. 'Binary Interaction Dominates the Evolution of Massive Stars.' *Science* 337, no. 6093 (July): 444.

Sana, Hugues. 2017. 'The multiplicity of massive stars: a 2016 view.' In *The Lives and Death-Throes of Massive Stars,* edited by J. J. Eldridge, J. C. Bray, L. A. S. McClelland, et al., 329:110–117. November.

Shevchenko, V. S., O. V. Ezhkova, M. A. Ibrahimov, et al. 1999. 'The stellar composition of the star formation region CMa R1 - I. Results from new photometric and spectroscopic classifications.' MNRAS 310, no. 1 (November): 210–222.

Shu, Frank H., Fred C. Adams, and Susana Lizano. 1987. 'Star formation in molecular clouds: observation and theory.' ARA&A 25 (January): 23–81.

Siess, L., E. Dufour, and M. Forestini. 2000. 'An internet server for pre-main sequence tracks of low- and intermediate-mass stars.' A&A 358 (June): 593–599.

Simon, M., and L. Prato. 1995. 'Disk Dissipation in Single and Binary Young Star Systems in Taurus.' ApJ 450 (September): 824.

Stahler, Steven W. 2011. 'Protostars.' In *Encyclopedia of Astrobiology,* edited by Muriel Gargaud, Ricardo Amils, José Cernicharo Quintanilla, et al., 1378–1385. Berlin, Heidelberg: Springer Berlin Heidelberg.

Stahler, Steven W., and Francesco Palla. 2004. *The Formation of Stars.*

Stassun, Keivan G., Gregory A. Feiden, and Guillermo Torres. 2014. 'Empirical tests of pre-main-sequence stellar evolution models with eclipsing binaries.' *New Astronomy Reviews* 60 (June): 1–28.

Stolker, T., C. Dominik, M. Min, et al. 2016. 'Scattered light mapping of protoplanetary disks.' A&A 596 (December): A70.

Strom, Karen M., Stephen E. Strom, Suzan Edwards, et al. 1989. 'Circumstellar Material Associated with Solar-Type Pre-Main-Sequence Stars: A Possible Constraint on the Timescale for Planet Building.' AJ 97 (May): 1451.

Tallon-Bosc, I., M. Tallon, E. Thiébaut, et al. 2008. 'LITpro: a model fitting software for optical interferometry.' In *Optical and Infrared Interferometry,* edited by Markus Schöller, William C. Danchi, and Françoise Delplancke, vol. 7013, 70131J. Society of Photo-Optical Instrumentation Engineers (SPIE) Conference Series. July.

Tan, J. C., M. T. Beltrán, P. Caselli, et al. 2014. 'Massive Star Formation.' In *Protostars and Planets VI,* edited by Henrik Beuther, Ralf S. Klessen, Cornelis P. Dullemond, et al., 149. January.

Tang, Jing, Alessandro Bressan, Philip Rosenfield, et al. 2014. 'New PARSEC evolutionary tracks of massive stars at low metallicity: testing canonical stellar evolution in nearby star-forming dwarf galaxies.' ADS Bibcode: 2014MNRAS.445.4287T, *Monthly Notices of the Royal Astronomical Society* 445 (December): 4287–4305. Accessed March 11, 2022.

Tatulli, E., A. Isella, A. Natta, et al. 2007. 'Constraining the wind launching region in Herbig Ae stars: AMBER/VLTI spectroscopy of HD 104237.' A&A 464, no. 1 (March): 55–58.

ten Brummelaar, T. A., H. A. McAlister, S. T. Ridgway, et al. 2005. 'First Results from the CHARA Array. II. A Description of the Instrument.' ApJ 628, no. 1 (July): 453–465.

Tjin A Djie, H. R. E., M. E. van den Ancker, P. F. C. Blondel, et al. 2001. 'The stellar composition of the star formation region CMa R1 - II. Spectroscopic and photometric observations of nine young stars.' MNRAS 325, no. 4 (August): 1441–1457.

Tobin, John J., Leslie W. Looney, Zhi-Yun Li, et al. 2016. 'The VLA Nascent Disk and Multiplicity Survey of Perseus Protostars (VANDAM). II. Multiplicity of Protostars in the Perseus Molecular Cloud.' ApJ 818, no. 1 (February): 73.

Tokovinin, A. 1992. 'Speckle Spectroscopic Studies of Late-Type Stars.' In *IAU Colloq. 135: Complementary Approaches to Double and Multiple Star Research,* edited by H. A. McAlister and W. I. Hartkopf, 32:573. Astronomical Society of the Pacific Conference Series. January.

Tovmasyan, G. M., R. Kh. Oganesyan, R. A. Epremyan, et al. 1993. 'Stellar associations in the region of CMa.' AZh 70 (June): 451–460.

Turner, J. A., S. J. Chapman, A. S. Bhattal, et al. 1995. 'Binary star formation: gravitational fragmentation followed by capture.' MNRAS 277, no. 2 (November): 705–726.

van Cittert, P. H. 1934. 'Die Wahrscheinliche Schwingungsverteilung in Einer von Einer Lichtquelle Direkt Oder Mittels Einer Linse Beleuchteten Ebene.' *Physica* 1, no. 1 (January): 201–210.

van den Ancker, M. E., D. de Winter, and H. R. E. Tjin A Djie. 1998. 'HIPPARCOS photometry of Herbig Ae/Be stars.' A&A 330 (February): 145–154.

van den Ancker, Mario. 2005. 'Tracing Accretion onto Herbig Ae/Be Stars Using Near-Infrared Spectroscopy.' In *High Resolution Infrared Spectroscopy in Astronomy,* 309–314. January.

Vioque, M., R. D. Oudmaijer, D. Baines, et al. 2018. 'Gaia DR2 study of Herbig Ae/Be stars.' A&A 620 (December): A128.

Walsh, Catherine, Hideko Nomura, and Ewine van Dishoeck. 2015. 'The molecular composition of the planet-forming regions of protoplanetary disks across the luminosity regime.' A&A 582 (October): A88.

Wichittanakom, C., R. D. Oudmaijer, J. R. Fairlamb, et al. 2020. 'The accretion rates and mechanisms of Herbig Ae/Be stars.' MNRAS 493, no. 1 (March): 234–249.

Wilking, Bruce A. 1989. 'The Formation of Low-Mass Stars.' PASP 101 (March): 229.

Williams, Jonathan P., and Lucas A. Cieza. 2011. 'Protoplanetary Disks and Their Evolution.' *Annual Review of Astronomy and Astrophysics* 49 (1): 67–117.

Woillez, J., J. A. Abad, R. Abuter, et al. 2019. 'NAOMI: the adaptive optics system of the Auxiliary Telescopes of the VLTI.' A&A 629 (September): A41.

Wolf, Emil, and Pierre Meystre. 2008. 'Introduction to the Theory of Coherence and Polarization of Light.' *Physics Today* 61, no. 12 (January): 59.

Yorke, H. W., and E. Kruegel. 1977. 'The dynamical evolution of massive protostellar clouds.' A&A 54, no. 1 (January): 183–194.

Young, T., and P. Kelland. 1845. *A Course of Lectures on Natural Philosophy and the Mechanical Arts: In Two Volumes. Plates.* v. 2. Taylor / Walton.

Zanazzi, J. J., and Dong Lai. 2018. 'Inclination evolution of protoplanetary discs around eccentric binaries.' MNRAS 473, no. 1 (January): 603–615.

Zarrilli, Sebastian A., Stefan Kraus, Alexander Kreplin, et al. 2022. 'Characterising the orbit and circumstellar environment of the high-mass binary MWC 166 A.' A&A 665 (September): A146.

Zernike, F. 1938. 'The concept of degree of coherence and its application to optical problems.' *Physica* 5, no. 8 (August): 785–795.

Zevin, Michael, Mario Spera, Christopher P. L. Berry, et al. 2020. 'Exploring the Lower Mass Gap and Unequal Mass Regime in Compact Binary Evolution.' ApJL 899, no. 1 (August): L1.

Zinnecker, Hans, and Harold W. Yorke. 2007. 'Toward Understanding Massive Star Formation.' ARA&A 45, no. 1 (September): 481–563.

Zúñiga-Fernández, S., J. Olofsson, A. Bayo, et al. 2021. 'The HD 98800 quadruple pre-main sequence system. Towards full orbital characterisation using long-baseline infrared interferometry.' A&A 655 (November): A15.